MARTIN MARIETTA ENERGY SYSTEMS LIBRARIES

3 4456 0275025 3

ORNL/TM-10444

ornl

OAK RIDGE NATIONAL LABORATORY

MARTIN MARIETTA

Evaluation of HFIR Pressure-Vessel Integrity Considering Radiation Embrittlement

Editors

R. D. Cheverton
J. G. Merkle
R. K. Nanstad

OAK RIDGE NATIONAL LABORATORY
CENTRAL RESEARCH LIBRARY
CIRCULATION SECTION
400A ROOM 175
LIBRARY LOAN COPY
DO NOT TRANSFER TO ANOTHER PERSON
If you wish someone else to see this report, send in name with report and the library will arrange a loan.

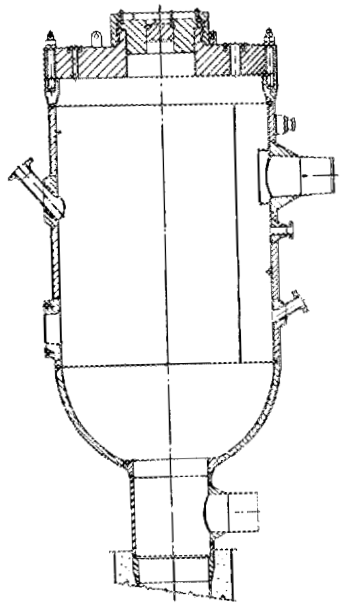

OPERATED BY
MARTIN MARIETTA ENERGY SYSTEMS, INC.
FOR THE UNITED STATES
DEPARTMENT OF ENERGY

Printed in the United States of America. Available from
National Technical Information Service
U.S. Department of Commerce
5285 Port Royal Road, Springfield, Virginia 22161
NTIS price codes—Printed Copy: A13; Microfiche A01

This report was prepared as an account of work sponsored by an agency of the United States Government. Neither the United States Government nor any agency thereof, nor any of their employees, makes any warranty, express or implied, or assumes any legal liability or responsibility for the accuracy, completeness, or usefulness of any information, apparatus, product, or process disclosed, or represents that its use would not infringe privately owned rights. Reference herein to any specific commercial product, process, or service by trade name, trademark, manufacturer, or otherwise, does not necessarily constitute or imply its endorsement, recommendation, or favoring by the United States Government or any agency thereof. The views and opinions of authors expressed herein do not necessarily state or reflect those of the United States Government or any agency thereof.

ORNL/TM-10444

EVALUATION OF HFIR PRESSURE-VESSEL INTEGRITY CONSIDERING RADIATION EMBRITTLEMENT

Editors

R. D. Cheverton J. G. Merkle
Engineering Technology Division

R. K. Nanstad
Metals and Ceramics Division

Date Published - April 1988

Prepared by the
OAK RIDGE NATIONAL LABORATORY
Oak Ridge, Tennessee 37831
operated by
MARTIN MARIETTA ENERGY SYSTEMS, INC.
for the
U.S. DEPARTMENT OF ENERGY
under Contract No. DE-AC05-840R21400

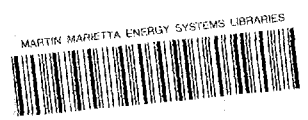

3 4456 0275025 3

PREFACE

In mid-November 1986, the High Flux Isotope Reactor (HFIR) Vessel Integrity Evaluation Committee was appointed by Oak Ridge National Laboratory (ORNL) management to evaluate the effects of radiation damage on the integrity of the HFIR vessel and to make recommendations regarding future operation of HFIR. Shortly thereafter, three Department of Energy (DOE) committees were appointed to review the ORNL effort: the McSpadden Committee (DOE/EH/HQ),* the Hendrie Committee (DOE/ER/HQ),† and the Brinkerhoff Committee (DOE/EH/HQ). The latter committee performed a design review that included "all" aspects of HFIR; the other two were primarily concerned with the vessel. Their efforts were concurrent with the ORNL study and, thus, provided input to the ORNL evaluation. The ORNL Committee is grateful for those contributions.

The nucleus of the ORNL Committee consisted of R. D. Cheverton (Chairman), J. G. Merkle, and R. K. Nanstad, who were the editors of this report. Many others, both technical and support, representing several ORNL divisions, made contributions to the evaluation effort, and those making specific contributions to this report are listed as authors of their sections.

Because of the urgency associated with the ORNL study, considerable extra effort was required and was applied by everyone involved. ORNL management assigned top priority to the HFIR issue, and the response was such that other programs were impacted significantly. The ORNL Committee appreciates the patience and understanding of the sponsors affected.

The ORNL Committee also acknowledges the support of ORNL management, particularly R. S. Wiltshire, ORNL Executive Director, and A. L. Lotts, Program Director for HFIR Operational Assessment and Director of the newly created Research Reactors Division.

---

*Department of Energy/Environment Safety and Health/Headquarters.

†Department of Energy/Energy Research/Headquarters.

CONTENTS

LIST OF FIGURES

LIST OF TABLES

EVALUATION OF HFIR PRESSURE-VESSEL INTEGRITY CONSIDERING RADIATION EMBRITTLEMENT

R. D. Cheverton J. G. Merkle
R. K. Nanstad

ABSTRACT

The High Flux Isotope Reactor (HFIR) pressure vessel has been in service for 20 years, and during this time, radiation damage was monitored with a vessel-material surveillance program. In mid-November 1986, data from this program indicated that the radiation-induced reduction in fracture toughness was greater than expected. As a result, a reevaluation of vessel integrity was undertaken. Updated methods of fracture-mechanics analysis were applied, and an accelerated irradiations program was conducted using the Oak Ridge Research Reactor. Results of these efforts indicate that (1) the vessel life can be extended 10 years if the reactor power level is reduced 15% and if the vessel is subjected to a hydrostatic proof test each year; (2) during the 10-year life extension, significant radiation damage will be limited to a rather small area around the beam tubes; and (3) the greater-than-expected damage rate is the result of the very low neutron flux in the HFIR vessel relative to that in samples of material irradiated in materials-testing reactors (a factor of ~10^4 less), that is, a rate effect.

---

1. INTRODUCTION AND SUMMARY

The design of the High Flux Isotope Reactor (HFIR) pressure vessel included consideration of radiation embrittlement, which enhances the chances of vessel failure as a result of propagation of crack-like defects (flaws). The intent was to surround the core and beryllium reflector with sufficient water and to use sufficiently tough beam-tube nozzle material so that a vessel lifetime of at least 20 effective full-power years (EFPY) could be achieved. The criterion by which vessel integrity was to be judged was that the operating temperature of the vessel should always be greater than the nil-ductility temperature (NDT) plus 60°F.[1] This would prevent very large flaws from propagating in a brittle manner at nominal stress levels equal to and less than the yield stress. For normal operating conditions, the stress level in the shell is maintained below one-half of the yield by operating procedures and relief valves.

The existence of the beam tubes is responsible for the significant radiation damage in the vessel. The tubes displace beryllium and water, which constitute a very effective shield for the vessel. Because of

this, the embrittled portion of the vessel is restricted to small areas around the beam tubes. Contrary to the situation in a light water reactor (LWR), there is not a large, continuous, circumferential band of highly irradiated material in the vessel.

The beam tubes, which are made of an aluminum alloy, are also a part of the primary-system pressure boundary. Because they extend into the beryllium reflector close to the core, they are subjected to rather high neutron fluxes, thus, introducing the possibility of radiation effects. Based on a consideration of corrosion and loss of ductility, the acceptable life of the beam tubes was estimated to be ~10 EFPY, and they were designed to be readily replaceable.

As a check on the predicted radiation damage rates for the HFIR vessel and beam-tube materials and on the beam-tube corrosion rate, a surveillance program was established.[1] Before initial operation of HFIR, Charpy V-notch (CVN) specimens representing the vessel shell and nozzle materials were installed adjacent to the inner surface of the vessel wall at locations of maximum fast-neutron flux, and beam-tube-material tensile and corrosion specimens were included in the beryllium reflector. Specimens of weld material for the vessel seam weld and the nozzle welds were intended to be included in the surveillance program but were not.

The HFIR commenced full-power operation in 1966, and surveillance specimens for the vessel were removed for testing in 1969 (2.3 EFPY), 1974 (6.4 EFPY), 1983 (15.0 EFPY), and 1986 (17.5 EFPY). Results of these tests indicate that in 1983 NDT + 60°F for a portion of the shell and for one nozzle exceeded the minimum temperature for pressurization (70°F) by 45 and 15°F, respectively.[2] The results for 1983 were not available until November 1986, and reactor operation was continued until that time. Since that time, the 1986 surveillance data were obtained, and they indicate that NDT + 60°F for the shell exceeds the normal operating temperature of 120°F by 15°F.[3]

It is believed that the NDT criterion applied to the HFIR vessel is unnecessarily conservative and that the life of the vessel can be extended several years. Because it is important to ORNL and other users of the HFIR experimental facilities that the reactor be operational for at least ten more years, a reevaluation of vessel integrity was conducted using more-sophisticated methods of analysis. These methods were developed since the HFIR vessel became operational and have been accepted by the nuclear industry and by the Nuclear Regulatory Commission (NRC) for application to commercial nuclear-reactor vessels.

As a part of the HFIR vessel-integrity reevaluation study, an irradiations program for the vessel weld and shell materials was conducted in the Oak Ridge Research Reactor (ORR). Nozzle weld material was obtained from a nozzle qualification weld, and seam-weld material was obtained from a recently made weld that duplicated the chemistry of the seam weld. The chemistry of the seam weld was determined from the analysis of drill chips removed from the outer surface of the vessel.

Shell material was included in the ORR irradiations program to index the ORR data to HFIR and to obtain data for flaw orientations relative to the rolling, cross rolling, and thickness directions of the shell plate other than that included in the surveillance program.

A comparison of data from the recent ORR irradiations program with that from much earlier test-reactor materials programs and from the HFIR

surveillance program indicates that the greater-than-expected rate of radiation damage in the HFIR vessel was the result of a 10^4 lower fluence rate in HFIR than in ORR and other materials testing reactors from which HFIR design data were obtained.

The HFIR surveillance program and the ORR irradiation program provided the basic materials data required for the more sophisticated evaluation of vessel integrity. To transpose the data from the surveillance-specimen locations to points of interest in the wall of the vessel, two- and three-dimensional (2- and 3-D) neutron transport calculations were made to obtain ratios of fluxes in the wall to those in the surveillance specimens. By comparing the calculated and "measured" fluxes for the flux monitors in the surveillance capsules, the accuracy of the calculated flux ratios was determined to be satisfactory ($\sigma = \pm 10\%$).

The recent evaluation of the HFIR vessel included the application of linear elastic fracture mechanics (LEFM) in accordance with the American Society of Mechanical Engineers (ASME) Code and a probabilistic fracture mechanics analysis in accordance with methods developed for NRC. The "applicable" section of the ASME Code was written for commercial LWRs and is considered to be unnecessarily conservative for the relatively small, low-temperature HFIR. [Because of the low coolant temperatures (120 to 160°F), HFIR cannot experience a steam explosion in the event of vessel rupture nor could the coolant be lost because the vessel is located in a pool.] Thus, if necessary, some exception might be taken to the Code to extend the life of the HFIR vessel provided that the extent of the exception could be justified.

Two analytical approaches were taken to justify taking some exception to the Code: a probabilistic fracture-mechanics analysis and an evaluation of the consequences of vessel failure. For a life extension of 10 EFPY, the calculated chance of failure for normal operation was $<2 \times 10^{-8}$, and the calculated frequency of failure for infrequent abnormal operating conditions was $<4 \times 10^{-8}$ failures per year, both considered to be very low and, thus, acceptable. In addition, the risk to the public in the event of vessel failure was determined to be negligible. Thus, it was concluded that some reduction in the conservatism in the Code was justified.

The Code analysis for the HFIR vessel included the specified large safety factor for pressure stress (factor of two for normal/upset conditions), the consideration of large flaws (1-in.-deep, 6/1, semielliptical surface flaws for the shell regions), and the use of lower-bound fracture-toughness data. Vessel stresses considered included the nominal pressure stresses, stress concentrations, residual stresses associated with welding, bending stresses associated with geometric discontinuities, and thermal stresses.

The calculated permissible vessel life extension, as determined from the LEFM analysis, is a function of reactor power (radiation damage rate) and primary-system pressure and coolant temperature, and these three parameters are interrelated in the core heat removal analysis. Core heat-removal calculations were made to obtain appropriate combinations of values of these parameters, and these combinations were used in a parametric fracture-mechanics analysis to obtain corresponding values of life extension. Criteria for the core heat removal analysis included a specification of no boiling in the core during normal operation. This meant

that the pressure selected for the low-pressure scram setting had to be sufficient to prevent hot-spot boiling with the power and the coolant inlet temperature at their high-level scram setpoints.

Vessel loadings were divided into normal/upset and emergency/faulted categories. The highest credible pressure was defined as that specified for the rupture disc (safety valves), and this pressure was placed in the emergency/faulted category for which the ASME Code requirements are less stringent. The highest normal/upset pressure was taken as the pressurizer-pump high-pressure trip setpoint. Fracture-mechanics calculations were made for both categories, considering the two applicable Code requirements.

Results of the fracture-mechanics parametric study indicated that for the normal coolant inlet temperature of 120°F and a nominal power level of 85 MW, the permissible life extension of the vessel is ~9 EFPY. This is based on an uncertainty factor of 1.0 for the embrittlement rate of the weld material, which was irradiated in ORR, and on the use of shell material properties pertaining to an axially oriented flaw propagating in a radial direction. The latter represents an exception to the Code, and the former represents an exception to a recommendation of a DOE/EH* review committee. If these exceptions were not taken, the calculated permissible life extension for the HFIR vessel would be <3 EFPY, which is about the minimum time required to make preparations for replacement of the vessel.

The specific exception relating to directional properties is reasonable and has been accepted by the DOE/EH committees, and the uncertainty factor of unity for the weld-metal damage rate might be justified if the surveillance program, with weld metal included, were continued; it is intended that this will be done. However, at the encouragement of one of the DOE/EH review committees, a decision was made to conduct a hydrostatic proof test periodically to further ensure the safe operation of the vessel. A successful hydro test (no vessel failure) proves that whatever combination of stress, fracture toughness, and flaw size actually exists, the vessel is safe to operate for an extended period. The permissible life extension is a function of the ratio of hydro-test pressure to operating pressure and with the aid of the surveillance data can be calculated and selected in a very conservative way. Thus, application of the hydro test negates the need for satisfying the Code without exceptions and permits the application of an appropriate uncertainty factor for the irradiation damage rate in the calculation of the permissible life extension following the hydro.

The beam tubes were replaced in 1975, as originally scheduled, and a reevaluation of beam-tube integrity since that time, based to a large extent on the beam-tube surveillance data and an examination of the replaced beam tubes, indicated that the second set could be used safely for 15 years. A brief discussion of the beam-tube evaluation appears in Appendix A.

Based on the HFIR vessel studies discussed in this report, the Oak Ridge National Laboratory (ORNL) HFIR Vessel Integrity Evaluation

---

*Department of Energy/Environment Safety and Health.

Committee concludes that HFIR can be operated at 85 MW (15% below the original full-power rating) with a nominal coolant inlet temperature of 120°F for a period of at least 10 EFPY, provided that the vessel is subjected to a hydrostatic proof test on a yearly basis and that the surveillance program is continued.

Replacement of the beam tubes should take place at the previously scheduled time, ~3 EFPY from now.

2. VESSEL DESIGN, CONSTRUCTION, AND OPERATING CONDITIONS

R. D. Cheverton J. R. McWherter

As shown in Figs. 2.1 and 2.2, the HFIR vessel is located in a pool, and the lower portion of the vessel extends through the bottom of the pool into the subpile room, where the control-rod drives are located. Figure 2.2 is a vertical cross section of the vessel and surrounding structure, showing the vessel internals; Fig. 2.3 is a vertical cross section providing general information regarding vessel dimensions, design, and materials. A horizontal cross section of the vessel and internals at the horizontal midplane of the core, showing the specific location of the beam tubes and beam-tube nozzles, is provided in Fig. 2.4.

The vessel was designed, fabricated, and inspected in accordance with the edition of the ASME Boiler and Pressure Vessel Code, Sect. VIII, in effect at that time. Section III, which pertains to nuclear vessels, had not been written at the time the vessel contract was awarded. However, all applicable ASME Code cases were applied:

1270 N — General Requirements for Nuclear Vessels (Required double welded butt welds, radiography, stress relief)

1271 N — Safety Devices (At least 2 relief valves, no atmospheric discharge)

1273 N — Nuclear Reactor Vessels and Primary Vessels (Thermal stress analysis required, consider creep and stress rupture, compensate for all openings, full penetration welds, complete radiography)

To meet ASME Code Case 1273 N, a structural analysis was performed by methods described in the Department of Commerce Bulletin, PB 151987, *Tentative Structural Design Basis for Reactor Pressure Vessels and Directly Associated Components*, December 1958 revision.

The vessel was designed for an internal pressure of 1000 psi and a temperature of 200°F. With the reactor at full power (100 MW), the vessel normal pressure and temperature have been ~750 psi and ~110°F. (A discussion of operational pressure and temperature limits is included in Ref. 4 and Appendix B.) The cylindrical part of the vessel is 8 ft in diameter and 10 ft high. The lower head is hemispherical and has a 3-ft-diam appendage that extends down to the subpile room; the top head is flat and is removable (Figs. 2.2 and 2.3). The shell of the vessel was fabricated from American Society for Testing and Materials (ASTM) A212 grade B steel and was roll-bond clad on the inner surface with Type 304L stainless steel and was weld-deposit clad with Type 347 stainless steel on the outer surface. The shell was rolled from a single plate and, thus, contains a single seam weld (Fig. 2.3). The upper flange and the semihead are, of course, attached with circumferential welds. These welds (seam and circumferential) were made using the submerged-arc process.

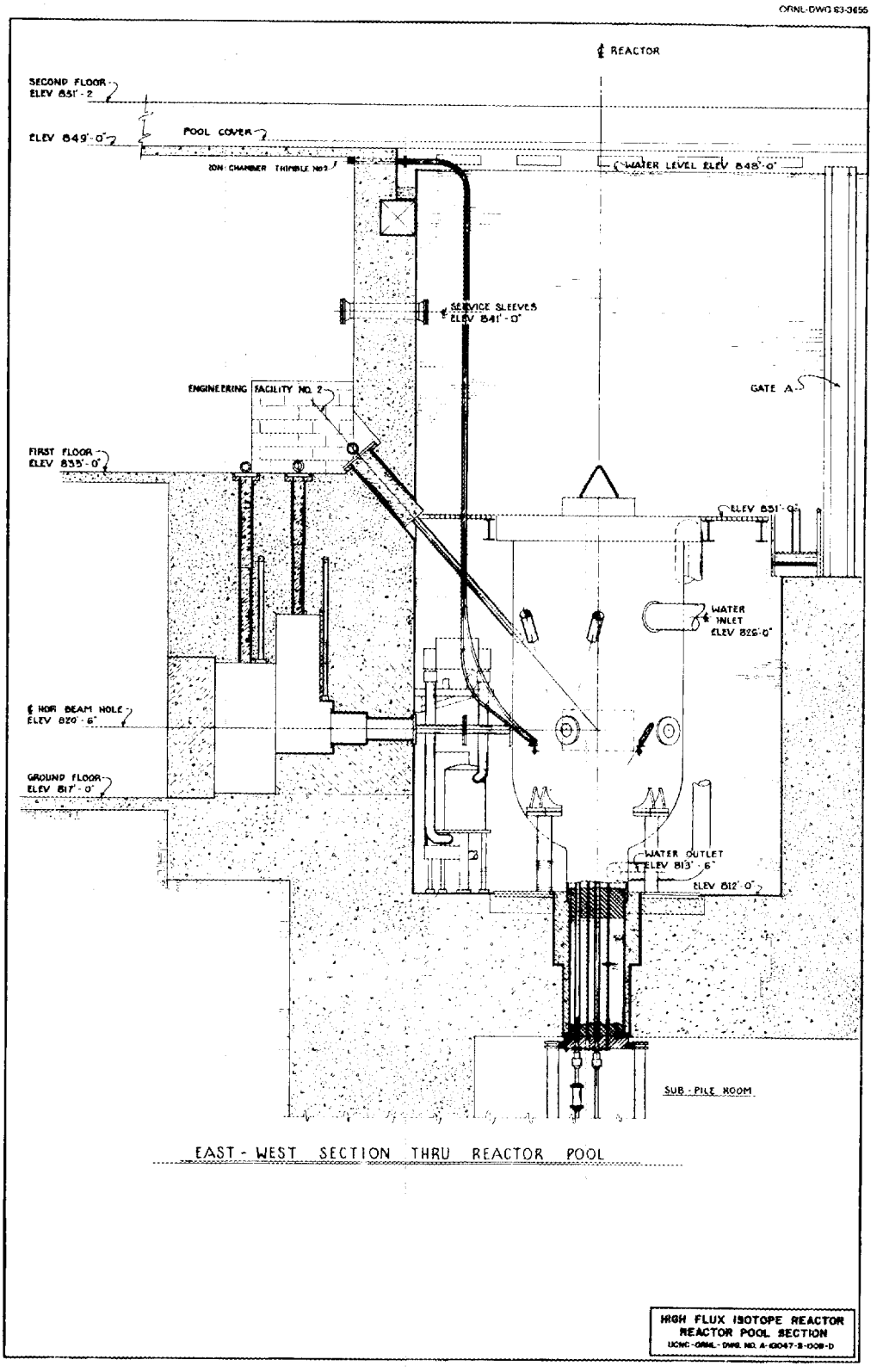

Fig. 2.1. Reactor pool, east-west section.

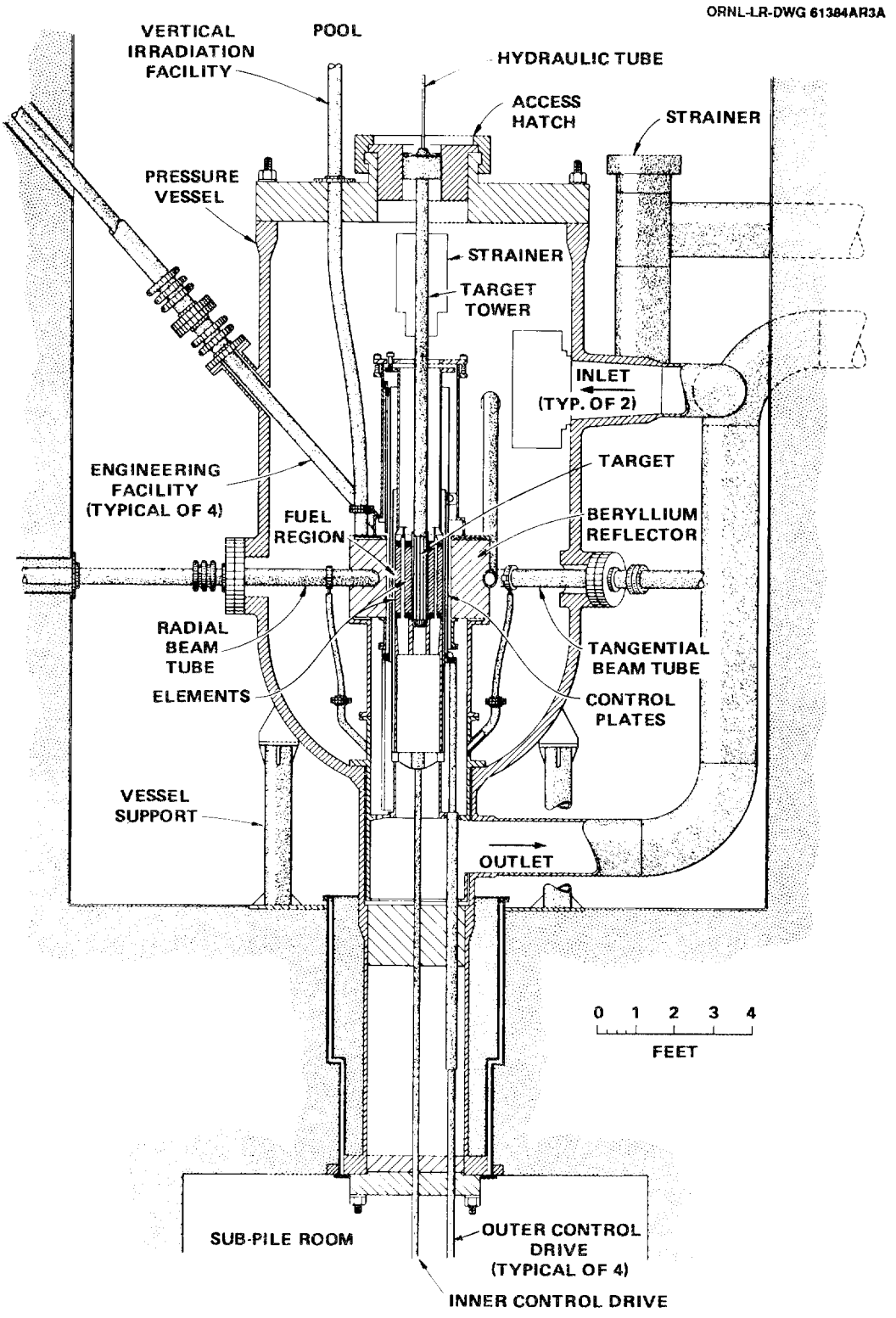

Fig. 2.2. Vertical section of HFIR vessel and core.

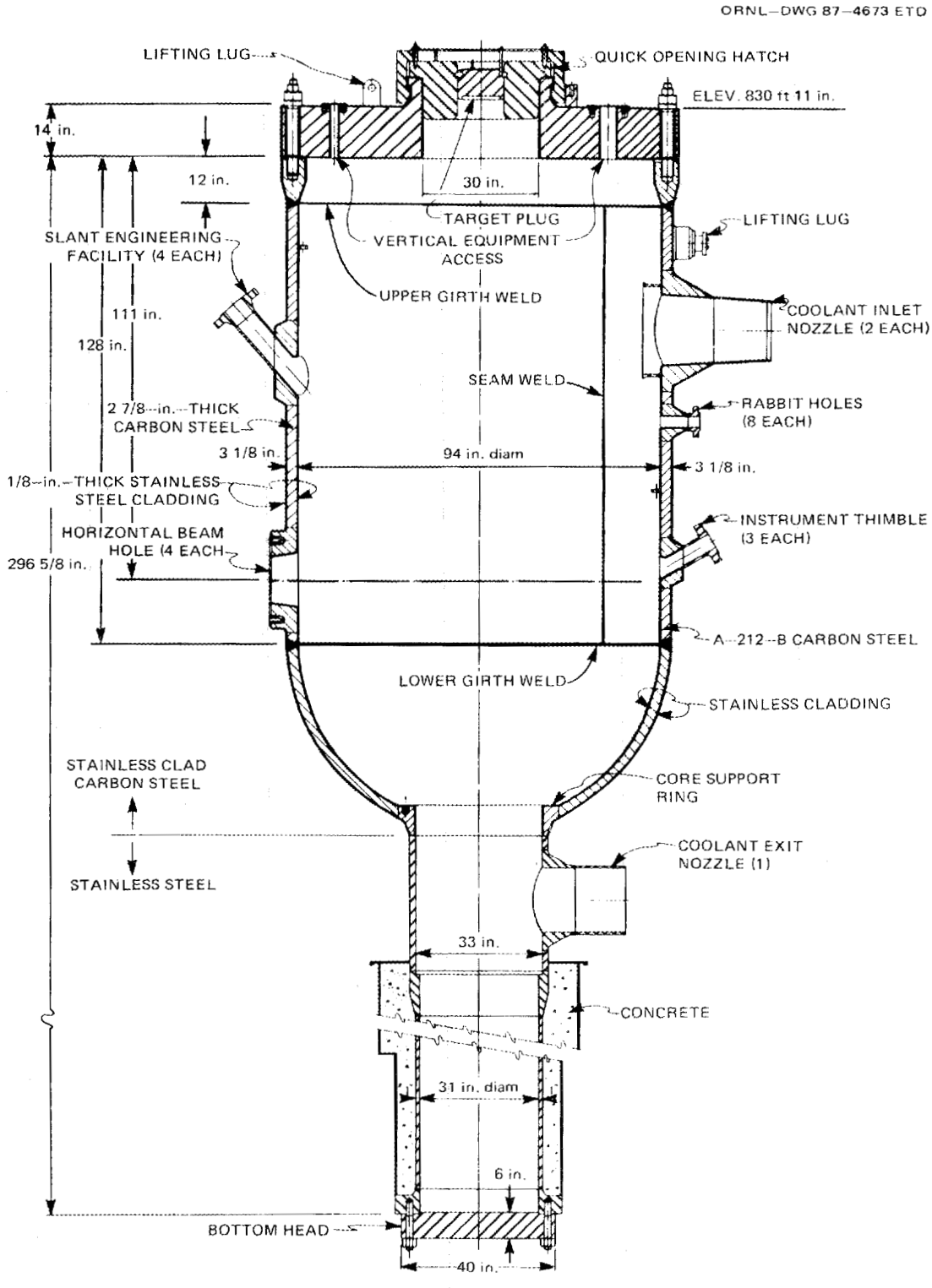

Fig 2.3. Reactor pressure vessel.

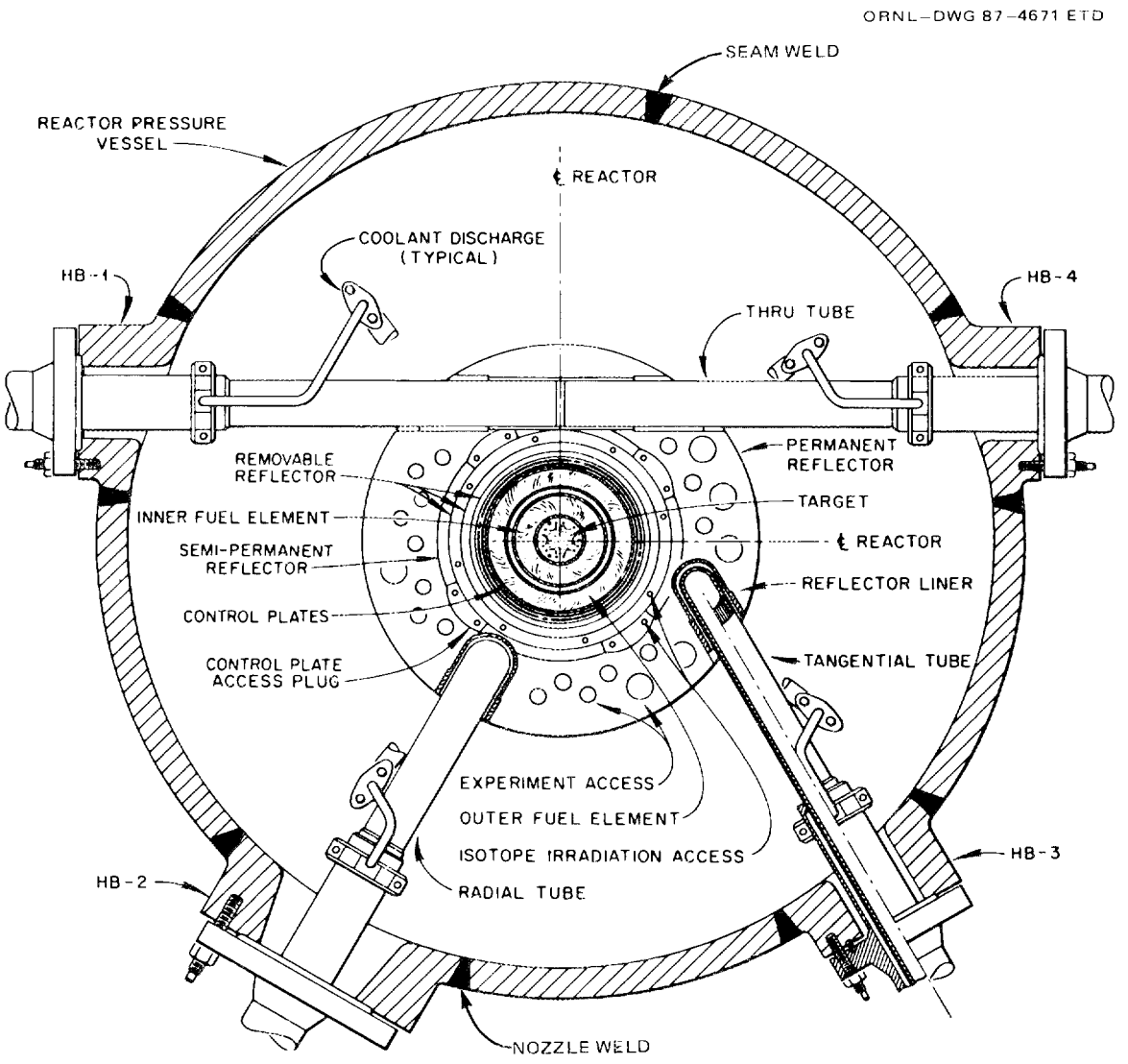

Fig. 2.4. Cross section of reactor core at horizontal midplane showing orientation of beam tubes in reactor core.

The shell contains numerous nozzles for coolant lines, instrumentation, and experimental facilities. All of the nozzles are forgings, some conforming to A105 grade II steel and others to A350 grade LF3 steel. The nozzles were welded in place using the shielded metal-arc process (coated electrodes), and the exposed nozzle surfaces and welds were clad by weld deposition.

The shell was quenched and tempered before rolling and subsequently was subjected to three 17-h stress relief operations at 950°F.

The core of the reactor is located in the lower portion of the vessel just above the lower circumferential weld. The total height of the core is 24 in. (20-in. active height), and the outside diameter of the beryllium reflector is 43 in. Thus, the radial distance between the

vessel and reflector is ~24 in. Water in this space and elsewhere around the core provides shielding for the vessel against gamma energy and fast neutrons.

As indicated in Figs. 2.2–2.4, there are four horizontal beam tubes and four engineering-facility tubes that penetrate the vessel and extend into the reflector. These tubes displace water and beryllium that otherwise would help to shield the vessel.

The design of the HFIR vessel considered neutron-induced radiation embrittlement of the shell, welds, and nozzles. It was intended that the vessel diameter and the nozzle diameter at the nozzle-vessel welds be large enough to preclude significant fast-neutron embrittlement of the shell and welds over 20 EFPY (~24 calendar years). Because of the displacement of water and beryllium by the beam tubes, the beam-tube nozzle forgings are exposed to a much higher fast-neutron flux than the shell. To compensate for this, nozzle materials were selected that could accommodate more radiation damage and still perform satisfactorily for 20 EFPY. The HB-2 and HB-3 beam-tube nozzles are subjected to the highest fast-neutron fluxes, and for these nozzles, A350 grade LF3 material was specified. All other nozzles were fabricated from A105 grade II material.

At the time that the HFIR vessel was designed, the criterion specified for evaluating vessel integrity related to radiation embrittlement was that the NDT of the various components of the vessel plus 60°F should be no greater than the operating temperature of the vessel (T_v); that is, the condition NDT + 60°F $\leq T_v$ was to be satisfied.[1] For normal operation of the reactor, the temperature of the vessel was 120°F, but during pressurization a temperature as low as 70°F was permitted. Thus, the criterion stated that NDT + 60°F $\leq$ 70°F must be satisfied.

As explained in greater detail in Appendix C, NDT is a material property that is related to the fracture toughness of the material, and it increases with increasing fast-neutron fluence, indicating a decrease in the fracture toughness. The increase in NDT can be determined by testing CVN specimens of the materials of interest that have been exposed to radiation.

At the time HFIR was being designed, data relating the increase in NDT to fast-neutron fluence for the HFIR materials and for the relatively low irradiation temperature (120°F) and fluences (~10^{18} n/cm^2) were very limited. Furthermore, the uncertainties associated with the methods used for estimating the fast flux at the vessel wall were large. The fluences predicted for 20 EFPY are included in Table 2.1, and the ΔNDT vs fluence data available at the time are shown in Fig. 2.5. Estimated values of ΔNDT and NDT for 20 EFPY based on these data are also included in Table 2.1. As indicated, it was not expected that NDT + 60°F $\leq$ 70°F would be violated at 20 EFPY.

In Table 2.1 the ability of the nozzle materials to accommodate more radiation damage than the shell material is indicated by the lower initial value of NDT for the nozzle materials. It is also possible that the rate of damage was different for the several materials and different from that indicated in Fig. 2.5 because of differences in the magnitude and spectrum of the fast-neutron flux, chemistry, and the temperature at which the materials were irradiated. Insufficient data were available at the time to account for such variations.

Table 2.1 NDT data for vessel materials based on ORNL curves

Component	Original NDT (°F)	Calculated fast fluence (nvt) 20 years	Expected 20-year shift (°F)	Predicted NDT after 20 years of 100-Mw operation (°F)
HB 1 and 4	−65	1.1×10^{18}[a]	37	−28
HB 2	−115	2.9×10^{18}[a]	80	−35
HB 3	−85	2.3×10^{18}[a]	67	−18
Shell	0	$<10^{18}$[b]	0	0
All other parts	≤+10	$<10^{18}$[b]	0	≤0

[a]Corrected for spectrum shift and other factors.

[b]Not corrected for spectrum shift.

Source: J. R. McWherter, R. E. Schappel, and J. R. McGuffey, *HFIR Pressure Vessel and Structural Components Material Surveillance Program*, ORNL/TM-1372, Union Carbide Corp. Nuclear Div., Oak Ridge Natl. Lab., January 1966.

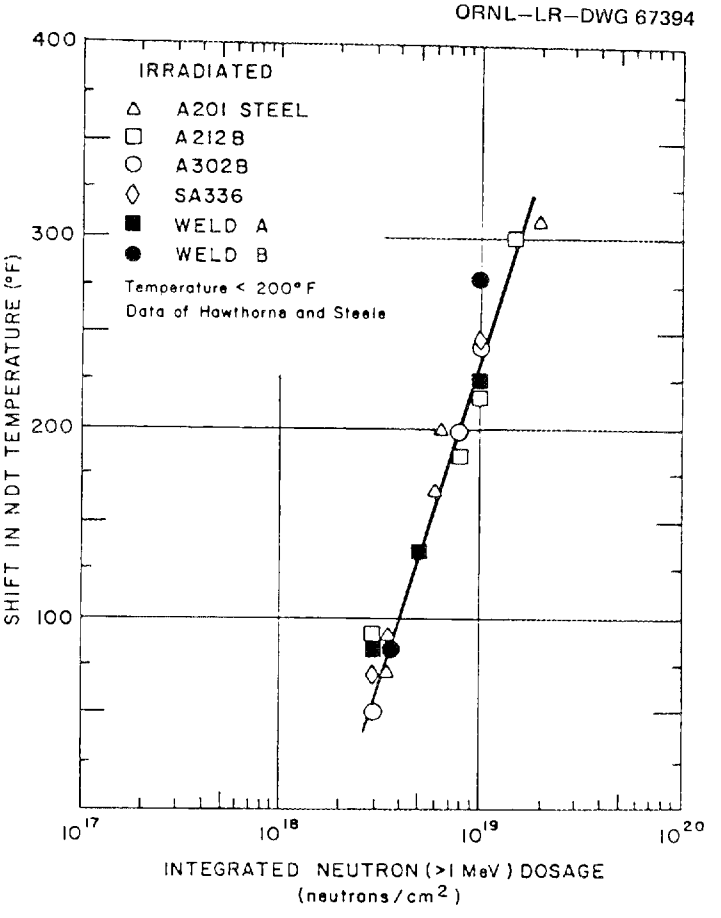

Fig. 2.5. Correlation of transition temperature shifts with total neutron exposure (E > 1.0 MeV) of steel.

In an effort to monitor the actual rate of embrittlement of the HFIR vessel, a surveillance program that has involved the irradiation of shell and nozzle-material CVN specimens in the HFIR vessel was developed. Details and results of this program are discussed in Sect. 3 and Appendix D.

3. SURVEILLANCE PROGRAM

R. D. Cheverton J. G. Merkle
R. K. Nanstad

The HFIR vessel surveillance program was conducted as a means for monitoring the radiation embrittlement rate of specific vessel materials that are subjected to significantly high fast-neutron fluxes. The program, as originally set forth, is described in Ref. 1, the results are reported in Refs. 2 and 3, and a summary of both is included herein.

As mentioned in Sect. 2, vessel integrity, as related to radiation embrittlement, was to be evaluated by comparing NDT of the vessel material to the vessel temperature (T_v). The vessel temperature of interest was the minimum at which pressurization was permitted (70°F). Thus, to be in compliance with the criterion, it was necessary that NDT + 60°F $\leq$ 70°F.

NDT was to be determined from CVN specimens irradiated in the vessel. (The procedure is described in Appendix C.) It was intended that specimens of shell, nozzle, and welds be included; however, only shell and nozzle specimens were placed in the vessel.

Shell CVN specimens were machined from the HB-2 nozzle dropout after the dropout with cladding on both sides was stress relieved at 950°F for 51 h. All (168) shell specimens were oriented so that the fracture surface of the specimen would be normal to the rolling direction of the plate and the fracture would run parallel to the surface of the plate (LT orientation). This orientation corresponds to an axially oriented surface flaw in the vessel extending in surface length and, as an approximation, to the same flaw extending radially through the wall. All specimens were located within 0.25 to 0.38 in. of the clad-base interface at the inner surface of the dropout.

Nozzle-material specimens were machined from nozzle-forging prolongations that received the same stress-relief treatment as the nozzle dropouts. For the HB-1 and HB-4 nozzles, the specimens were oriented parallel to the axis of the nozzle with the notch pointing in a circumferential direction. For HB-2 and HB-3 the specimens were oriented in a radial direction relative to the axis of the nozzle, and the notches pointed in a circumferential direction.

All CVN specimens placed in the HFIR vessel were encapsulated with three specimens per capsule and a single triangular flux monitor in the side-by-side notch. Capsule-specimen clearances were minimized, and the clearance space was purged with helium to minimize the specimen-to-coolant temperature drop resulting from gamma heating. The maximum drop is estimated to be 9°F. Thus, the irradiation temperature of the CVN specimens was in the range of 120 to 129°F.

The general locations of the capsules in the HFIR vessel are shown in Fig. 3.1 and are referred to by "key" number. Nozzle specimens are located in a ring around each beam tube (keys 1–4), and shell specimens are located along an azimuthal line at midheight of the core (keys 6 and 7) and just below midheight (key 5). The key-5 location is behind an ion-chamber thimble; the key 6 and 7 locations are adjacent to the HB-1 and 4 nozzle welds on the high-flux side of the corresponding beam tubes.

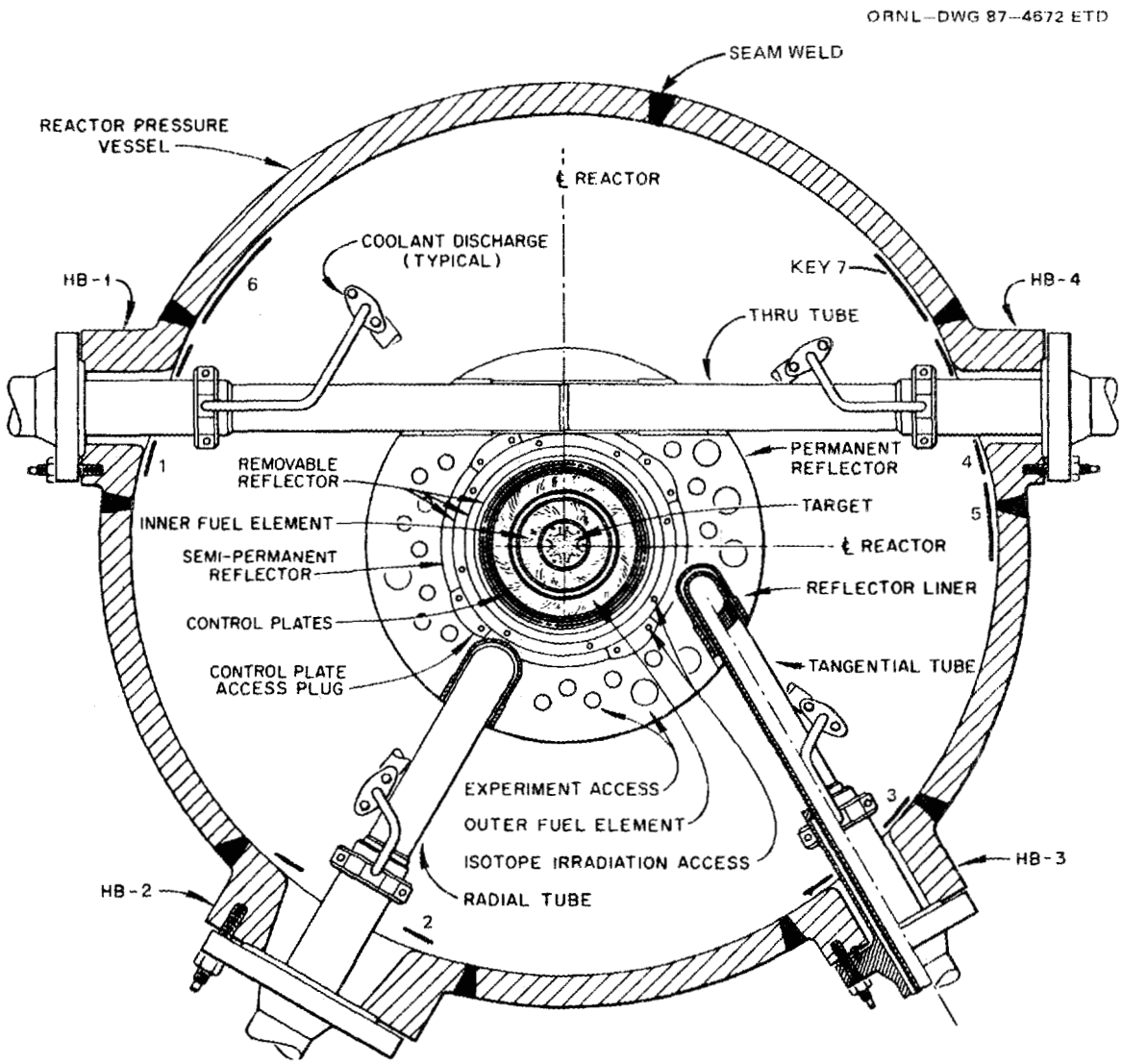

Fig. 3.1. Cross section of HFIR vessel showing locations of surveillance capsules.

The key 6 and 7 capsules closest to the HB-1 and -4 nozzles were expected to see the highest flux for the shell material. However, as indicated in Appendix E, it has recently been determined that the highest flux in the shell is adjacent to HB-3.

All capsules are located close to the inner surface of the vessel. The water gap between capsule and wall is in the range of 0.4 to 0.8 in.

Keys 1, 3, and 4 originally contained 10 capsules each (30 CVN specimens; key 2 contained 16 (48); key 5 contained 5 (15); and keys 6 and 7 contained 8 each (24). Surveillance specimens were withdrawn from the vessel in 1969 (2.3 EFPY), 1974 (6.4 EFPY), 1983 (15.0 EFPY), and 1986 (17.5 EFPY). A summary of the results is included in Table 3.1 and Fig. 3.2. It is apparent that the embrittlement rate was greater than

Table 3.1. NDT temperatures for HFIR vessel CNV surveillance specimens[a]

Component	Material	Key	NDT_o (°F)	NDT + 60 (°F)	
				1983	1986
HB1, HB4 nozzles	A105-II	1, 4	−65	45	
HB2 nozzle	A350-LF3	2	−115	55	75
HB3 nozzle	A350-LF3	3	−85	85	100
Shell (IC3)	A212-B	5	0	80	
Shell (HB1A, HB4A)	A212-B	6, 7	0	115	135

[a]The values in this table are consistent with the data in Refs. 2 and 3. Adjustments were made at a later date and were included in Appendix D. The data in Fig. 3.2 are consistent with Appendix D.

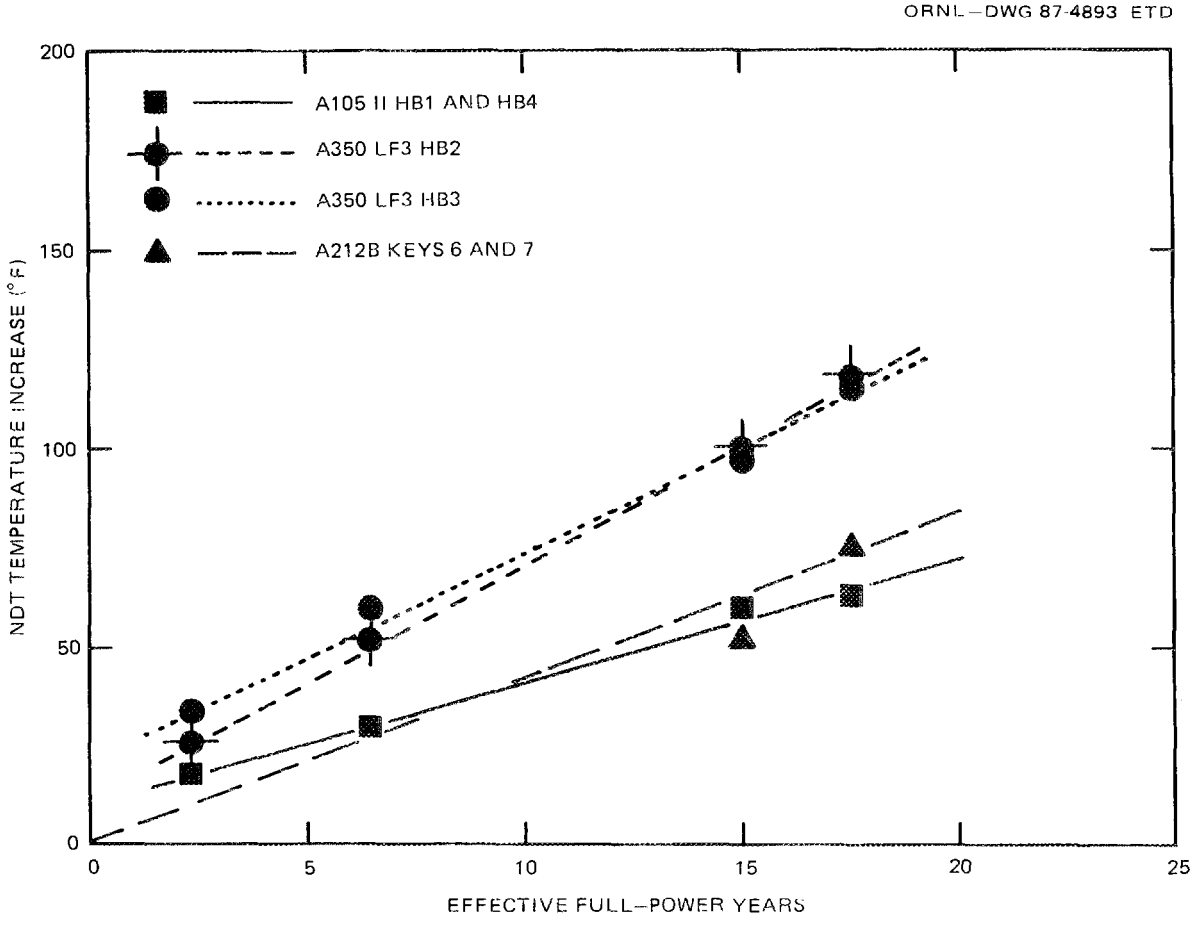

Fig. 3.2. HFIR vessel surveillance data.

predicted (see Table 2.1) and that NDT + 60°F exceeded 70°F before 1983. By 1986, NDT + 60°F for the shell material had exceeded the normal operating temperature of the vessel (120°F) by 15°F. Thus, it was necessary to discontinue operation of the HFIR until a reevaluation of vessel integrity could be completed.

As discussed later, the reevaluation indicates that the life of the vessel can be extended and that in so doing it is desirable to augment and continue the surveillance program. A general discussion of the proposed continuing program is included in Appendix D (Sect. 7), and specific details are included in a separate document (in preparation).

4. PRESSURE-VESSEL INTEGRITY EVALUATION CONCEPTS APPLIED TO HFIR

R. D. Cheverton J. G. Merkle

The specific concern in the reevaluation of the integrity of the HFIR pressure vessel is radiation damage, which reduces the material's ability to resist the propagation of flaws that might exist in the wall. An evaluation of the potential for vessel failure as a result of flaw propagation requires knowledge of the existence and characterization of flaws, of the stresses in the wall, and of the material's fracture resistance. At the time the HFIR vessel was being designed, the Pellini fracture-control criteria[5] were specified and relied upon to protect against vessel failure associated with propagation of flaws. This fracture-control concept, which is discussed in greater detail in Appendix C, constitutes an empirical relation [fracture-analysis diagram (FAD)] among critical values of flaw size, stress level, and temperature relative to NDT. For instance, the FAD indicates that for a temperature of NDT + 60°F, a nominal stress level equal to the yield stress is required for very large flaws to propagate. If there is concern about actual stress levels and flaw sizes, this specific criterion ($T_v \geq$ NDT + 60°F) might be appropriate. As indicated in Sects. 1 and 3, it was specified for the HFIR vessel.

A more sophisticated and accurate method of evaluating flaw behavior for stresses below yield is referred to as LEFM.[6] As discussed in Appendix C, this method involves the calculation of the stress-intensity factor K_I and the measurement of a critical value K_{Ic} or K_{Id} such that crack propagation takes place when $K_I = K_{Ic}$ or K_{Id}. K_{Ic} corresponds to static loading, K_{Id} to dynamic loading, and $K_{Id} \leq K_{Ic}$. There is also a critical value of K_I corresponding to arrest of a running crack (K_{Ia}), and $K_{Ia} < K_{Id}$. K_I increases with stress and crack size, and fracture toughness (K_{Ic}, K_{Id}, K_{Ia}) increases with temperature and decreases with fast-neutron fluence.

The present version of the ASME Code specifies the use of LEFM in the design of LWR vessels, and in so doing, it also specifies the minimum flaw size that must be considered and the maximum fracture toughness (as a function of $T - RT_{NDT}$*) that must be used in the absence of plant-specific data. It also includes a degree of conservatism that is appropriate for commercial LWR vessels, considering the consequences of vessel failure. However, because HFIR is so much smaller than a commercial LWR and because HFIR operates at a low enough coolant temperature to preclude a steam explosion in the event of vessel failure, the degree of conservatism in the Code is unnecessarily high for the HFIR vessel. This would not be of concern except that the relatively low operating temperature for HFIR results in relatively low values of $T - NDT$; that is, in accordance with the Code, much less radiation damage can be tolerated in the

---

*RT_{NDT}, the reference nil-ductility temperature, is closely related to NDT. See Appendixes C and D and Sect. 5 for further discussion.

HFIR vessel. At this time in the life of the HFIR vessel, it is possible that some exception might have to be taken to the Code to permit a reasonable life extension. This idea is considered to be acceptable because the consequences of vessel failure are acceptable (see Appendix F) and because the calculated probability of failure is very low (see Appendix G). However, specifying the extent to which exceptions can be taken can be difficult.

There is a satisfactory alternative; it involves conducting a hydrostatic proof test at specified intervals of time. A successful test (no through-wall cracking) demonstrates in a very convincing way that whatever combination of stress, fracture toughness, and flaw size actually exists, the vessel is safe to operate. The permissible life extension following a proof test is related to the difference between proof-test pressure and operating pressure and can be calculated in a conservative manner, using data from a continuing surveillance program.

The use of LEFM and hydrostatic proof testing does not eliminate the need to consider the proximity of the vessel temperature to NDT. As indicated above, the fracture toughness used in the LEFM analysis is a function of $T - RT_{NDT}$. In addition, if a flaw did propagate, the tendency for fragmentation would be greater for smaller values of $T - NDT$. Fragmentation is considered not to be a problem for the HFIR vessel if it is confined to a small area around the beam tubes. This is ensured by specifying that a large fraction of the circumference of the HFIR vessel at an elevation corresponding to midheight of the core satisfies $T_V \geq NDT + 30°F$.

The application of the above techniques to the evaluation of the integrity of the HFIR vessel is discussed in detail in Sect. 5.

5. FRACTURE-MECHANICS EVALUATIONS

J. G. Merkle R. D. Cheverton

5.1 ASME CODE APPROACH

The basic problem concerning the HFIR vessel is changed material properties as a result of neutron irradiation; no recordable flaw indications have been discovered by nondestructive inspection. The initial approach taken to this problem was to formulate a set of LEFM criteria based on procedures presently contained in Sects. III and XI of the ASME Code.[7,8] Pending the completion of a neutron flux analysis, surveillance properties were applied without making corrections for actual position in the vessel. Vessel welds were not included in the surveillance program, but accelerated irradiation data for the welds were obtained using the ORR. Pressure-induced stresses only were considered, and a factor of safety of 2.0, as required by the Code, was applied to the pressure stresses. Following Appendix G of Sect. III, a reference surface flaw 1.0 in. deep and 6.0 in. long in the vessel cylinder was considered. For normal operating conditions, this flaw represents the size and shape of a perimeter in base or weld metal within which a hypothetical crack propagating from a small region of local embrittlement must be arrested. A 1.0-in.-deep crack at the inside corner of the HB-3 nozzle was also considered. Without considering flux attenuation, the nozzle corner appeared to be the governing location.

To obtain at least 3 years of additional safe remaining service life, it was found necessary either to justify an elevation of toughness above the Code default (lower bound) values or to reduce the pressure with a probable concurrent reduction in power level. Some evidence to support a toughness elevation was presented, both in terms of (1) a correlation between the surveillance specimen Charpy data and dynamic fracture toughness and (2) measurements by others of the crack-arrest toughness of A212 steel.[9] However, the McSpadden Committee was unwilling to accept either one as meeting the intent of the Code with respect to data for the particular material of interest, requiring, instead, actual crack-arrest toughness measurements of the HFIR plate. To date, such tests have not been performed because it now appears that a satisfactory resolution of the issue can be achieved without them.

Because of the low stresses induced by pressure, and without considering residual and thermal stresses or including large uncertainty factors for the radiation damage data, it was possible to show an adequate amount of remaining service life for the HFIR vessel by reducing the power level ~15%. However, the Hendrie Committee felt that despite the fact that the vessel had been stress relieved at 950°F for 51 h after welding, residual welding stresses might be significant relative to pressure-induced stresses because of the low magnitude of the latter and, thus, should be added to the pressure stresses rather than be accommodated by the Code safety factors. In addition, the Brinkerhoff Committee postulated that because of uncertainties in the estimation of irradiation damage-rate effects for the weld material tested in ORR, a large uncertainty factor (1.5) should be applied to the NDT shift for weld metal.

These considerations complicated the analysis largely because they led to the need to consider multiple flaw locations and orientations; of course, they also reduced the calculated life extension.

Revised LEFM analyses that included all secondary stresses, as recommended by the DOE/EH committees, and that used detailed calculated fluxes as they became available were developed. The secondary stresses included residual stresses after stress relief, based on elastic-plastic thermal stress analysis and stress relaxation data; thermal stresses; and the effects of stress gradients caused by local bending around nozzles.

Following Appendix G of Sect. III of the ASME Code for Nuclear Vessels,[7] the stress-intensity factors associated with primary (pressure-induced) and secondary (thermal and weld-residual) stresses are weighted by safety factors and added to produce a total, which is compared with the lower-bound toughness of the material. The safety factors are 2.0 for primary stresses and 1.0 for secondary stresses. Thus,

$$K_{I_{TOT}} = 2\,K_{I_p} + (K_{It} + K_{Ir}) \,. \tag{1}$$

For normal and upset conditions, the applicable toughness is defined by the K_{IR} curve shown in Fig. 5.1. K_{IR} is a lower bound to dynamic initiation and crack-arrest data. The equation of the K_{IR} curve is[10,11]

$$K_{IR} = 26.8 + 1.223\, e^{0.0145(T-RT_{NDT}+160)} \,. \tag{2}$$

For emergency and faulted conditions, the applicable toughness is defined by the K_{Ic} curve shown in Fig. 5.2. The K_{Ic} curve is a lower bound to static initiation data. The equation of the K_{Ic} curve is[11]

$$K_{Ic} = 33.2 + 2.806\, e^{0.02(T-RT_{NDT}+100)} \,. \tag{3}$$

Because Eqs. (2) and (3) are both of the form

$$K_{IR} \text{ or } K_{Ic} = A + B\, e^{c(T-RT_{NDT}+D)} \,, \tag{4}$$

the permissible extended operating time for each load and flaw configuration can be calculated in two steps. First, the minimum allowable value of $T - RT_{NDT}$ is determined from Eq. (4) by specifying that $K_{I_{TOT}} \leq K_{Ic}$ or K_{IR}. Thus,

$$T - RT_{NDT} = \frac{1}{c}\, \ell n \left[\frac{\dfrac{K_{I_{TOT}}}{q} - A}{B} \right] - D \,, \tag{5}$$

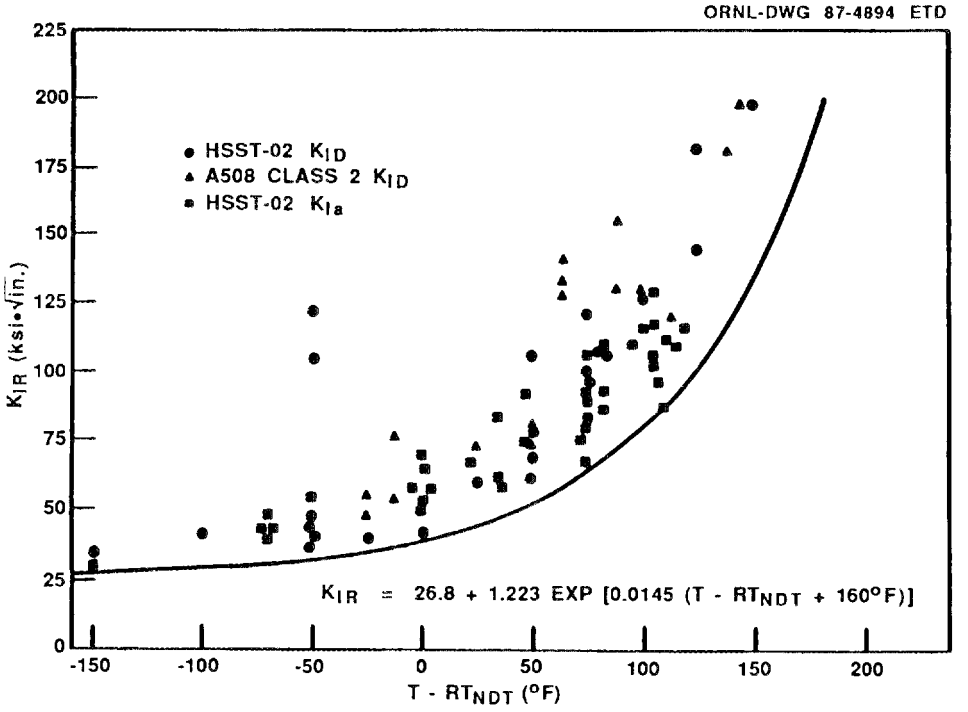

Fig. 5.1. ASME lower-bound K_{IR} curve and supporting data.

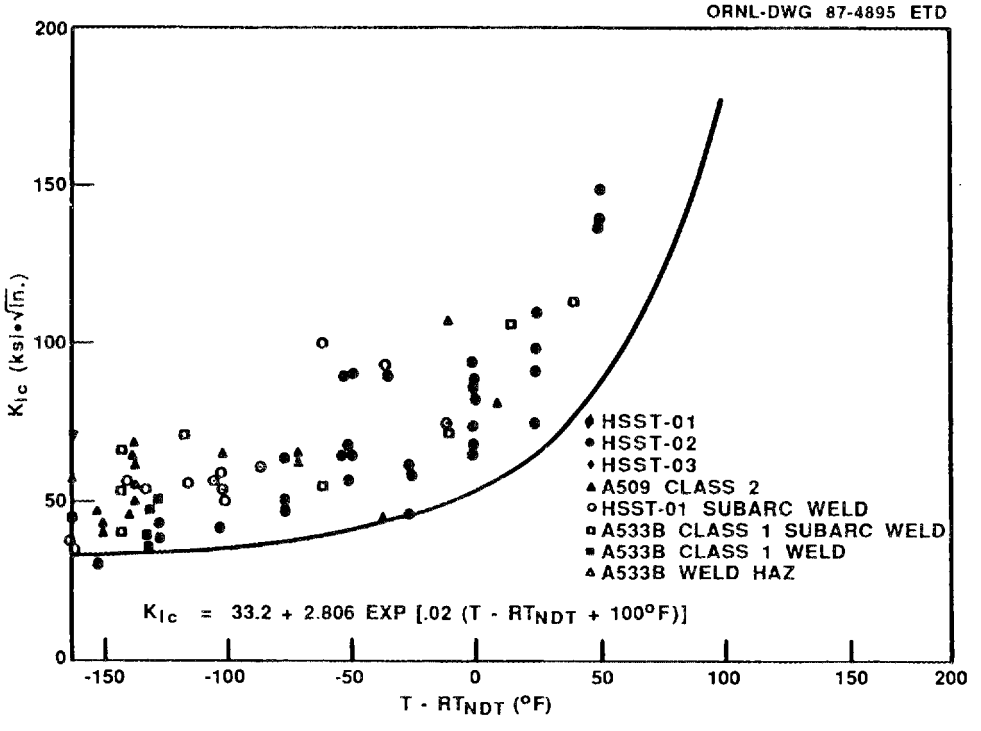

Fig. 5.2. ASME lower-bound K_{Ic} curve and supporting data.

where q is the toughness elevation factor, which is 1.0 without a toughness elevation, and T is the crack-tip temperature. Then the permissible operating time is calculated from

$$\Delta t = \frac{RT_{NDT} - RT_{NDT-86}}{f \cdot S_{FP}} , \qquad (6)$$

where RT_{NDT-86} is the present value (November 1986) of RT_{NDT} at the crack-tip location; f is the power reduction factor; and S_{FP} is the rate of increase of RT_{NDT}, with respect to operating time, at the specified crack-tip location and at a power level of 100 MW.

5.2 LOADING CONDITIONS

The ASME Code identifies four categories of loading conditions: normal; upset; emergency and faulted; and a set of corresponding stress limit categories: A, B, C, and D.[12] The loading conditions are defined by the ASME Code in terms of either the loads included or the physical consequences to the component. Normal loads include all normal service loads, plus the pressure surges and effects of instrument errors that can occur during normal operation. Upset conditions must not cause damage necessitating repair. Emergency conditions may cause discontinuity strains necessitating inspection and repair. Faulted conditions may cause general deformations necessitating repair or replacement of the component. The NRC *Standard Review Plan*[13] defines the same load and stress-limit categories in terms of the specific loads included in each. Normal and upset loads include sustained loads, specified operating transients, and the operating basis earthquake (OBE). The OBE loading for HFIR is 0.078 g of horizontal acceleration. The earthquake-induced axial stresses in the HFIR vessel at the core elevation are small (a few hundred pounds per square inch), and the circumferential stresses are even smaller.[14] These stresses are not significant. Consequently, if the control system for limiting the primary system pressure is made to satisfy safety-grade requirements, then the pressurizer-pump trip pressure should be the pressure limit for upset conditions, and it has been so assumed in this evaluation.

For power reactors, the standard review plan lists the loads that must be considered as potential emergency and faulted loads. These include those associated with guillotine pipe breaks, the safe shutdown earthquake (SSE), and loss of coolant accidents. Because the primary system piping is constructed of stainless steel, it should not be necessary to consider guillotine cleavage pipe fractures. Furthermore, because the release of ~30 gal of water is sufficient to depressurize the primary system, pipe whip effects would be negligible even if a guillotine pipe break did occur. In the event of a pipe break, external pool water would enter the primary system through a check valve when primary system pressure becomes less than pool hydrostatic pressure. Because the pool water temperature is only 25°F less than the vessel temperature and

the flow rate through the check valve is rather low, a severe thermal shock to the reactor vessel following a pipe break is not possible. The SSE acceleration is 0.15 g, for which the stresses in the vessel at core elevation are not significant with regard to causing crack extension.

The HFIR control system is designed to function under all loading conditions that are considered credible, and for all of these, there is no significant increase in the pressure applied to the vessel. Consequently, a conservative value of the maximum stresses produced by emergency and faulted conditions should be obtainable by calculating the stresses produced by the pressure required to fail the rupture disc.

Although pressure transients severe enough to raise the pressure significantly above that corresponding to the rupture disc specification are considered to be incredible, an ORNL HFIR review committee requested an evaluation of the ability of the vessel to withstand much more severe transients. This evaluation is discussed in Appendix H.

Startup procedures pose no problem for the HFIR vessel because the primary system will be heated before being pressurized. Past practice for shutdown has been to scram the reactor and leave the pressurizer pumps running. This resulted in cooling of the primary system with the system pressurized. For future operation, the control system will be modified to maintain the primary system temperature or, if necessary, to depressurize the primary system by tripping the pressurizer pump and opening an auxiliary letdown valve.

5.3 MATERIAL PROPERTIES

Material properties for all of the HFIR pressure-vessel materials are discussed in Appendix D. A summary of the data used as input to the fracture-mechanics analysis is presented in Table 5.1, which appears as Table D.21 in Appendix D. ORR irradiations data listed in the "HFIR" column are the equivalent values for 1986 (17.5 EFPY) at the key 7, position 8 location in the HFIR vessel if those materials had been included in the HFIR surveillance program. It was possible to obtain such data from ORR by including A212B (LT) material in both the HFIR surveillance program and in the ORR program. As indicated below, it is necessary to transpose the values in the "HFIR" column to other points of interest in the vessel by using the ratio of the neutron flux at the point of interest to that of the appropriate surveillance location (key 7, position 8 for the ORR data).

The data in Table 5.1 and the calculated fluxes from Appendix E are combined to obtain values of S_{FP} and RT_{NDT-86} for seven potential crack locations and multiple depth positions for each location (Table 5.2). In Table 5.2, ϕ_{REF} is the neutron flux corresponding to the reference surveillance specimen location, and S_{REF} is the rate of increase of RT_{NDT}, consistent with a power level of 100 MW, at the surveillance specimen position. Note that the rates of increase of NDT and RT_{NDT} are assumed to be the same.

Table 5.1. Summary of irradiation effects on HFIR pressure-vessel materials

Material	Unirradiated		ΔNDT (°F)		Damage rate[b] (°F/EFPY)
	NDT (°F)	RT_{NDT}[a] (°F)	ORR	HFIR 17.5 EFPY	
ORR irradiations					
A212B (LT)	−5	20	100	75	4.28
A212B (TL)	10	15[c]	85	64	3.64
A212B (TS)	−5	0	100	75	4.28
A212B (LS)	−10	−10	*d*	75[d]	4.28
Nozzle weld	0	10	80	60	3.42
Seam weld	−5	60	85	64	3.64
Surveillance data					
A212B (LT)[b]	−5	20		75	4.28
A105 II	−80	−40		63	2.96
A350 LF3 (HB2)	−110	−110		117	5.94
A350 LF3 (HB3)	−80	−78		113	5.09

[a]Determined from T_{50} − 60°F, where T_{50} is the temperature at which the mean Charpy energy less one standard deviation is equal to 50 ft-lb.

[b]Power level = 100 MW.

[c]50 ft-lb not achieved in this orientation; RT_{NDT} determined from the temperature at which 0.035-in. lateral expansion is achieved less 60°F.

[d]Not irradiated in ORR; assume ΔNDT = ΔNDT of A212B (LT) and A212B (TS).

The neutron flux at a given depth position in the wall is calculated from

$$\phi = \phi_o e^{-\lambda x} , \tag{7}$$

where ϕ_o is the calculated inside-surface flux, x is depth in inches from the inside surface, and λ is a constant obtained from the calculated values of ϕ at x = 0 and 1 in. The value of S_{FP} at a given position is calculated from

$$S_{FP} = S_{REF} \cdot \frac{\phi}{\phi_{REF}} , \tag{8}$$

Table 5.2. Calculated values of S_{FP} and RT_{NDT-86}

Location	Material[a]	Depth (in.)	$\phi_{REF}/10^8$ (n/cm²·s)	$\phi_{FP}/10^8$ (n/cm²·s)	S_{REF} (°F/year)	S_{FP} (°F/year)	k (°F)	e = 17.53 EFPY ΔNDT^b (HFIR-86) (°F)	RT_{NDTo} (−1σ) (°F)	$RT_{NDT}{}^b$ (HFIR-86) (°F)	λ (in.$^{-1}$)
Vertical seam weld, core horizontal midplane (HMP)	Seam weld	0	2.68	1.17	3.64	1.59	0	27.86	60	87.86	0.1462
		0.5	2.68	1.09	3.64	1.48	0	25.89	60	85.89	
		1.0	2.68	1.01	3.64	1.37	0	24.07	60	84.07	
		2.0	2.68	0.873	3.64	1.19	0	20.80	60	80.80	
		2.5	2.68	0.812	3.64	1.10	0	19.33	60	79.33	
		3.0	2.68	0.755	3.64	1.03	0	17.97	60	77.97	
Base metal, key 7, position 8 (HMP)	A212, grade B, keys 6 and 7 (LT)	0	2.68	2.58	4.28	4.12	0	72.22	20	92.22	
		0.5	2.68	2.25	4.28	3.59	0	62.93	20	82.93	
		1.0	2.68	2.00	4.28	3.19	0	55.92	20	75.92	
		2.0	2.68		4.28		0		20		
		2.5	2.68		4.28		0		20		
		3.0	2.68		4.28		0		20		
Base metal adjacent to HB-3 weld (HMP)	A212, grade B, keys 6 and 7 (LT)	0	2.68	4.65	4.28	7.43	0	130.25	20	150.25	0.1506
		0.5	2.68	4.31	4.28	6.88	0	120.61	20	140.61	
		1.0	2.68	4.00	4.28	6.39	0	112.02	20	132.02	
		2.0	2.68	3.44	4.28	5.49	0	96.32	20	116.32	
		2.5	2.68	3.19	4.28	5.10	0	89.34	20	109.34	
		3.0	2.68	2.96	4.28	4.73	0	82.86	20	103.86	
Nozzle weld adjacent to nozzle forging (HMP)	Nozzle weld	0	2.68	5.30	3.42	6.76	0	118.50	10	128.50	0.1417
		0.5	2.68	4.94	3.42	6.30	0	110.44	10	120.44	
		1.0	2.68	4.60	3.42	5.87	0	102.90	10	112.90	
		2.0	2.68	3.99	3.42	5.09	0	89.30	10	99.30	
		2.5	2.68	3.72	3.42	4.75	0	83.20	10	93.20	
		3.0	2.68	3.46	3.42	4.42	0	77.51	10	87.51	
HB-3 nozzle corner, directly above nozzle axis	A350, LF-3, HB-3	z = 5.5	17.25	7.90	5.09	2.33	23.9	64.74	−78	−13.26	
		x = 1.5	17.25	11.10	5.09	3.28	23.9	81.40	−78	3.40	
Base metal adjacent to HB-3 weld, directly above nozzle axis	A212, grade B, keys 6 and 7 (LT)	0	2.68	1.73	4.28	2.76	0	48.43	20	68.43	0.1506
		0.5	2.68	1.60	4.28	2.56	0	44.92	20	64.92	
		1.0	2.68	1.49	4.28	2.38	0	41.72	20	61.72	
		2.0	2.68	1.28	4.28	2.04	0	35.84	20	55.84	
		2.5	2.68	1.19	4.28	1.90	0	33.24	20	53.24	
		3.0	2.68	1.10	4.28	1.76	0	30.83	20	50.83	
Nozzle weld adjacent to nozzle forging directly above nozzle axis	Nozzle weld	0	2.68	1.97	3.42	2.51	0	44.07	10	54.07	0.1417
		0.5	2.68	1.84	3.42	2.34	0	41.06	10	51.06	
		1.0	2.68	1.71	3.42	2.18	0	38.25	10	48.25	
		2.0	2.68	1.48	3.42	1.89	0	33.19	10	43.19	
		2.5	2.68	1.38	3.42	1.76	0	30.92	10	40.92	
		3.0	2.68	1.29	3.42	1.64	0	28.81	10	38.81	

[a] Conversion table for A212 B, (LS), (TS), and (TL)

Material	S	RT_{NDTo} (−1σ)
A212 B (LS)	A212 B (LT)	A212 B (LT) − 30°F
A212 B (TS)	A212 B (LT)	A212 B (LT) − 20°F
A212 B (TL)	Seam weld	Seam weld − 45°F

[b] Adjusted for flux at the crack-tip location.

where ϕ is the neutron flux at the crack tip in the wall. RT_{NDT-86} is then calculated from the expression

$$RT_{NDT-86} = \underset{(-1\sigma)}{RT_{NDTo}} + k + 17.53\ S_{FP}\ , \tag{9}$$

where 17.53 is the number of full-power (100-MW) years accumulated up to shutdown in 1986. Note that k is the linear intercept of the ΔNDT vs t plot for 100 MW, and it was assumed not to vary with power level.

5.4 THERMAL AND BENDING STRESSES

In preliminary calculations, thermal and bending stresses were considered small enough to be neglected or accounted for in the large safety factor in the Code. In the present calculations they are considered as separate entities. The temperature gradients are calculated using the coolant and pool temperatures, the vessel conductivity, and a boundary-layer heat transfer coefficient as independent variables. For the dimensions of the HFIR vessel, the inside-surface thermal stress is calculated from[15]

$$\sigma_{ta} = -0.53\ \frac{E\alpha\ \Delta T}{(1-\nu)}\ , \tag{10}$$

and the outside-surface thermal stress from[15]

$$\sigma_{tb} = 0.47\ \frac{E\alpha\ \Delta T}{(1-\nu)}\ , \tag{11}$$

where E is the elastic modulus, α is the coefficient of thermal expansion, ΔT is the inside-surface temperature minus the outside-surface temperature, and ν is Poisson's ratio. The temperature at the crack-tip depth is calculated from

$$T = T_c - 12.5\ \eta\ \left(\frac{1}{2} + \frac{x}{W}\right)\ , \tag{12}$$

where

$$\eta = \frac{T_c - T_p}{50}\ . \tag{13}$$

T_c and T_p are the coolant and pool temperatures, respectively, x is depth

from the vessel inner surface, and W is the vessel wall thickness. Thermal stresses are treated as linearly varying bending stresses for the fracture-mechanics analysis. The thermal stress contribution to the stress-intensity factor is generally small.

The finite-element calculations performed for analyzing a nozzle corner crack in the HB-3 nozzle[16] also yielded detailed stress distributions in the vicinity of the nozzle-to-shell weld. At the core horizontal midplane, the circumferential membrane stress is 20% less than the nominal value because of the proximity of the inside surface of the nozzle. In addition, the circumferential bending stress at the inside surface at the core horizontal midplane is compressive. Both of these effects are beneficial with regard to the propagation tendency of an inside-surface axial flaw in the highest-fluence region of the nozzle-to-shell weld. On the other hand, directly above the nozzle axis in the vicinity of the nozzle-to-shell weld, the circumferential membrane stress is 7% above the nominal value, and the bending stress is tensile on the inside surface of the vessel. However, the inside-surface fluence at this location is less than one-half of the value at the core horizontal midplane. The shell bending stresses are generally larger than the thermal stresses and, thus, contribute more to the total stress-intensity factor, generally about 10 to 15%.

5.5 RESIDUAL STRESSES

Appendix G of Sect. III,[7] Appendix A of Section XI,[8] and the NRC *Standard Review Plan*[13,17] make no specific mention of residual welding stresses in the description of methods acceptable for providing adequate margins against brittle fracture. This is apparently because it is assumed that if the vessel is properly stress relieved after welding, then the residual welding stresses will be small compared with the other stresses. In the case of the HFIR vessel, the pressure-induced stresses are unusually low. For this reason, the Hendrie Committee postulated that the residual welding stresses, although low, might still be significant relative to the pressure induced stresses and should, therefore, be considered. Direct measurement of the residual stresses in the HFIR vessel nozzle welds would be impractical. Furthermore, standard procedures for estimating welding residual stresses do not exist, and reliance must, therefore, be placed on analytical and experimental research results.

Residual stresses are the result of restrained thermal contraction, yielding, and postweld stress-relieving conditions. They are both geometry and material dependent. For example, the residual stresses in a circumferential pipe weld would be expected to be quite different from those in a longitudinal vessel seam weld or a nozzle-to-vessel cylindrical shell weld. Experimental data for residual stresses in longitudinal welds in 1-in.-thick, 3 ft by 3 ft A212 grade B plates, both before and after stress relief, were obtained by Nordell and Hall[9,18] at the University of Illinois. Figure 5.3(*a*) shows the through-thickness average residual stresses in the as-welded plate, and Fig. 5.3(*b*) shows the longitudinal stresses after stress relief at 1150°F for 1 h. The through-

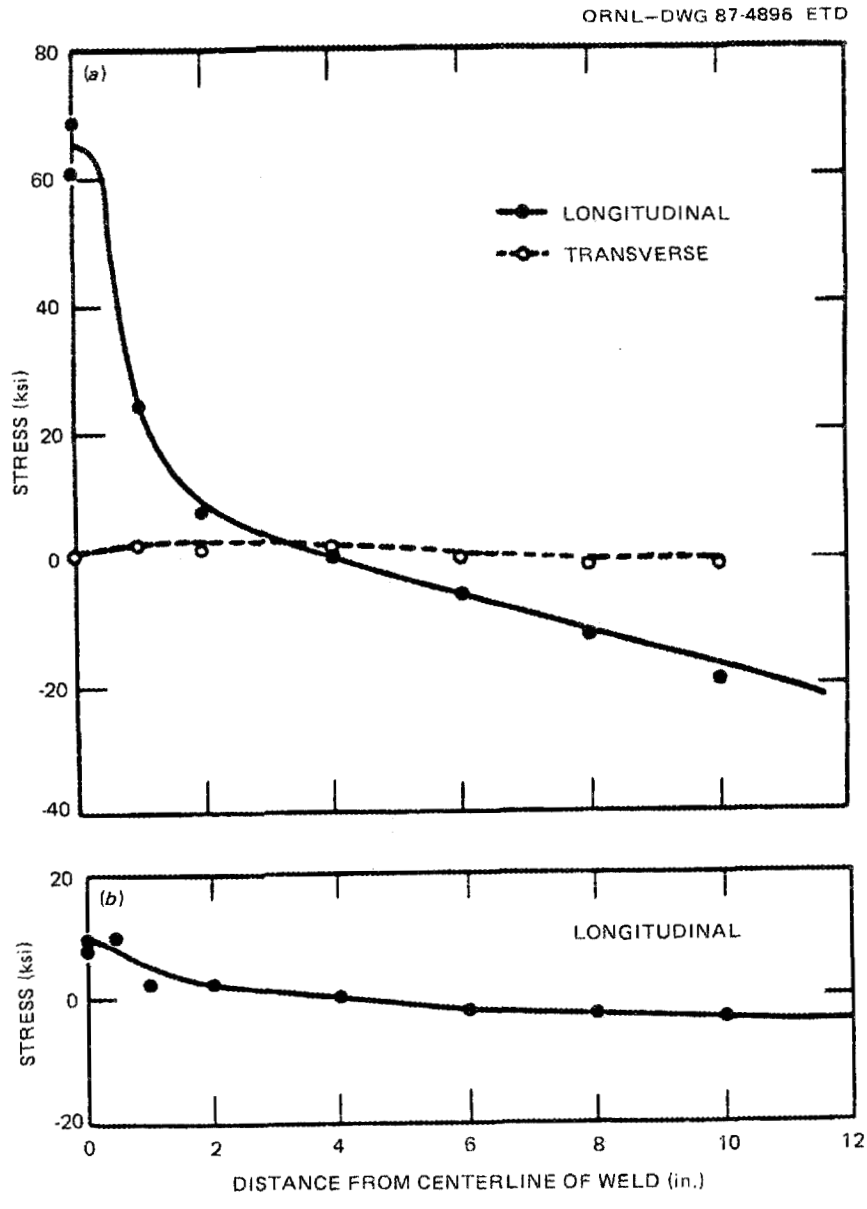

Fig. 5.3. Measured values of residual stress for longitudinal welds in 1 in. × 3 ft × 3 ft plates of A212 grade B steel (*a*) before and (*b*) after stress relief for 1 h at 1150°F. *Source*: W. J. Nordell and W. J. Hall, "Two Stage Fracturing in Welded Mild Steel Plate," *Weld. J.*, Research Supplement, 44(3), 124-s to 134-s (1965).

thickness average transverse residual stresses after stress relieving were negligible, and the peak local value measured was 2 ksi. The low value of the transverse relative to the longitudinal weld residual stress shown in Fig. 5.3 was recognized as a potentially important factor in the fracture safety evaluation of the HFIR vessel.

Analytical data for a nozzle-to-cylinder weld in an experimental pressure vessel[19] were located and studied to provide insight into the relative magnitude of transverse and weld direction residual stresses in a nozzle-to-cylinder weld. Results obtained by Dhalla[19] for the Creep Ratchetting Test Facility pressure vessel, using the ABAQUS finite-element computer code, specified weld-zone transient temperature distributions and time-dependent inelastic material properties, indicated that the through-thickness average transverse residual stresses were less than the welding direction residual stresses. In Ref. 19 it was not considered necessary to simulate the deposition of individual weld passes or to consider angular variations of temperature around the nozzle to estimate the essential features of the resulting residual stresses.

Using the foregoing results as a guide, the nozzle-to-shell weld for the HB-3 nozzle in the HFIR vessel was modeled analytically as an annular region of uniformly reduced temperature in a plate containing a hole. The annular region had an inside radius of 9.25 in. and a width of 1.5 in., representing the HB-3 nozzle weld, and the hole had a diameter of 8.0 in., the same as the HB-3 nozzle. Three analyses were performed; the first was elastic, the second was elastic-plastic for plane stress conditions, and the third was elastic-plastic for plane strain conditions. All three analyses indicated a transverse stress considerably less than the weld-direction (circumferential) stress, and all three analyses gave similar transverse to circumferential-stress ratios, indicating that this ratio is strongly affected neither by yielding nor by through-thickness constraint. Based on the elastic-plastic plane stress analysis and a temperature decrease in the annular region corresponding to the difference between the estimated creep threshold of the material (750°F) and the minimum welding preheat temperature of 200°F, the attempted thermal contraction below the creep range was slightly over twice the yield strain, and the transverse stress was 20% of the weld-direction (circumferential) stress.

The final step in estimating the residual stresses in the HB-3 nozzle weld was to assume that the ratio of the transverse to the weld-direction residual stresses remained constant during stress relief and to estimate the post-stress-relief weld-direction residual stress based on time at temperature and published stress relaxation data. The latter estimate was made graphically on the basis of a compilation of stress relaxation data for engineering alloys,[20] including carbon steels, using the prescribed stress-relief conditions of 51 h at 950°F. The weld-direction residual stress was estimated to be 8.5 ksi, a value lying between the mean and the upper bound of the published data. The transverse residual stress was then calculated as 20% of the weld-direction residual stress (1.7 ksi).

5.6 LEFM EVALUATION RESULTS

5.6.1 Analytical Procedure

Because of the multiplicity of hypothetical crack locations, orientations, crack-front positions, stress components, temperatures, toughness types, and safety factors to be considered, it was necessary to

develop a systematic analytical procedure to produce and interpret results in a timely and orderly fashion. This was facilitated by summarizing the input data in tabular form, according to the various possible crack configuration cases, and developing a calculation sheet with an initial crack configuration section that matches that of the input data tables. Table 5.3 lists the membrane, bending, thermal, and residual stress magnitudes used as input to the stress-intensity-factor calculations for each stress component for the various crack configurations considered in or near the HB-3 nozzle weld. Because the stress magnitudes govern the stress-intensity factor and the largest variable circumferential stress components are due to pressure, the largest stress-intensity factors for axial cracks generally occur for crack configurations for which the pressure-induced bending stress is positive. Thus, Case 2W, an axial inside-surface crack above the nozzle axis, and Case 3, an axial outside surface crack at the core horizontal midplane, give the highest stress-intensity factors.

Table 5.4 lists the values of the geometry factor (C) in the expression

$$K_I = C\ \sigma\sqrt{\pi a} \qquad (14)$$

for each crack configuration case and for three points on the crack front: the deepest point (a), the half-depth point (a/2), and the surface. Stress gradients sometimes cause the maximum value of K_I for a surface crack to occur somewhere between the deepest point of the crack and the surface. However, for the relatively long reference crack prescribed by the ASME Code and used here and for the relatively mild stress gradients occurring in the HFIR vessel, that does not happen. Therefore, the maximum value of K_I occurs at the deepest point of the crack.

The geometry factors for membrane stress caused by internal pressure were obtained from the work of Newman and Raju.[21,22] The values for inside-surface cracks, including the effects of pressure in the crack, were obtained from Ref. 21, and those for outside-surface cracks without internal pressure in the crack were obtained from Ref. 22. The latter values were also used for the effects of uniform residual stress transverse to the welding direction. The geometry factors for bending were obtained from work performed at ORNL[23] in support of the Heavy-Section Steel Technology (HSST) Program intermediate-vessel and thermal-shock tests. The geometry factors for the effects of the welding-direction residual stress, which is a maximum in the middle of the weld and decreases sharply with distance perpendicular to the weld (illustrated in Fig. 5.3), were obtained from the ORNL analysis[24] of HSST Program intermediate-vessel V-8, based on the work of Shah and Kobayashi.[25] Vessel V-8 was a low-temperature test of a vessel containing a sharp crack deliberately placed in a zone of high residual welding stress.

Table 5.5 is the calculation form for 1.0-in.-deep surface cracks in the vicinity of the HB-3 nozzle weld. Other crack depths can be considered by multiplying the factor π under the radical by the crack depth a. The factor C is the geometry factor from Table 5.4, and the factor S is the multiplier of p or η, or the residual stress itself, from Table 5.3.

Table 5.3. Stress magnitudes in and near HB-3 nozzle weld

Case	Crack configuration								Stresses (ksi)			
	Axial	Circumferential	Inside	Outside	Core HMP	Above axis	Weld	Base	Pressure		Thermal	Residual
									Membrane	Bending		
1	x		x		x		x	x	12.49 p	−3.27 p	−1.85 η	1.7
2W	x		x			x	x		16.82 p	4.24 p	−1.85 η	8.5
2B	x		x			x		x	16.82 p	3.64 p	−1.85 η	8.5
3	x			x	x		x	x	12.49 p	3.27 p	1.63 η	1.7
4W	x			x		x	x		16.82 p	−4.24 p	1.63 η	8.5
4B	x			x		x		x	16.82 p	−3.64 p	1.63 η	8.5
5		x	x		x		x	x	9.00 p	−2.74 p	−1.85 η	8.5
6W		x	x			x	x		8.30 p	−0.39 p	−1.85 η	1.7
6B		x	x			x		x	8.30 p	−0.39 p	−1.85 η	1.7
7		x		x	x		x	x	9.00 p	2.74 p	1.63 η	8.5
8W		x		x		x	x		8.30 p	0.39 p	1.63 η	1.7
8B		x		x		x		x	8.30 p	0.39 p	1.63 η	1.7

Table 5.4. K_I geometry factors for cracks in or near HB-3 nozzle weld
(a = 1 in., a/2b = 1/6)

Case	Crack configuration						Geometry factor, C											
							Pressure						Thermal			Residual		
							Membrane			Bending								
	Axial	Circumferential	Inside	Outside	Core HMP	Above axis	a	a/2	Surface	a	a/2	Surface	a	a/2	Surface	a	a/2	Surface
1	x		x		x		1.146	0.901	0.753	0.741	0.752	0.633	0.741	0.752	0.633	1.095	0.861	0.720
2	x		x			x	1.146	0.901	0.753	0.741	0.752	0.633	0.741	0.752	0.633	0.860	0.275	0.113
3	x			x	x		1.095	0.861	0.720	0.741	0.752	0.633	0.741	0.752	0.633	1.095	0.861	0.720
4	x			x		x	1.095	0.861	0.720	0.741	0.752	0.633	0.741	0.752	0.633	0.860	0.275	0.113
5		x	x		x		1.146	0.901	0.753	0.741	0.752	0.633	0.741	0.752	0.633	0.860	0.275	0.113
6		x	x			x	1.146	0.901	0.753	0.741	0.752	0.633	0.741	0.752	0.633	1.095	0.861	0.720
7		x		x	x		1.095	0.861	0.720	0.741	0.752	0.633	0.741	0.752	0.633	0.860	0.275	0.113
8		x		x		x	1.095	0.861	0.720	0.741	0.752	0.633	0.741	0.752	0.633	1.095	0.861	0.720

Table 5.5. Worksheet for life-extension calculations

Name _____ Date _____ _____ of _____

HFIR K_I Calculation P = _____ MW p = _____ ksi

Case	Axial	Circum.	Inside	Outside	Core HMP	Above axis	Weld	Base metal

T_c = °F	T_p = °F	η =	f =

Material	Orien.	RT_{NDT} (HFIR — 1986) °F	$12.5\left(\frac{1}{2}+\frac{x}{W}\right)$ =	S_{FP} = °F/year

Deepest Point Case

	C	S	p or η	
$2K_{Ipm}$ = 2	( )	( )	( ) $\sqrt{\pi}$ =	ksi $\sqrt{in.}$
$2K_{Ipb}$ = 2	( )	( )	( ) $\sqrt{\pi}$ =	ksi $\sqrt{in.}$
K_{It} =	( )	( )	( ) $\sqrt{\pi}$ =	ksi $\sqrt{in.}$
K_{Ir} =	( )	( ) $\sqrt{\pi}$	=	ksi $\sqrt{in.}$

$T - RT_{NDT}$ = °F	Total =	ksi $\sqrt{in.}$

T = °F	RT_{NDT} = °F	Δt = years

Material	Orien.	RT_{NDT} (HFIR - 1986) °F	$12.5\left(\frac{1}{2}+\frac{x}{W}\right)$ =	S_{FP} = °F/year

Half Depth Point

	C	S	p or η	
$2K_{Ipm}$ = 2	( )	( )	( ) $\sqrt{\pi}$ =	ksi $\sqrt{in.}$
$2K_{Ipb}$ = 2	( )	( )	( ) $\sqrt{\pi}$ =	ksi $\sqrt{in.}$
K_{It} =	( )	( )	( ) $\sqrt{\pi}$ =	ksi $\sqrt{in.}$
K_{Ir} =	( )	( ) $\sqrt{\pi}$	=	ksi $\sqrt{in.}$

$T - RT_{NDT}$ = °F	Total =	ksi $\sqrt{in.}$

T = °F	RT_{NDT} = °F	Δt = years

Material	Orien.	RT_{NDT} (HFIR — 1986) °F	$12.5\left(\frac{1}{2}+\frac{x}{W}\right)$ =	S_{FP} = °F/year

Surface

	C	S	p or η	
$2K_{Ipm}$ = 2	( )	( )	( ) $\sqrt{\pi}$ =	ksi $\sqrt{in.}$
$2K_{Ipb}$ = 2	( )	( )	( ) $\sqrt{\pi}$ =	ksi $\sqrt{in.}$
K_{It} =	( )	( )	( ) $\sqrt{\pi}$ =	ksi $\sqrt{in.}$
K_{Ir} =	( )	( ) $\sqrt{\pi}$	=	ksi $\sqrt{in.}$

$T - RT_{NDT}$ = °F	Total =	ksi $\sqrt{in.}$

T = °F	RT_{NDT} = °F	Δt = years

Note that the safety factor of 2.0 is included in the first two stress-intensity-factor components, the first for the membrane stress caused by pressure and the second for the bending stress caused by pressure.

For an inside-surface crack in a nozzle corner region, the geometry factor C was initially estimated from finite-element results published by Gilman and Rashid.[26] These results are shown in Fig. 5.4, taken from Ref. 10. The experimental data shown in Fig. 5.4 were obtained at ORNL from relatively thicker-walled epoxy models,[27] for which the effect of pressure in the crack is larger than for the HFIR vessel. Finite-element results for two of the HFIR nozzles have been obtained by B. R. Bass at ORNL.[16] These results confirm the estimates based on Fig. 5.4 within a few percent. Although preliminary calculations not considering neutron attenuation between the surveillance specimen location and the nozzle corners indicated that the nozzle corners could be the governing location, the consideration of neutron attenuation reverses that conclusion, leaving the HB-3 nozzle weld as the governing region.

As a conservatism in the preliminary calculations, crack-tip plastic-zone-size effects for membrane stress were interpolated linearly from calculations for a pressure of 1500 psi. However, for pressures reduced to one-third of that value or less, plastic-zone-size effects are not significant, and they have, therefore, not been included in the final calculations.

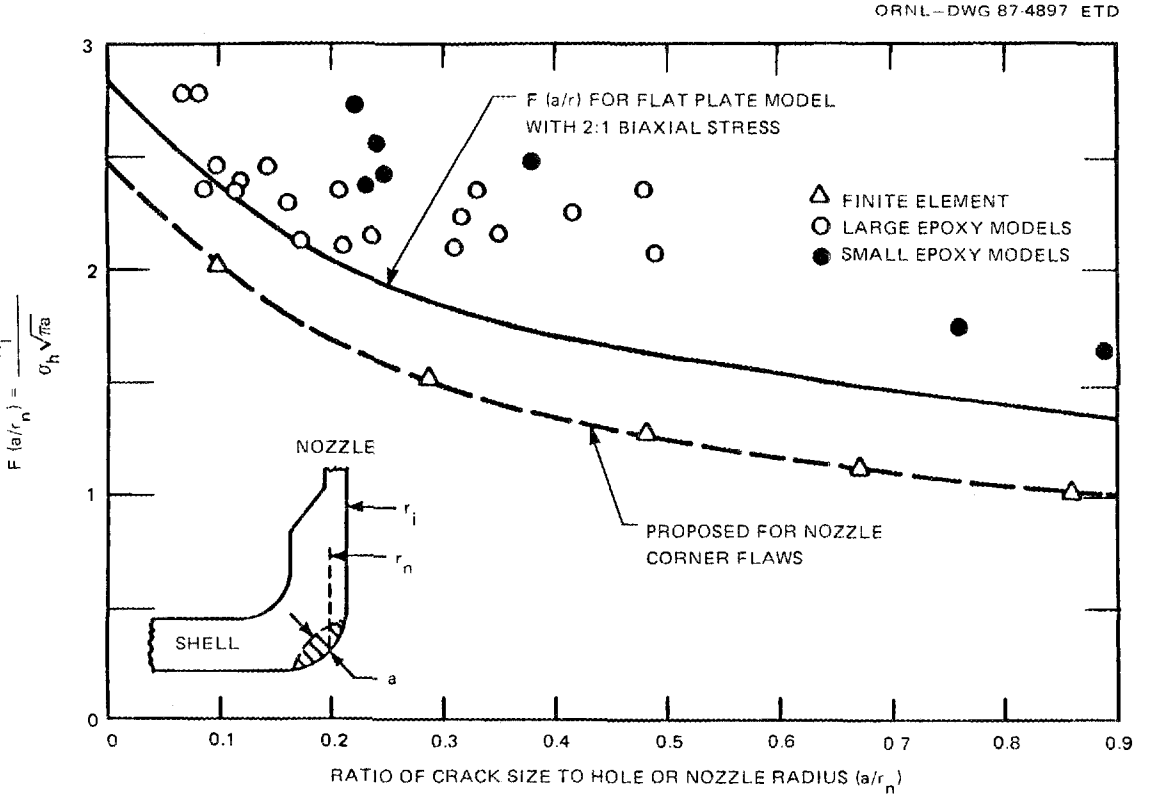

Fig. 5.4. Estimates of stress-intensity factors for inside-nozzle-corner cracks.

Results of the fracture-mechanics analysis are discussed in the following several subsections. Preliminary results, which do not include the effects of secondary stresses, are discussed in Sect. 5.6.2, and results that do include these effects are discussed in Sects. 5.6.3 and 5.6.4.

5.6.2 Preliminary Results

Before the time that the secondary stresses were considered in the calculation of vessel life extension, a parametric study was conducted to determine the sensitivity of life extension to power level and primary-system pressure and coolant temperature, among other things. (Specific combinations of these three parameters are required in the fracture-mechanics analysis because of their interrelation in the core heat-removal analysis discussed in Appendix B.) The results are summarized in Fig. 5.5 for a radiation-damage-rate uncertainty factor of 1.0 and for

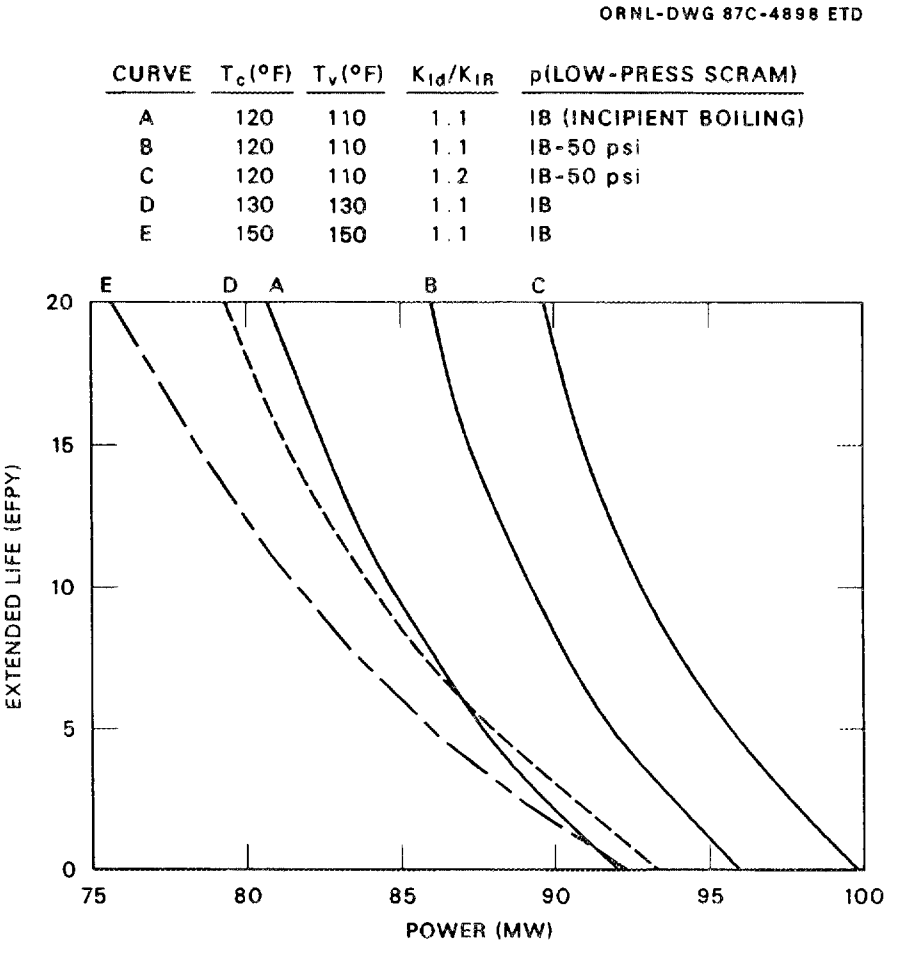

Fig. 5.5. Life extension vs normal power (preliminary analysis).

the controlling flaw, which was axially oriented and located at the horizontal midplane adjacent to the HB-3 nozzle weld on the high-flux side. Because a life extension of 10 calendar years (~8.5 EFPY) was desired at a reasonably high power level, it appeared that a power level of 85 MW and a coolant inlet temperature of 120°F (previous value) would be a good choice (curve A). Curve B was obtained by reducing the pressure normally required for heat removal by 50 psi, and curve C is the same as curve B with a 10% higher fracture toughness. A comparison of curves A, D, and E indicates that for power levels below ~87 MW, increasing the vessel (coolant) temperature decreases the calculated life extension. (The effect of the required increase in pressure was greater than the increase in K_{IR}.) However, the crossover point is sensitive to the nominal value of $T - RT_{NDT}$ because of the changing slope of the K_{IR} curve and, when secondary stresses are included, to the ratio of primary to secondary stress. As indicated later in this section, application of the more complex model for estimating life extension results in the opposite trend for a power of 85 MW.

By the time the more complex model was applied, a decision had been made to conduct a hydrostatic proof test to accommodate possible exceptions to the Code (see Sect. 5.7). To guard against an excessive number of pressurizer-pump trips caused by low temperature, a low low-temperature trip was desirable. Based on secondary- and pool-coolant temperature control considerations and the temperature at which previous hydrotests had been conducted on the HFIR vessel, the hydrotest temperature and the low-temperature trip were tentatively selected as 85°F. With the primary system at 85°F, the pool temperature could approach 90°F. Thus, a vessel low temperature in the range of 85 to 90°F needed to be considered in estimating life extension and would result in smaller values than those in Fig. 5.5.

Also before the time the more complex model was applied, one of the DOE/EH committees recommended that operation of the vessel be extended no more than 3 EFPY. Anticipating the outcome of including lower temperatures and applying the more complex model and taking advantage of the hydro test to justify possible noncompliance with the Code, a decision was made to tentatively specify a power level of 85 MW and a normal coolant inlet temperature of 120°F. As indicated in Appendix B, the corresponding vessel differential pressures associated with pressurizer-pump trip and rupture of the rupture disc are 508 and 679 psid, respectively.

Results obtained using the more complex model are discussed in Sects. 5.6.3 and 5.6.4.

5.6.3 Normal and Upset Conditions

Tables 5.6–5.8 show calculated results for normal and upset conditions, based on a pressure of 508 psi (the pressurizer-pump trip pressure for a power level of 84.6 MW), a core inlet temperature of 120°F, a pool temperature of 95°F, a normal power level of 84.6 MW, an uncertainty factor of 1.0 for the radiation damage rate, and the ASME lower-bound K_{IR} curve defined by Eq. (2). The stress-intensity-factor totals shown are values at the deepest point of the crack, and for a flaw in plate material, this value is compared with the toughness calculated for the LS

Table 5.6. Life extension and other parameters corresponding to 1-in.-deep, axial, inside-surface, part-through crack[a] across HB-3 nozzle weld, above nozzle axis (normal and upset conditions)

Parameter	Base metal (LS)	Weld metal
$2\ K_{Ip} + K_{Is}$, ksi•$\sqrt{in.}$	50.08	50.90
$T - RT_{NDT}$, °F	43.26	45.64
RT_{NDT}, °F	66.74	63.95
RT_{NDT}, °F (HFIR-86)	31.72	48.25
Δt, EFPY	17.4	8.5

[a]Crack tip temperature = 110°F, P = 84.6 MW, p = 508 psi.

Table 5.7. Life extension and other parameters corresponding to 1-in.-deep, axial, outside-surface, part-through crack[a] in or near HB-3 nozzle weld and at core horizontal midplane (normal and upset conditions)

Parameter	Base metal (LS)	Weld metal
$2\ K_{Ip} + K_{Is}$, ksi•$\sqrt{in.}$	34.41	34.41
$T - RT_{NDT}$, °F	−33.71	−33.71
RT_{NDT}, °F	138.71	138.71
RT_{NDT}, °F (HFIR-86)	86.32	99.30
Δt, EFPY	11.3	9.2

[a]Crack tip temperature = 105°F, P = 84.6 MW, p = 508 psi.

Table 5.8. Effect of heating the HFIR vessel wall on calculated remaining service time for normal and upset conditions[a]

Flaw location and material, near HB-3 weld	Life extension (Δt, EFPY)			
	No heat, ~110°F	Uniform heating		
		120°F	130°F	150°F
Axial, inside, above axis				
Weld	8.5	10.6	12.8	17.5
LS	17.4	18.9	20.9	25.2
Axial, outside at core HMP				
Weld	9.2	17.8	15.8	13.9
LS	11.3	19.3	17.5	15.6

[a] P = 84.6 MW, Δt in EPFY.

direction. [The LS orientation corresponds to a stress in the longitudinal (L) direction and crack extension in the short transverse (S), that is, the through-thickness direction.] By design, this is the crack extension orientation for which this material has the greatest resistance to crack extension. This physically realistic procedure was recommended to ORNL by the McSpadden Committee, contingent upon the demonstration of a low calculated probability of vessel failure and a low risk to the public of such an event because of the favorable characteristics of the HFIR system. Calculated values of K_I at the surface are generally close to the lower shelf of the K_{IR} curve. Therefore, even though LT properties determine the toughness there, it is not a governing location.

Comparing Tables 5.6 and 5.7 shows that for normal and upset conditions the governing flaw configuration is an inside-surface flaw in weld metal above the HB-3 nozzle axis and that the calculated vessel life is 8.5 EFPY. Table 5.8 shows that there is an advantage, in terms of vessel service life, to heating the vessel at the core elevation up to a temperature between 130 and 150°F. However, this approach is not necessary for extending the vessel service life by the proposed 10 calendar years.

In the above calculations (Sect. 5.6.3 and Tables 5.6–5.8), the coolant and pool temperatures were the normal values. For upset conditions it is necessary to consider the lower limit associated with temperature control. These values are 85 and 90°F, respectively. The calculated life extensions based on these lower temperatures are <10 years unless an exception is taken to the Code. A small increase in fracture toughness (~25%) is sufficient. Because of the application of the hydro test, this is considered acceptable.

5.6.4 Emergency and Faulted Conditions

Tables 5.9–5.11 show calculated results for emergency and faulted conditions, based on a vessel pressure of 679 psi, which corresponds to the maximum pressure for rupture of the rupture disc with no flow in the

Table 5.9. Life extension and other parameters corresponding to 1-in.-deep, axial, inside-surface, part-through crack[a] across HB-3 nozzle weld and above nozzle axis (emergency and faulted conditions)

Parameter	Base metal (LS)	Weld metal
$2K_{Ip} + K_{Is}$, ksi$\cdot\sqrt{in.}$	63.42	64.49
$T - RT_{NDT}$, °F	18.83	20.57
RT_{NDT}, °F	90.75	89.01
RT_{NDT}, °F (HFIR-86)	31.72	48.25
Δt, EFPY	29.3	22.1

[a]Crack tip temperature = 110 °F, P = 84.6 MW, p = 679 psi.

Table 5.10. Life extension and other parameters corresponding to 1-in.-deep, axial, outside-surface, part-through crack[a] in or near HB-3 nozzle weld and at core horizontal midplane (emergency and faulted conditions)

Parameter	Base metal (LS)	Weld metal
$2K_{Ip} + K_{Is}$, ksi$\cdot\sqrt{in.}$	44.19	44.19
$T - RT_{NDT}$, °F	−31.73	−31.73
RT_{NDT}, °F	137.15	137.15
RT_{NDT}, °F (HFIR-86)	86.32	99.30
Δt, EFPY	10.9	8.8

[a]Crack tip temperature = 105°F, P = 84.6 MW, p = 679 psi.

Table 5.11. Effect of heating the HFIR vessel wall on calculated remaining service time for emergency and faulted conditions[a]

Flaw location and material, near HB-3 weld	Life extension (Δt, EFPY)			
	No heat, ~110°F	Uniform heating		
		120°F	130°F	150°F
Axial, inside, above axis				
Weld	22.1	25.7	29.3	36.5
LS	29.3	32.6	35.8	42.4
Axial, outside at core HMP				
Weld	8.8	14.7	15.0	16.1
LS	10.9	16.4	16.7	17.7

[a] P = 84.6 MW, Δt in EPFY.

primary system and with other inputs the same as for the preceding analysis. The toughness used is the ASME lower-bound K_{Ic} curve defined by Eq. (3). Comparing Tables 5.9 and 5.10 shows that for emergency and faulted conditions, the governing flaw configuration is an outside-surface flaw in the HB-3 nozzle weld at the core horizontal mid-plane and that the calculated vessel life is 8.8 EFPY, almost the same as the governing value for normal and upset conditions given in Table 5.6.

5.7 APPLICATION OF HYDROSTATIC PROOF TESTING

As mentioned in Sect. 4, hydrostatic proof testing provides a means for demonstrating that whatever combination of stress, fracture toughness, and flaw size actually exists, the vessel is safe to operate. The permissible life extension is a function of the ratio of hydro-test pressure to operating pressure and can be calculated in a conservative manner using LEFM. This approach can be used to help justify exceptions to the Code, and the probability of vessel failure (through-wall cracking) during the hydro test can be evaluated with a probabilistic fracture-mechanics analysis.

A hydro test can also negate the need for volumetric inspection of the vessel wall for flaws, provided that a reasonable estimate of the probability of failure of the vessel during the hydro test can be obtained without such information. (Generic data regarding flaw density and flaw-size distribution for pressure vessels are available and are appropriate for application to HFIR.)

When the DOE/EH committees recommended that secondary stresses and a large uncertainty factor for the radiation damage rate of the welds be included in the fracture-mechanics model, it was suggested by the McSpadden committee that a hydro test be performed to justify possible exceptions to the Code. This idea was adopted by ORNL, and an effort was directed at determining an appropriate pressure.

An appropriate hydro-test pressure can be calculated by considering the desired life extension and the probability of failure during the hydro test. The pressure increment between the hydro-test pressure and operating pressure corresponds to a permissible decrease in the fracture toughness caused by radiation damage and, thus, to a specific life extension. Calculation of the hydro-test pressure begins by assuming that

$$\frac{K_I(HT)}{K_I(S,\Delta t)} = \frac{K_{Ic}(HT)}{K_{Ic}(\Delta t)} , \tag{15}$$

where

$K_I(HT)$ = K_I for hydro-test pressure,

$K_{Ic}(HT)$ = actual fracture toughness at hydro-test temperature,

$K_I(S,\Delta t)$ = K_I for safety-valve pressure at end of vessel extended life (Δt),

$K_{Ic}(\Delta t)$ = actual fracture toughness at minimum permissible operating temperature at end of vessel extended life (Δt).

The actual value of K_{Ic} is not known; thus, it is assumed that

$$K_{Ic} = f\, K_{IR} , \tag{16}$$

where

K_{IR} = ASME lower bound of dynamic fracture toughness (Eq. 2),

f = correction factor.

The stress-intensity factor is obtained from Eq. (14):

$$K_I = \sum_i C_i \sigma_i \sqrt{\pi a} , \tag{17}$$

where i refers to different type loads. Combining Eqs. (15)—(17) yields

$$\frac{\left(\sum_i C_i \sigma_i\right)_{HT}}{\left(\sum_i C_i \sigma_i\right)_{S,\Delta t}} = \frac{K_{IR}(HT)}{K_{IR}(\Delta t)} \quad , \tag{18}$$

$$\frac{\sqrt{\pi a}}{f} = \frac{K_{IR}(\Delta t)}{\left(\sum C_i \sigma_i\right)_{S,\Delta t}} \, . \tag{19}$$

Values of a and f, both unknowns, cannot be determined from the hydro test, yet K_{IR} is a function of a because of the gradient in toughness in the wall. This would appear to represent a dilemma; however, as shown later, the required hydro-test pressure is insensitive to crack depth.

The stresses included in the analysis are the pressure-induced membrane (σ_m) and bending (σ_b) stresses and residual stresses (σ_r). Thermal stresses are relatively small and are neglected. Thus, combining Eqs. (2) and (18) and letting $\sigma_m = pS_m$ and $\sigma_b = pS_b$ gives

$$p_{HT} = \frac{AB}{D(C_m S_m + C_b S_b)} - \frac{C_r \sigma_r}{(C_m S_m + C_b S_b)} \quad , \tag{20}$$

where

$$A = \left(\sum_i C_i \sigma_i\right)_{S,\Delta t} = p_S(C_m S_m + C_b S_b) + C_r \sigma_r \, , \tag{21}$$

$$B = K_{IR}(HT) = 26.8 + 1.22 \, EXP \left\{0.0145[T_v - RT_{NDT}(HT) + 160]\right\} \, , \tag{22}$$

$$D = K_{IR}(\Delta t) = 26.8 + 1.22 \, EXP\{0.0145[T_v - RT_{NDT}(\Delta t) + 160]\} \, , \tag{23}$$

p_{HT} = hydro-test pressure,

p_S = safety-valve pressure,

$$RT_{NDT}(HT) = RT_{NDT}(1986) \, , \tag{24}$$

$$RT_{NDT}(\Delta t) = RT_{NDT}(1986) + \frac{P}{100} S_{FP} \Delta t \, , \tag{25}$$

S_{FP} = ΔRT_{NDT} rate at crack front for P = 100 MW, °F/EFPY,

Δt = vessel life extension, EFPY,

P = reactor power for extended life, MW.

Values of S_{FP}, $RT_{NDT}(1986)$, S_i, σ_r, and C_i are given in Tables 5.2–5.4.

The results of life-extension studies reported in Tables 5.6 and 5.7 indicate that the deepest point of an inner-surface flaw across the HB-3 nozzle weld and directly above the nozzle is the most limiting "flaw." Thus, the hydro-test pressure was calculated using this "flaw." The vessel temperature for the hydro test and for "normal" operation was specified as 85°F (minimum permissible for operation), and the maximum vessel pressure differential associated with rupture of the rupture disc [679 psid (Table B.5)] was used for p_S. To accommodate the uncertainty in the embrittlement rate of the nozzle weld, ΔRT_{NDT} was multiplied by 1.5 (recommended by Brinkerhoff Committee). The power level for the extended life was that specified in Sect. 6 (85 MW).

Results of the analysis to determine p_{HT} are presented in Table 5.12. It is apparent that p_{HT} is insensitive to crack depth.

Table 5.12. Calculated hydro-test pressures for HFIR vessel

Δt (EFPY)	p_{HT} (psid)	
	a = 0.5 in.	a = 1.0 in.
0	679	679
5	754	750
10	825	821
15	888	883

Applying a 10% margin to the pressures in Table 5.12 for uncertainties in the analytical approach and in the temperature and pressure measurements during the hydro test results in a hydro-test pressure of ~900 psig for a life extension of 10 EFPY. A probabilistic fracture-mechanics analysis (Appendix G) indicates that the chances of vessel failure during a hydro test at 900 psig, at 85°F, and at the end of a 10-EFPY life extension at 85 MW are $\sim 6 \times 10^{-7}$. This was considered to be acceptable, and hydro-test conditions of 900 psig and 85°F were specified.

As indicated above, the hydro-test pressure was calculated assuming that the test would be performed before restart and at no other time during the specified 10-EFPY life extension unless the damage rate of the nozzle-weld material, as determined by the continuing surveillance program, is greater than assumed (1.5 times value measured in ORR). Aside

from this latter possibility, the McSpadden Committee has recommended that the hydro test be conducted annually. If this were done, the hydro-test pressure could be substantially less. At this time, it is intended that the hydro test will be conducted annually and that the first test will be at 900 psig. Thus, if at some future time $\Delta t'$ the requirement for annual testing were lifted, it would be safe to continue operation of the vessel without further hydro testing. Furthermore, each future time that the vessel is tested, the test pressure can be reduced if the total life extension is not increased. In line with this thinking, reduced hydro-test pressures were calculated assuming that the life extension from restart date was fixed at 10 EFPY, that each hydro test at $\Delta t'$ had to justify continued operation without further hydro testing, and that each test be conducted as if no previous hydro testing had been conducted. The results of this analysis are presented in Fig. 5.6.

The hydro-test pressure at 10 EFPY is greater than that associated with rupture of the rupture disc (679 psid) because of the ~10% uncertainty factor mentioned above. The maximum permissible "operating" pressure, based on hydro testing only, is ~10% less than the curve shown.

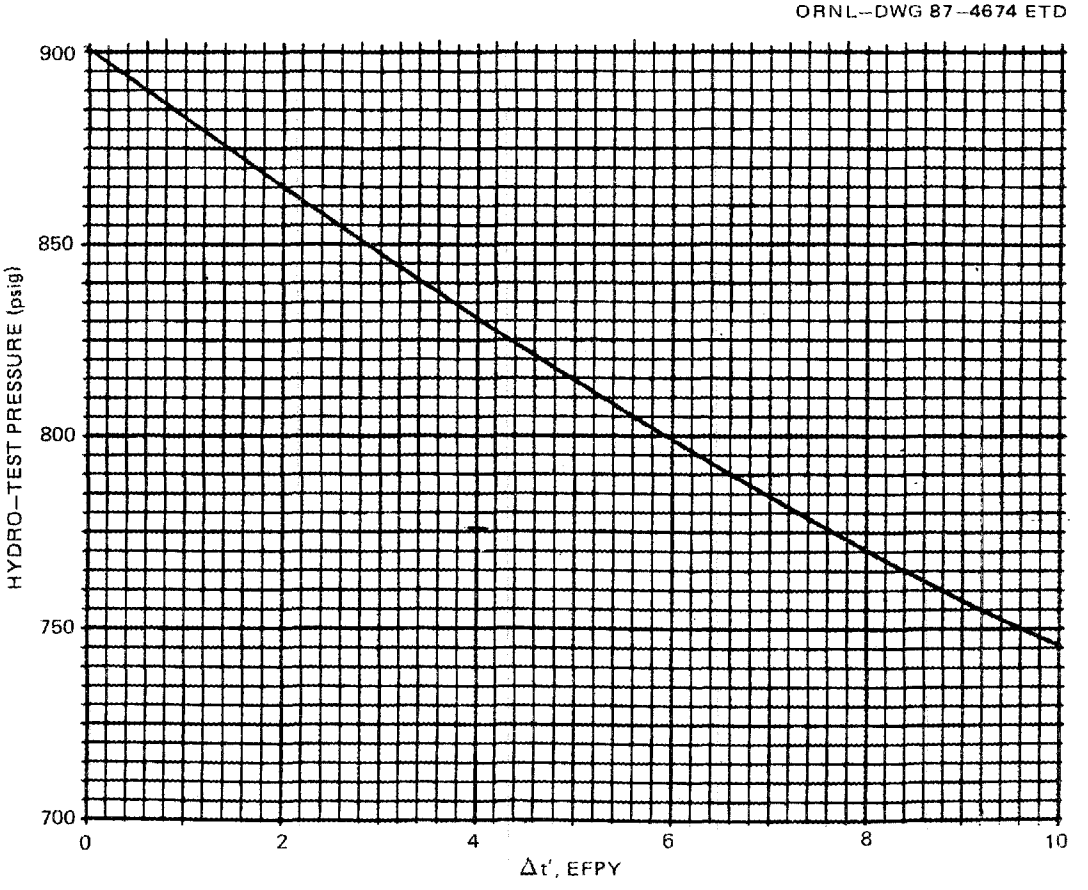

Fig. 5.6. Required hydro-test pressure based on 10-EFPY life extension, assuming that each hydro test at $\Delta t'$ is the last that will be performed during remainder of 10-EFPY period.

A hydro test at 900 psig and 85°F was conducted successfully on the HFIR vessel on August 4, 1987. Details of this test and the proposed procedure for future tests are discussed in separate reports.[28,29]

5.8 ESTIMATION OF CRITICAL FLAW SIZE

As radiation embrittlement increases with time, the critical flaw size decreases, and the smaller the size, the more likely the flaw is to exist, all of which is considered in the probabilistic fracture-mechanics analysis. Nevertheless, it is of some interest to estimate just how small the critical flaw might be. This can be done using Eq. (19), which was derived in a manner consistent with the assumptions associated with the hydro-test analysis. The most likely critical flaw size is obtained letting $f \simeq 2$, and the smallest is obtained with $f = 1$. At the end of the 10-EFPY extended life and with the vessel subjected to the above specified hydro-test conditions, the corresponding critical crack sizes are ~2 and 0.6 in.

5.9 PRESSURE-TEMPERATURE LIMIT CURVE

As mentioned above, the application of a hydro test can provide an indication of flaw size for a specified type of flaw, assuming that during the hydro, $K_I = K_{Ic}$. Using this flaw size and otherwise complying with the Code, a pressure-temperature limit curve can be obtained. This was done for HFIR based on an inner-surface flaw in the HB-3 nozzle weld above the nozzle axis, an effective fracture toughness equal to K_{IR}, a ΔRT_{NDT} rate equal to 1.5 times the nominal value determined from the ORR irradiation program, and no safety factor on load. The critical flaw size was 0.762 in. for the hydro pressure of 900 psid.

The 0.762-in.-deep flaw was then used in a Code-type analysis (safety factor of 2 on load, use of K_{IR} curve), once again using the 1.5 factor on ΔRT_{NDT} rate. The results (Fig. 5.7) indicate that for a life extension of 1 EFPY, the lowest permissible vessel temperature with the pressure at the pressurizer-pump trip point (508 psid) is 85°F. Thus, based on the hydro test, by using a flaw depth that is less than that specified in the Code and by considering the actual frequency of performing the hydro test, it is possible to show "compliance" with the Code for the most severe upset condition.

Note that the 0.762-in. flaw size is smaller than the most probable size because a low fracture-toughness value was used (K_{IR} and a high embrittlement rate). However, it is necessary to use the same fracture toughness for the determination of flaw size as that used for the subsequent Code analysis. Essentially the same pressure-temperature limit curves would be obtained with a different assumed fracture-toughness and corresponding calculated crack depth.

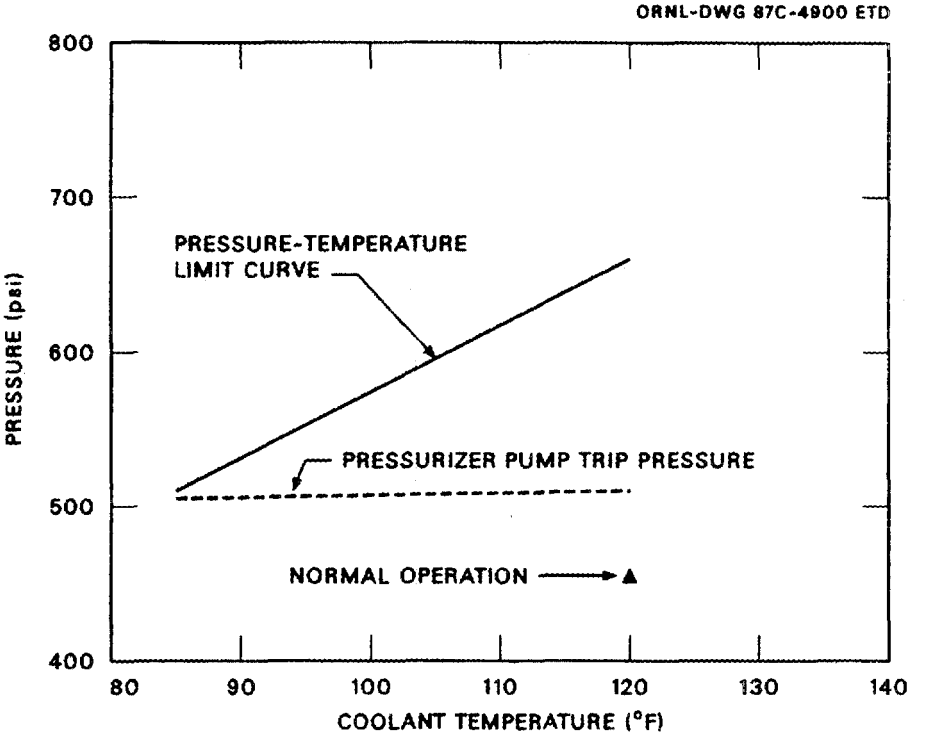

Fig. 5.7. LEFM pressure-temperature limit curve for HFIR vessel, based on K_{IR}; safety factor of 2.0 on pressure; 50% uncertainty in RT_{NDT} shift of weld metal; and annual proof testing to 900 psi at 85°F and crack depth of 0.762 in., which would be critical in the first proof test.

5.10 POTENTIAL FOR FRAGMENTATION

As mentioned in the summary in Sect. 1 and discussed in greater detail in Appendix G, the probability of failure of the HFIR vessel caused by propagation of flaws is extremely small if the reactor is operated in accordance with the recommendations set forth in this document (see Sect. 6). Even so, there is a desire to limit NDT relative to the wall temperature so that even if crack propagation did occur, fragmentation would not occur, or at least it would be confined to a small area around the beam tubes. The "concern" over fragmentation is that a piece of the vessel might somehow strike the core assembly in such a way as to impair operation of the control rods and/or cooling of the core. With reference to Figs. 2.1 and 2.2, it is apparent that the specific design of the core assembly and the relative position of the embrittled area of the vessel with respect to the core assembly make it highly unlikely that this would happen. Even so, prevention of extensive fragmentation in the event of crack propagation represents another line of defense against core melt. (This does not significantly reduce the probability of core melt because the probability of core melt associated with factors other than vessel failure is much greater than the probability of vessel failure.)

The chances of fragmentation increase as T_V — NDT decreases, and a reasonable lower limit of T_V — NDT for prevention of fragmentation is 30°F. At the horizontal midplane of the core, values of T_V — NDT for shell material adjacent to the HB-3 weld, in the HB-3 weld adjacent to the nozzle, and at the HB-3 nozzle corner are —36, —31, and 41°F, respectively, for a vessel temperature of 85°F (minimum permissible while at full pressure), a power level of 85 MW, and a life extension of 2.6 EFPY. Thus, this localized area of the shell and weld does not satisfy (T_V — NDT) ≥ 30°F. However, as indicated in Fig. 5.8 and discussed in greater detail in Appendix E, the attenuation of the neutron flux away from the center of the beam tube is substantial. As a result, 74% of the circumference of the vessel at the horizontal midplane of the core and at a depth in the wall of ≥1 in. does satisfy T_V — NDT ≥ 30°F for a life extension of 2.6 EFPY. For 8.5 EFPY the percentage is 68. For T_V — NDT ≥ 60°F, the percentages are 35 and 31. When the vessel is at its normal operating temperature of ~110°F, the percentages are 77 and 73 for T_V — NDT ≥ 30°F and 70 and 65 for T_V — NDT ≥ 60°F. Thus, only a very small area of the vessel adjacent to the beam tube nozzles does not satisfy T_V — NDT ≥ 30°F for a life extension of ~9 EFPY. This is considered to be acceptable.

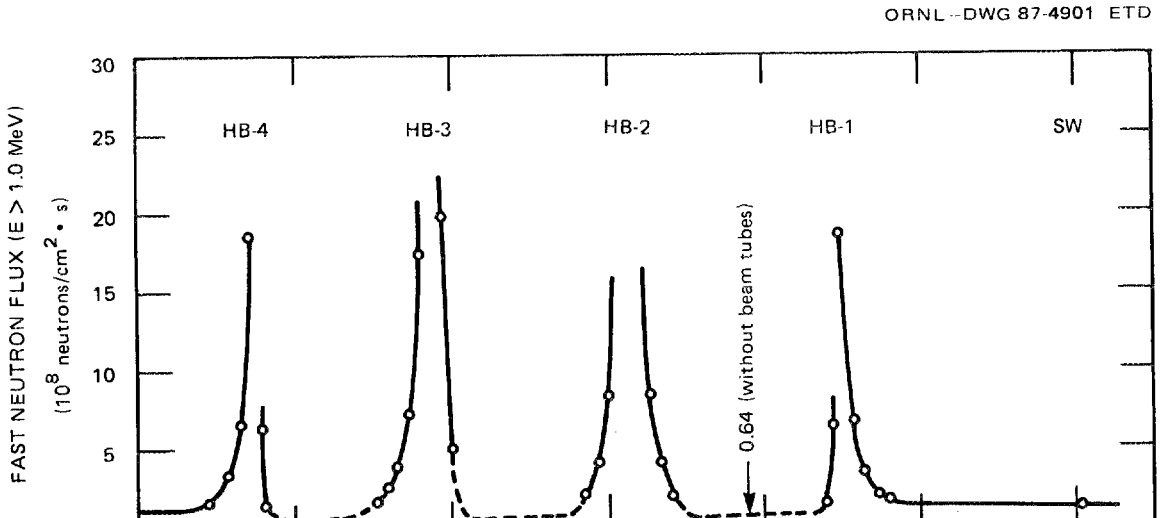

Fig. 5.8. Calculated fast neutron flux (E > 1 MeV) in HFIR vessel wall (a = 1 in.) at HMP for 100 MW.

5.11 EXTENT OF CRACK PROPAGATION ON SURFACE

Besides considering the temperature margins with respect to RT_{NDT} existing at the core horizontal midplane, the consequences of crack extension from this region and from the HB-3 nozzle perpendicular to the maximum principal tensile stress (the circumferential stress) were investigated. As shown in Appendix I, crack arrest would occur for all three hypothetical crack paths considered, including a straight axial crack, a crack following the HB-3 nozzle-to-cylinder weld, and a crack running axially above the nozzle.

6. RECOMMENDATIONS AND COMMENTS

R. D. Cheverton J. G. Merkle
R. K. Nanstad

Based on the results of the study included in this report and on comments from the DOE/EH and DOE/ER committees, the following recommendations and comments are made regarding future operation of HFIR.

Recommendations:

1. The nominal power level should be limited to 85 MW.
2. The primary system nominal and minimum coolant inlet temperatures should be 120 and 85°F, respectively.
3. The corresponding set of primary-system pressures is presented in Table B.5. Normal operating pressure at the inlet to the core is 475 psia.
4. The pool temperature should be controlled between 90 and 100°F.
5. A hydrostatic proof test at 900 psi and 85°F should be conducted on the vessel before restart, and hydrostatic proof tests should be conducted at 1 EFPY intervals thereafter.
6. The surveillance program for the vessel materials should be continued and should include specimens of seam-weld and nozzle-weld material, which were not included in the previous surveillance program. Details of the recommended program are provided in a separate document.

Comments:

1. Adherence to the above recommendations provides a means for extending the life of the vessel by 10 EFPY.
2. Greater care must be taken now to protect the vessel against high pressure and low temperature. In accordance with data presented in this report, modifications are being made to the control system in accordance with data presented in this report, to provide the required protection and to accommodate the changes in power level, temperatures, and pressures.

REFERENCES

1. J. R. McWherter, R. E. Schappel, and J. R. McGuffey, *HFIR Pressure Vessel and Structural Components Material Surveillance Program*, ORNL/TM-1372, Union Carbide Corp. Nuclear Div., Oak Ridge Natl. Lab., January 1966.

2. R. K. Nanstad, letter to G. R. Hicks, Oak Ridge Natl. Lab., November 5, 1986.

3. R. K. Nanstad, letter to G. R. Hicks, Oak Ridge Natl. Lab., November 20, 1986.

4. T. M. Sims and J. H. Swanks, *Heat Transfer Calculations for the High Flux Isotope Reactor (HFIR) Technical Specifications Bases for Safety Limits and Limiting Safety System Settings*, ORNL/TM-5844, Union Carbide Corp. Nuclear Div., Oak Ridge Natl. Lab., September 1977.

5. W. S. Pellini, L. E. Steele, and J. R. Hawthorne, *Analysis of Engineering and Basic Research Aspects of Neutron Embrittlement of Steels*, NRL Report 5780, April 17, 1962; also, *Weld. J.*, Research Supplement, 41(10), p. 455–3, October 1962.

6. S. T. Rolfe and J. M. Barsom, *Fracture and Fatigue Control in Structures, Applications of Fracture Mechanics*, Prentice-Hall, Inc., Englewood Cliffs, N.J., 1977.

7. *1986 ASME Boiler and Pressure Vessel Code*, Sect. III, Div. 1, "Nuclear Power Plant Components," Appendix G: "Protection Against Nonductile Failure," Appendices, American Society of Mechanical Engineers, New York, pp. 555–65.

8. *1983 ASME Boiler and Pressure Vessel Code*, Sect. XI, Div. 1, "Rules for Inservice Inspection of Nuclear Power Plant Components," Appendix A: "Analysis of Flaws," American Society of Mechanical Engineers, New York, pp. 262–282.2.

9. W. J. Nordell and W. J. Hall, "Two Stage Fracturing in Welded Mild Steel Plate," *Weld. J.*, Research Supplement, 44(3), 124-s to 134-s (1965).

10. PVRC Ad Hoc Group on Toughness Requirements, "PVRC Rcommendations on Toughness Requirements for Ferritic Materials," *Weld. Res. Counc. Bull.* 175 (August 1972).

11. T. U. Marston, ed., *Flaw Evaluation Procedures: ASME Section XI*, EPRI NP-719-SR, Electric Power Research Institute, Palo Alto, Calif., August 1978, including corrections dated April 14, 1980.

12. *1986 ASME Boiler and Pressure Vessel Code*, Sect. III, "Nuclear Power Plant Components," Subsection NCA, Article NCA-2000, "Classification of Components," pp. 9–12.

13. *Standard Review Plan*, NUREG-0800, Part 3.9.3, ASME Code Class 1, 2, and 3 Components, Component Supports, and Core Support Structures, U.S. NRC, Office of Nuclear Reactor Regulation, Rev. 1 — July 1981.

14. T. Y. Carley and W. C. Stoddart, *HFIR Seismic Stress Calculations*, communication with J. G. Merkle, Martin Marietta Energy Systems, Inc., Oak Ridge Natl. Lab., December 4, 1986.

15. S. Timoshenko, *Strength of Materials Part II, Advanced Theory and Problems*, 2d ed., D. van Nostrand, 1953.

16. B. R. Bass, *ORMGEN-ADINA-ORVIRT Calculations for HFIR HB-3*, communication with J. G. Merkle, Martin Marietta Energy Systems, Inc., Oak Ridge Natl. Lab., February 19–20, 1987.

17. *Standard Review Plan*, NUREG-0800, Part 5.3.2, Pressure-Temperature Limits, U.S. NRC, Office of Nuclear Reactor Regulation, Rev. 1, July 1981.

18. W. J. Hall et al, *Brittle Fracture of Welded Plate*, Prentice-Hall, Englewood Cliffs, N.J., 1967.

19. A. K. Dhalla, *Analysis of Weld Cracks in a Shell Nozzle*, WAESD-HT-94000-33, Westinghouse Electric Corporation, Advanced Energy Systems Division, Pittsburgh, Pa., September 1983.

20. M. J. Manjoine and H. R. Voorhees, *Compilation of Stress-Relaxation Data for Engineering Alloys*, ASTM DS 60, American Society for Testing and Materials, Philadelphia, 1982.

21. J. C. Newman, Jr. and I. S. Raju, "Stress-Intensity Factors for Internal Surface Cracks in Cylindrical Pressure Vessels," *J. Pressure Vessel Technol.* 102, 342–46 (November 1980).

22. J. C. Newman, Jr. and I. S. Raju, *Stress-Intensity Factor Equations for Cracks in Three Dimensional Finite Bodies*, NASA Technical Memorandum 83200, NASA Langley Research Center, Hampton, Va., August 1981.

23. J. G. Merkle, "Stress Intensity Factor Estimates for Part-Through Surface Cracks in Plates Under Combined Tension and Bending," pp. 3–22 and 31–32 in *Heavy-Section Steel Technology Program Quart. Prog. Rep. July–September 1974*, ORNL/TM-4729, Vol. II, Union Carbide Corp. Nuclear Div., Oak Ridge Natl. Lab., November 1974.

24. R. H. Bryan et al., *Test of 6-in.-thick Presure Vessels. Series 3: Intermediate Test Vessel V-8*, ORNL/NUREG-58, Union Carbide Corp. Nuclear Div., Oak Ridge Natl. Lab., December 1979.

25. R. C. Shah and A. S. Kobayashi, "Stress Intensity Factor for an Elliptical Crack Under Arbitrary Normal Loading," *Eng. Fract. Mech.* 3, 71–96 (1971).

26. J. D. Gilman and Y. R. Rashid, *Three-Dimensional Analysis of Reactor Pressure Vessel Nozzle*, Paper G 2/6, presented at the First International Conference on Structural Mechanics in Reactor Technology, Berlin, September 20–24, 1971.

27. R. W. Derby, "Shape Factors for Nozzle Corner Cracks," *Exp. Mech.* 12(12), 580–84 (December 1972).

28. R. D. Cheverton, B. L. Corbett, and D. J. Naus, *HFIR Vessel Hydrostatic Proof Test*, ORNL/RRD/INT-9, Martin Marietta Energy Systems, Inc., Oak Ridge Natl. Lab., October 6, 1987.

29. R. D. Cheverton et al., *HFIR Pressure Vessel and Structural Components Materials Surveillance Programs, Supplement 1*, ORNL/TM-1372/S1, Martin Marietta Energy Systems, Inc., Oak Ridge Natl. Lab., October 1987.

Appendix A

REEVALUATION OF THE HORIZONTAL BEAM TUBES

J. R. McWherter C. W. Collins

The High Flux Isotope Reactor (HFIR) is provided with three nominally 4-in.-ID horizontal beam-tube experimental facilities that extend outward from the reactor core at the midplane (Figs. 2.1, 2.2, and 2.4). One beam tube, HB-2, extends radially from the reactor centerline, its inner end penetrating the permanent reflector. Another tube, HB-3, extends tangentially from the inner surface of the permanent reflector. The remaining tube is aligned on a tangential line with both ends extending outward from the reactor. This latter tube is arranged to allow the installation of either two individual facilities or a single through tube. The two ends of this tube are designated HB-1 and HB-4.

Each of the tubes is sealed to, and supported by, the reactor pressure vessel by a system of clamped and bolted flanged joints. From the flanged connection at the pressure vessel, each tube continues through the reactor pool and pool wall and terminates in a recess located in a large cavity in the reactor pool wall. Except in the case of the through tube, the inner ends of the tubes float freely in recesses in the reflector and have sufficient clearance to prevent stresses resulting from differential expansion. The through-tube assembly extends continuously through the pressure vessel. To accommodate expansion and contraction within the vessel, the flanged joints that connect the through tube to the nozzles of the pressure vessel are sealed by stainless steel bellows expansion joints.

A beam-tube assembly consists of two concentric beam tubes that are flanged together in the beam room. The primary beam tube extends from the beryllium reflector to the beam room and is flanged to a vessel nozzle, as mentioned above, to accept the thrust load from the primary-system pressure. A double-bellows assembly at the beam-room flanged end of the beam-tube assembly provides a seal between the beam-tube assembly and the pool wall and accommodates displacement between the vessel wall and beam-tube assembly.

The secondary tube is located inside the primary tube and extends from its flanged end in the beam room to a location corresponding to the vessel wall, where it is capped with a hemihead. The portion of the primary beam tube within the vessel was designed for 1000-psid external pressure and was hydro tested to 1500-psid external pressure during the initial hydro test of the vessel. The extension of the primary tube was designed for 500-psid internal pressure and the secondary tube for 500-psid external pressure. A beam-tube-assembly hydro test was conducted by pressurizing the space between the primary and secondary tubes to 1500 psi.[1] The presently installed set of beam tubes was subjected to a vessel hydro test of 1100 psi in 1983 and to 900 psi on August 4, 1987. In the future the maximum vessel pressure will be ≤900 psi (hydro-test pressure), and the normal operating pressure will be ~500 psi.

The space between the primary and secondary beam tubes is monitored for pressure and is vented to the pool through a 1-in.-diam tube and a 250-psi rupture disc.

A conservative 10-year life was specified for the first set of beam tubes. Surveillance specimens were installed in the reflector region to monitor any effect of radiation on the physical properties or corrosion of the aluminum. The original beam tubes were replaced as scheduled in 1975. The good condition of the original beam tubes and the results of the evaluation of the irradiated specimens led to a recommendation that the replacement beam-tube life be extended to a total of 15 years.[2,3]

The structural evaluation of the beam tubes and the effects of radiation damage thereon included consideration of short-term stability, creep buckling, creep rupture, and propagation of flaws that might be present.[4] The short-term stability analysis was performed in accordance with the *American Society of Mechanical Engineers (ASME) Code*, and as mentioned above, the allowable external pressure for no radiation effects was determined to be ~1000 psi. Because the effect of radiation is to increase the strength of the material, radiation would tend to increase the resistance to buckling.

The creep-buckling analysis was performed in accordance with Ref. 5, using ischronous stress-strain diagrams that are available for the beam-tube material in the unirradiated condition. With a safety factor of 3 applied to the nominal pressure, an allowable pressure of 750 psi was calculated for the desired beam-tube lifetime of 15 years. Once again, and for the same reason, radiation tends to increase the allowable pressure.

The creep-rupture analysis was performed using data from the HFIR beam-tube-material surveillance program (Fig. A.1).* With reference to Fig. A.1, it is apparent that radiation increases the rupture stress and that the stress required for rupture in 15 years (~1×10^5 h) is >30,000 psi, which corresponds to a pressure of ~5000 psi. Until now, the normal pressure on the beam tube has been 750 psi, and for the proposed remaining 10 years it will be ~500 psi. Thus, a safety factor on pressure of ~7 is accommodated and is certainly adequate.

In each of the above calculations, the cylindrical portion of the beam tube was controlling because stresses in the hemihead are less and the fluence is greater.

The potential for propagation of flaws in the beam tube has been evaluated recently by first performing a detailed stress analysis (using finite-element-analysis techniques) to see if significant tensile and shearing stresses exist as a result of beam loading and geometric discontinuities. The results indicate a small tensile stress (~1200 psi) on the outer surface of the beam tube close to the vessel flange. Because the stress is so small and because most of the cross section of the tube wall at this location is in compression, 1/4-T flaws will not propagate through the wall.

---

*The dotted lines in Fig. A.1 indicate a sequence of loadings with successive increases. Each discontinuity represents a different load and loading time. The final load is indicated by a data point, and if the data point has an arrow to the right, the specimen did not rupture. The total time of loading is the sum of those for each different load.

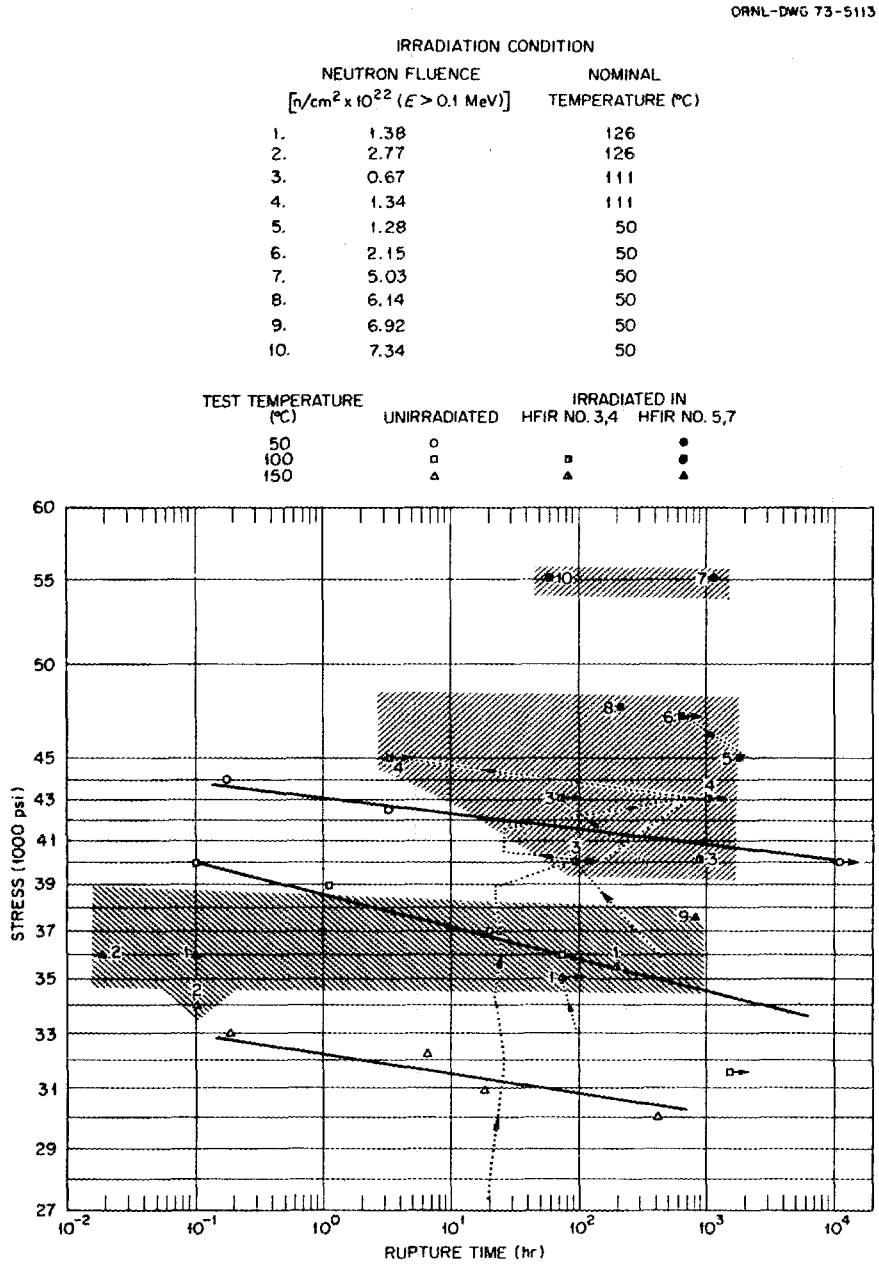

Fig. A.1. Effect of neutron irradiation on creep-rupture of 6061-T6 aluminum. *Source*: K. Farrell, Oak Ridge Natl. Lab., letter to P. Lotts, Oak Ridge Natl. Lab., January 8, 1987.

REFERENCES

1. F. J. Binford, T. E. Cole, and E. N. Cramer, *The High Flux Isotope Reactor Accident Analysis*, ORNL-3573, Union Carbide Corp. Nuclear Div., Oak Ridge Natl. Lab., April 1967, p. 175.

2. K. Farrell, Oak Ridge Natl. Lab., personal communication to A. L. Lotts, Oak Ridge Natl. Lab., January 8, 1987.

3. J. R. McGuffey, J. C. Griess, and G. J. Dixon, Oak Ridge Natl. Lab., personal communication to J. A. Cox, Oak Ridge Natl. Lab., *First Progress Report on the HFIR In-Pile Corrosion Surveillance Program*, December 15, 1969.

4. C. W. Collins, personal communication to R. D. Cheverton, Oak Ridge Natl. Lab., "Review of HFIR Horizontal Beam Tubes," April 10, 1987.

5. J. M. Corum, Oak Ridge Natl. Lab., *Investigation of the Collapse Resistance of the HFIR Horizontal Beam Tubes*, internal correspondence, August 12, 1963.

MARTIN MARIETTA

Internal Correspondence

MARTIN MARIETTA ENERGY SYSTEMS, INC.

January 8, 1987

P. Lotts

Ref. Letter from K. Farrell to Gene Hicks on Recycling of HFIR Horizontal Beam Tubes, dated May 18, 1982.

The DOE-ORO Rothrock Committee inquiring into the HFIR situation has questioned a conclusion I presented in the subject letter. You asked me for an explanation.

The letter was written in 1982 in response to a request from Operations Division asking my opinion on whether it was feasible to reuse the current 6061-T6 aluminum alloy beam tubes in HFIR when the beryllium reflector was replaced in 1983. The expected lifetime of the new reflector was about 8 years. In 1983, the beam tubes would already have been in service for 8 years. Could they go another 8 years? The question was based not only on economic considerations but on whether there was a genuine need to replace the tubes. Had they really exhausted their useful life? After all, the first beam tubes in HFIR had served 9 years without problems and they were in excellent outward condition when they were replaced in 1975. Also, the 6061-T6 alloy beam tubes in the Brookhaven High Flux Reactor had been in service for 17 years and were still going strong. Furthermore, we now had some measurements of the effects of irradiation in HFIR on the properties of 6061 alloy. So there were good grounds for asking the question. In my letter, I discussed what we had learned about radiation damage in 6061-T6 aluminum. I concluded that even though the 6061-T6 aluminum tubes must have suffered some embrittlement during their prior use, I did not see a serious objection to their extended use provided they could be removed and reinstalled without handling damage.

I have not been told exactly what part or parts of my letter has caused the Committee's query. I assume it is the fact that I condoned reuse of embrittled components in HFIR. That decision must be assessed in its proper context. My decision to support reinsertion of the used beam tubes was not based solely on the technical details discussed in the letter. Since the letter was not intended for public consumption, it did not contain a number of important considerations which are familiar to the people in Operations Division to whom the letter was addressed, but without which a less well-informed party might make a different judgement. These considerations must be taken into account. They are as follows:

1. Catastrophic-type failure is unlikely in aluminum alloys.

To some people, the word "embrittled" might mean a glass-like, nil-ductility shatter-type condition. In my letter I used the term in a broader sense, meaning loss of some ductility. Also, the subject is irradiated aluminum, not glass or steel. Fracture of aluminum alloys is quite different from the sudden, unheralded, passage of a single large crack that characterizes catastrophic failures of pressure vessel steels. Aluminum alloys are not strain rate sensitive like steels, and they do not undergo a sharp ductile-to-brittle transition with strain rate or with temperature.

On the contrary, cracks in aluminum usually develop slowly and discontinuously, and they proceed with much local deformation. Furthermore, the increase in strength that accompanies radiation embrittlement in aluminum alloys is advantageous, not detrimental as in ferritic steels. The increased strength means that larger forces are required to plastically deform and fracture the aluminum. I believe it is highly unlikely that the beam tubes will fail catastrophically. Rather, if failure should happen at all, it will probably ensue as perforations which would leak coolant water into the tubes and thus give warning of their presence. Such failure would not be disastrous. A fractured beam tube is not a safety or environmental hazard and is replaceable.

2. The beam tubes are not a potential safety hazard.

This fact was recognized when HFIR was designed, and is discussed in HFIR documentation (The High Flux Isotope Reactor Accident Analysis, ORNL-TM-3573, April 1967). The beam tubes contain helium inside and water outside. If they break, they will collapse into themselves; they will not explode. The worst-case scenario envisages the cooling water flooding into the tubes. Should the seals at the ends of the tubes give way, the water will then escape into the beam rooms where drains are installed to receive it. No fission products would be involved. Fracture of a beam tube would not impair the operation of the control plates for shutting down the reactor.

3. The beam tubes are protected from in-service handling damage.

The beam tubes are passive components that serve only to hold the beam collimators. They are well-protected from accidental damage in service. They are enclosed in the beryllium reflector which guards them from projectiles on their outsides. Internally, the beam collimators are sealed in, thus shielding the tube inner surfaces. The greatest likelihood for accidental damage to the tubes is during their insertion and removal. To date, this manipulation has occurred only when the beryllium reflector was replaced, once in 1975 and again in 1983. Leak tests and TV examination are used to check the tubes for damage.

4. The beam tubes are not essential for HFIR operation.

The beam tubes are accessories and the reactor can function with or without them. If a tube becomes perforated, the reactor can continue to operate provided the tube end seals remain unbroken.

5. Brookhaven Laboratory has good experience with 6061-T6 beam tubes.

The high flux reactor (HFBR) at Brookhaven National Laboratory, became operational in 1965. It uses 6061-T6 beam tubes under similar conditions and temperatures as those in HFIR. The HFBR are welded into the reactor vessel and are not readily removable. Consequently, the HFBR tubes had, in 1982, been in service for 17 years. Inspections have not revealed any cracks, and the tubes are still in use today in 1987.

6. New beam tubes provide only brief respite from embrittlement.

We have learned from our studies of aluminum alloys in HFIR and ORR that radiation hardening and associated loss in ductility in aluminum is caused in large part by tiny precipitates of insoluble silicon atoms generated from reactions of thermal neutrons with aluminum. Ductility is reduced early in exposure life when some critical level of silicon is generated. Thenceforth, the ductility remains constant despite very significant increases in radiation and silicon level. In 6061-T6 alloy tensile specimens irradiated in HFIR target positions at 55°C (130°F) the ductility falls from the unirradiated value of 15% total elongation to a plateau level of about 9% (5-6% uniform elongation) at a neutron-generated silicon level of about 0.5 wt %. For the beam tubes, it is estimated that this level of silicon is reached in an exposure time of six months to one year. Thereafter, the tubes operate in a fully-embrittled condition. This means that the two sets of beam tubes that have each given 8 years of service spent more than seven-eighths of that period in fully embrittled conditions. And they did so without showing any signs of failure. Obviously, the benefit of higher ductility in new tubes is fleeting. Equally obviously, the embrittled condition is not detrimental to satisfactory service.

Those were some of the unwritten considerations that influenced my conclusion. Note that none of these six items, singly or collectively, forbids attempted extension of beam tube service life. On the contrary, they suggest that the chances of tube failure are small and that the consequences of such failure are bearable.

There was one more consideration that was not so favorable--nor was it convincingly unfavorable. This last consideration, described in my letter, was the recognition that the neutron spectrum, specifically the ratio of the thermal flux to the fast flux, might be an important but unquantified factor for radiation damage created at the beam tube sites. This arises because radiation hardening and embrittlement depend on the scale of the distribution of the silicon precipitates; the finer their distribution, the larger the effects. I suspect that the ratio of the thermal to fast neutron fluxes affects the size and the distribution of the precipitates. A low ratio involves a larger fraction of atomic displacements by the fast neutrons, which allows more growth and coarsening of the silicon precipitates and hence less hardening. Conversely, a high ratio implies more hardening and associated loss in ductility. The thermal-to-fast flux ratio for our test data was about 2. The corresponding ratio in the most heavily irradiated sections of the beam tubes is about 7 because of moderation of neutrons by the beryllium reflector. The effects of this higher ratio were unknown in 1982. I speculated that it would cause more hardening and less ductility than indicated by our measured data. The latter showed a ductility plateau of about 9% total elongation, suggesting that further exposure might not cause significant further degradation of ductility. This 9% elongation is far from a truly brittle condition. However, in view of the unknown effects of the high flux ratio, I had to accept that the ductility would be less than 9%. Not very encouraging but hardly the end of the world. Although some remnant ductility in the beam tubes is desirable it is not essential since, as I have

argued, sudden failure is unlikely and does not constitute a dangerous situation. Weighing these pros and cons, I found no good grounds to oppose continued use of the old beam tubes. They were reinstalled in late 1983 and HFIR went back on line on January 2, 1984.

Looking back, I see no scientific reasons to doubt my decision. The beam tubes have accumulated another three years of service for a total of 11 years without mishap. The Brookhaven beam tubes have entered their 22nd year. In the meantime, Brookhaven personnel have measured the mechanical properties of 6061-T6 alloy components, some at high thermal-to-fast flux ratios (C. J. Czajkowski and J. R. Weeks, Brookhaven National Laboratory Report, in press). In the attached Figure, I have plotted their data points superimposed on lines representing the ultimate tensile strengths and total elongations for the HFIR tensile specimens from the target regions. The numbers alongside the BNL circular strength points are the flux ratios; the associated ductility data are shown by the square points. In conformity with my speculation, flux ratios greater than the value of 1.7 for the HFIR data show greater strengthening. But ductilities are not correspondingly degraded even at flux ratios greater than the value of 7 expected in the HFIR beam tubes. It seems, then, that my concern over the effects of the flux ratio was perhaps exaggerated.

One final comment: Surveillance specimens from reactors do not always provide information that is directly pertinent to specific reactor components, as we can see in the present case. When specific data is mandatory, it is best obtained by testing the particular components when they are retired from service. No such tests were requested for the first set of HFIR beam tubes, removed in 1975; they are still available.

This letter was incited by the Rothrock Committee and constitutes part of that enquiry; please ensure that it is entered into the Rothrock report.

KF.

K. Farrell, 5500, MS 376, ORNL (4-5059)

KF:mt

cc: E. E. Bloom
G. H. Burger
~~R. D.~~ Cheverton
H. D. Cochran
B. L. Corbett
E. E. Hill
L. L. Horton
E. E. Hoffman
S. S. Hurt
R. V. McCord
D. M. McGinty
L. K. Mansur
G. C. Manthey
R. K. Nanstad
D. Rothrock
D. W. Sheffey
J. O. Stiegler
J. H. Swanks
J. R. Weir
R. S. Wiltshire

BNL DATA — EFFECTS OF RATIO THERMAL/FAST FLUX RATIO

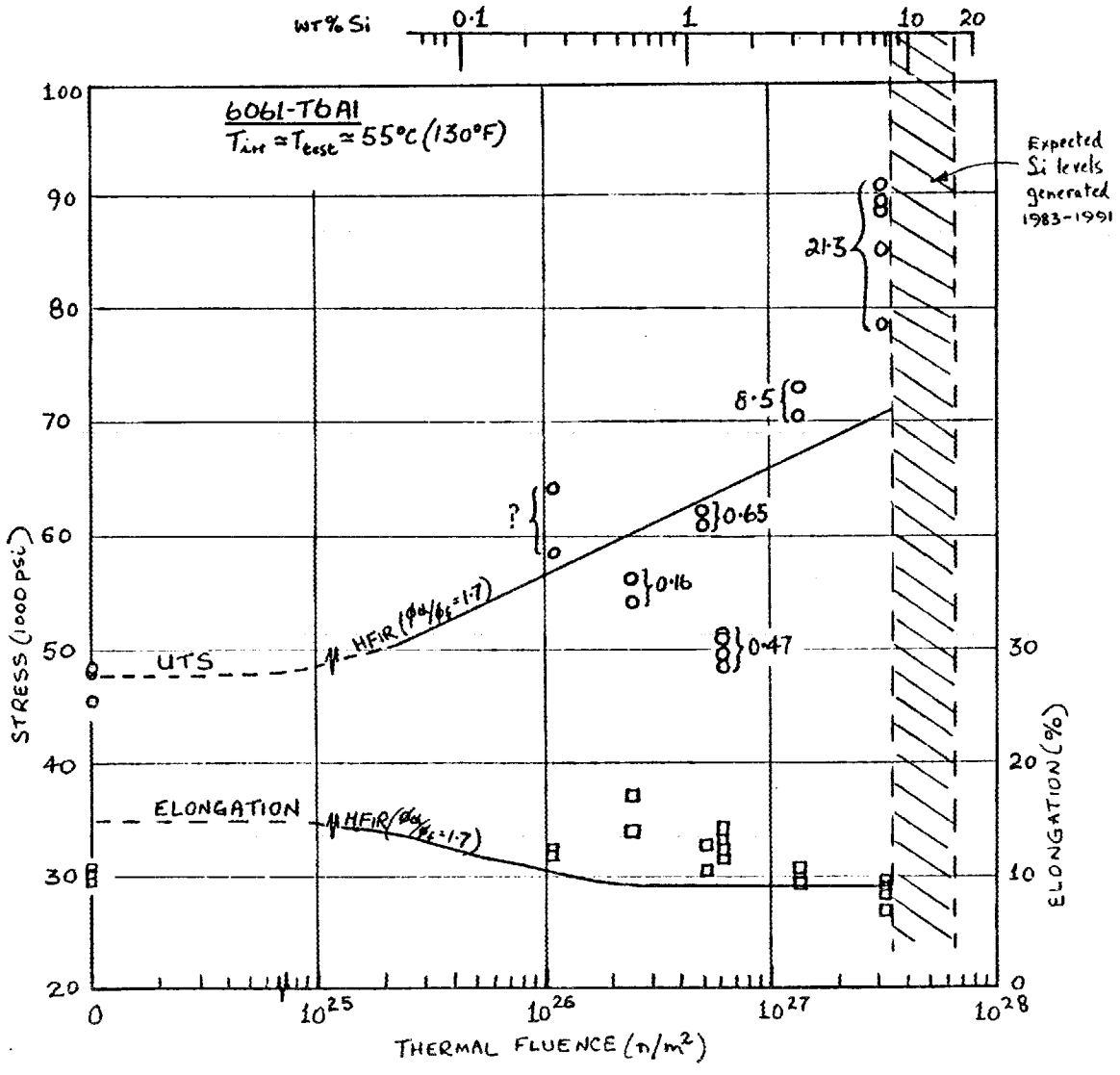

INTRA-LABORATORY CORRESPONDENCE

OAK RIDGE NATIONAL LABORATORY

December 15, 1969

TO: J. A. Cox

SUBJECT: First Progress Report on the HFIR In-Pile Corrosion Surveillance Program

An in-pile corrosion program was established at the start of operation of the HFIR to aid in determining the rate of corrosion of materials used in the primary coolant system.[1] Seven sets of samples each containing 8 coupons were installed in an aluminum holder so that a set of samples could be removed without affecting the remaining coupons. Each set consists of duplicate coupons of the following materials:

6061 T6 aluminum stress relieved at 450° and vapor blasted.
6061 T6 as above plus pretreated in 100°C water for 100 hours.
Beryllium as machined.
347 stainless steel stress relieved at 1560°F and vapor blasted.

The corrosion assembly was placed in the permanent beryllium VXF-1 opening on January 24, 1966 and removed for the first time on August 4, 1969. The set number 5 samples midway along the length of the assembly were removed for examination and weight measurements. Mr. T. M. Sims calculated that these eight coupons had an nvt $\geq$ 0.821 Mev of 2.1×10^{21} and were exposed for 852 effective full power (100 Mw) days.

Visual inspection of the samples revealed a rust colored oxide coating on the aluminum samples with the pretreated coupons appearing to have less oxide coating than the regular aluminum coupons. The beryllium coupons had a typical matte, white coating, while the stainless steel had a thin rust tinted film. All of the coupons, the 1100 aluminum spacers, and the holder had a metallic appearance with no evidence of gross pitting or metal loss.

The samples were weighted, chemically defilmed and reweighted, (see Table I) and then visually reinspected at magnifications up to 30X.

[1] HFIR Pressure Vessel and Structural Components Material Surveillance Program, J. R. McWherter, R. E. Schappel and J. R. McGuffey, ORNL-TM-1372, January 1966.

TABLE I

Data from HFIR Corrosion Specimens

Sample No.	Material	Original Weight (g)	Scrubbed Weight (g)	Defilmed Weight (g)	Total Weight Loss (mg)	Weight Loss (mg/cm^2)	Film Weight (mg/cm^2)
5-1	6061-T6	0.8300	0.8596	0.8262	3.8	0.75	6.5
5-2	6061-T6	0.8180	0.8476	0.8138	4.2	0.82	6.6
5-3	Be	0.5694	0.5792	0.5677	1.7	0.33	2.3
5-4	Be	0.5676	0.5755	0.5663	1.4	0.27	1.8
5-5	347 SST	2.4143	2.4327	2.4206	+6.3	+1.23	2.4
5-6	347 SST	2.4262	2.4452	2.4327	+6.5	+1.28	2.5
5-7	6061-T6 (Pretreated)	0.8319	0.8583	0.8263	5.6*	1.10	6.3
5-8	6061-T6 (Pretreated)	0.8313	0.8570	0.8265	4.8*	0.94	6.0

*Includes weight lost during 100-hr exposure in 100°C water prior to insertion in the HFIR.

The weight measurements in Table I indicate corrosion rates as follows:

Regular 6061-T6 aluminum	0.03 mils/year
Pretreated 6061-T6 aluminum	0.04 mils/year
Beryllium	0.02 mils/year
Stainless steel	- Negligible

Visual examination after the defilming operation revealed that the aluminum is undergoing slight, uniform pitting (see Photos No. 1 and 2) with no single deep pit; there was no evidence of crevice corrosion at or near the contact surface with the holder or the spacers. The machining marks are still clearly visible.

The beryllium showed little evidence of corrosion; there are a few pits where the beryllium made contact with the aluminum spacers. There are cracks near most of the stamped numbers with at least one extending through the thickness of the coupon. This phenomenon was previously observed in out-of-pile corrosion tests. The milling marks are clearly visible on the surface (see Photo No. 3).

The stainless steel had a thin black film present even after repeated defilming. There was no pitting visible at 30 X magnification (see Photo No. 4).

For future reference new samples were inserted in the holder in the number 5 position prior to returning the apparatus to the reactor.

The results and observations indicate that the major materials in the primary system are undergoing very little corrosion even in a high flux field and coupled as galvanic cells. It is recommended that the next examinations be made in the summer of 1971.

The work of the hot cell personnel is appreciated.

J. R. McGuffey

J. C. Griess, Jr.

G. J. Dixon

cc: R. V. McCord

R49452

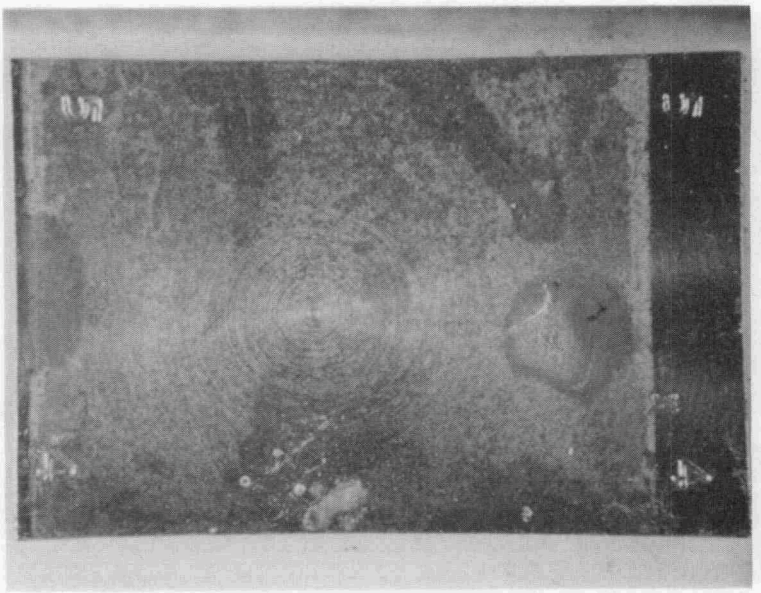

Surface of regular 6061-T6 aluminum coupon showing slight pitting.

R49453

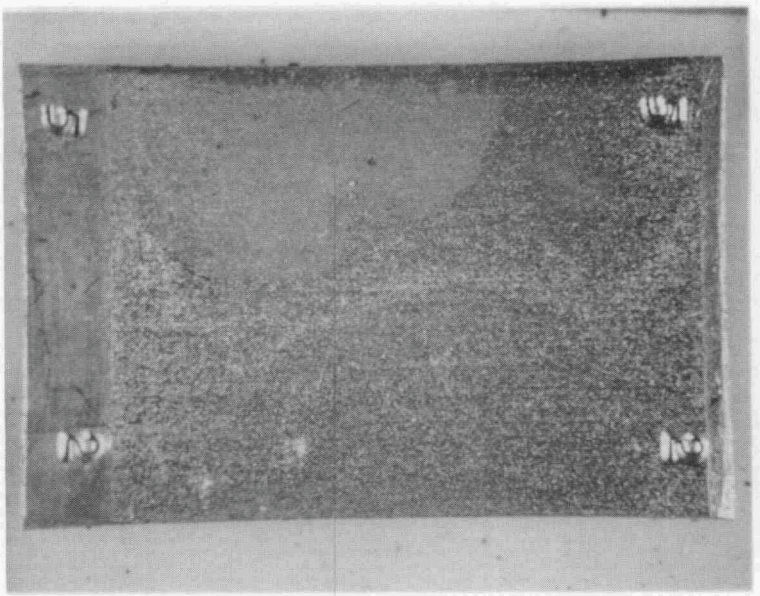

Surface of pretreated 6061-T6 aluminum coupon showing slight pitting.

R49455

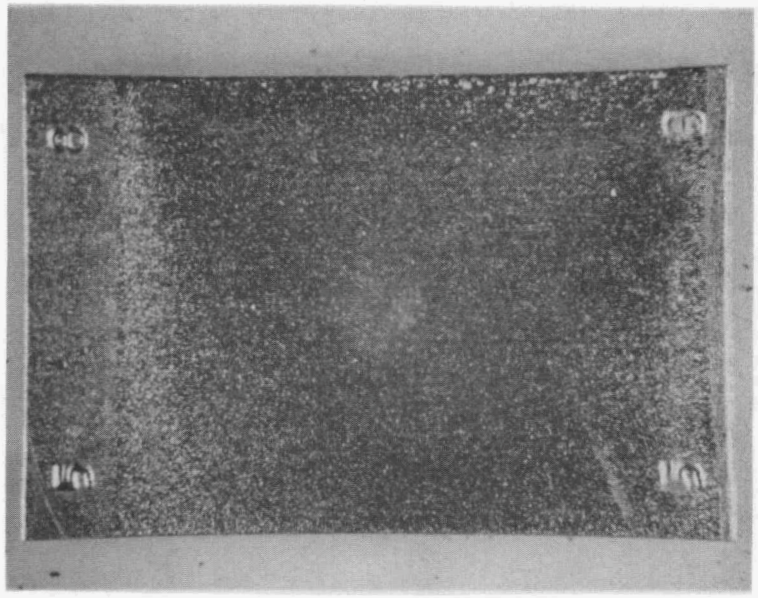

Surface of beryllium coupon showing cracks.

R49454

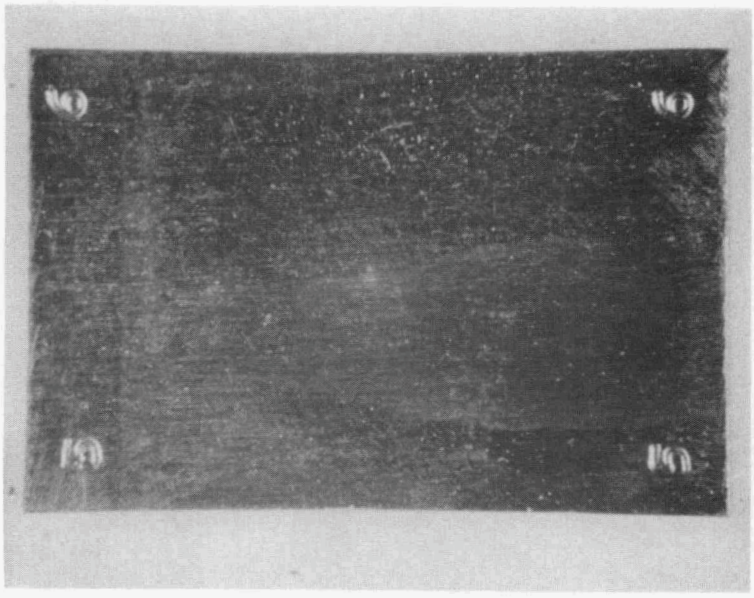

Surface of 347 stainless steel coupon.

Appendix B

HFIR CORE HEAT-REMOVAL ANALYSIS

W. E. Thomas R. D. Cheverton

B.1 INTRODUCTION

The calculated permissible life extension of the High Flux Isotope Reactor (HFIR) vessel is sensitive to primary-system pressure, vessel temperature, and reactor power level. Decreasing the pressure reduces the vessel stresses and, thus, reduces the chances for propagation of flaws that might exist in the vessel. Increasing the vessel temperature increases the material's fracture toughness and, thus, the resistance to propagation of flaws; decreasing the power level reduces the rate at which the fracture toughness is reduced by exposure of the vessel to fast neutrons. These three parameters (pressure, temperature, and power) are interrelated in the core heat-removal analysis. For instance, decreasing the power permits a decrease in pressure and/or an increase in temperature. Furthermore, removing unnecessary conservatism from the analysis permits a decrease in pressure and/or an increase in temperature without decreasing the power. Thus, as a part of the HFIR vessel life-extension studies, it was necessary to review the core heat-removal analysis.

B.2 REVIEW OF CORE HEAT-REMOVAL-ANALYSIS METHODOLOGY

The heat-removal analysis for HFIR is conducted with a code written specifically for HFIR.[1,2] The code includes correlations for incipient boiling and burnout heat fluxes and applies uncertainty factors to "all" of the parameters affecting heat removal from the core. Because of the inclusion of these uncertainty factors, the application of arbitrary safety factors is not appropriate. The code has been updated over the years, and just recently an additional 5% tilt in power distribution was added to accommodate a proposed experiment in the reflector. Another recent change was the removal of the power-level and the coolant-inlet-temperature uncertainty factors associated with instrument error. These are now included in the final evaluation of the results and are based on the data in Ref. 3.

Among other features, the code includes the effect of the changes in power distribution and cladding oxide buildup with time in the fuel cycle. Because the change in power distribution dominates, the most severe set of conditions for heat removal is at the beginning of the fuel cycle when the oxide thickness is least. Thus, all calculations for this study were for the beginning of the cycle only.

For given values of core inlet pressure and coolant temperature, the code calculates the incipient boiling and incipient burnout power levels for specified times in the fuel cycle. The locations for these events are usually at the lower end of the core adjacent to the inner radius of the outer fuel element.

B.3 DESIGN AND OPERATING CRITERIA

Oak Ridge National Laboratory (ORNL) design criteria for HFIR specified no boiling in the core during "normal" operation. Thus, with power and inlet coolant temperature at their high-level scram points, the minimum permissible pressure is that corresponding to incipient boiling; this pressure is used for the low-pressure scram.

The American National Standards Institute (ANSI)/American Nuclear Society (ANS) standards[4] and the Energy Research and Development Administration (ERDA)[5] imposed additional limitations. Reference 4 requires the consideration of safety limits (SL) and limiting safety system settings (LSSS). They are defined as follows.

> 2.1 Safety Limit. Safety limits are limits on important process variables which are found to be necessary to reasonably protect the integrity of the principal physical barriers which guard against the uncontrolled release of radioactivity. The principal physical barrier is often the fuel cladding (which in a solution type reactor, for example, is the reactor vessel).
>
> 2.1.1 Important Process Variables. Important process variables are measurable parameters which individually or in combination reflect the basic physical condition of physical barriers. They may include fuel temperature, reactor power, reactor coolant flow rate, reactor coolant inlet or outlet temperature, pool level, or coolant pressure.
>
> 2.1.2 Criteria — Reactors Requiring Convective Cooling. Safety Limits (SL) shall be established from a basic physical condition, as determined by appropriate process variables, such that the integrity of the principal physical barrier is assured if the SLs are not exceeded. Calculations of SLs shall allow, where applicable, for engineering uncertainties, uncertainties in power distribution, hot channel factors and other appropriate uncertainties.
>
> 2.2 Limiting Safety System Settings. Limiting safety system settings (LSSS) shall be established for the operation of each reactor. LSSSs are those limiting values for settings of the safety channels by which point protective action must be initiated. The LSSSs are chosen so that automatic protective action will terminate the abnormal situation before a safety limit is reached. The calculation of the LSSS shall include the process uncertainty, the overall measurement uncertainty, and transient phenomena of the process instrumentation. To achieve operational flexibility, it is recommended that actual trip points, where possible, be set more conservatively than specification values.
>
> 2.2.1 Criteria — Reactors Requiring Convective Cooling. A LSSS shall be specified for each process variable for which an SL has been established. The setting shall be so chosen that automatic protective action will prevent the most severe anticipated transient from reaching an SL.

Reference 5 states that for steady-state operation "with any given variable at its safety limit (SL), all other variables at their limiting safety-system setting (LSSS), and all uncertainties in the technical knowledge of the process resolved unfavorably, no hot-spot burnout can occur."

The original criteria for HFIR specified that the flux (power)-to-flow ratio for high-level scram be set at 130% of nominal, and eventually this level was specified for the LSSS setting. The SL flux-to-flow ratio is equal to the LSSS value plus the uncertainty in the measurement. It is now specified as 136% of nominal.

The inlet-temperature high-level scram was originally set at nominal + 10°F. When imposed, the LSSS and SL values were specified as nominal + 15°F and nominal + 20°F, respectively, and the +10°F value was retained for scram. Thus, a measurement uncertainty of 10°F is accommodated and is sufficient.

In the heat-removal analysis, the flow rate in the various fuel-element coolant channels is obtained by first specifying the measured pressure drop across the core (108 psi for full flow). Uncertainties in the measured value are included in the 6% uncertainty in the flux-to-flow-ratio level, as mentioned above.

B.4 RESULTS OF ANALYSIS PERTAINING TO VESSEL LIFE-EXTENSION STUDIES

Core heat-removal calculations were made to obtain burnout and incipient-boiling power levels as a function of fuel-element inlet pressure and inlet coolant temperature. The results are shown in Figs. B.1 and B.2 and in Table B.1. The values in the table were obtained by interpolation of the results in Fig. B.1 so that integer values of the critical power levels could be displayed. The corresponding nominal power levels in Table B.1 are equal to the critical values divided by 1.30.

Table B.1 contains several pressures of interest: the core inlet, which is specified for the analysis; the pressure at the top of the control-rod shroud, which is 8 psi greater at full flow; and the pressure differential across the vessel wall, which is the same as that at the top of the shroud minus the differential hydrostatic head on the vessel at midheight of the core.

B.5 PRESSURE SETPOINTS REQUIRED FOR REACTOR OPERATION

Before illustrating the application of the above data, it is necessary to review the pressure setpoints required for reactor operation. The setpoints used previously are specified in Refs. 6 and 7 and are presented here in Table B.2 (the specific values correspond to a nominal power level of 100 MW and to a pressure-measurement location in the primary coolant line upstream of the strainer).

In an effort to reduce the pressures for which the integrity of the vessel must be evaluated, the setpoints for which pressures must be

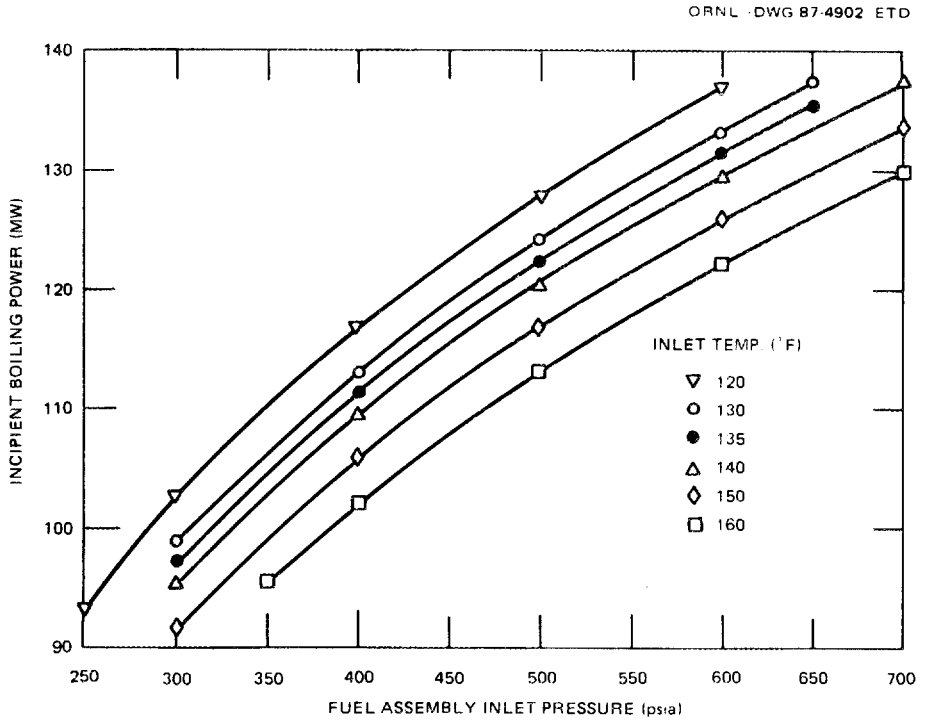

Fig. B.1. Incipient boiling parameters (beginning of cycle, core Δp = 108 psi).

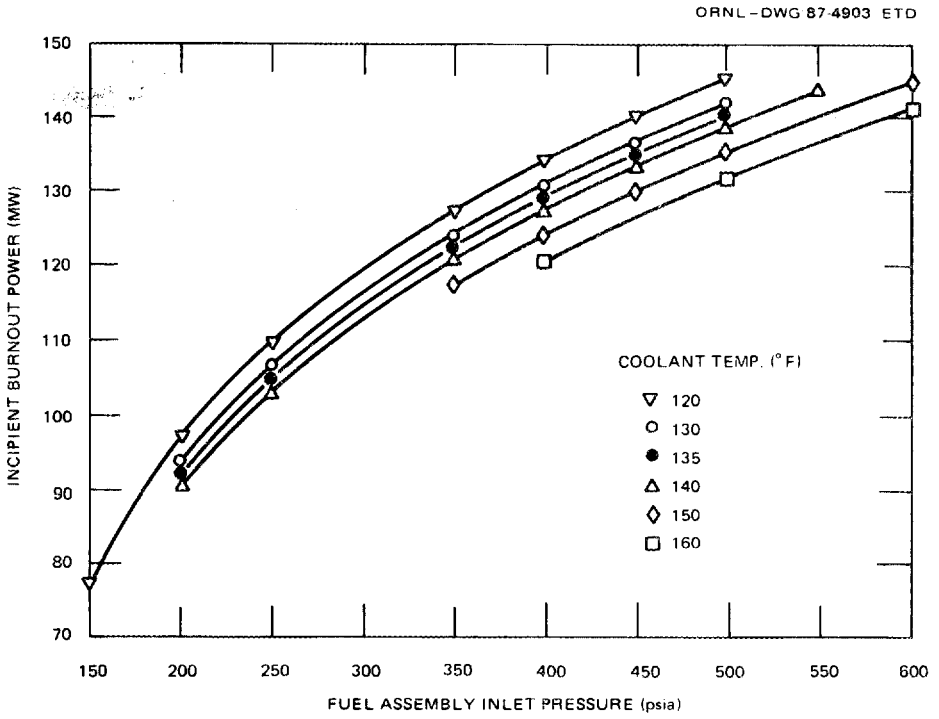

Fig. B.2. Incipient burnout parameters (beginning of cycle, core Δp = 108 psi).

Table B.1. Primary system pressure corresponding to incipient boiling

HFIR power (MW)		Coolant inlet temperature (°F)	Fuel assembly inlet pressure (psia)	Vessel pressure		
Incipient boiling	Normal[a] operation			(psia)	(psig)	(psid)
130	100	120	525	533	518	508
130	100	130	564	572	557	547
130	100	135	583	591	576	566
130	100	140	605	613	598	588
130	100	150	653	661	646	636
130	100	160	700	708	693	683
125	96.2	120	474	482	467	457
125	96.2	130	510	518	503	493
125	96.2	135	528	536	521	511
125	96.2	140	547	555	540	530
125	96.2	150	590	598	583	573
125	96.2	160	638	646	631	621
125						
120	93.8	120	429	437	422	412
120	93.8	130	461	469	454	444
120	93.8	135	478	486	471	461
120	93.8	140	494	502	487	477
120	93.8	150	533	541	526	516
120	93.8	160	575	583	568	558
115	89.8	120	386	394	379	369
115	89.8	130	416	424	409	399
115	89.8	135	430	438	423	413
115	89.8	140	446	454	439	429
115	89.8	150	480	488	473	463
115	89.8	160	519	527	512	502
110	84.6	120	350	358	343	333
110	84.6	130	375	383	368	358
110	84.6	135	390	398	383	373
110	84.6	140	405	413	398	388
110	84.6	150	436	444	429	419
110	84.6	160	470	478	463	453
105	80.8	120	317	325	310	300
105	80.8	130	342	350	335	325
105	80.8	135	354	362	347	337
105	80.8	140	367	375	360	350
105	80.8	150	394	402	387	377
105	80.8	160	424	432	417	407
100	76.9	120	286	294	279	269
100	76.9	130	308	316	301	291
100	76.9	135	320	328	313	303
100	76.9	140	333	341	326	316
100	76.9	150	358	366	351	341
100	76.9	160	383	391	376	366

[a]Normal power = incipient boiling power/1.3.

Table B.2. HFIR pressure setpoints before January 1, 1987

Condition	Pressure at sensing point (psia)
Relief valve	1115
Pressurizer-pump trip	865
High-pressure alarm	815
Normal operation	765
Low-pressure alarm	715
Start standby pressurizer pump	715
Primary-system isolation	690
Low-pressure scram	615
LSSS	590
SL	565
Primary circulating-pump cutoff	415

derived were modified as shown in Table B.3. The pressure for the last item in Table B.3 is arrived at independently from the others. The specific value listed is based on the necessity for preventing cavitation in the primary circulating pumps. The calculated nominal critical value was 165 psia; the proposed 200-psia value includes an appropriate uncertainty. There may be other factors that could tend to increase the specified pump cutoff pressure. However, this pressure must not be greater than the SL pressure.

Table B.3. Proposed HFIR pressure setpoints for future operation (relative to low-pressure-scram setpoint)

Condition	Primary-system pressure [psi (relative)]
Rupture disc (relief valve)	>250
Pressurizer-pump cutoff	+150
High-presure alarm	+125
Normal operation	+100
Low-pressure alarm	+50
Start standby pressurizer pump	+50
Low-pressure scram	0
LSSS	−25
SL	−50
Primary pump cutoff	200 psia (core inlet)

B.6 APPLICATION OF RESULTS

B.6.1 Illustration for Operation at 100 MW

For a nominal power level of 100 MW, the incipient-boiling and, thus, LSSS power level is 130 MW, and the SL power level is 136 MW. If the nominal core-inlet coolant temperature is 120°F, the high-temperature scram, LSSS, and LS temperatures are 130, 135, and 140°F, respectively. Thus, from Table B.1, the low-pressure-scram pressure at the core inlet is 564 psia, and the corresponding normal operating pressure is 664 psia (from Table B.3).

To obtain the SL and LSSS pressures, three combinations of the SL and LSSS incipient burnout power levels and core inlet temperatures must be considered, as shown in Table B.4, for a nominal power of 100 MW. The corresponding pressures are obtained from Fig. B.2, and as indicated in Table B.4, the SL pressure is 410 psia, and the LSSS pressure is 461 psia (the greater of the two values designated LSSS). These values are more than 25 and 50 psi below the low-pressure scram value, and, thus, this

Table B.4. LSSS and SL power, temperature, and pressure, based on incipient burnout

Normal[a] reactor power (MW)	Incipient burnout power (MW)	Coolant inlet temperature (°F)	Fuel assembly inlet pressure (psia)	Vessel pressure[b]		
				(psia)	(psig)	(psid)
100.0	130 LSSS	135 LSSS	410 SL	424	409	399
100.0	136 SL	135 LSSS	461 LSSS	475	460	450
100.0	130 LSSS	140 SL	424 LSSS	438	423	413
96.2	125 LSSS	135 LSSS	370 SL	384	369	359
96.2	131 SL	135 LSSS	418 LSSS	432	417	407
92.3	120 LSSS	135 LSSS	337 SL	351	336	326
92.3	126 SL	135 LSSS	378 LSSS	392	377	367
88.5	115 LSSS	135 LSSS	306 SL	320	305	295
88.5	121 SL	135 LSSS	342 LSSS	356	341	331
84.6	110 LSSS	135 LSSS	278 SL	292	277	267
84.6	116 SL	135 LSSS	314 LSSS	328	313	303
80.8	105 LSSS	135 LSSS	250 SL	264	249	239
80.8	111 SL	135 LSSS	282 LSSS	296	281	271
76.9	100 LSSS	135 LSSS	231 SL	245	230	220
76.9	106 SL	135 LSSS	255 LSSS	269	254	244

[a]Normal power = LSSS burnout power/1.3.

[b]Corrected for instrument error.

latter value is satisfactory. Also, these values are greater than that specified for the main circulating-pump cutoff, another condition that has to be satisfied.

B.6.2 Illustration for Operation at 85 MW

A parametric fracture-mechanics analysis for the HFIR vessel indicates that a nominal power level of ~85 MW and a nominal core inlet temperature of 120°F are reasonable for future operation of HFIR. The corresponding set of pressures, consistent with Table B.3 and based on the data in Tables B.1 and B.4, is presented in Table B.5.

As indicated by the results in Table B.4, the core inlet SL and LSSS pressures could be set as low as 278 and 314 psia, respectively. However, the higher pressures included in Table B.5 are sufficiently below the low-pressure-scram value (in accordance with Table B.3) and provide a greater margin on primary-circulating-pump cavitation.

Table B.5. Proposed HFIR pressure setpoints for future operation at 85 MW

Condition	Pressures			
	Core inlet (psia)	Vessel (psia)	Vessel ΔP (psid)	Rupture-disc rating (psig)
Rupture-disc failure				$650^{+6\%}_{-3\%}$
No flow (maximum pressure)	704	704	679	
Full flow, plugged strainer	672	680	655	
Pressurizer-pump cutoff	525	533	508	
High-pressure alarm	500	508		
Normal operation	475	483	458	
Low-pressure alarm	425	433		
Start standby pressurizer pump	425	433		
Low-pressure scram	375	383		
LSSS	350	358		
SL	325	333		
Main circulating-pump cutoff	200	208		

REFERENCES

1. H. A. McLain, *HFIR Fuel Element Steady State Heat Transfer Analysis, Revised Version*, ORNL/TM-1904, Union Carbide Corp. Nuclear Div., Oak Ridge Natl. Lab., December 1967.

2. T. E. Cole, L. F. Parsly, and W. E. Thomas, *Revisions to HFIR Fuel Element Steady State Heat Transfer Analysis Code*, ORNL/CF-85/68, Martin Marietta Energy Systems, Inc., Oak Ridge Natl. Lab., April 1986.

3. M. J. Roberts, *HFIR Instrument Error Analysis*, ORNL/TM-5055, Union Carbide Corp. Nuclear Div., Oak Ridge Natl. Lab., December 1975.

4. *American National Standard for the Development of Technical Specifications for Research Reactors*, ANSI/ANS-15.1-1982, Sect. 2, American Nuclear Society, LaGrange Park, Ill.

5. T. M. Sims and J. H. Swanks, *Heat Transfer Calculations for the High Flux Isotope Reactor (HFIR) Technical Specifications — Bases for Safety Limits and Limiting Safety System Settings*, ORNL/TM-5844, Union Carbide Corp. Nuclear Div., Oak Ridge Natl. Lab., September 1977.

6. *High Flux Isotope Reactor Technical Specifications*, ORNL/TM-5711/R2, Martin Marietta Energy Systems, Inc., Oak Ridge Natl. Lab., November 1985.

7. *Operating Manual for the High Flux Isotope Reactor Operating Procedures*, ORNL/TM-1168/R2, Martin Marietta Energy Systems, Inc., Oak Ridge Natl. Lab., September 1985.

Appendix C

PRESSURE-VESSEL INTEGRITY EVALUATION CONCEPTS

J. G. Merkle

C.1 MODES OF FRACTURE

In the design and safety analysis of a nuclear pressure vessel, all physically possible modes of failure must be considered and avoided by the provision of adequate safety margins. These modes of failure include plastic collapse and subsequent tensile instability; buckling; crack formation by fatigue and environmental effects; and crack extension by fatigue, ductile tearing, and cleavage (brittle fracture). It is the first and last modes of failure that are of particular interest in this evaluation because both the tensile ductility and the resistance to crack extension (the fracture toughness) are reduced by neutron irradiation. The latter is the most directly related to the results of the recent surveillance specimen tests, and, therefore, it will be discussed first.

C.2 MEASURES OF FRACTURE RESISTANCE OF STEELS

For practical reasons several measures of the fracture resistance of steels are in use in the nuclear industry. Although the most direct method of measuring the fracture resistance of steels is a linear elastic fracture mechanics (LEFM) test, the specimen sizes required to prevent yielding before fracture are usually unfeasible for surveillance program applications. Therefore, older, simpler, and smaller, but less-direct tests are often employed. The Charpy V-notch specimen, which measures 10 × 10 × 55 mm and contains a 2-mm-deep notch, is broken in bending by a hammer attached to a swinging pendulum, and the impact energy absorbed by the specimen is empirically related to fracture performance.[1] The drop-weight test, which uses a somewhat larger beam specimen, measures a temperature called the nil-ductility transition (NDT) temperature, above which a crack running out of a notch in a brittle weld bead will not propagate completely across the tension face of the specimen at a specified deflection.[1] These two tests are used in combination in the *American Society of Mechanical Engineers (ASME) Code*[2] to define a reference nil-ductility transition temperature (RT_{NDT}), which is itself used as an indexing parameter for making lower-bound estimates of fracture toughness as a function of temperature. The RT_{NDT} is either the NDT or 60°F below the temperature at which transversely oriented Charpy specimens develop more than 50 ft-lb of impact energy and 35 mils of lateral expansion, whichever is higher.

C.3 VESSEL FRACTURE SAFETY EVALUATION APPROACHES

C.3.1 The Fracture Analysis Diagram

Before the development of the analytical procedures underlying LEFM, a semiempirical approach to the prevention of fracture associated with flaws, based on the Fracture Analysis Diagram (FAD) (Fig. C.1) developed at the Naval Research Laboratory (NRL), was in general use.[3] FAD incorporates two primary concepts: a Crack-Arrest-Temperature (CAT) curve below which cracks are not expected to propagate and a family of crack initiation curves that provide an approximate relationship between stress, flaw size, and temperature.[4]

Because cracks may propagate through strain-rate-sensitive materials at lower nominal stresses than are required to initiate the same size crack, a test was devised to measure the minimum propagation stress. This became known as the Crack Arrest Test, and its results were called the CAT curve. The CAT curve is a plot of minimum propagation stress vs temperature, and it undergoes a transition in the same manner as Charpy V-notch impact energy. The minimum propagation stress is measured as the largest stress at which an artificially initiated crack in a large wide plate will not continue to propagate at a given temperature. Despite

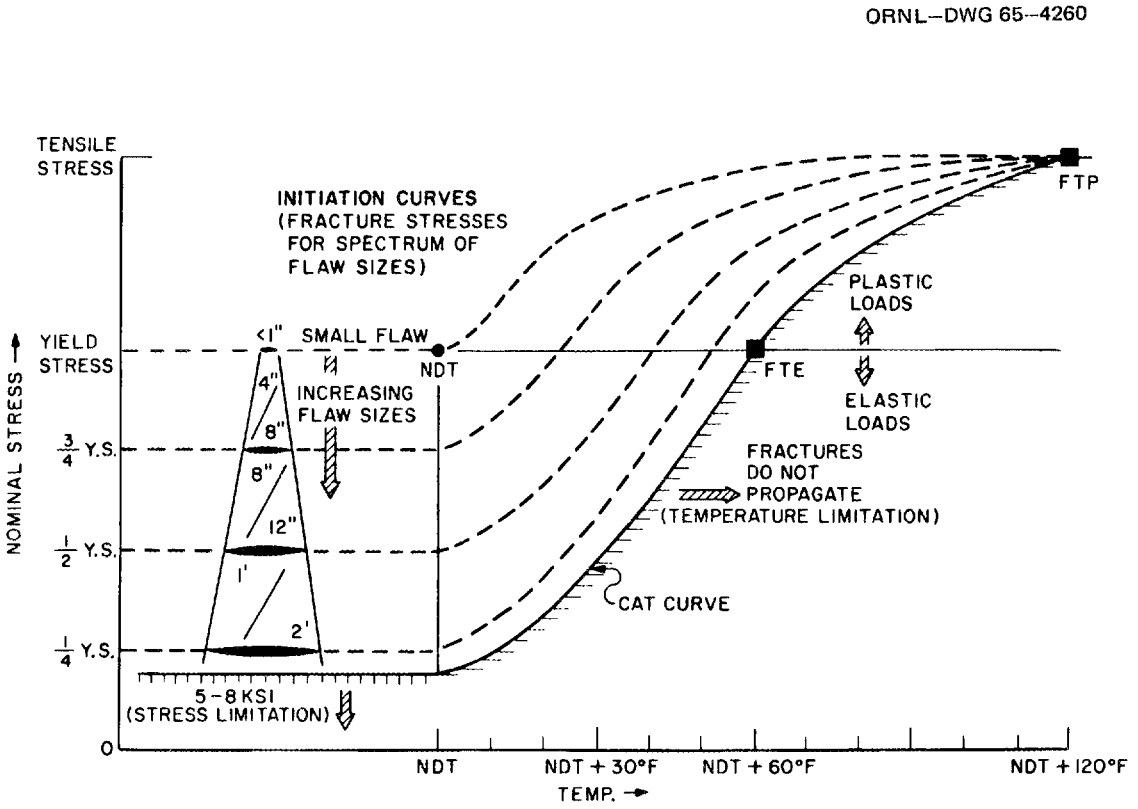

Fig. C.1. Fracture analysis diagram (FAD).

observed size effects, which would be expected on the basis of fracture mechanics analysis, the CAT curve was an important part of the FAD.[3,4]

The dashed lines in Fig. C.1 give, as a function of temperature referenced to the NDT temperature, the stress at which a crack of a given size will start to propagate. The NDT temperature is determined directly from a drop-weight test or indirectly by correlation with the simpler Charpy impact test. The parametric crack-size curves were determined partially by fracture mechanics analysis and partially by plotting actual failure data. For most strain-rate-sensitive steels, the CAT curve crosses the yield stress curve at about the NDT temperature plus 60°F [the fracture transition elastic (FTE)] and joins the ultimate strength curve at about the NDT temperature plus 120°F [the fracture transition plastic (FTP)]. For temperatures above the FTE temperature, cracks supposedly will not propagate through regions carrying a nominal stress below yield. Because primary stresses are limited to values below yield, full-load operation was generally permitted above the NDT temperature plus 60°F with only reduced loads permitted below the NDT temperature plus 60°F to stay below the CAT curve. This was the basis for the minimum full-load operating temperature of NDT + 60°F applied to the High Flux Isotope Reactor (HFIR) vessel. The large flaw sizes corresponding to the CAT curve were implicitly considered to provide a degree of conservatism for smaller flaws more than sufficient to compensate for the lack of analysis of the crack-arrest temperature tests. The small flaw initiation curve did not seem to involve any deliberate conservatism.

In application, drop-weight tests were not always conducted. For convenience, NDT was sometimes estimated by a correlation equating it to the temperature of occurrence of a specific and material-dependent Charpy V-notch impact energy. In fact, the predecessor[5,6] to the ASME Code for Nuclear Vessels contained the information for making such estimates. This information, shown in Table C.1, indicates that for A212 steel the Charpy V-notch impact energy that occurs at the NDT is ~15 ft-lb. Similar information for weld metals appears in graphical form in a book by Shank.[7]

Based on Table C.1, the NDT correlation energies for the materials contained in the HFIR vessel were estimated[8,9] as shown in Table C.2. Only one of the materials, A-212, grade B, appears explicitly in Table C.1. The NDT correlation energy for the A-105, grade II forging material was apparently estimated as 15 ft-lb because the material's chemistry is close to that of the A-212 plate. The NDT correlation energy for the A-350, grade LF3 forging material was no doubt estimated as 30 ft-lb because the material's yield stress exceeds 45 ksi.

C.3.2 Linear Elastic Fracture Mechanics

LEFM is a collection of analytical and experimental techniques used in conjunction with stress analysis to prevent fracture associated with flaws in engineering structures. The basic premise of fracture mechanics is that fractures are caused by flaws. Thus, fracture mechanics focuses its attention on the stresses and strains near the tips of flaws. As a conservative first approximation, flaws are treated mathematically as cracks with zero radii of curvature at their ends.

Table C.1. Estimated values of Charpy V-notch impact energy occurring at the NDT for specific steels and yield stress ranges

a. Correlation for specific materials

Material	Charpy V-notch energy absorption (ft-lb) correspondence to NDT temperature
ASTM A-212	15
AISI Type 410	20
ASTM A-302	30
SAE 4340	35

b. Conservative correlation for use in the absence of better data

Material class by yield strength	Charpy V-notch energy absorption (ft-lb)
<45,000 psi	20
45,000 to 75,000 psi	30
>75,000 psi	40

Table C.2. Estimated Charpy V-notch impact energies occurring at the drop-weight NDT for the materials in the HFIR pressure vessel

Material	CVN at NDT (ft-lb)
A-212, grade B	15
A-105, grade II	15
A-350, grade LF3	30

The ability of a material to sustain a stress in the presence of a sharp crack is called its fracture toughness. In fracture mechanics, fracture toughness is represented by the value of a single stress analysis parameter that completely controls the stress conditions near the crack tip.

The basis of LEFM is partly experimental and partly analytical.[10] The experimental basis is the observation that for geometrically similar specimens that contain sharp cracks, the nominal fracture stress σ_f is inversely proportional to the square root of the crack size, provided that the crack size is greater than some minimum crack size and that the fracture stress is less than some stress near the yield stress. Mathematically, the inverse square root law can be stated as

$$\sigma_f \sqrt{a} = \text{constant} \ . \tag{C.1}$$

The analytical basis of LEFM is the elastic stress analysis of sharp cracks. The stress distribution near the tip of a sharp crack is completely controlled by the presence of the crack so that the equations for the elastic stress distribution near the tip of a sharp crack have the same asymptotic form for all cracks. The equations for the stresses near the tip of a sharp crack are all of the form

$$\lim_{r \to o} \sigma_{ij} = K_I \left[\frac{f_{ij}(\theta)}{\sqrt{2\pi r}} \right] \ , \tag{C.2}$$

where r is the radial distance in inches from the crack tip and θ is the angle measured counterclockwise from the plane of extension of the crack. The magnitudes of the stresses near the tip of a sharp crack are completely controlled by the factor K_I, called the "stress intensity factor," a common factor in the equations for all the stress components. The factor K_I is always given by an equation of the form

$$K_I = C\sigma\sqrt{\pi a} \ . \tag{C.3}$$

In Eq. (C.3) C is a nondimensional "shape factor" that depends on the relative size and shape of the flaw and the structure and on the mode of loading, σ is the nominal stress at the location of the flaw in ksi, and a is the flaw size in inches. At fracture, $\sigma = \sigma_f$. Thus, at fracture, Eq. (C.3) gives

$$K_I = (C\sqrt{\pi})(\sigma_f \sqrt{a}) \ . \tag{C.4}$$

For geometrically similar specimens, the factor ($C\sqrt{\pi}$) is constant. From Eq. (C.1) the factor ($\sigma\sqrt{a}$) is also constant at fracture. Therefore, K_I has a constant value at fracture.

The value of K_I at fracture is affected by thickness. The effect of increasing the thickness is to increase the transverse restraint against crack-tip yielding and, thus, to raise the maximum tensile stresses near the crack tip. This tends to reduce the calculated value of K_I at fracture to its minimum value, which is designated as K_{Ic} and called the "plane-strain fracture toughness." For structural steels, K_{Ic} also varies with temperature and with strain rate. K_{Ic} tends to decrease with both decreasing temperature and with increasing strain rate. In summary, K_I is an elastic stress analysis parameter that is found experimentally to have a constant value at fracture for defined conditions within a certain range of stress, flaw size, and thickness.

The foregoing discussion has been concerned with the initiation of fracture from a stationary flaw. The concept of the stress-intensity factor also applies to the stress conditions governing the arrest of a running crack. In structural steels the crack-arrest toughness, designated as K_{Ia}, is apt to be less than the static-initiation toughness K_{Ic} at a given temperature. It is important that this fact be considered when performing a safety analysis for a structure constructed of a mild or an intermediate grade steel, including a nuclear pressure vessel.

To achieve structural reliability, a margin of safety is provided in design between the estimated strength of a structure and the maximum load expected to occur in service. The strength of a structure is defined as a combination of loads that would cause failure. The actual strength of a structure is often not known exactly. However, it is usually possible to underestimate the strength of a structure, based on a plastic collapse analysis, neglecting strain hardening. The underestimated strength divided by a factor of safety, which is usually between 1.5 and 2.0, becomes the highest permissible load in service.

According to Sect. III of the ASME Pressure Vessel Code, all parts of a nuclear pressure vessel are presumed to be capable of reaching plastic limit conditions under primary stresses. Primary stresses are defined as those that are not limited by the process of deformation itself. This is the basis for determining allowable stresses as the yield stress divided by a factor of safety. When considering the effects of undetected flaws, the safety factors are usually distributed between the stress level, the assumed flaw size and the estimated fracture toughness with due consideration being given to ensuring that a reasonable safety margin exists for unanticipated overloads, as well as for the known operating conditions.

REFERENCES

1. J. M. Barsom and S. T. Rolfe, *Fracture and Fatigue Control in Structures*, 2d ed., Prentice-Hall, Inc., Englewood Cliffs, N.J., 1987.

2. *ASME Boiler and Pressure Vessel Code*, American Society of Mechanical Engineers, New York.

3. W. S. Pellini, L. E. Steele, and J. R. Hawthorne, *Analysis of Engineering and Basic Research Aspects of Neutron Embrittlement of Steels*, NRL Report 5780, April 17, 1962.

4. G. D. Whitman, G. C. Robinson, and A. W. Savolainen, eds., *Technology of Steel Pressure Vessels for Water-Cooled Nuclear Reactors*, ORNL/NSIC-21, Union Carbide Corp. Nuclear Div., Oak Ridge Natl. Lab., December 1967.

5. *Tentative Structural Design Basis for Reactor Pressure Vessels and Directly Associated Components (Pressurized Water Cooled Systems)*, rev. Tech. Pub. PB 151987, U.S. Department of Commerce, December 1, 1958.

6. P. P. Puzak and W. S. Pellini, "The Evaluation of the Significance of Charpy Tests for Quenched and Tempered Steels," *Weld. J.*, Research Supplement, 35(6), 275-S (June 1956).

7. M. E. Shank, ed., *Control of Steel Construction to Avoid Brittle Fracture*, Welding Research Council, New York, 1957.

8. P. Patriarca, "Some Thoughts Regarding the Possibility of Brittle Fracture of the HFIR Reactor Pressure Vessel," internal correspondence, Union Carbide Corp. Nuclear Div., Oak Ridge Natl. Lab., March 17, 1961.

9. J. R. McWherter, R. E. Schappel, and J. R. McGuffey, *HFIR Pressure Vessel and Structural Components Material Surveillance Program*, ORNL/TM-1372, Union Carbide Corp. Nuclear Div., Oak Ridge Natl. Lab., January 1966.

10. J. G. Merkle, "Fracture Safety Analysis Concepts for Nuclear Pressure Vessels, Considering the Effects of Irradiation," *J. of Basic Eng.* 93(2), 265–73 (June 1971).

Appendix D

MATERIALS EVALUATION

:TION (R. K. Nanstad)

Evaluation of the materials in the High Flux Isotope Reactor (HFIR) pressure vessel is, of course, an integral part of the overall assessment of vessel integrity. In the original design and assessment of the pressure vessel, base metals and welds were evaluated according to standard specifications and some special Oak Ridge National Laboratory (ORNL) specifications. Typical tensile properties of strength and ductility, as well as Charpy V-notch (CVN) impact toughnesses, were measured and determined to be in compliance with all applicable specifications. All of the structural materials used for the vessel are ferritic, and it was recognized that neutron-induced embrittlement would occur dependent on the levels of exposure. Various actions were implemented to mitigate the effects of embrittlement: for example, the use of a low-temperature material, A350 grade LF3, for the two beam-tube nozzles expected to receive the highest exposures; design changes to reduce the neutron fluence; and a material surveillance program to monitor the extent of embrittlement.

The pressure-vessel surveillance program was established before operation of HFIR on November 8, 1965. A detailed description of the surveillance program is contained in ORNL/TM-1372.[1] The program includes base metal CVN specimens removed from prolongations of the beam-tube nozzles and dropouts of vessel shell material removed before installation of the nozzles.

No welds were included in the surveillance program, however, and an irradiation task has been conducted to determine irradiated toughness of the welds in the beltline region of the vessel. Additionally, the vessel shell material was tested and irradiated in three different orientations to provide a data base for a comprehensive evaluation of crack propagation. The availability of archival material was severely limited, and documentation regarding materials, heat treatments, and fabrication procedures was incomplete. Because of those deficiencies, the materials evaluation project involved detailed metallurgical examination of surveillance specimens, qualification weldments, and other materials identified as candidates for the irradiation task. It also included the fabrication of a submerged-arc weldment to represent the longitudinal seam and circumferential girth welds of the pressure vessel.

Additional studies of materials included various microstructural examinations to reveal embrittlement mechanisms and microstructural characteristics relevant to a full understanding of the materials' responses to irradiation. Also, in the event that thermal annealing of the vessel is considered a potential method to extend vessel life beyond that resulting from this study, microstructural characterizations will be necessary. Many of these examinations are essential in large part because the HFIR vessel operates at 120°F, compared with commercial light-water reactors (LWRs), which operate at ~550°F, and the bulk of radiation damage knowledge for ferritic steels evolves from LWR technology.

The materials evaluation project has provided mechanical property data and has characterized the relevant materials to allow for a full evaluation of vessel integrity for continued operation. The following sections will summarize, and describe in detail where necessary, a bibliography relevant to the HFIR vessel embrittlement, the surveillance program results, a description of materials and properties, results of the irradiations task, materials studies intended to provide information regarding mechanisms of radiation damage at low neutron fluxes and low irradiation temperatures, and the concept for reoperation surveillance.

D.2 PRESSURE-VESSEL MATERIALS SURVEILLANCE RESULTS
(R. K. Nanstad)

The surveillance program is described in Chap. 3. The materials in the program represent the various components of the pressure vessel, that is, the shell and the beam-tube nozzles located in regions of high flux at the reactor beltline. As described in Ref. 1, the testing philosophy is to test three CVN impact specimens at selected temperatures to bracket the nil-ductility transition (NDT) temperature, followed by three tests at the estimated NDT temperature. Also as described in Ref. 1, the NDT temperatures are indexed at CVN energies of 15 ft-lb for A105 grade II and A212 grade B and 30 ft-lb for A350 grade LF3. In some cases, only one capsule (three CVN specimens) was removed for testing. Thus, the numbers of specimens are relatively small and are intended to provide estimates of the materials toughness as exposure time increases.

Specimens located at keys 1 and 4 were considered symmetric as were those from keys 6 and 7. Thus, specimens from those keys were combined for testing. Tables D.1—D.4 provide all of the test results obtained in the surveillance program, including the neutron flux (ϕ) and fluence (Φ) (>1 MeV). The unirradiated tests were conducted in 1965 except for additional tests at 60, 90, and 120°F, which were conducted as part of this assessment.

Although details of the earlier tests are unclear, the specimens removed after 15 and 17.5 equivalent full-power years (EFPY) were tested with a machine calibrated in accordance with American Society for Testing and Materials (ASTM) E23.[2] Additionally, the temperature measuring system was calibrated and verified temperature measurements within 1°C over the test temperature range. Figures D.1—D.5 graphically depict the surveillance test results for each key location. The curve fits shown in the figures are computer-produced fits for each data set. Table D.1 and Fig. D.1 show results for both high-flux and low-flux A105 grade II specimens from the 17.5-EFPY case. The variation in neutron fluence can be quite large within a given key location (see Appendix E on dosimetry), and a capsule was removed from a low-flux region of key 4. No specimens were removed from key 5 after 17.5 EFPY because the shell material test specimens at keys 6 and 7 verified that the fluence at key 5 is substantially lower and key 6 and 7 results provide the highest NDT for shell material.

A summary of the test results is given in Table D.5. The listed NDT values for each data set were determined through construction of hand-

Table D.1. Charpy impact surveillance test results for HFIR components HB1 and HB4, A105 grade II steel

Specimen	Key	Test temperature (°F)	Energy (ft-lb)	Appearance (% shear)	Lateral expansion (mils)	Neutron flux, >1 MeV ($n/cm^2 \cdot s \times 10^8$)	Neutron fluence, >1 MeV ($n/cm^2 \times 10^{17}$)
			Unirradiated				
B-58		−80	11.5	0	13		
B-67		−80	7.0	0	9		
B-68		−70	20.5	8	20.2		
B-79		−70	19.0	10	17.2		
B-120		−70	31.5	5	27.7		
B-18		−60	19.5	10	19.5		
B-29		−60	22.5	0	22.9		
B-30		−60	21.5	9	20.1		
B-80		−50	18.0	5	19.7		
B-89		−50	27.5	11	26.8		
B-119		−50	29.5	0	27.7		
B-39		−40	18.5	9	22.2		
B-40		−40	26.5	0	26.9		
B-49		−40	31.5	10	30		
B-54		−40	27		21.0		
B-90		−40	17.5	5	21.2		
B-100		−30	25.5	16	27.5		
B-109		−30	31.0	18	30		
B-110		−30	30.5	16	31.5		
B-9		−20	46.0	27	40		
B-10		−20	43.5	30	39		
B-17		−20	39.5	26	34.8		
B-53		0	42		36.9		
B-57		0	43.5	53	42.9		
B-99		0	45.5	48	43		
B-52		40	55		48.2		
B-50		74	83.0	100	73.4		
B-51		75	89		68.2		
B-98		120	78.0	100	67.7		
			Irradiated (11-8-65 through 8-4-69)				
B-1	1	−80	14	5		4.16	0.31
B-2	1	0	44	43		4.16	0.31
B-3	1	60	65	66		4.16	0.31
B-7	1	−40	20	9		5.17	0.38
B-19	1	0	43	26		5.17	0.38
B-8	1	40	46	51		5.17	0.38
B-101	4	−60	14	5		5.17	0.38
B-102	4	0	48	40		5.17	0.38
B-103	4	60	44	57		5.17	0.38
B-104	4	−40	17	10		4.16	0.31
B-106	4	0	30	37		4.16	0.31
B-105	4	40	45	49		4.16	0.31
			Irradiated (11-8-65 through 2-14-74)				
B-42	1	−42	20		13.8	3.73	0.76
B-4	1	−22	37		27.5	6.06	1.23
B-38	1	0	39		29.9	3.73	0.76
B-5	1	40	41		33.3	6.06	1.23
B-6	1	80	67.5		51.6	6.06	1.23
B-37	1	90	89		63.7	3.73	0.76
B-63	4	−20	22		14.6	3.73	0.76
B-83	4	0	21		17.6	6.06	1.23
B-62	4	20	29		26.1	3.73	0.76
B-84	4	40	37		31.3	6.06	1.23
B-61	4	60	69		49.4	3.73	0.76
B-85	4	80	75		55.5	6.06	1.23

Table D.1 (continued)

Specimen	Key	Test temperature (°F)	Energy (ft-lb)	Appearance (% shear)	Lateral expansion (mils)	Neutron flux, >1 MeV ($n/cm^2 \cdot s \times 10^8$)	Neutron fluence, >1 MeV ($n/cm^2 \times 10^{17}$)
Irradiated (11-8-65 through 10-18-83)							
B-44	1	−40	9.7	10	8.5	6.06	2.87
B-43	1	0	20.1	30	4.5	6.06	2.87
B-45	1	40	30.0	30	19.0	6.06	2.87
B-116	4	−20	19.5	10	6.5	3.73	1.77
B-117	4	−20	17.1	20	4.5	3.73	1.77
B-118	4	−20	13.4	10	1.0	3.73	1.77
Irradiated (11-8-65 through 11-15-86) — high flux							
B-36	1	−50	15.4	5	1.7	7.27	4.02
B-34	1	−20	5.7	5	0.7	7.27	4.02
B-35	1	50	61.8	55	31.7	7.27	4.02
B-81	4	−50	11.6	20	0.2	7.27	4.02
B-82	4	−20	15.3	20	1.3	7.27	4.02
B-70	4	−20	13.9	10	0.7	7.27	4.02
Irradiated (11-8-65 through 11-15-86) — low flux							
B-65	4	−50	6.1	5	1.2	3.34	1.85
B-66	4	−20	18.1	20	0.7	3.34	1.85
B-64	4	50	41.8	55	22.6	3.34	1.85

Table D.2. Charpy impact surveillance test results for HFIR component HB2, A350 grade LF3 steel

Specimen	Key	Test temperature (°F)	Energy (ft-lb)	Appearance (% shear)	Lateral expansion (mils)	Neutron flux, >1 MeV ($n/cm^2 \cdot s \times 10^8$)	Neutron fluence, >1 MeV ($n/cm^2 \times 10^{17}$)
			Unirradiated				
C-55		−160	17.5		15		
C-45		−140	19.5		17.8		
C-46		−130	27.5		26.1		
C-5		−120	23.5		23.5		
C-34		−120	25.5	16.7	24.5		
C-44		−120	29.5		27.2		
C-13		−110	32.5	18.9	30.5		
C-35		−110	25.5		26.5		
C-36		−110	32.5		31.3		
C-7		−104	36		30.3		
C-12		−100	33.0	17.8	33.4		
C-43		−100	34.5		31.6		
C-53		−100	27.5		27.3		
C-54		−90	37.0	32.9	37.2		
C-56		−90	40.5	27.6	38.9		
C-2		−80	38.5	35.9	36.7		
C-3		−80	42.5		40.9		
C-4		−80	38.5	31.5	37		
C-24		−60	39.5		42		
C-25		−60	45.5	24.3	46		
C-33		−60	54.0	40.0	50.2		
C-23		−40	67.0	40.6	58.9		
C-15		0	84.0	65.9	71		
C-22		0	87.5	95.1	73		
C-59		40	106		83.4		
C-14		74	95.5	100	43.2		
C-61		120	119	100	87.6		
			Irradiated (11-8-65 through 8-4-69)				
C-18	2	−140	17	0		11.10	0.82
C-19	2	−80	30	6		11.10	0.82
C-20	2	−20	52	58		11.10	0.82
C-37	2	−140	16	0		11.10	0.82
C-32	2	−60	43	44		11.10	0.82
C-31	2	0	66	77		11.10	0.82
			Irradiated (11-8-65 through 2-14-74)				
C-29	2	−100	9		4.9	11.10	2.26
C-41	2	−60	31		20.9	11.10	2.26
C-28	2	−40	47		35.8	11.10	2.26
C-49	2	−4	49		42.3	11.10	2.26
C-30	2	0	53		46.6	11.10	2.26
C-48	2	60	95		73.8	11.10	2.26
			Irradiated (11-8-65 through 10-18-83)				
C-38	2	−25	24.0	30	6.0	11.10	5.26
C-40	2	−10	26.2	25	8.5	11.10	5.26
C-39	2	25	53.6	40	25.0	11.10	5.26
			Irradiated (11-8-65 through 11-15-86)				
C-21	2	−20	17.8	25	2.1	11.10	6.14
C-16	2	15	25.8	40	4.0	11.10	6.14
C-17	2	15	34.2	30	9.0	11.10	6.14
C-27	2	15	36.9	50	17.8	11.10	6.14
C-10	2	40	56.0	55	28.8	11.10	6.14
C-26	2	40	48.8	60	17.8	11.10	6.14

Table D.3. Charpy impact surveillance test results for HFIR component HB3, A350 grade LF3 steel

Specimen	Key	Test temperature (°F)	Energy (ft-lb)	Appearance (% shear)	Lateral expansion (mils)	Neutron flux, >1 MeV ($n/cm^2 \cdot s \times 10^8$)	Neutron fluence, >1 MeV ($n/cm^2 \times 10^{17}$)
			Unirradiated				
D-39		−120	21.5	14.5	20.3		
D-40		−120	22.0		23		
D-41		−120	19.0				
D-13		−110	21		16.5		
D-10		−100	14.5		18		
D-11		−100	21.5		23.1		
D-12		−100	27.5		27		
D-32		−100	26.5	20	27.2		
D-42		−90	29.5	25	29.5		
D-49		−90	27.5		29.5		
D-19		−80	28.5	19	30.5		
D-20		−80	28.5		31		
D-21		−80	31.5		31.7		
D-1		−65	35.5		35.1		
D-2		−65	33.5	27	24.2		
D-9		−65	40.5	27	39.6		
D-14		−65	38		32.5		
D-30		−40	43.0	38	44.2		
D-31		−40	40.5	38	40.9		
D-29		−20	57.0	46	54.4		
D-18		75	101		85.1		
D-22		78	109	100	91		
D-7		120	107	100	90		
			Irradiated (11-8-65 through 8-4-69)				
D-43	3	−120	8	0		11.70	0.86
D-44	3	−40	32	28		11.70	0.86
D-45	3	20	58	65		11.70	0.86
D-56	3	−100	20	0		14.20	1.05
D-57	3	−20	48	57		14.20	1.05
D-58	3	40	84	100		14.20	1.05
			Irradiated (11-8-65 through 2-14-74)				
D-55	3	−60	20		14.4	17.80	3.23
D-26	3	−40	23.5		18.9	10.30	2.09
D-54	3	−20	29		21.7	17.80	3.23
D-27	3	0	40		33.6	10.30	2.09
D-53	3	30	63		48.6	17.80	3.23
D-28	3	60	95		76.0	10.30	2.09
			Irradiated (11-8-65 through 10-18-83)				
D-25	3	−20	18.6	25	3.0	10.30	4.88
D-23	3	20	28.6	35	11.5	10.30	4.88
D-24	3	60	44.4	40	29.0	10.30	4.88
			Irradiated (11-8-65 through 11-15-86)				
D-17	3	0	14.8	20	0.4	11.70	6.47
D-16	3	35	22.0	40	6.7	11.70	6.47
D-47	3	35	34.4	45	17.0	9.10	5.03
D-48	3	35	37.7	40	15.0	9.10	5.03
D-15	3	80	57.5	50	38.8	11.70	6.47
D-46	3	80	49.1	55	30.7	9.10	5.03
D-36	3	120	79.8	85	62.4	17.80	9.84
D-37	3	120	70.5	80	59.3	17.80	9.84
D-38	3	120	75.2	85	53.1	17.80	9.84

Table D.4. Charpy impact surveillance test results for HFIR shell at IC3, HB1A, and HB4A, A212 grade B

Specimen[a]	Key	Test temperature (°F)	Energy (ft-lb)	Appearance (% shear)	Lateral expansion (mils)	Neutron flux, >1 MeV ($n/cm^2 \cdot s \times 10^8$)	Neutron fluence, >1 MeV ($n/cm^2 \times 10^{17}$)
			Unirradiated				
A-17		−20	11.5				
A-21		−20	5.5	20	9.0		
A-22		−20	10.0	16.8			
A-64		−10	9.0	10	10		
A-70		−10	24.5	10	27.5		
A-75		−10	9.5	20.7	11.9		
A-49		0	21.5	5	23.9		
A-56		0	13.5	27.8	17.5		
A-63		0	11.0	20	14.2		
A-34		10	21.0	21.2	22.0		
A-35		10	17.5	28.3	18.2		
A-46		10	17.5	10	19.5		
A-24		20	19.5	32.9	22.0		
A-26		20	28.5	29.5	31.2		
A-29		20	26.5	31.7	26.2		
ND-2C		20	20.4	34	26		
ND-6C		20	26.5	25	28		
ND-2D		20	26.1	39	28		
A-83		60	39.5	42.6	40.3		
ND-6B		60	43.8	45	40		
D94-E		60	41.8	41	43		
D94-L		60	40.8	38	40		
D94-A		90	63.6	51	58		
D94-F		90	60.9	45	55		
D94-K		90	65.5	49	58		
D94-J		90	72.8	57	61		
A-80		100	71.5	94.0	66.0		
A-53		120	77.5	99	64.5		
A-14		120	78.2	100	66.0		
ND-2B		120	81.3	99	65		
			IC3, irradiated (11-8-85 through 10-18-88)				
A-30	5	0	5.6	10	1.0	0.253[b]	0.12[b]
A-36	5	30	22	25	8.5	0.253[b]	0.12[b]
A-31	5	60	41.3	25	21.0	0.253[b]	0.12[b]
			HB1A, HB4A, irradiated (11-8-85 through 10-18-88)				
A-1	6	0	3.6	10	1.5	2.38	1.13
A-7	6	40	7.4	20	1.5	2.38	1.13
A-2	6	80	35.1	35	10.0	2.38	1.13
A-94	7	55	22.4	25	8.5	2.50	1.19
A-95	7	55	24	20	7.5	2.50	1.19
A-92	7	60	19.3	25	6.5	2.50	1.19
			HB1A, HB4A, irradiated (11-8-85 through 11-15-88)				
A-136	6	55	7.6	30	0.4	2.40	1.33
A-145	6	55	14.9	20	0.7	2.21	1.22
A-140	6	65	10.9	30	0.3	2.40	1.33
A-141	6	65	8.5	25	0	2.21	1.22
A-135	6	120	37.1	65	18.8	2.40	1.33
A-142	6	150	70.6	90	39.6	2.21	1.22
A-96	7	65	6.2	20	0	2.76	1.53
A-120	7	65	18.6	35	5.0	2.37	1.31
A-97	7	85	36.7	45	17.5	2.76	1.53
A-99	7	85	23.5	35	7.8	2.76	1.53
A-161	7	85	20.1	30	7.2	2.37	1.31
A-124	7	120	38[c]	65	24.4	2.37	1.31

[a] A-xxx are original surveillance samples from HB-2 nozzle dropout. All others are from the NDE calibration block.

[b] Estimated values.

[c] Determined by measuring area under load-time trace.

Table D.5. Summary of NDT temperatures for HFIR surveillance tests

Component (location)	Material	Key No.	Nil-ductility transition temperature[a] (°F)					
			Equivalent full power years					20-year prediction[b]
			0	2.34	6.45	15.01	17.53	
HB1, HB4	A105 grade II	1, 4	−80	−62	−50	−20	−17[c]	−28
HB4 (low flux)	A105 grade II	4	*d*	*d*	*d*	*d*	−20	−28
HB2	A350 grade LF3	2	−110	−84	−58	−10	8	−35
HB3	A350 grade LF3	3	−80	−46	−20	17	35	−18
Shell (IC3)	A212 grade B	5	−5	*d*	*d*	20	*d*	0
Shell (HB1A, HB4A)	A212 grade B	6, 7	−5	*d*	*d*	47	70	0

[a]Estimated error of mean NDT temperatures is ±10°F.

[b]From ORNL/TM-1372, Table 2.

[c]Rough estimate based on severe data scatter.

[d]No tests.

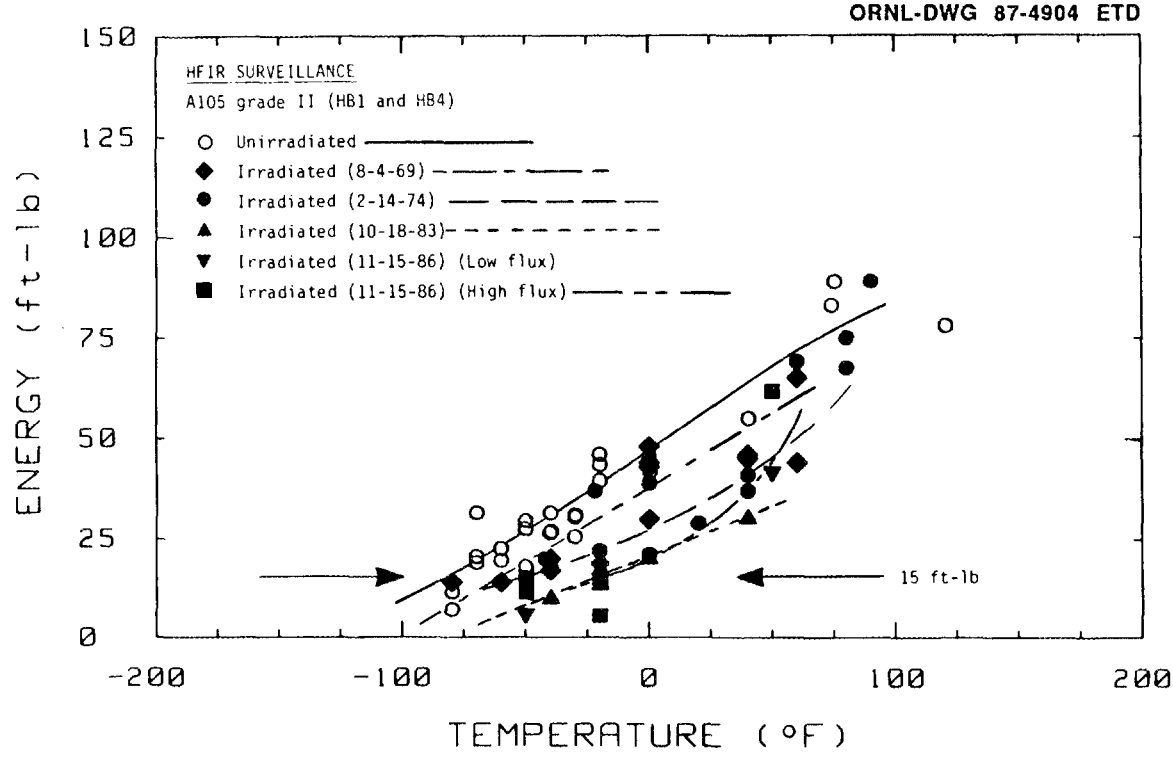

Fig. D.1. Charpy V-notch impact surveillance test results for A105 grade II, components HB1 and HB4 (key Nos. 1 and 4).

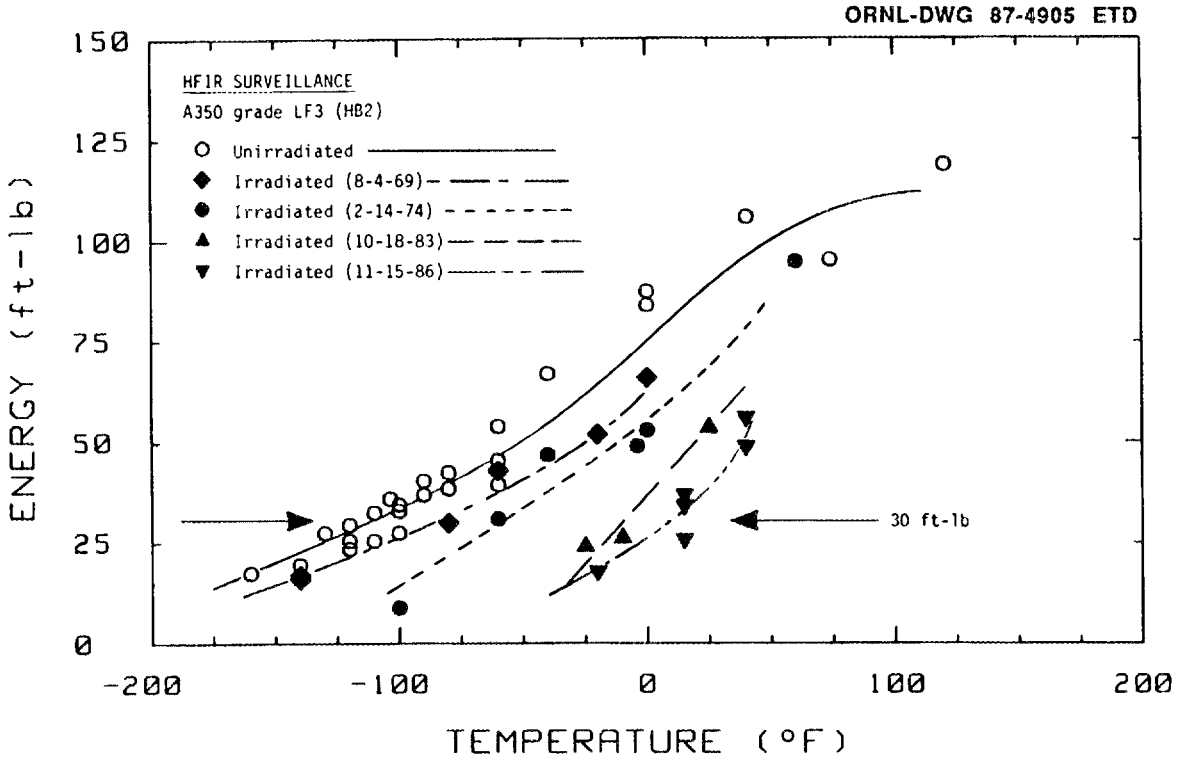

Fig. D.2. Charpy V-notch impact surveillance test results for A350 grade LF3, component HB2 (key No. 2).

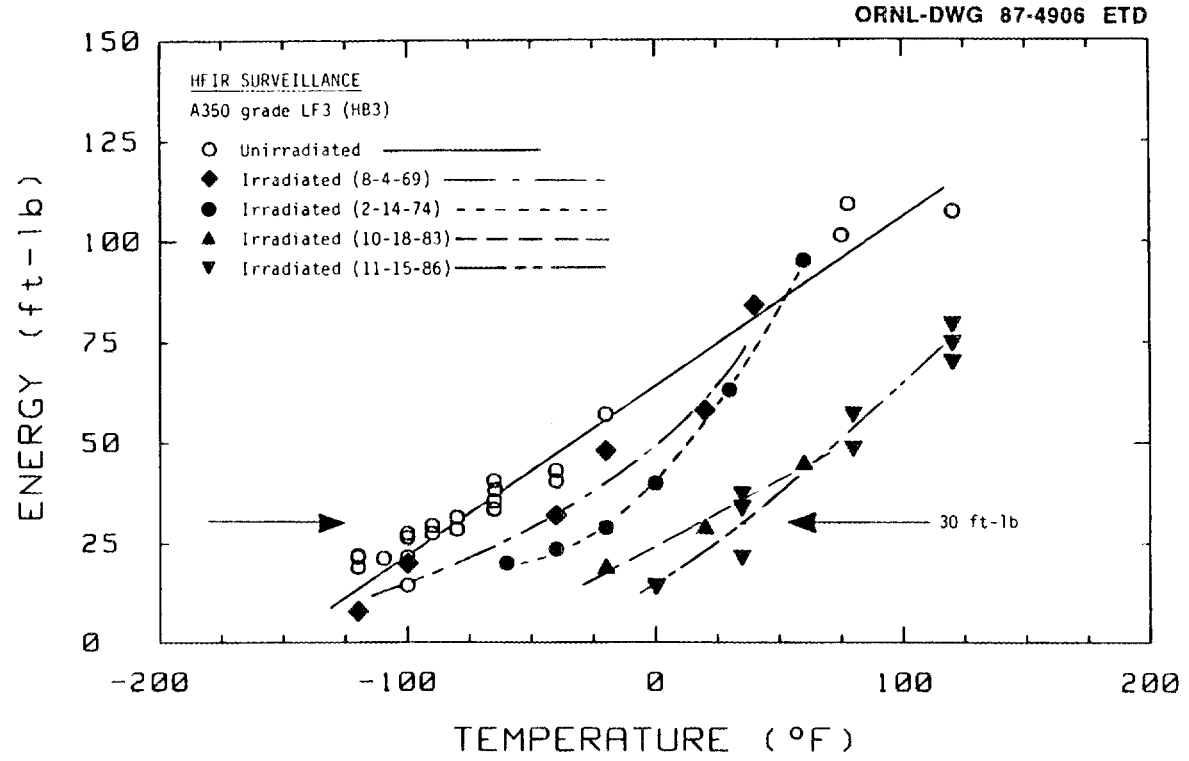

Fig. D.3. Charpy V-notch impact surveillance test results for A350 grade LF3, component HB3 (key No. 3).

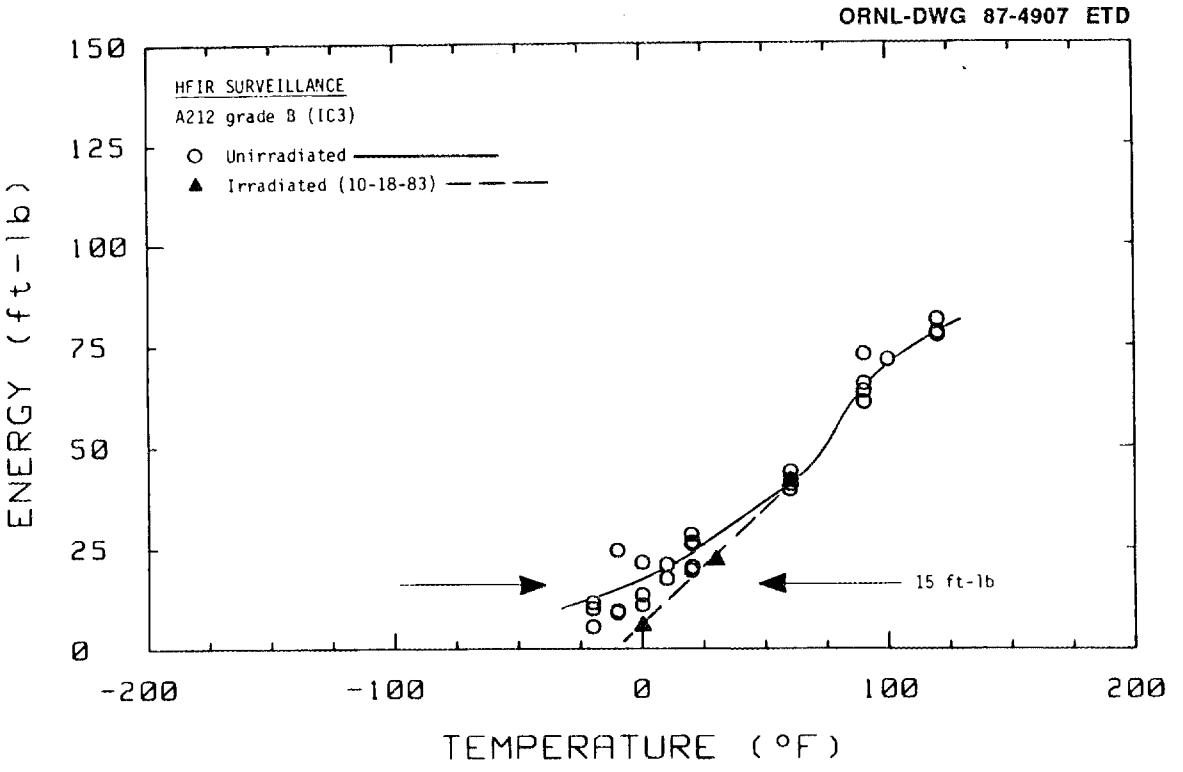

Fig. D.4. Charpy V-notch impact surveillance test results for A212 grade B, HFIR shell material, location IC3 (key No. 5).

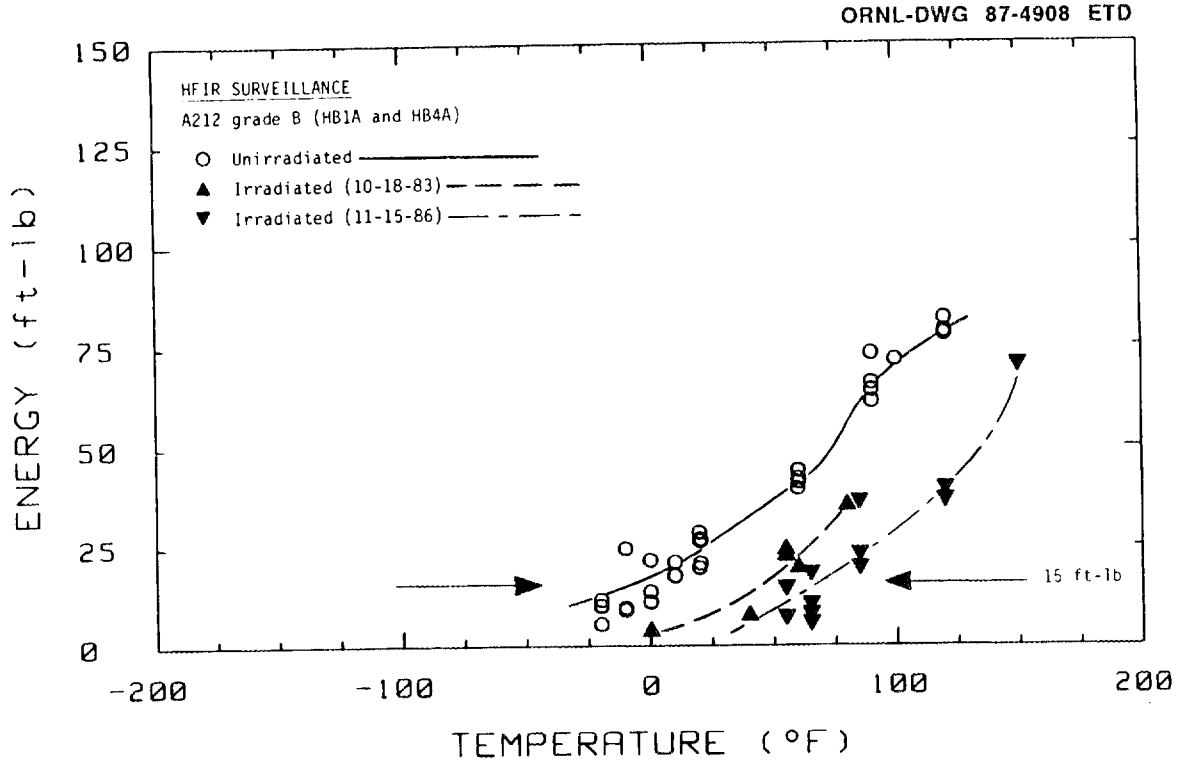

Fig. D.5. Charpy V-notch impact surveillance test results for A212 grade B, HFIR shell material, locations HB1A and HB4A (key Nos. 6 and 7).

drawn curves fit to the mean energy values determined for each test temperature. The temperature corresponding to the appropriate CVN energy level (15 or 30 ft-lb) from each curve was graphically determined and listed as the NDT temperature. As stated in Table D.5, the estimated error of the mean NDT temperatures is ±10°F. The figures and Table D.5 all show distinct reductions in CVN toughness with exposure time. In spite of few test specimens, it is clear that embrittlement has taken place. Consistency of results is demonstrated by those for HB2 and HB3 (keys 2 and 3) that, for about equal fluences, show NDT shifts of 118 and 115°F, respectively. Although those nozzles have different initial NDTs, presumably because of different amounts of work, they were fabricated from the same heat of steel. The surveillance results do not indicate any significant reduction in upper-shelf toughness. That is a relevant result primarily because it supports the observation that the general shape of CVN energy vs test temperature has not changed significantly. This is of particular importance to the irradiation task.

Figure D.6 shows a plot of change in NDT vs EFPY for the nozzles and the shell. The changes for the nozzles can be fit quite well with a

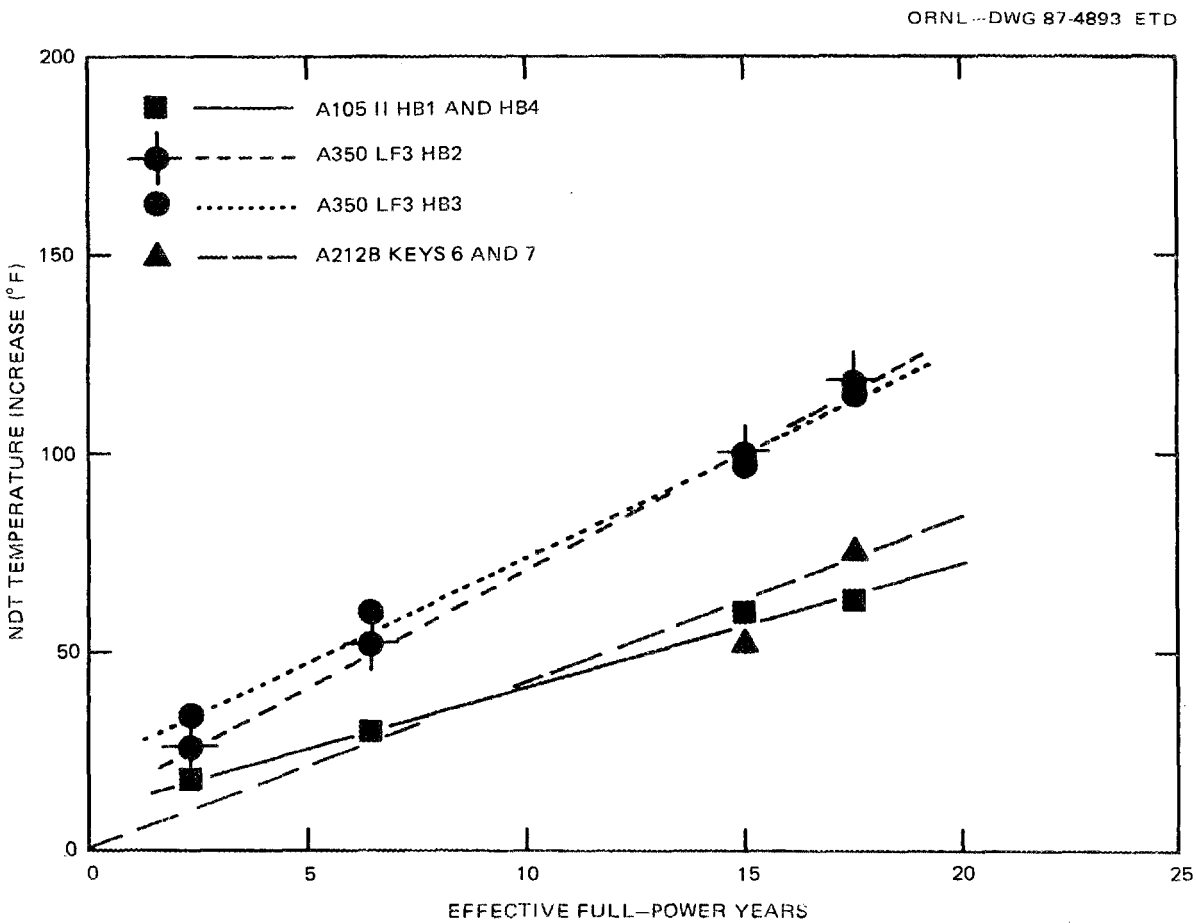

Fig. D.6. Change in NDT vs effective full-power years for HFIR pressure-vessel surveillance program.

linear expression starting from about the 2-EFPY point. The shell material has only two data points, and a curve fit is more uncertain. The data appear to provide a basis upon which relatively short-term extrapolations can be confidently based. Figure D.7 shows a plot of the surveillance program increases in NDT relative to fast-neutron fluence (>1 MeV). The figure shows that the A212 grade B steel exhibits a greater sensitivity to irradiation than the nozzle materials that all responded similarly. Appendix E presents detailed discussions of dosimetry and neutronics calculations to include analyses of exposures in displacements per atom (dpa), as well as neutron fluences for neutron energies >1 and 0.1 MeV. Examination of these results revealed no significant changes in the relative sensitivities of the materials.

Figure D.8 shows the HFIR surveillance results for the A212B compared with low-temperature test reactor irradiations with similar materials.[3] The HFIR surveillance results (low flux) show an NDT shift of 75°F at a neutron fluence more than one order of magnitude less than the test reactor irradiations (high flux). This observation implies a significant dose rate effect, which is discussed in more detail later.

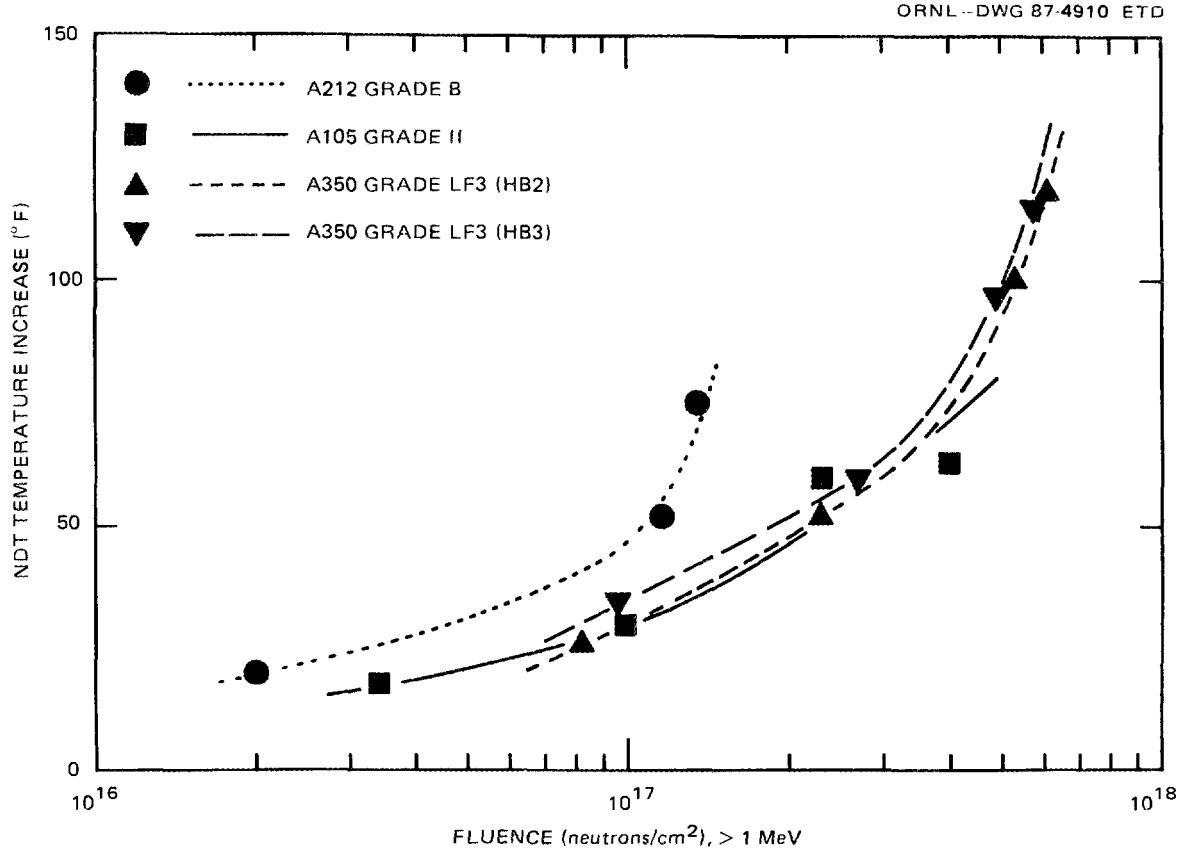

Fig. D.7. Change in NDT vs neutron fluence (>1 MeV) for HFIR pressure-vessel surveillance program.

ORNL-DWG 87-8154A

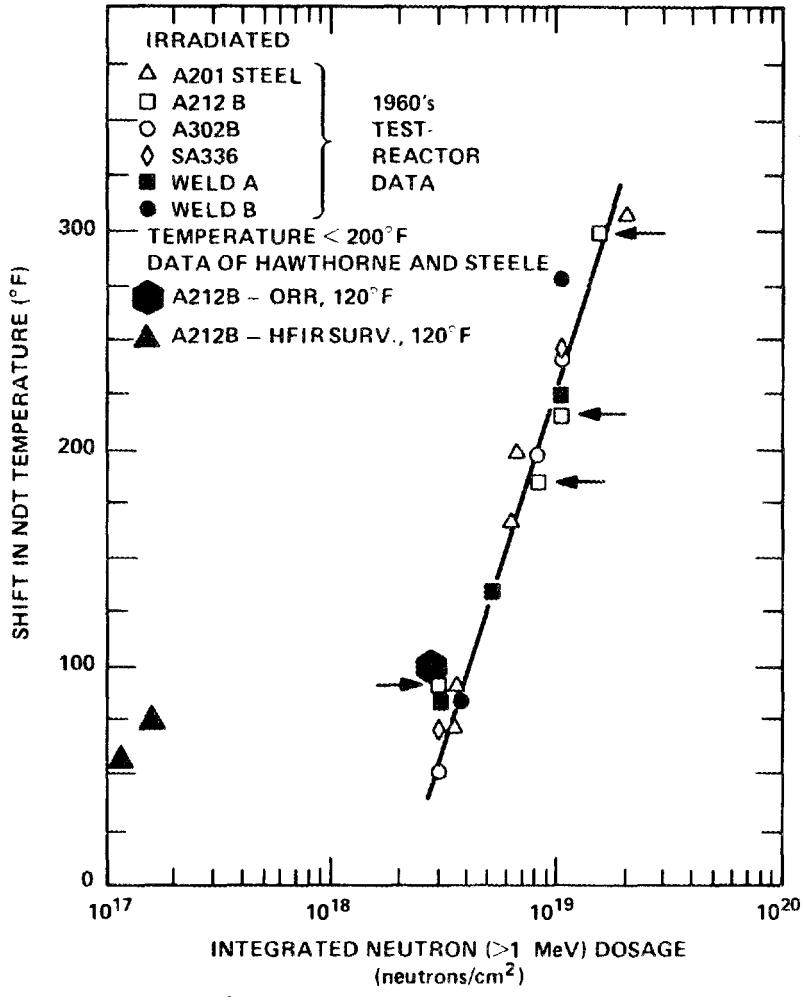

Fig. D.8. Comparison of HFIR A212B surveillance and ORR data with test reactor irradiations of similar materials at <200°F.

Further, Fig. D.9 shows a comparison of the HFIR surveillance results for the A212B compared with the results of two irradiations performed in the Oak Ridge Research Reactor (ORR). The HFIR A212B and an A212B from the former experimental gas-cooled reactor (EGCR) vessel were irradiated in ORR as part of this study (described in detail in Sect. D.5 of this appendix). Information from the files showed that a previous irradiation had been performed at ORR with the same EGCR material, and the results of each are shown in Fig. D.9. The figure indicates, as did Fig. D.8, that damage occurs at a much greater rate in a low-flux environment. At the flux levels indicated, a given NDT shift occurs at an exposure level about an order of magnitude lower in the low-flux surveillance environment than in the high-flux test reactor environment. Sections D.5 and D.6 of this appendix discuss the ORR experiments and metallurgical investigations in more detail.

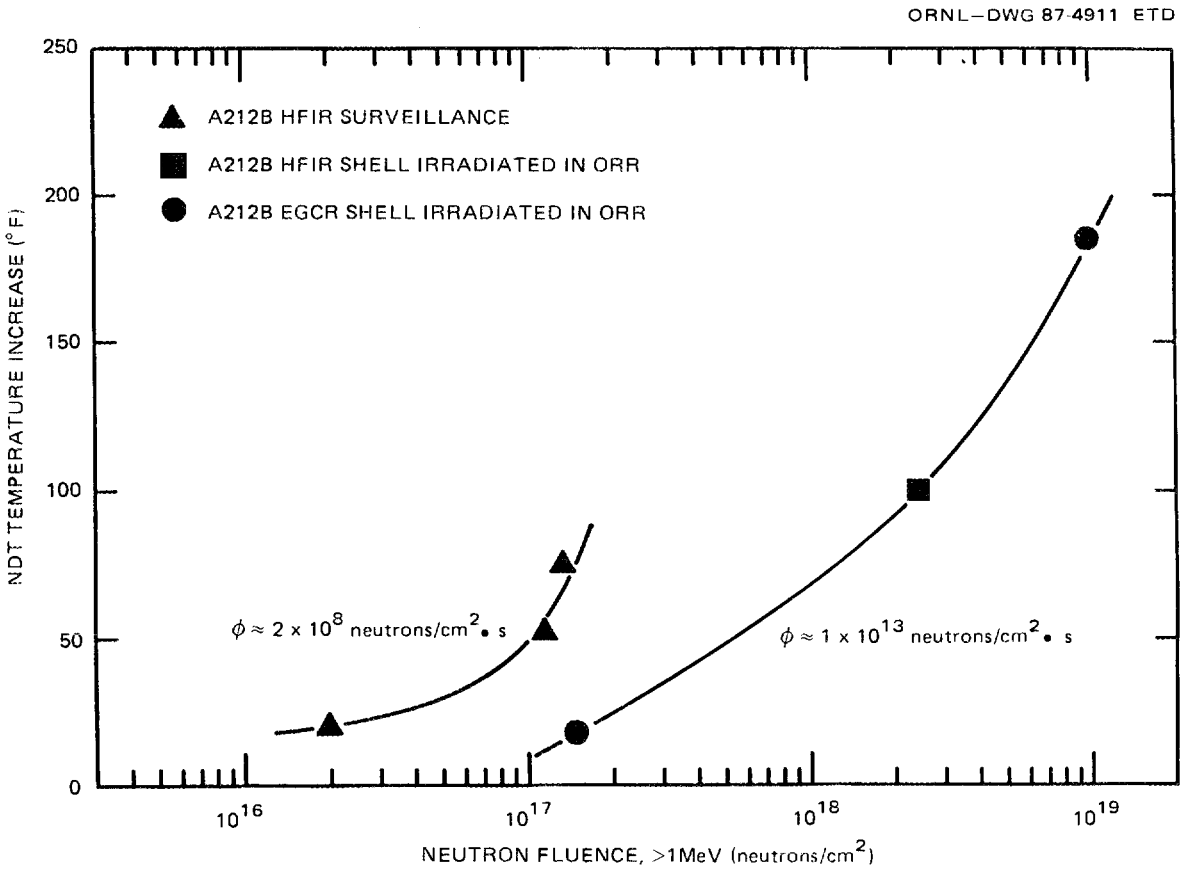

Fig. D.9. Comparison of HFIR A212B surveillance data with ORR irradiations of the HFIR A212B and a similar A212B steel.

D.3 BIBLIOGRAPHY ON THE EFFECTS OF IRRADIATION ON HFIR RPV MATERIALS (S. K. Iskander)

The purpose of this bibliography is to provide a means for judging the reasonableness of the results from the experimental program.

Note that the high confidence required for the HFIR data dictates the use of data obtained from actual HFIR materials whenever possible. The very limited amounts of available data and the need for fabricating a weld to simulate the actual seam weld of the HFIR reactor pressure vessel (RPV) make the use of any available data to verify actual data on the HFIR RPV a reasonable approach.

A serious limitation to the use of the data available in the literature is the lack of information on the chemistry of the materials used in the investigations. For example, the deleterious effect of copper on the irradiated behavior of steels was not discovered until about 1970. Also, other elements, such as nickel and phosphorus, are now known to affect the irradiated behavior. Copper and nickel were not generally reported unless they were alloying elements. Moreover, the influence of chemistry on the irradiated behavior has been thoroughly researched for irradiation

temperatures of 550°F. The effect of chemistry on the irradiated behavior at 120°F is more uncertain.

Among the limitations on the use of the available data base is that it is, by and large, for irradiation temperatures of 550°F and for fluences of ~1 × 10^{19} neutrons/cm^2 (>1 MeV). The HFIR RPV wall operates at ~120°F, and the fluences of interest are of the order of 10^{17} to 10^{18} neutrons/cm^2 (>1 MeV). The shifts of NDT reported in the literature for sensitive steels at the higher fluences are generally in the range of 200 to 300°F; shifts of interest for HFIR are ~100°F. It may not be possible to extrapolate the data for high fluences back to low fluence because of possible saturation and rate effects.

A very large number of references were searched for data on materials of interest in this program. The bibliography below contains only a few of those references searched that contain material on the irradiated properties of materials of interest (A212 grade B, A350 grade LF3, A105 grade III, and welds).

Of particular interest were the following items:

1. shift in NDT for welds compared with that of base metal;
2. drop weight NDT temperature and corresponding Charpy energy for materials of interest; and
3. comparisons between the shifts, due to irradiation, of the drop-weight NDT and the CVN transition temperature.

The literature review confirms the scatter of data associated with Charpy testing, even for material obtained from the same plate but from different areas of the plate. For example, in a study conducted by U.S. Steel on so-called reference pressure-vessel steels that included A212 grade B 4-in. plate, material from different areas of the plate subjected to the same heat treatments gave average values of 28 and 38 ft-lb at 10°F for the "longitudinal" direction (i.e., a difference of ~36%).

1. M. L. Bleiberg, *Effect of Neutron Bombardment Upon the Properties of ASTM Type SA212b Steel*, WAPD-T-206, Westinghouse Electric Corp., Atomic Power Division, Pittsburgh, October 12, 1955.

2. J. C. Wilson and D. S. Billington, "Effect of Nuclear Radiation on Structural Problems in Nuclear Engineering," pp. 97—106 in *Selected Papers from the First Nuclear Engineering and Science Congress held at Cleveland, Ohio* (sponsored by the American Institute of Mining and Metallurgical Engineering), ed. D. J. Hughes, S. McLain, and C. Williams, Pergamon Press, New York, 1957.

3. C. O. Smith, "Nuclear Reactor Materials," pp. 58—87 in *Effects of Nuclear Radiation*, Addison-Wesley, Reading, Mass., 1967.

4. R. G. Berggren and J. C. Wilson, *Recent Data on the Effects of Neutron Irradiation on Structural Metals and Alloys*, ORNL/CF-56-11-1, Union Carbide Corp. Nuclear Div., Oak Ridge Natl. Lab., January 30, 1957.

5. L. E. Steele and J. R. Hawthorne, "Irradiation Effects on Structural Materials," *Quarterly Progress Report to the USAEC Coordinated Program (May–July 1962)*, NRL-MR-1351, Naval Res. Lab., Washington, D.C., 1962.

6. L. E. Steele, J. R. Hawthorne, and C. Z. Serpan, Jr., "Irradiation Effects on Structural Materials," *Quarterly Progress Report (August–October 1963)*, NRL-MR-1468, Naval Res. Lab., Washington, D.C., 1963.

7. L. E. Steele, J. R. Hawthorne, and C. Z. Serpan, Jr., *Effects of Neutron Irradiation on the Properties of Reactor Structural Materials*, NRL MR-1502, Naval Res. Lab., Washington, D.C., January 1964.

8. L. E. Steele et al., *Irradiated Materials Evaluation and Reactor Pressure Vessel Surveillance for the Army Nuclear Power Program*, NRL MR-1644, Naval Res. Lab., Washington, D.C., 1965.

9. L. E. Steele et al., "Irradiation Effects on Structural Materials," *Quarterly Progress Report* (February–April 1970), NRL MR-2126, Naval Res. Lab., Washington, D.C., 1970.

10. J. R. Hawthorne and L. E. Steele, *The Effect of Neutron Irradiation on the Charpy V and Drop-Weight Test Transition Temperature of Various Steels and Weld Metals*, NRL Report 5479, Naval Res. Lab., Washington, D.C., May 27, 1960.

11. J. R. Hawthorne and L. E. Steele, "Effect of Neutron Irradiation on the Charpy V and Drop-Weight Test Transition Temperature of Various Steels and Weld Metals," *Symposium on Radiation Effects and Radiation Dosimetry*, ASTM 286, American Society for Testing and Materials, Philadelphia, 1961. (This paper has more information than the preceding reference.)

12. J. R. Hawthorne and L. E. Steele, *Preliminary Observations on the Effectiveness of Heat Treatment for the Recovery of Properties of Irradiated Steels*, NRL Report 5582, Naval Res. Lab., Washington, D.C., February 16, 1961.

13. W. S. Pellini and J. E. Srawley, *Procedures for the Evaluation of Fracture Toughness of Pressure-Vessel Materials*, NRL Report 5609, Naval Res. Lab., Washington, D.C., June 8, 1961.

14. L. E. Steele and J. R. Hawthorne, *Effect of Irradiation Temperature on the Neutron-Induced Changes in Notch Ductility of Pressure-Vessel Steels*, NRL Report 5629, Naval Res. Lab., Washington, D.C., June 28, 1961.

15. L. E. Steele, J. R. Hawthorne, and W. S. Pellini, *Effects of Neutron Irradiation on the Properties of Reactor Structural Materials*, NRL Report 5731, Naval Res. Lab., Washington, D.C., Jan. 22, 1962.

16. W. S. Pellini, L. E. Steele, and J. R. Hawthorne, *Analysis of Engineering and Basic Research Aspects of Neutron Embrittlement of Steels*, NRL Report 5789, Naval Res. Lab., Washington, D.C., April 17, 1962.

17. L. E. Steele and J. R. Hawthorne, *Surveillance of Critical Reactor Components to Assess Radiation Damage*, NRL Report 5830, Naval Res. Lab., Washington, D.C., Sept. 7, 1962.

18. L. E. Steele and J. R. Hawthorne, *Neutron Embrittlement of Pressure Vessel Steels*, NRL Report 5984, Naval Res. Lab., Washington, D.C., Oct. 22, 1963.

19. L. E. Steele and J. R. Hawthorne, *New Information on Neutron Embrittlement and Embrittlement Relief of Reactor Pressure Vessel Steels*, NRL Report 6160, Naval Res. Lab., Washington, D.C., Oct. 6, 1964.

20. E. P. Klier, J. R. Hawthorne, and L. E. Steele, *The Tensile Properties of Selected Steels for Use in Nuclear Reactor Pressure Vessels*, NRL Report 6649, Naval Res. Lab., Washington, D.C., Dec. 26, 1967.

21. R. H. Sterne, Jr., and L. E. Steele, "Steels for Commercial Nuclear Power Reactor Pressure Vessels," *Nucl. Eng. Des.* 10, 259–307 (1969).

22. *Steels for Nuclear Applications*, U.S. Steel, Pittsburgh, 1967.

23. "Effect of Radiation on Ductile-Brittle Transition of Steel," pp. 38–57 in *Power Reactor Technology: A Review of Recent Developments*, Vol. 3, No. 4, Argonne Natl. Lab., Argonne, Ill., September 1960.

24. R. G. Berggren, "Radiation Effects in Ferritic Steels," pp. 91–127 in *USAEC Conference on the Status of Radiation Effects Research on Structural Materials and the Implications to Reactor Design* (Chicago, Oct. 15–16, 1959), TID-7588, Office of Technical Information, U.S. Atomic Energy Commission, Oak Ridge, Tenn., 1960.

25. E. P. Klier, J. R. Hawthorne, and L. E. Steele, *The Tensile Properties of Selected Steels for Use in Nuclear Reactor Pressure Vessels*, NRL Report 6649, Naval Res. Lab., Washington, D.C., Dec. 26, 1967.

26. L. E. Steele and J. R. Hawthorne, *New Information on Neutron Embrittlement and Embrittlement Relief of Reactor Pressure Vessel Steels*, NRL Report 6160, Naval Res. Lab., Washington, D.C., October 1964.

27. R. G. Berggren, "Critical Factors in the Interpretation of Radiation Effects on the Mechanical Properties of Structural Metals," draft of a paper submitted for publication.

28. R. G. Berggren, "Radiation Effects in Metal Materials," paper presented at Symposium on Advanced Technology, American Society of Mechanical Engineers, New Mexico Sect., Albuquerque, Nov. 3, 1962.

29. R. G. Berggren, "Neutron Irradiation Effects in Steel: Studies at Oak Ridge National Laboratory," paper submitted for presentation at the Symposium on Steels for Reactor Pressure Circuits, London, Nov. 30, 1960.

30. G. D. Whitman, G. C. Robinson, Jr., and A. W. Savolainen, eds., *Technology of Steel Pressure Vessels for Water-Cooled Nuclear Reactors: A Review of Current Practice in Design, Analysis, Materials, Fabrication, Inspection, and Test*, Nuclear Safety Information Center, ORNL-NSIC-21, Union Carbide Corp. Nuclear Div., Oak Ridge Natl. Lab., December 1967.

D.4 DESCRIPTION OF MATERIALS AND PROPERTIES (R. K. Nanstad)

The materials of interest are those used for fabrication of the four beam-tube nozzles, the vessel shell, the longitudinal seam and circumferential girth welds in the shell, and the nozzle-to-shell welds. Table D.6 is a summary of the component fabrication details gleaned from available documents. The information is incomplete, but a number of important items are known:

1. only one heat of submerged-arc weld wire and one lot of flux were used for both the longitudinal shell seam weld and the circumferential weld joining the shell and bottom head,
2. the same lot of shielded metal-arc welding electrodes was used for all four nozzle-to-shell welds,
3. the shell consists of only one rolled and formed plate,
4. nozzles HB1 and HB4 were formed from the same heat of A105 grade II steel, and
5. nozzles HB2 and HB3 were formed from the same heat of A350 grade LF3 steel.

Those items are very important in simplifying the evaluation of the vessel materials, especially the welds for which there are no surveillance specimens. Table D.7 provides a summary of vendor tensile properties for the various materials. Section D.4.3 provides additional tensile test results of A212 grade B conducted during this study and shows that the material has an unirradiated yield strength of 47 ksi and an ultimate strength of 82 ksi.

D.4.1 Surveillance Specimen Examination (R. K. Nanstad and J. A. Carter)

Table D.8 gives the chemical composition of the base metals, determined from analyses of unirradiated surveillance specimens. The analyses show the materials have chemical compositions within expected ranges.

Table D.6. Summary of HFIR pressure-vessel component fabrication information

Component	Material specification	Form	Heat No.	Fabricator	Heat treatment[a]	Reheat treatment[a]
HB1, HB4	A105 grade II	Carbon steel forging	6335890			
HB2	A350 grade LF3	3.5% Ni forging	3336610	Taylor Forge	1525°F, 4 h, AC 1525°F, 4 h, AC 1100°F, 8 h, AC	1625°F, 4 h, AC 1525°F, 4 h, AC 1100°F, 8 h, AC
HB3	A350 grade LF3	3.5% Ni forging	3336610	Taylor Forge	1525°F, 4 h, AC 1525°F, 4 h, AC 1100°F, 8 h, AC	
Nozzle-to-shell welds	7018-A1, 3/16-in. rod	Shielded metal-arc weld	0C11A	Allis Chalmers	950°F, 17 h	
Seam weld	ACM 1436, 3/16-in. copper-coated wire, 7018-A1 root, 3/16-in. rod	Submerged-arc, shielded metal-arc	P5480B, 0C11A	Allis Chalmers	950°F, 17 h	
Vessel shell	A212 grade B	Carbon steel plate, 3 in. thick	P0818	Lukens Steel	2000°F 1650°F, 3 h, WQ 1225°F, AC	

[a]AC = air cooled; WQ = water quenched.

Table D.7. Vendor-supplied tensile properties of HFIR pressure-vessel materials

Item	Material	Melt	Strength (ksi)		Elongation in 2 in. (%)	Reduction of area (%)
			Yield	Tensile		
Shell	A212B	P0818	41	76	28	
Hemi-heat	A212B	22650		74		
		Nozzles				
HB2	A350LF3	3336610	62/64	77/78	34/35	66/68
HB3	A350LF3	3336610	61/60	77/78	34/33	64/64
HB1, HB4	A105II	6335890	57	82	29	65
		Weld wire deposit				
Seam	7018 A1	OC11A	69	82	29	72
	ACM 1436	P5480B	58	80	28	65
Nozzle	7018 A1	OC11A	69	82	29	72
		Qualification test welds				
Seam[a]			49/54	83/87 72/74[b]	15/17	
Nozzle/ shell[a]			47/47	81/81	17/20	

[a]Broke in base metal.

[b]Requalification test.

Table D.8. Chemical composition of base metals for HFIR pressure vessel

Element	A212B Shell (wt %)	A105II HB1, HB4 (wt %)	A350LF3 HB2 (wt %)	A350LF3 HB3 (wt %)
C	0.26	0.24	0.18	0.17
Al	0.07	0.06	0.08	0.08
Co	0.015	0.005	0.03	0.03
Cr	0.075	0.042	0.090	0.080
Cu	0.15	0.030	0.11	0.10
Mn	0.85	1.12	0.55	0.50
Mo	0.02	0.07	0.03	0.03
Nb	<0.001	<0.001	<0.001	<0.001
Ni	0.20[a]	0.14	3.3	3.2
Si	0.29	0.21	0.29	0.27
Sn	0.02	<0.005	0.02	0.02
Ti	0.01	<0.001	<0.001	<0.001
V	0.0005	0.0005	0.001	<0.001
W	<0.005	<0.005	<0.005	<0.005
Zr	<0.001	<0.001	<0.001	<0.001
P	0.006	0.003	0.01	0.007
S	0.04	0.02	0.02	0.01
As	0.007	0.002	0.01	0.009
B	<0.0005	<0.0005	<0.0005	<0.0005
N	0.0060	0.0063	0.0090	0.0083
O	0.0024	0.0033	0.0027	0.0026

[a]Believed to be high; independent analysis at another laboratory showed 0.09.

The sulfur content of 0.04 wt % in the A212 grade B is quite high and resulted in a relatively high sulfide density and gave rise to concerns about significant orientation effects in the plate. The original surveillance specimens were removed in the longitudinal-transverse (LT) orientation in accordance with the American Society of Mechanical Engineers (ASME) Code procedures in effect at that time. Section D.4.3 of this appendix provides details of orientation effects.

The A350 grade LF3 analyses verify that nozzles HB2 and HB3 were fabricated from the same heat of steel. Nitrogen contents were analyzed because of suspected contribution to radiation sensitivity during low-temperature irradiation. They appear to be present in normal amounts, but the critical contents of nitrogen, as well as most of the other elements, are not well understood relative to irradiations at 120°F. The compositions of weld metals are discussed in later sections.

Optical metallography was performed on unirradiated specimens to examine general microstructure and identify probable orientation effects resulting from varying amounts of work. Of primary interest is the A212 grade B plate. Micrographs are shown in Figs. D.10 and D.11, unetched

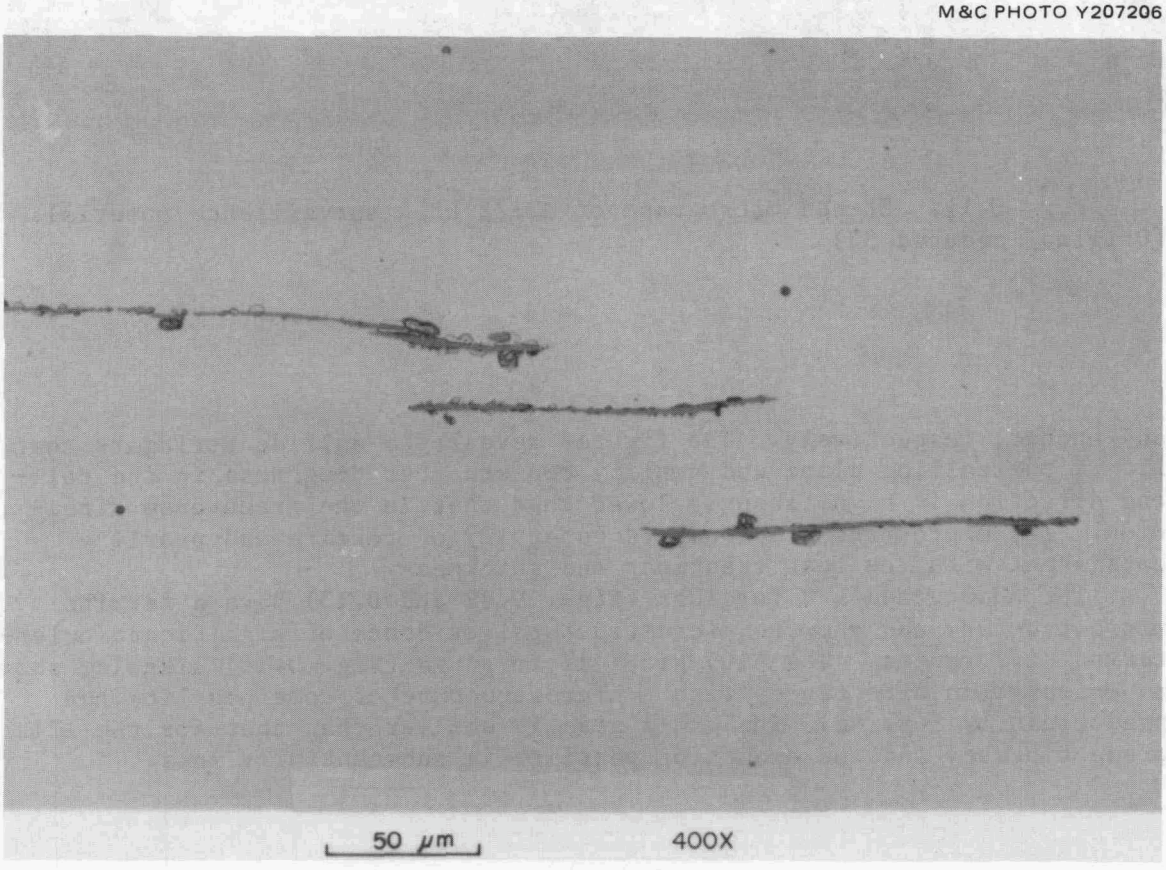

Fig. D.10. Unetched micrograph of A212B HFIR surveillance material. (Original reduced 3%)

M&C PHOTO Y207207

Fig. D.11. Etched micrograph of A212B HFIR surveillance material. (Original reduced 3%)

and etched, respectively. The figures reveal the sulfide stringers that lie in the rolling plane and amplify concern that toughness in the rolling direction is significantly lower than that in the transverse direction. The microstructure consists generally of ferrite and pearlite consistent with the heat treatment and thickness.

The A350 grade LF3 forgings (Figs. D.12 and D.13) have a ferrite microstructure and show no microstructural evidence of significant orientation differences. The A105 grade II forgings (Fig. D.14) likewise show no orientation differences with a microstructure of some pearlite but predominantly ferrite. The grain size is smaller than that for the A212 grade B plate, and the amount of pearlite is substantially less.

M&C PHOTO Y207213

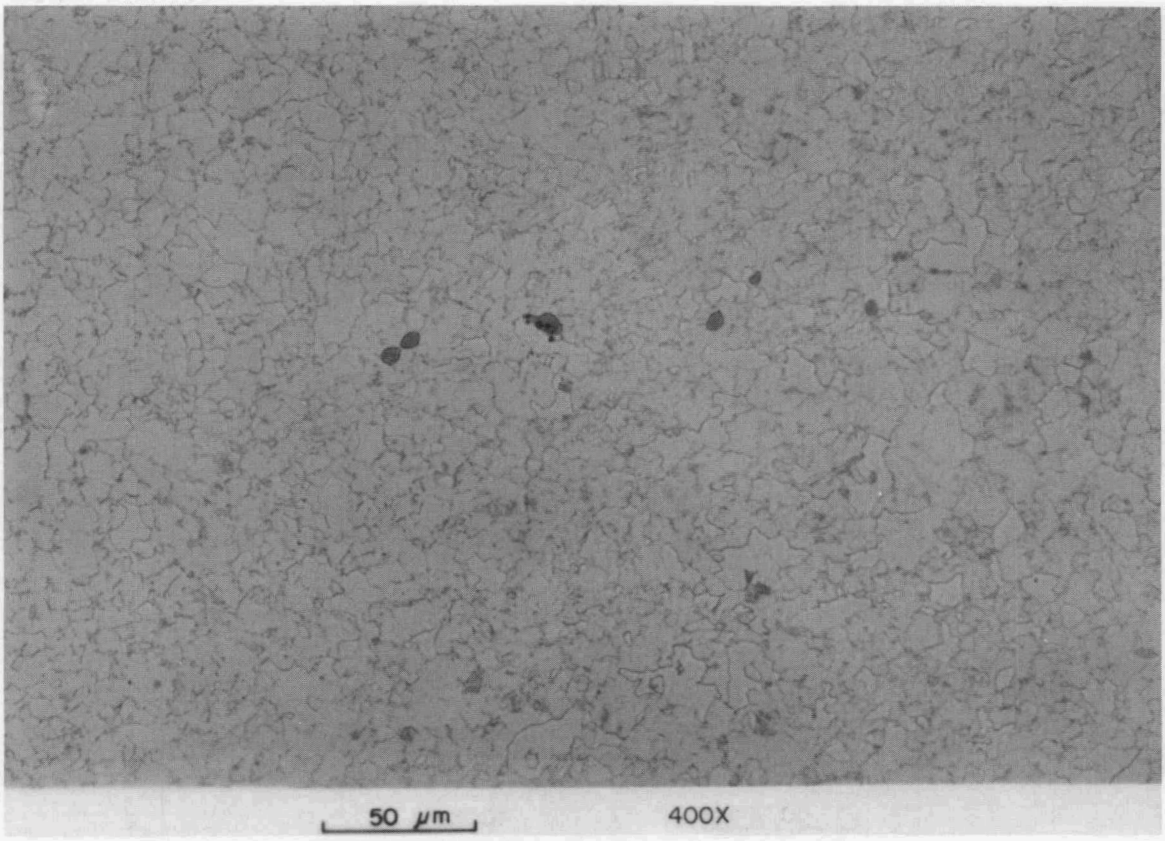

Fig. D.12. Etched micrograph of A350 LF3 (HB2) HFIR surveillance material. (Original reduced 3%)

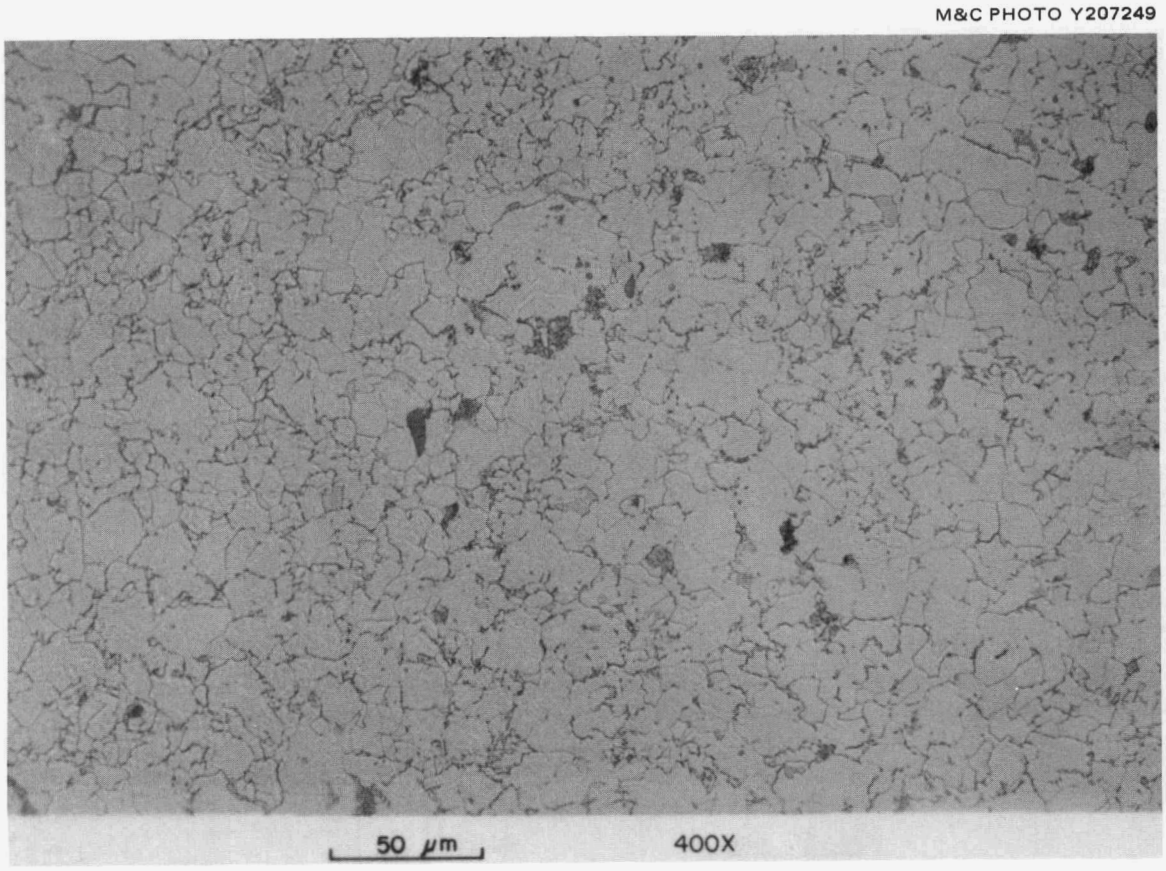

Fig. D.13. Etched micrograph of A350 LF3 (HB3) HFIR surveillance material. (Original reduced 3%)

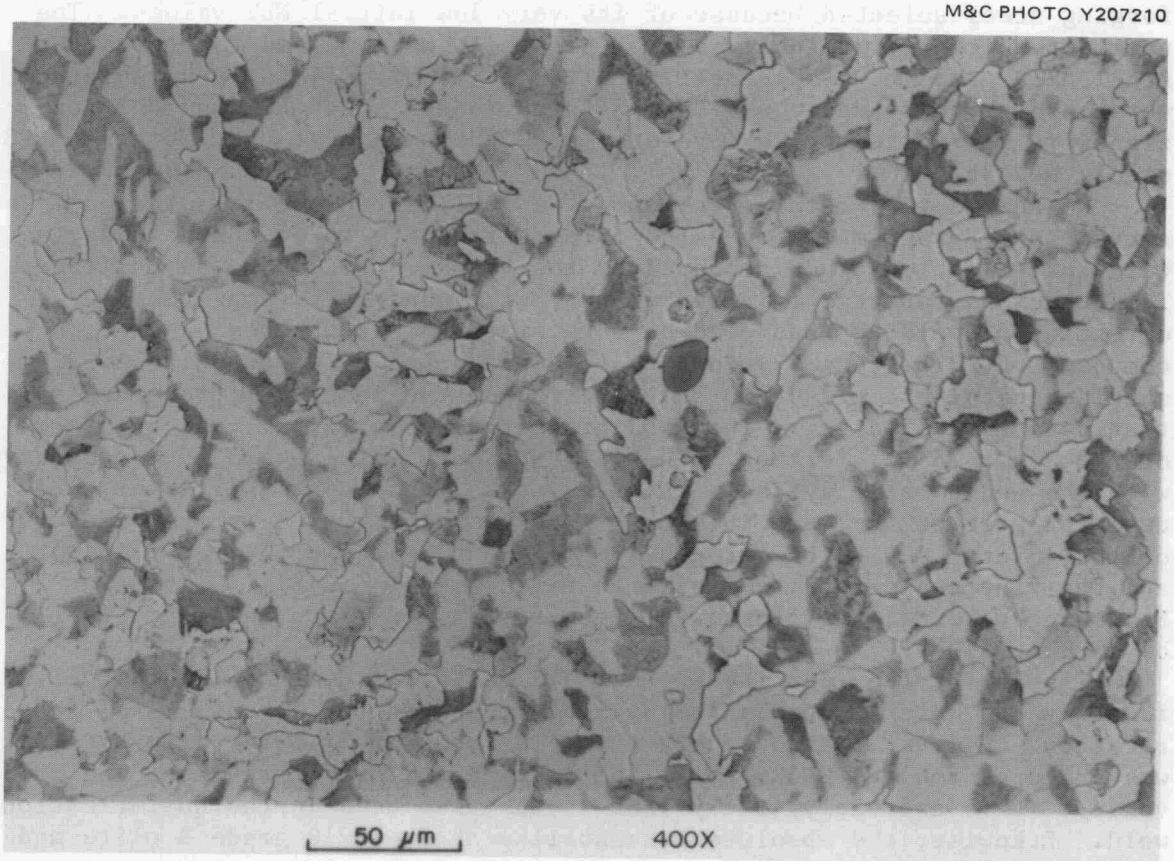

Fig. D.14. Etched micrograph of A105 grade II HFIR surveillance material. (Original reduced 3%)

D.4.2 Evaluation of the HB2 and HB3 Nozzle Material and Their Welds (W. R. Corwin and G. M. Goodwin)

D.4.2.1 Introduction

The two beam-tube nozzles, HB2 and HB3, which by their placement see the greatest fluence in the vessel, were fabricated from A350 grade LF3 forging steel selected because of its very low initial NDT values. The nozzles, which are nominally a 3.5%-Ni steel, were welded to the carbon steel A212 grade B vessel shell material by using 3/16-in.-diam shielded metal arc carbon steel class E7018A1 electrodes. Both HB2 and HB3 nozzles were fabricated by Taylor Forge from the same heat of A350 grade LF3 steel, No. 3336610.

No nozzle weld metal specimens were included in the irradiation surveillance program. To examine irradiation effects on these welds, a weld qualification block produced by the vessel fabricator was utilized. This block was about 3 in. thick, 9 in. wide, and 9 in. long (in the direction of welding) and clad on both sides, as is the vessel. It is composed of A212 grade B welded to A350 grade LF3 by using 3/16-in.-diam shielded metal arc class E7018A1 electrodes, the identical procedure as that used in the vessel. The A350 grade LF3 was originally in the form of a 3 × 6 × 36 in. forging. The weld was made using a single-J geometry with the angled side lying in the A212. Two weld passes per layer were used for most of the weld thickness, increasing to three in the wider part of the joint. A section through the weldment is shown in Fig. D.15(*a*), and the fine-scale ferrite microstructure is shown in Fig. D.15(*b*). Following welding, the block was given a postweld heat treatment (PWHT) of 17 h at 950°F.

Tracing of the identity of the weld materials did not conclusively identify the welding rod as the same heat used in the actual vessel fabrication. However, because only a single batch of 3/16-in.-diam E7018A1 was procured for the HFIR vessel fabrication and used throughout the vessel, it is extremely likely that it was also used in the qualification weld. Likewise, the absolute traceablilty of the A212 grade B plate and A350 grade LF3 forgings used in the qualification weldment has not been established, although they are also very likely from the actual vessel materials with checks of their chemistry revealing excellent matches to those made on the actual vessel materials.

D.4.2.2 Weld metal evaluation

CVN impact specimens were fabricated from the weld metal such that the axis of the specimen was perpendicular to the welding direction. Four specimens were machined across each section cut from the weldment. Of these, three were considered representative of the bulk weldment and were used in irradiation effects determinations. The fourth specimen from each slab, taken near the weld root, was used only for scoping purposes. Chemical composition of the weld material was determined and is reported in Table D.9.

Because the weld joins base metals of substantially different nickel contents, and recognizing the deleterious effects of nickel on the

ORNL-PHOTO 1276-88

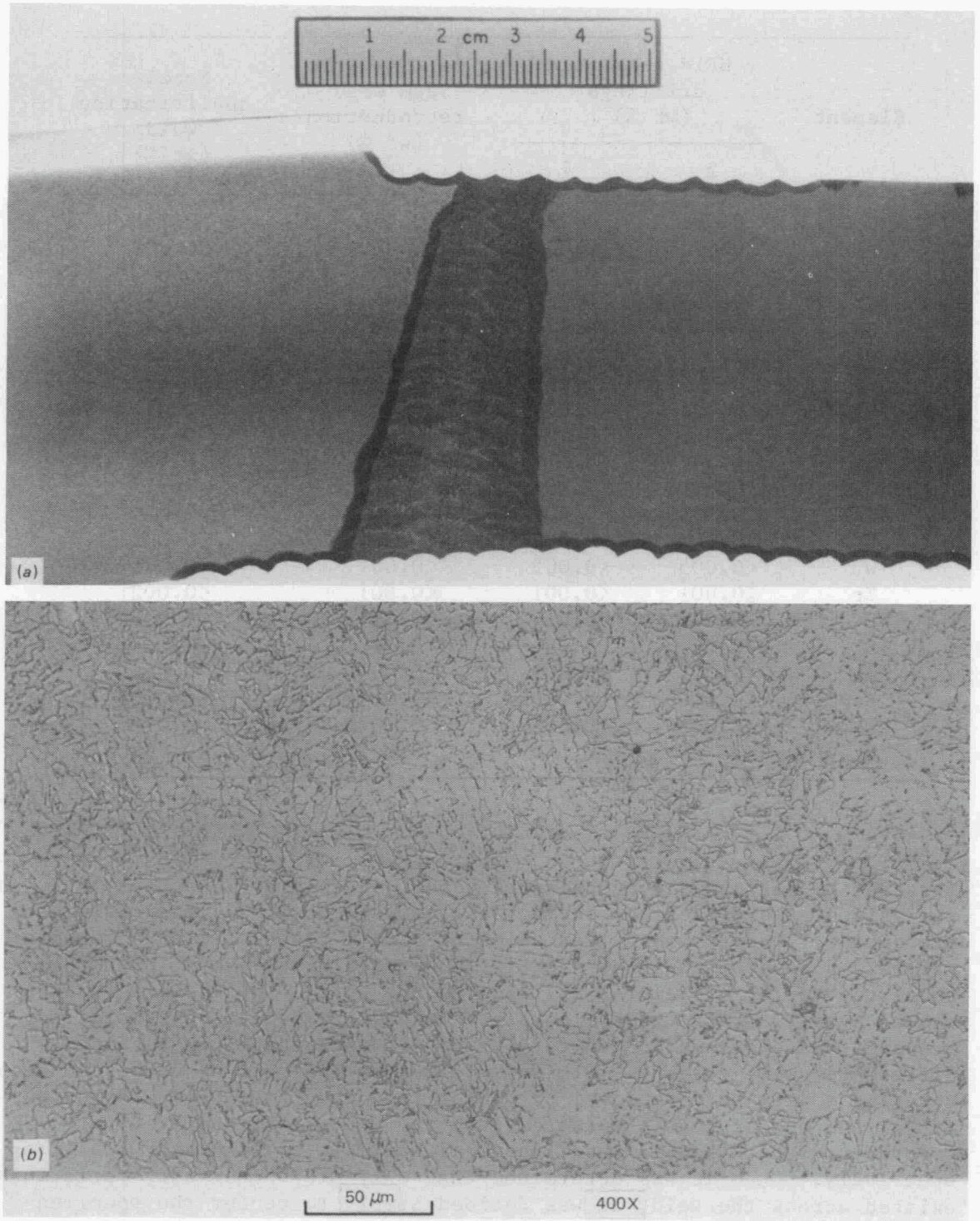

Fig. D.15. HB2 and HB3 qualification weldment showing (*a*) section through weldment and (*b*) weld metal etched microstructure. (Original reduced 3%)

Table D.9. Weld metal chemical compositions

Element	HFIR seam weld drillings (wt %)		Seam weld reproduction (wt %)	Nozzle qualification weld (wt %)
	5	7		
C	0.080	0.075	0.058	0.045
Al	0.02	0.03	0.006	0.007
Co	0.01	0.01	0.007	0.02
Cr	0.05	0.05	0.04	0.04
Cu	0.16	0.17	0.18	0.05
Mn	1.5	1.5	1.5	0.92
Mo	0.58	0.56	0.48	0.52
Nb	<0.001	<0.001	0.002	0.01
Ni	0.06	0.05	0.01	0.10
Si	0.54	0.51	0.54	0.55
Sn	0.01	0.008	0.003	0.01
Ti	0.001	0.002	0.001	0.02
V	0.002	0.002	0.004	0.005
W	<0.005	<0.005	<0.001	<0.005
Zr	<0.001	<0.001	<0.001	<0.002
P	0.008	0.014	0.015	0.008
S	0.02	0.04	0.02	0.04
As	0.007	0.009	0.004	0.005
B	<0.0005	<0.0005	<0.001	<0.0005
N	0.0069	0.0067	0.0070	0.0105
O			0.0074	0.0320

irradiation performance of pressure-vessel steels, at least at 550 F, an analysis of the nickel content across the weld metal was made using the microprobe. Only a modest variation of nickel content existed between the weld passes on the high-nickel (A350) side of the weld, 0.20%, and those on the low-nickel (A212B) side of the weld, 0.06%. As a further check, a section through the complete weldment was metallographically prepared and examined for uniformity of microstructure; no detectable differences were evident. Similar microprobe analysis of copper content revealed a very uniform level of 0.045% throughout the weld. Both the nickel and copper levels measured with the microprobe compared very favorably with bulk weld metal chemical analysis of 0.10 and 0.05%, respectively. Once it was determined that only minor chemistry variations existed across the weld, it was decided simply to center the specimen within the weld.

To examine the effect of crack propagation within the weld, CVN specimens were notched such that the crack ran either through the thickness of the plate perpendicular to the direction of welding (orientation 1) or in the direction of welding (orientation 2). The root pass

scoping specimens were used for these tests with a few of the bulk weld-metal specimens tested for comparison. Tests were performed at −100, 0, and 120°F, and both orientations produced data with similar mean energy levels at any temperature. Orientation 2 specimens exhibited slightly less scatter and were, therefore, chosen for subsequent accelerated irradiation experiments.

Additional bulk weld-metal specimens were then tested (Fig. D.16) to define the NDT of the weld metal and its behavior at 120°F. The results agree well with those from the root pass specimens. The data also compare very well with three tests performed and reported as part of the original weld qualification procedure at 10°F (orientation undetermined). Because fracture appearance measurements showed that the weld metal was not on the upper shelf at 120°F, one additional specimen was tested at 150°F and exhibited a very small percentage of brittle fracture. The temperature at which the weld metal exhibits 20 ft-lb (corresponding to the NDT energy level in the weld metal) is 0°F. At 120°F the mean impact energy is ~86 ft-lb with 80% shear.

Also shown in Fig. D.16, obtained from vendor documentation, are the CVN results for heat-affected zone (HAZ) tests on the nozzle qualification weld. A straight line was drawn through the mean energy value approximately parallel to that of the A212B (LT) curve. The NDT was estimated (at the 15-ft-lb energy level) to be −20°F, below that of the weld metal and the A212B.

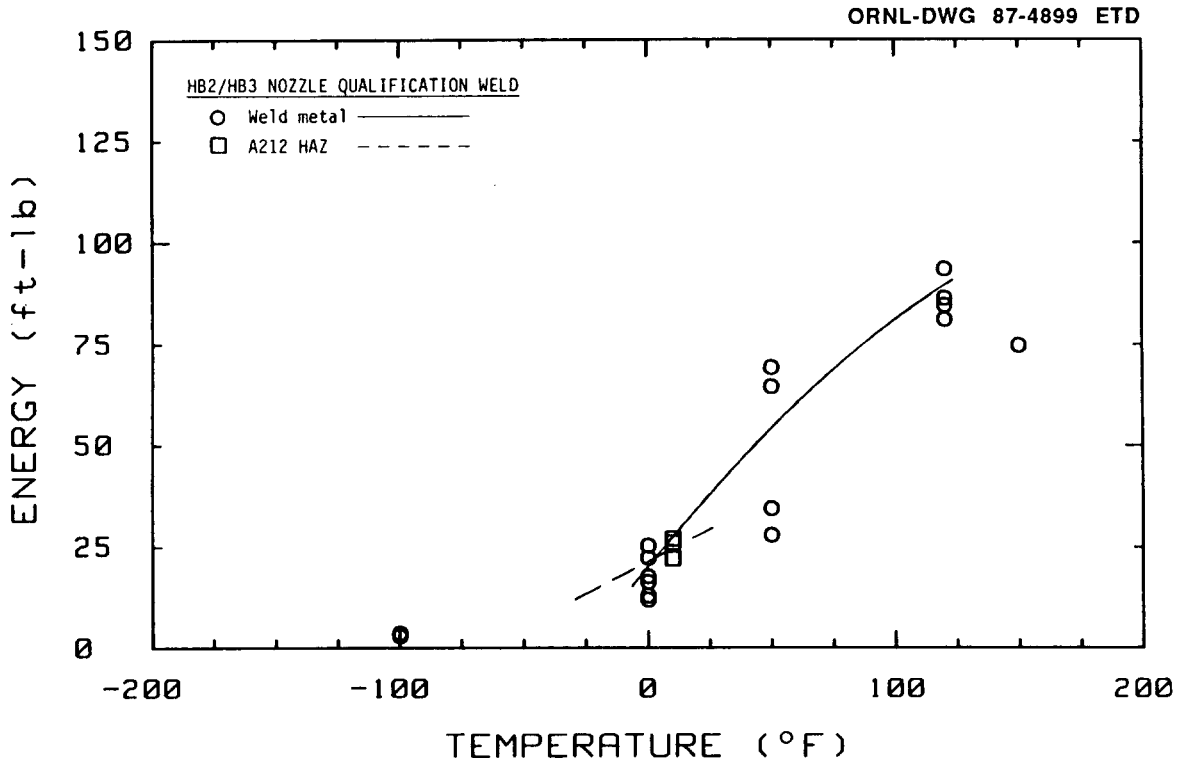

Fig. D.16. Unirradiated Charpy impact properties of the HB2/HB3 nozzle qualification weld metal and A212 heat-affected zone.

D.4.2.3 Evaluation of A350 LF steel (nozzles HB2 and HB3)

To examine potential orientation effects in the A350 forgings, metallographic evaluations of the A350 in both the nozzle qualification weldment and an actual nozzle were performed to establish primary working orientation. The results definitively revealed that the principal working direction of the A350 in the qualification weld was parallel to the welding direction in agreement with the logical layout of the 3 × 6 × 36 in. forging used for the weld. The unirradiated HB2 surveillance specimens were fabricated from the prolongation of the pipe end of the nozzle with the axis of the specimen lying in the radial direction. Examining one of the HB2 specimens definitively revealed the principal working to have been the axial direction. Thus, the radial-circumferential (RC) orientation of the surveillance specimens corresponds to specimens taken in the thickness-transverse (ST) orientation from the A350 forging in the weld qualification block. Charpy impact specimens were then taken from the A350 in the qualification block in the ST, TS, and thickness-longitudinal (SL) orientations. Multiple specimens were tested at several temperatures from low in the transition to the upper shelf, and no effect of orientation was observed. Even the potentially weaker SL-oriented specimens with their crack propagation in the working direction gave results that agreed very well with the other orientations. The results also agree well with the CVN data (orientation undetermined) obtained as part of the weld qualification procedure. Thus, it was concluded that the RC orientation of the HB2 and HB3 surveillance specimens is very likely representative of the nozzle properties in all directions.

The NDT (determined at 30 ft-lb) of the A350 in the qualification weld is approximately −45°F. This is substantially higher than the −110 and −80°F determined for the HB2 and HB3 nozzles, respectively. It is not known why the NDT is so much higher. Likely reasons include variations in either the amount of working or the heat treatment (interim or final) between the nozzles and the forging in the qualification weldment. Also, it is possible that the material in the qualification weldment is not from the same heat. The metallographic studies done on the qualification weldment and actual specimens from both HB2 and HB3 nozzles show that the grain size of the A350 in the weldment is the largest, followed by that in HB3, and then followed by that in HB2. This corresponds exactly to both the observed order of decreasing NDT temperature and that which would be predicted purely on the basis of the relative grain size, all other things being equal. However, whatever the cause, in the present condition the A350 in the weld qualification block is not wholly representative of the nozzles HB2 and HB3 and could be used only with caution in any mechanical or irradiation studies.

During the course of the investigation, the remaining portion of the ring from which the original HB2 surveillance impact specimens were taken was located. The portion of the ring remaining is ~170° of the original annular section, which was 0.434 in. thick by 23.26 in. in inner diameter by 27.74 in. in outer diameter. This material is being carefully archived for possible future use.

D.4.2.4 Evaluation of the A212 grade B plate (in the nozzle qualification weldment)

Because there appears to be substantially more A212 material available from a dropout used for a HFIR nondestructive examination standard, which has been verified to be from the HFIR vessel shell plate, only a cursory examination of the A212 in the qualification weldment has been made. Only microstructural examination and chemical analysis were performed. However, special care was taken in sectioning the weldment so that it will be possible to obtain CVN specimens notched in the HAZ if desired. Charpy testing performed for the weld qualification procedure produced an average energy of 25 ft-lb for the A212 HAZ at 10°F.

D.4.3 Tests Performed on A212 Grade B Nozzle Dropouts (S. K. Iskander and W. R. Corwin)

D.4.3.1 Introduction

As mentioned elsewhere, CVN surveillance specimens had been placed in the HFIR pressure vessel. They were made from A105 grade II, A212 grade B, and A350 grade LF3 as representative of materials used in the construction of the RPV. The A212 grade B (which will be referred to as simply A212B for brevity) surveillance specimens were from the LT orientation. There were no weld metal surveillance specimens.

To assess the integrity of the RPV, CVN specimens from weld material and A212B material from TL and TS orientations were tested in both unirradiated and irradiated conditions. The objectives of the tests on irradiated CVN specimens were to measure the shift in the CVN transition temperature. Tests were also performed on CVN specimens from the LS orientation in the unirradiated condition only. The objective of the testing on the LS orientation was to obtain a qualitative indication of the resistance of the material to propagation of axial cracks in the thickness direction.

The irradiation was performed in ORR. To assess possible dose rate effects and differences in spectrum, it was necessary to index the radiation damage experienced in ORR to that of the HFIR surveillance specimens. For this purpose, archival A212B specimens (remaining from the original HFIR surveillance program) were included in the ORR irradiation capsules as indexing material.

This section will describe the material used to fabricate the CVN and drop-weight specimens from A212B, as well as some of the tests performed to verify that the material used is indeed the same as that used to manufacture the surveillance CVN specimens. Then, the results of the testing program will be presented.

For the purposes of this report, only partial results of the verification phase of the testing program are presented. The verification phase consumed a considerable proportion of the total effort in testing the A212B, and a more detailed report is planned in the future.

D.4.3.2 Description of materials, verification, and heat treatment

At the beginning of the test program on A212B, the only archival material available was an 18-in.-diam block, ~3 in. thick. It was reported to be a nozzle dropout from the HFIR RPV and is used as a nondestructive examination (NDE) calibration block. Presumably for NDE, it had been cut into a semicircular segment and two 90° segments and then welded back into a circular shape [Fig. D.17(*a*)]. For purposes of this program, a 105° segment of the calibration block was sawed out for manufacturing CVN specimens [Fig. D.17(*b*) and (*c*)]. The 105° segment will be referred to as the "NDE block." All CVN specimens were machined from the NDE block.

Toward the end of the testing program on A212B, more A212B archival material, consisting of four blocks remaining from the manufacture of the surveillance specimens from the HB-2 nozzle dropout, was located.

A complete documentation trail of the NDE calibration block or the remaining HB-2 nozzle dropout pieces that would identify it as representative of the RPV material and its heat treatment could not be found. Tests were performed to ascertain that the material is truly representative of the HFIR RPV in its unirradiated condition.

The only identification on the NDE calibration block were the letters "NP4," "4," and the remainder of what appears to be a "7" [Fig. D.17(*b*)]. Documentation on file states ". . . 1 PC marked NP-471 taken from Shell Plate." Handwritten letters that requested 12 nozzle dropouts be subjected to a stress-relief heat treatment at a temperature of 950°F for 51 h were also found, apparently to correspond to the 3 separate heat treatments of the RPV at 950°F for 17 h.

The shape of the remaining pieces from the HB-2 nozzle dropout provided substantial evidence to their origins, but again there was no documentation of the heat treatment the four pieces had undergone.

The A212B surveillance specimens were all manufactured from material ~1/4 in. from the inner RPV clad-to-base metal interface. The inner surface of the RPV is roll-bond clad, and the outer is weld-overlay clad. Thus, the interface region of each cladding would have different mechanical properties. Because of the very limited amounts of A212B NDE block material available, it was assumed that material from the same depth, as measured from the base-to-clad interface, would have the same properties. All of the CVN specimens manufactured from the NDE block were machined from either a layer ~1/4 or 1 in. from the interface and will be referred to as simply "1/4-in." or "1-in." material irrespective of whether it was manufactured from the inner or outer portion of the A212B NDE block.

The NDE block's circular surfaces are both clad. The surface that appears to be the inside one has roll-bond cladding, and the other has a weld overlay clad, as was the case for the HFIR RPV. The block appears to be cut from a cylinder because of the curvature of the circular surfaces: they are curved in one direction and straight along the normal direction. Measurements of the curvature from the 9-in. NDE block indicated a radius similar to (~10% greater) that of the HFIR RPV.

Metallographic examination and chemical analysis confirmed that the calibration block is the same material as the A212B used for the RPV.

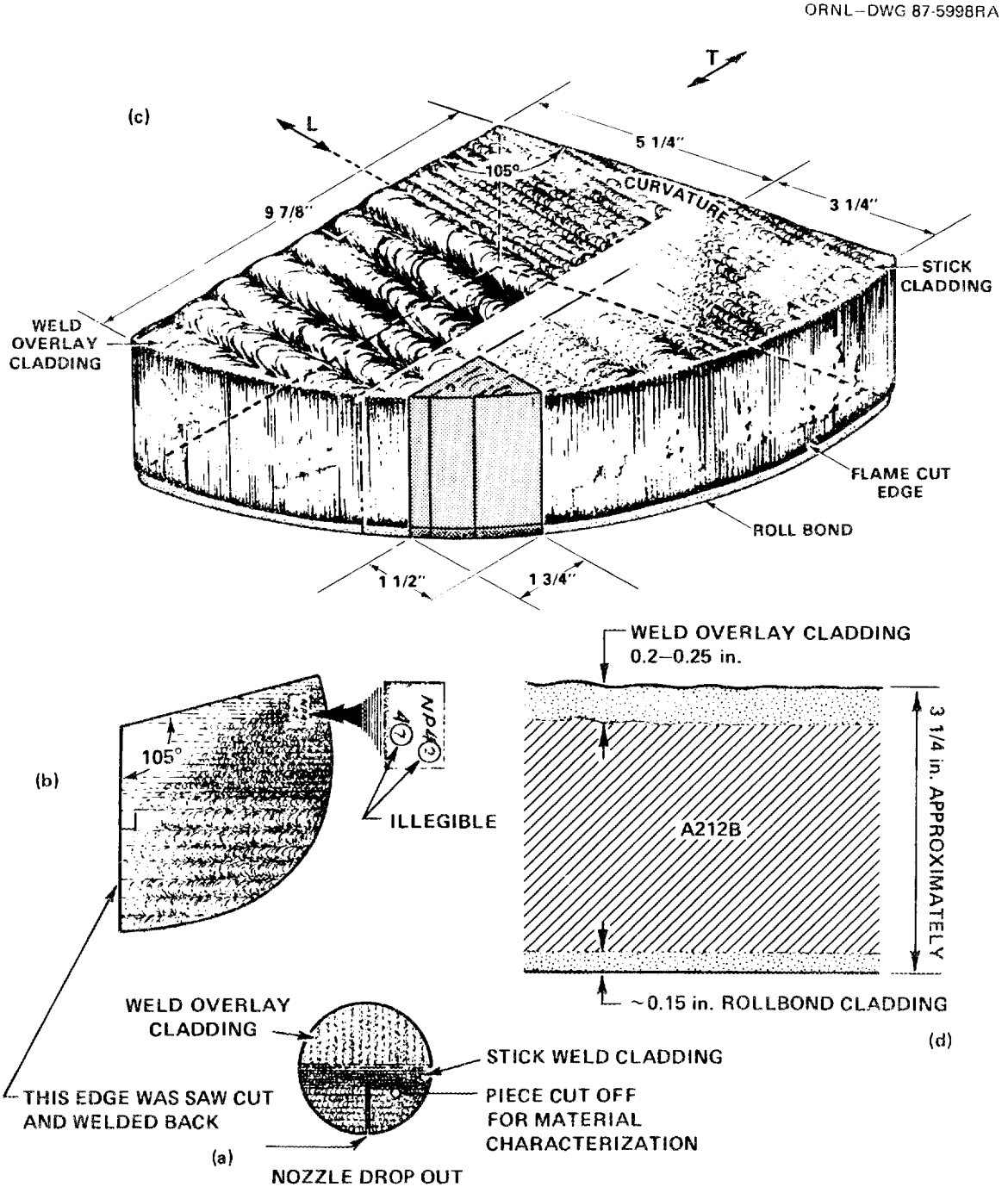

Fig. D.17. NDE calibration block used to fabricate CVN specimens. (*a*) Original piece, (*b*) and (*c*) segment cut out, and (*d*) details of the cladding. The L and T refer to the longitudinal (rolling direction) and transverse orientations, respectively.

However, diamond pyramid microhardness (DPH) tests performed on the surveillance specimens and 1/4-in. CVN specimens from the NDE block showed that the latter was significantly harder, 194 vs 172 DPH. As shown in Table D.10, the CVN energy of 1/4-in. LT-oriented specimens from the NDE block and tested at 0 and 20°F is lower than that of surveillance specimens at these temperatures.

Thus, it appeared that the NDE block had received no PWHT. Accordingly, three LT-oriented CVN specimens were given a PWHT for 51 h at 950°F and tested at 20°F. The average CVN energy after the PWHT of the three specimens agreed very well with the average of the surveillance specimens (Table D.10), and the hardness decreased to 172 DPH. The remainder of the NDE block was then subjected to the same PWHT.

Table D.10. Comparison of CVN impact energy of A212B surveillance specimens with specimens from 1/4-in. location of NDE block (LT orientation) before and after PWHT at 950°F for 51 h

Specimen No.	Test temperature (°F)	Fracture energy (ft-lb)	Average fracture energy (ft-lb)
	Surveillance test results		
A-49	0	21.5	
A-56	0	13.5	15.3
A-63	0	11.0	
A-24	20	19.5	
A-26	20	28.5	24.8
A-29	20	26.5	
	As-received (no PWHT)		
ND-6D	0	7.8	9.4
ND-6E	0	10.9	
ND-2A	20	13.0	15.4
ND-6A	20	17.8	
	After PWHT		
ND-2C	20	20.4	
ND-6C	20	26.5	24.3
ND-2D	20	26.1	

In spite of the excellent agreement discussed above, because of the uncertainties about the NDE block and because of time constraints, spare unirradiated surveillance samples of A212B were used as a reference or indexing material in the first two irradiation capsules. The NDE block material was archived for irradiation needs beyond the available spare surveillance samples.

D.4.3.3 CVN test results

CVN specimens from each of the LT, TL, TS, and LS orientations have been machined from the NDE block and tested. The objectives of testing the LT orientation are explained below. The objective of tests on TL and TS orientations was to obtain the shift in transition temperature as a result of irradiation. The LS orientation was tested to obtain a qualitative indication of the resistance of the material to propagation of axial cracks in the thickness direction.

The tests performed on A212B (LT) specimens were performed at various temperatures to obtain a better definition of the Charpy energy vs temperature curve. Of importance were two regions of the curve. One region was the vicinity of 50 ft-lb. The temperature at which this energy level is attained is used to estimate RT_{NDT}, as explained in Sect. D.4.5. The other was the Charpy upper-shelf energy (USE) region. Two spare unirradiated surveillance specimens, as well as one specimen from the NDE block tested at 120°F, exhibited almost 100% shear on their fracture surfaces and, thus, defined the USE region.

The results of recent unirradiated testing of LT-oriented CVN specimens have been included in Table D.4. The specimen numbers in Table D.4 that begin with an "A" are original surveillance specimens; all other numbers are from the NDE block.

The results of testing both the TS and TL orientations in the unirradiated condition from the A212B NDE block are shown in Tables D.17 and D.18, respectively (see Sect. D.5.6). These results, together with the Charpy energy values obtained from testing these orientations after irradiation in ORR, have been plotted in Figs. D.27 (Sect. D.5.6) and D.18, respectively. Note that a 50-ft-lb level was not achieved for the TL orientation, and to estimate the RT_{NDT}, the temperature at which 35-mils lateral expansion is achieved has been used instead (Fig. D.18).

Of particular interest is the LS orientation (Table D.11 and Fig. D.19). The Charpy energy obtained for the unirradiated material at 20°F exceeded the 150-ft-lb range. At 60°F the Charpy energy was ~233 ft-lb. In fact, all four specimens tested at these two temperatures did not fracture completely in the Charpy test but remained attached together with a large ligament. In Fig. D.19 the CVN results for the LT, TL, and TS orientations have also been plotted for comparison.

D.4.3.4 Unirradiated drop-weight and crack-arrest testing

Limited drop-weight testing was performed on specimens removed from the HB2 nozzle dropout (A212B). The specimens were fabricated in the LT orientation from the outer half-thickness of the dropout that remained following machining of the original A212 grade B surveillance specimens.

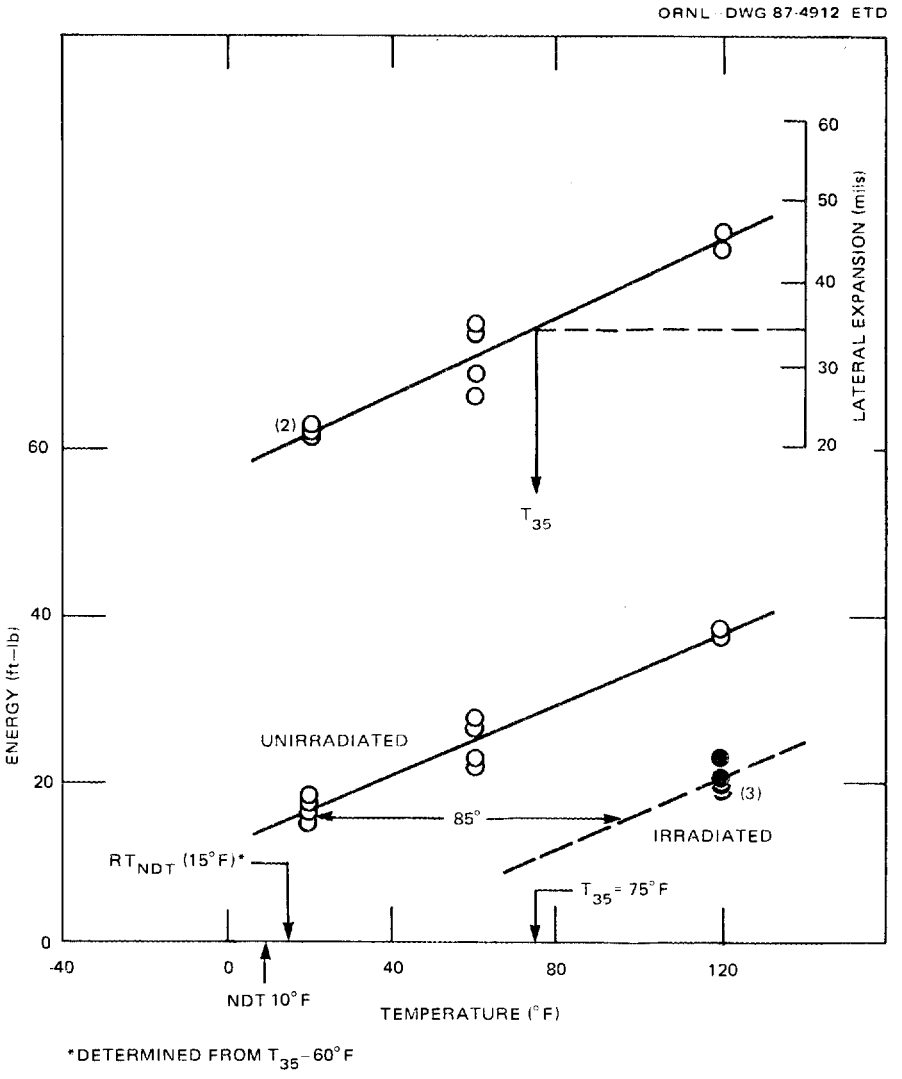

Fig. D.18. Estimation of RT_{NDT} from the 0.035-in. lateral expansion of A212B TL-oriented CVN impact specimens because the 50-ft-lb impact energy was not attained.

To conserve material, two layers of drop-weight specimens were machined at all locations, resulting in pairs of specimens: one good, unadulterated specimen and one specimen containing a thin skin (0.03 to 0.05 in.) of weld-overlay cladding. In addition, only the central 3.5 in. of the specimen was composed of the actual test material. The remainder of the 5-in. total specimen length was composed of similar A212 steel that had been EB welded to the central test section. The specimens containing the cladding were welded and tested such that the clad surface was the compressive surface in the test to minimize any nonuniform effects, and their results were used only to scope the test temperatures of the more homogeneous specimens. Testing of the specimens with the thin layer of cladding resulted in an NDT of 0°F. However, testing of the specimens

Table D.11. Unirradiated Charpy impact test results for A212 grade B, LS orientation (material from 1-in. depth)

Specimen No.	Test temperature (°F)	Fracture energy (ft-lb)	Fracture appearance (% shear)	Lateral expansion (mils)
D92H	−20	10.2	12	9
D92E	−20	12.8	15	14
D92L	0	119.2	30	89
D92A	0	24.1	15	23
D92K	0	17.3	21	18
D92F	20	211.3	100	94
D92J	20	165.3	99	90
D92D	20	183.4	100	94
D92N	60	233	100	[a]

[a]Specimen did not break; still joined ~50% of ligament.

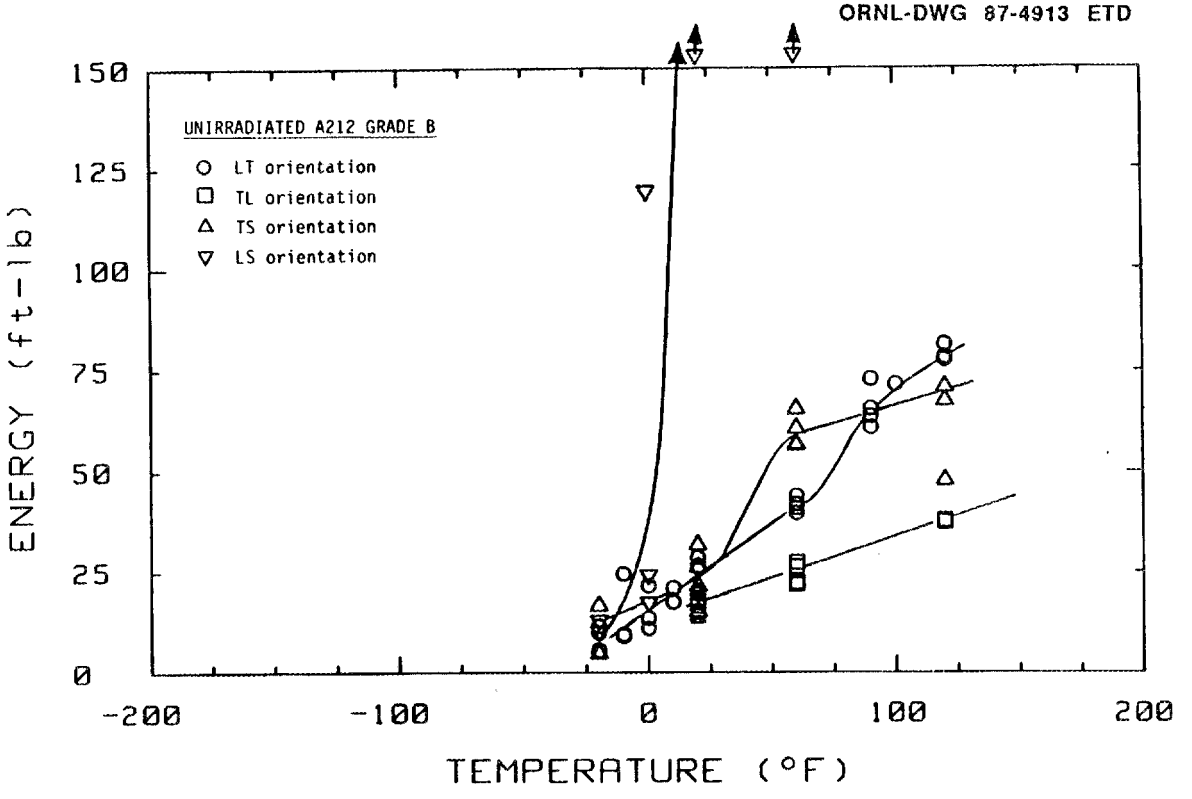

Fig. D.19. Charpy properties of unirradiated A212 grade B HFIR vessel steel as a function of orientation.

that did not contain cladding failed to produce any breaks at temperatures as low as −10°F, which would suggest an NDT of −20°F or lower for the unadulterated plate.

Preparations were also made to perform crack-arrest testing on the same dropout. To again conserve material, the use of an EB-welded specimen containing only a nugget of the material of interest was investigated. Specimens were fabricated from another piece of A212 grade B and successfully tested to ensure their experimental viability. It was, however, eventually decided that crack-arrest testing of the HB2 nozzle dropout would not be performed and that the material would be archived for future use.

D.4.3.5 Tensile test results on unirradiated A212B material

The effect of irradiation on the tensile properties of A212B shell material has been assessed by means of small, flat specimens, ~0.03 in. thick. These tensile specimens were machined from unirradiated and irradiated broken halves of Charpy specimens. The results of the tests on these small specimens are discussed in Sect. D.6. To determine the effect, if any, of specimen size on the tensile properties, two longitudinally oriented (1-in.-deep) Charpy specimens were machined into tensile specimens with a gage diameter of 0.2 in. and tested. The averages of the properties determined are shown below.

Strength (ksi)		Elongation (%)		Reduction of area (%)
0.2% Yield	Ultimate	Uniform	Total	
47.1	82.4	17	31	69

D.4.4 Fabrication and Evaluation of Submerged-Arc Weld
(G. M. Goodwin, R. K. Nanstad, and W. R. Corwin)

As mentioned previously, no archive weldments that represent the longitudinal seam and circumferential girth welds in the HFIR vessel are available. Welding procedure and welder qualification test documentation are available and provide the details of the welding procedures, materials, test results, etc., used for fabrication of the submerged-arc welds. As discussed in a separate chapter of the report, drillings were removed from the seam weld of the vessel, and chemical composition was determined. Linde 40 (AWS type EA3), 3/16-in.-diam, copper-coated weld wire and Linde 80 flux were ordered to reproduce the vessel weld as closely as possible.

A weld pad was made to determine chemical composition and showed copper composition to be lower than the vessel seam weld. A mock-up test weld was also made to qualify procedures. A subsequent weld pad was made with added copper whereby a length of thin (~0.009-in.) copper wire was tack-welded in the weld groove before each weld pass. The violent action

in the weld puddle is believed to distribute the melted copper throughout the weld beads. Chemical analyses and microprobe analyses show this to be a successful procedure.

A double-J weld groove was prepared, and 1/4-in.-diam E7018-A1 shielded metal-arc rod was used in two layers in the root region. The base metal used was from a 2 1/2-in.-thick A212 grade B dropout from the HFIR vessel bottom head. The weld was completed with 30 passes of submerged-arc weld. The weldment was then stress relieved at 950°F for 17 h to duplicate the seam-weld qualification. The 15-in. weldment was sectioned, and one piece was given an additional 34-h heat treatment at 950°F to reproduce the stress-relief time of the HFIR vessel.

Chemical analyses given in Table D.9 show the copper content of the reproduction weldment to be only slightly higher than the vessel seam weld. Overall, the chemistry and toughness of the weld are considered a successful reproduction of the vessel seam weld. A microprobe analysis (195 readings across the weld) of copper distribution in the reproduction weld showed the copper content varied ~0.065 wt % about the mean value in the weld metal, which is very similar to the variation shown by similar analyses of the A212 grade B plate. The copper wire additions appear to have provided uniform distribution of copper in the weld.

Figure D.20(*a*) shows a macroscopic etched photograph of the weld with lines drawn on the photograph representing the traverse paths for the microprobe scans. Figure D.20(*b*) shows the etched microstructure of the submerged-arc weld metal after PWHT. It is primarily ferrite with relatively small grain size.

The results of Charpy impact tests performed on the newly fabricated HFIR seam-weld reproduction (0.18 Cu) were compared with those performed as part of the original qualification procedure for the HFIR seam weld. In both cases, the weldments received a 17-h PWHT at 950°F. All specimens were fabricated about the centerline of the weld with their axis perpendicular to the weld centerline and the direction of crack propagation parallel to the welding direction. The comparison showed an excellent correspondence of impact properties between the welds. At 10°F six specimens of the seam-weld reproduction produced an average impact energy of 28.7 ft-lb with a standard deviation of 12.0 ft-lb; the average impact energy of the original qualification weld at 10°F, however, was 28.4 ft-lb with a standard deviation of 7.4 ft-lb.

To obtain material as similar to the seam weld in the vessel as possible, the seam-weld reproduction was then given an additional 34-h PWHT at 950°F for a total time of 51 h. The temperature at which the unirradiated Charpy impact properties of the seam-weld reproduction (Fig. D.21) produced an average energy of 20 ft-lb, the level equated with NDT for the weld, was −5°F.

One minor complication developed in examining the data for the seam weld reproduction. The impact energy through the thickness of the weld varies modestly but reproducibly over the temperature range examined; the toughest portion lies at the top of the weld corresponding to the outer surface of the vessel. The reason for this was not investigated but is likely a consequence of the thermal history of the individual weld passes. Because impact specimens were only taken at one location, mid-thickness, during the original weld qualification procedure, it is not known whether or not such a variation exists in the actual HFIR vessel,

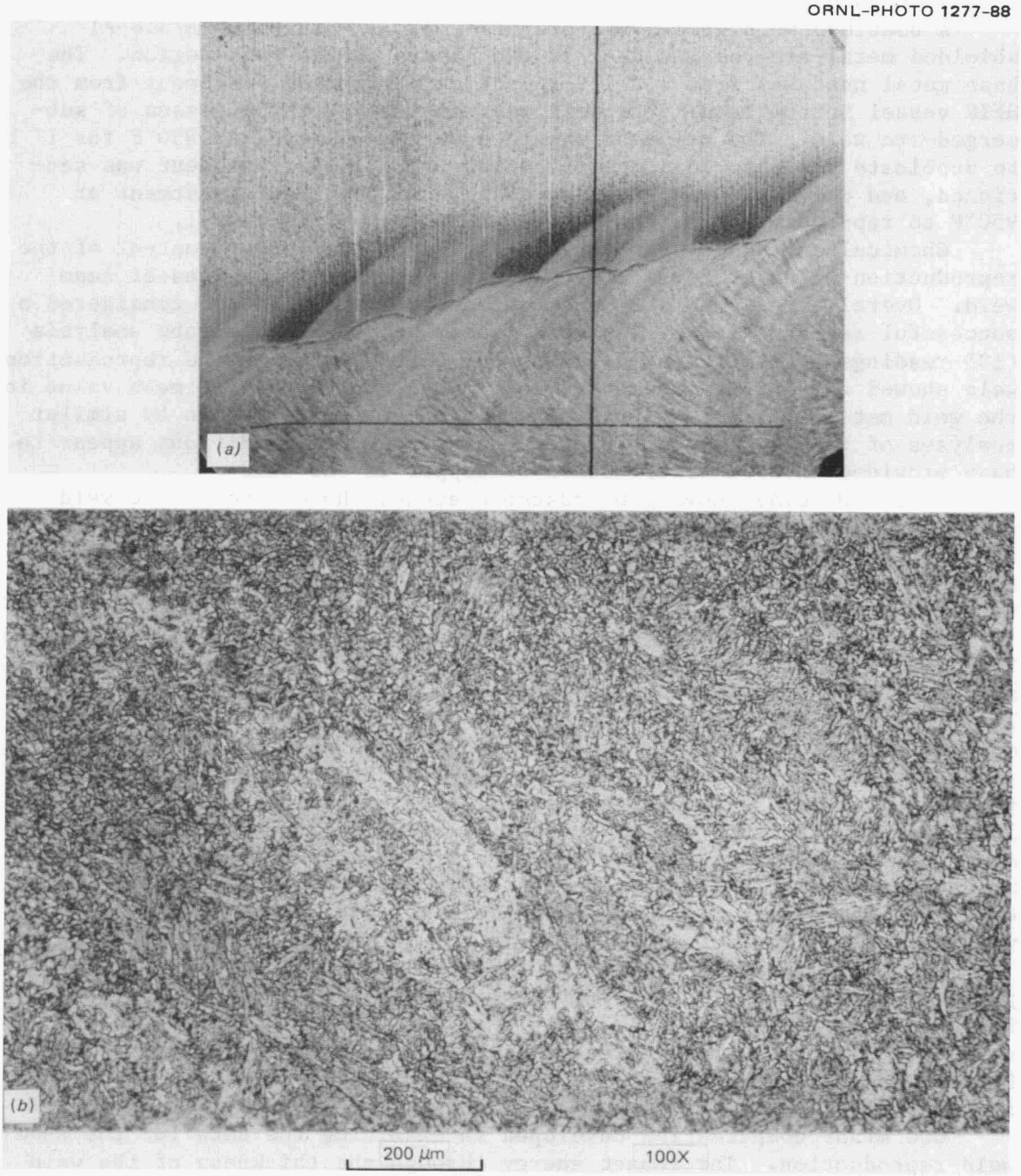

Fig. D.20. Submerged-arc reproduction seam weld for HFIR pressure vessel. (*a*) Etched microstructure (lines show traverse paths of microprobe scans, 5×), (*b*) etched microstructure of weld metal. (Original reduced 3%)

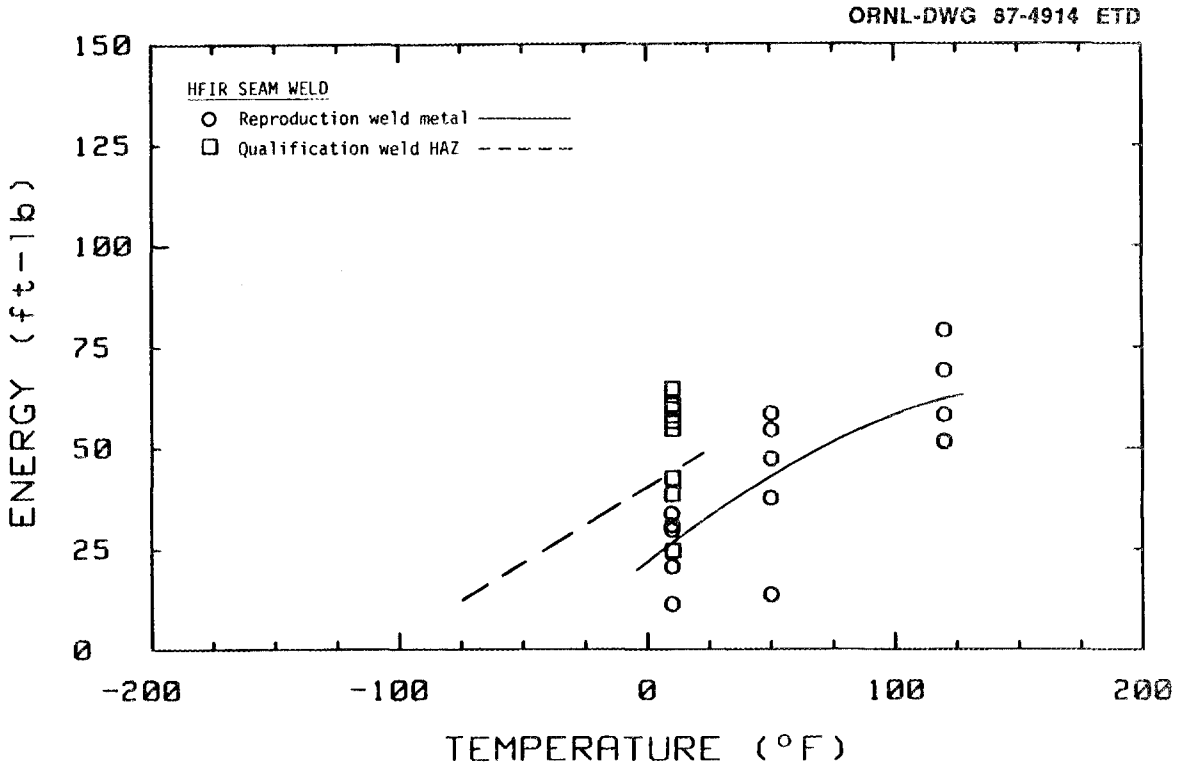

Fig. D.21. Unirradiated Charpy impact properties of the submerged-arc reproduction seam weld metal and qualification weld A212B heat-affected zone.

but it is likely because the same procedure was used for both welds. The approach taken in analyzing the data for the seam-weld reproduction was to disregard the properties from the bottom 1 in. of the weld thickness corresponding to a hypothetical 1-in.-deep flaw on the vessel's inner surface and simply to average the impact properties through remaining thickness.

Also shown in Fig. D.21 are the CVN results obtained from vendor documentation for the HAZ tests on the vessel qualification seam weld. A straight line was drawn through the mean energy value approximately parallel to that of the A212B (LT) curve. The NDT was estimated (at the 15-ft-lb energy level) to be −68°F, far below those of the weld metal and the A212B (LT).

D.4.5 Determination of RT_{NDT} (R. K. Nanstad and T. L. Hebble)

The ASME Code, Sect. III, Subsect. NB (Class 1 Components),[4] requires the establishment of a reference temperature RT_{NDT}. The procedure

involves the testing of drop-weight specimens to determine the NDT and CVN specimens to determine a temperature at which three CVN specimens each exhibit at least 50 ft-lb and 35-mils lateral expansion (T_{50}). This is normally accomplished by determining the NDT temperature T_{NDT} with drop-weight tests, followed by three CVN tests at a temperature not greater than T_{NDT} + 60°F. If the CVN minimum toughness requirements are met, then T_{NDT} is the RT_{NDT}. If they are not met, then the CVN test temperature is increased until the requirements are met and the RT_{NDT} is determined by T_{50} − 60°F. As stated earlier, the HFIR surveillance plan[1] defined the NDT at a specific CVN energy value, and mean curves have been used to determine these NDTs. In the case of the A212 grade B, however, sufficient material was located to provide for the conduct of limited drop-weight tests according to ASTM E208 (Ref. 5). The test results showed the drop-weight NDT for A212 grade B to be not higher than 0°F and possibly as low as −20°F, very close to the value of −5°F determined from the CVN 15-ft-lb temperature.

Because values of the RT_{NDT} could not be determined for most of the HFIR materials with the ASME Code procedures, an alternative procedure was developed using the available CVN data. Because the ASME Code method requires that all three CVN specimens exhibit 50 ft-lb or greater at the so-called 50-ft-lb temperature T_{50}, use of the mean curve fit to the CVN data is not considered similarly conservative.

To maintain simplicity and to provide a conservative bound for fracture energy from Charpy impact tests on irradiated material, an approach using a coefficient of variation was adopted. Numerous other approaches exist; however, coefficient of variation is simple and easily understood. The unknown, nonlinear character of the relationship between fracture energy and test temperature and large variances make the use of methods such as confidence intervals more difficult and time consuming to apply.

The coefficient of variation is defined as the ratio of the standard deviation to the mean fracture energy at a particular temperature. It is without units and may be expressed as a fraction or as a percent. Problems do exist when applying the coefficient of variation (e.g., establishing a smooth boundary curve that monotonically increases with temperature to eliminate the confusion of multiple values). The coefficient of variation for fracture toughness data is not constant because both the variance and fracture energy change with temperature. To find a reasonable coefficient of variation for our purpose, variance estimates were made from the data. The corresponding standard deviations and resulting coefficients of variation are given in Table D.12.

Each material contained several sets of observations from which a variance could be estimated. If the coefficient of variation was based on the variance from a single set, the source of variance was denoted "individual." If the variance was derived by pooling the variability from all sets within a given material, the source was denoted "pooled." The variance is the square of the standard deviation.

Table D.12. Standard deviations and coefficients of variation for HFIR surveillance materials

Material	Sources of variance	Standard deviation (ft-lb)	Coefficient of variation (%)	Median coefficient (%)
HB1 and HB4	Individual	1.4–6.8	3–29	17
A105 grade II	Pooled	4.9	11–52	21
HB2	Individual	2.3–7.3	3–16	12
A350 grade LF3	Pooled	4.2	5–16	11
HB3	Individual	1.4–6.0	4–27	7
A350 grade LF3	Pooled	3.7	9–18	13
IC3, HB1A, HB4A	Individual	2.0–8.8	1–62	27
A212 grade B	Pooled	5.1	7–57	30

From these and other results, the following values for the coefficients of variation are considered reasonable and will be used:

Material	Coefficient of variation (%)
A350 grade LF3	10
A212 grade B and A105 grade II	15
Seam weld	20
Nozzle weld	20

The application of the coefficients of variation to determine the unirradiated RT_{NDT} is straightforward. The mean CVN curve for a given material is used to identify the temperature at which the mean CVN energy less one standard deviation is equal to 50 ft-lb. For example, the coefficient of variation for A212 grade B is 15%; thus, a mean CVN energy of 58.8 ft-lb gives a standard deviation of about 8.8 ft-lb (coefficient of variation times the mean energy), and the mean value less the standard deviation is 50 ft-lb. The temperature at which the A212 grade B achieves a mean CVN energy of 58.8 ft-lb is, therefore, defined as T_{50}, and RT_{NDT} is determined from the higher of T_{50} – 60°F or the NDT, T_{NDT}. This procedure was applied to all materials except the A212B (TL), which did not achieve 50 ft-lb. For that case, the RT_{NDT} was estimated by determining the temperature at which it achieved 0.035-in. (35-mils) lateral expansion less 60°F (Fig. D.18). For irradiated material, the ASME Code references ASTM E185, "Standard Practice for Conducting Surveillance Tests for Light-Water Cooled Nuclear Power Reactor Vessels."[6] The RT_{NDT} is determined by adding the difference in the 30-ft-lb temperature from the mean CVN curves before and after irradiation to the unirradiated RT_{NDT}. The results of these analyses are summarized in Sect. D.5.6 with the results of the irradiation program.

D.5 IRRADIATION PROGRAM IN THE ORR

D.5.1 Materials (R. K. Nanstad)

As stated previously, the pressure-vessel surveillance program does not include welds. An irradiation program was conducted, first, to compare the effects of neutron irradiation on the HFIR vessel seam weld and nozzle welds with the vessel shell material. Second, the A212 grade B surveillance specimens were machined from a nozzle dropout with the LT orientation (axis of the specimen in the longitudinal or rolling direction and the notch oriented for crack propagation transverse to the rolling direction). Depending on chemical composition, cross rolling, etc., plate steels can exhibit differences in toughness with orientation, and the irradiation program includes the TL and TS orientations as well (see Sect. D.4.3).

As shown in Sect. D.4.1, the A212 grade B shell material for the HFIR vessel has a relatively high sulfur content and metallographic evidence of sulfide stringers that can adversely affect toughness. Although there are reports of greater effects of irradiation on transverse oriented specimens, the effects on this material at these relatively low exposures was quite uncertain. As presented in Sect. D.4.3, the CVN toughness of TL specimens from the HFIR vessel shell was low relative to the LT-oriented surveillance specimens. As expected, the greatest difference is in the upper-shelf toughness. The actual upper-shelf toughnesses following irradiation, however, are not very relevant for the A212B because the shifts of the CVN curves put fully ductile behavior higher than the current operating temperature of 120°F.

The materials for this irradiation task are the A212 grade B plate in the LT, TL, and TS orientations; the nozzle qualification weld metal; and the reproduction seam weld fabricated at ORNL. The A212 grade B specimens in the LT orientation were selected from a group of spare unirradiated surveillance specimens. The material is described in Sect. D.4.1. The nozzle qualification weld was sectioned and CVN specimens machined to accommodate crack propagation in the welding direction and located in the bulk area of the weldment (described in Sect. D.4.2). Specimens of A212 grade B with TL and TS orientations were removed from a nozzle dropout (described in Sect. D.4.3). The specimens included in the irradiation capsule were removed from the same depth in the plate thickness as were the original surveillance specimens. Finally, CVN specimens from the seam-weld reproduction were machined and notched in the same manner as those for the nozzle weld. Fabrication of the seam weld is described in Sect. D.4.4.

D.5.2 Irradiation Conditions (K. R. Thoms, R. K. Nanstad, and W. R. Corwin)

D.5.2.1 Introduction

Specimens were irradiated in core position A9 of the ORR. Reactor coolant water flowed directly over the specimens, which were contained in

capsules described in Sect. D.5.3. To minimize specimen corrosion, specimens were coated with a stable black oxide (Fe_3O_4). The basis for that coating is the result of a coatings evaluation task described in Sect. D.5.4.

Twenty CVN specimens, along with flux monitor gradient wires, were housed in each capsule. The capsule was positioned with the specimens centered axially about the expected flux peak (i.e., ~3 in. below the core midplane). Table D.13 summarizes the thermal hydraulic analysis for the capsules. Gamma-heating rate measurements were made in the A1 core position, which is symmetrical to the A9 position used for these irradiations. The peak heating rate in steel at the deviation of the test specimens was found to be 1.2 W/g.[7] To predict accurately specimen temperatures, the effect of the stable black oxide coating was incorporated in the thermal analysis. Metallographic examination of coated specimens showed the average coating thickness to be 0.001 in. The thermal conductivity of Fe_3O_4 at these temperatures is reported to be 3.1 Btu/h-ft^2-°F (0.055 W/cm-K).[8] Based on these assumptions, the specimen centerline temperature is predicted to be ~123°F and the surface temperature ~119°F. Because neutron irradiation of oxides is known to reduce their thermal conductivity by as much as 50% at temperatures where annealing of defects does not occur,[8] this was also taken into account but only increased the specimen centerline temperature by ~0.2°F. Additionally, the consequences of the gamma-heating rate being twice the measured value were investigated. A summary of the specimen heat-transfer analyses using various assumptions is presented in Table D.14.

To determine exposure levels in core position A9, a dosimetry capsule was inserted into position A9 on December 22, 1986. Three long bars equal in length to four CVN specimens and equal in cross section to a CVN specimen, along with eight CVN specimens of another A212 grade B material, were contained in the capsule. An ~0.200-in.-ID hole was drilled along the centerline of each bar, flux monitors were inserted therein, and the bar ends were seal welded closed in a helium atmosphere and leak checked. The CVN specimens were variously coated and notched or unnotched. A photograph of the capsule during final assembly is shown in Fig. D.22. The capsule was irradiated at 30 MW for 4.08 h. The dosimetry results from this capsule formed part of the basis for selection of exposure time of the HFIR specimen capsules.

D.5.2.2 Irradiation dose rate experiment on A212 grade B steel

The neutron flux in the core of the ORR is about 4 to 5 orders of magnitude greater than exists at the HFIR pressure vessel. To evaluate the shift in the NDT of A212 grade B steel at the high flux levels to be used in the ORR irradiation experiments, an experiment was, therefore, conducted utilizing the ORR dosimetry measurement capsule.

Eight CVN impact specimens from a heat of A212 grade B steel previously examined for the EGCR Program were coated with various corrosion-resistant coatings (see Sect. D.5.4) and placed within the capsule used for establishment of irradiation exposure conditions in the core of ORR. The capsule was irradiated at full power for 4.08 h and received an exposure of 1.54×10^{17} neutrons/cm^2 (>1 MeV) at a flux of 1.05×10^{13}

Table D.13. Summary of thermal hydraulics analysis of HFIR material Charpy specimen irradiation capsules

Parameter	Value
Input data	
Coolant water	
Inlet temperature, °F	118
Pressure drop across capsule, psi	25
Viscosity (at 120°F), lb/ft-s	0.000373
Prandtl No. (at 120°F)	3.64
Conductivity (at 120°F), Btu/ft(h)°F	0.370
Density, lb/ft^3	62
Specific heat, Btu/lb-°F	1.0
Gamma heating rate, w/g	
Peak	1.2
Average	1.0
Results	
Coolant channels	
Channel between capsule and core piece	
Flow rate, gpm	41
Reynolds No.	42,741
Water temperature rise, °F	1
Specimen channels	
Flow rate/channel, gpm	5.8
Reynolds No. (around specimens)	33,900
Reynolds No. (remainder of channel)	44,000
Water temperature rise, °F	1
Total heat generated, kW	
Aluminum parts	5.9
Steel specimens	1.4

Table D.14. Specimen temperatures for various values of gamma heating and coating thermal conductivity

Assumptions		Temperature drop (°F)			Specimen centerline temperature (°F)
Gamma heating rate (w/g)	Thermal conductivity of Fe_3O_4 (Btu/h-ft^2-°F)	Through surface film	Through Fe_3O_4 layer	Through body of specimen	
1.2	3.1	1.2	0.3	3.5	122.9
1.2	1.5	1.2	0.5	3.5	123.1
2.4	3.1	2.4	0.5	7.0	127.9
2.4	1.5	2.4	1.0	7.0	128.4

PHOTO YP 3423

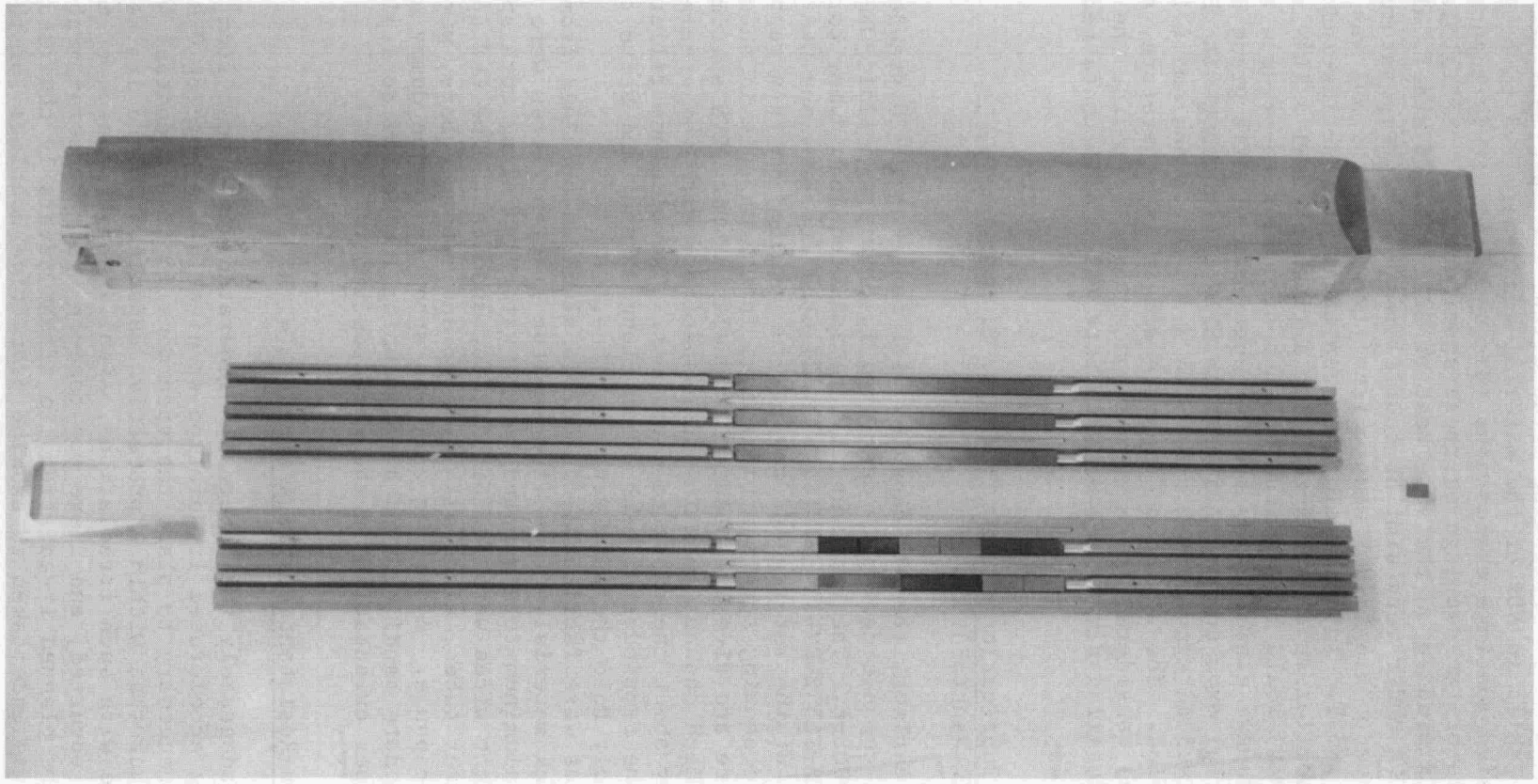

Fig. D.22. Dosimetry capsule during final assembly and dummy core piece in which it was irradiated.

neutrons/cm^2/s (>1 MeV). Following irradiation, the specimens were tested, and the shift in NDT of the material was determined to be 18°F. Based on extensive coatings evaluations (Sect. D.5.4), it is apparent that the effects of the coatings on these specimens were negligible. In the earlier EGCR studies on the same heat of A212 grade B steel, also irradiated at ORR under very similar conditions of both temperature and flux to a fluence of 9.8×10^{18} neutrons/cm^2 (>1 MeV), the NDT was determined to shift 185°F. Interpolation between the two high-flux-induced NDT shifts in semilog space predicted that a fluence of $\sim 1 \times 10^{18}$ neutrons/cm^2 (>1 MeV) would be required at that high flux to produce a similar degree of damage exhibited by the CVN specimens of A212 grade B vessel shell material exposed for 17.5 EFPY in HFIR, even though the HFIR specimens received an exposure of only $\sim 1.5 \times 10^{17}$ neutrons/cm^2 (>1 MeV) during that period. The apparent dose rate effect is, therefore, substantial and was considered in selecting the exposure time for the HFIR materials. A detailed discussion of dose rate effects is contained in Sect. D.6.

D.5.3 Capsule Fabrication (K. R. Thoms, B. H. Montgomery, and R. K. Nanstad)

As stated earlier, the ORR capsules will house up to 20 standard CVN specimens. The capsule design is described in drawings M-11511-OR-001-E and M-11511-OR-002-E. The capsules will be inserted in a dummy core piece (Drawing M-11552-EM-114-D) (Fig. D.22) used for previous ORR experiments (none of the referenced drawings is included in this report).

A schematic showing specimen placements in the capsule is shown in Fig. D.23. There are five independent channels in which CVN specimens were located. Each channel contains four specimens with the specimens centered axially about the expected flux peak. Two aluminum filler pieces occupy the remainder of each 30-in.-long channel and serve to locate and rigidly hold the specimens in place.

The capsules were fabricated of 6061-T6 aluminum obtained from certified HFIR stock material. Five flux-monitor gradient wires were contained in each aluminum tube mounted in the water gap along each specimen V-notch. Gradient wires were Fe, Ni, Ti, Cu, and CoAl. The CVN specimens and dosimeter tubes, along with locator and retainer bars, were mounted in the capsule. A lifting bail was attached to the dummy core piece to accommodate handling, and a positioning lug on the core piece allowed for proper orientation in the core position.

D.5.4 Corrosion-Resistant Coatings Studies (W. R. Corwin)

To remove adequately the internally generated gamma heat from CVN specimens during accelerated irradiation studies in the core of ORR at ~120°F, it was necessary to place the specimens in direct contact with the coolant rather than within a protective capsule. In the limited previous experience with such irradiations, significant corrosion of mild steel specimens occurred, and there was concern that corrosion might be sufficient in the planned irradiations to affect adversely the results. Hence, a study was undertaken to examine protective coatings for the specimens.

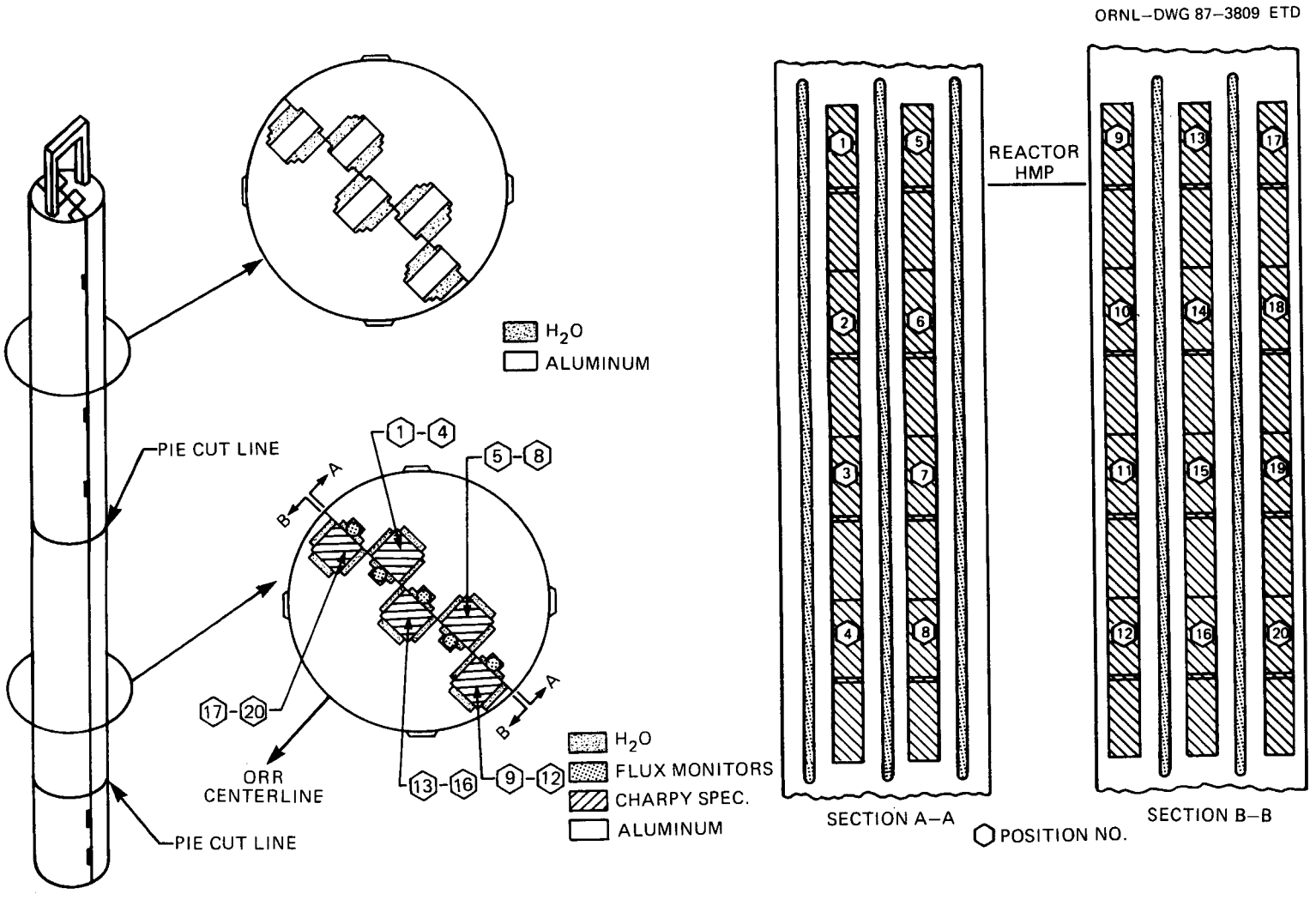

Fig. D.23. Schematic drawing showing placement of Charpy specimens in ORR irradiation capsule.

The types of coatings that could be used were limited by (1) availability within the short time frame required, (2) reactor constraints, (3) potential adverse effects on impact testing, and (4) coating application temperatures with the concern that it might at some time be necessary to coat previously irradiated specimens. After due consideration five types of protective coatings were selected for evaluation: electroplated nickel, electroless plated nickel, both aluminum and titanium coatings applied by physical vapor deposition (PVD), and a stable black oxide coating routinely used for protection of tooling. All coatings were applied to CVN specimens fabricated in a single orientation from one heat of A212 grade B steel. Special concern over coating effects within the CVN specimen notch resulted in the coatings being applied both before and after notching. Coated specimens were evaluated for both corrosion resistance within the reactor environment and any effect that the coating might have on impact toughness.

Immersion in water from 1 to 4 d (the anticipated duration of the ORR irradiations) would normally cause only limited rusting of mild steel specimens. However, experiments were conducted to examine the effects of both the bulk composition of the demineralized water used for the ORR coolant and the very short-lived but highly corrosive radicals postulated to exist within the high-flux regions of the core on the corrosion behavior of the A212 grade B CVN specimens. Specimens, both uncoated and coated as previously described, were exposed in the core of ORR for ~4 h at full power during the irradiation of the first irradiation capsule (used for dosimetry measurements), as well as in flowing reactor coolant (away from the core) for ~4 d. In both exposures, the uncoated specimens corroded appreciably while those with coating were better but variable. The nickel coating provided the best protection, followed by the black oxide coat and then by the PVD coatings.

In the parallel effort to evaluate coating effects on the impact properties of the CVN specimens, multiple tests were conducted at temperatures ranging from low in the transition region to just beyond onset of upper shelf. In comparing the results of the coated and uncoated specimens, it became apparent that both of the nickel coatings substantially altered the CVN test results; the other coatings, however, had virtually no effect whether the specimens were notched before or after coating.

Because the black oxide coating appeared to have the best corrosion resistance of the coatings acceptable from testing aspects, additional prenotched and then black-coated specimens (up to six at any temperature) were tested for a better statistical evaluation, and their results were compared with uncoated specimens. The result was that no discernible effect of the presence of the black coat on the Charpy impact toughness could be detected. Moreover, the ability to notch the specimens before coating eliminated the need for, and complications of, notching the specimens after the irradiation. The black oxide coating was, therefore, chosen for specimen protection in subsequent irradiation experiments. The stable black oxide coating is applied following rigorously controlled cleaning by boiling the specimens at 290°F in a concentrated salt solution containing principally sodium hydroxide for ~1/2 h. The coating produced is a nonstoichiometric form of magnetite, Fe_3O_4; it is a standard, consistent, and reproducible coating procedure.

To determine what effect the black oxide coating might have on the thermal transfer characteristics of the specimens, the thickness of the coating was determined by taking a small-angle section through the coating and examining it visually under high magnification. The thickness varied substantially as a function of the local surface finish. Any small low spots, such as pits or scratches, that were present on the surface before coating tended to be filled in, resulting in local thick spots. Out of 60 measurements, the maximum and minimum coating thickness ranged from 0.0023 to 0.0003 in. with an average thickness of 0.0009 in. Calculations of the effect on heat transfer of the specimens for a coating in this thickness range were found to be very small (see Sect. D.5.2).

D.5.5 Irradiation Plan and Analysis Methods (R. K. Nanstad)

The objective of the irradiation task was to determine the toughness of the seam weld, nozzle welds, and A212 grade B steel of the HFIR pressure vessel. To accommodate that objective in a reasonable time, CVN specimens were irradiated in the core of ORR where the neutron fluxes are much higher than near the HFIR pressure vessel.

As stated earlier, each test specimen capsule contained 20 CVN specimens of various materials. The contents of the four capsules are shown in Table D.15. Because of the strict limitations on available HFIR vessel materials, the plan was formulated to obtain the information deemed most necessary with the least amount of material.

The A212 grade B (LT) vessel shell material was used to index the ORR results to the HFIR surveillance results. This was deemed necessary because of uncertainties in the neutron spectrum and dose-rate effects as a result of the accelerated irradiations (hours in ORR vs years for HFIR vessel). As discussed in Sect. D.5.2, an exposure time in ORR was selected to result in the radiation damage necessary for the A212 grade B (LT) to exhibit an NDT shift somewhat greater than that exhibited by the HFIR surveillance specimens. That allowed other materials to be similarly exposed and tested and the results related to the HFIR vessel. Obtaining a slightly greater shift allows for short-time extrapolation for the extended service predictions.

Figure D.24 is a schematic that describes the concept of analysis by assuming that data at only one test temperature are available. An unirradiated CVN energy vs test temperature curve is available for each material being irradiated. Following irradiation of capsule 2, the five A212 grade B (LT) specimens were tested at a temperature estimated to provide an average CVN energy of ~15 ft-lb (NDT). Figure D.24 shows three sets of five data points at the same test temperature to illustrate the analysis procedure, which is based on the observation from the HFIR surveillance program that the slopes of the CVN curves have not decreased significantly as a result of embrittlement. At the relatively low values of ΔNDT observed, that is an expected observation. For case 1, if the irradiated CVN test results are above 15 ft-lb, a curve is drawn through the mean of the data set and parallel to the transition region of the unirradiated curve. The intersection of the constructed curve with the CVN 15 ft-lb energy value determines the NDT temperature. The ΔNDT is

Table D.15. Capsule complement for ORR irradiation

Complement	Material	Test procedures
	Capsule 1	
3 long bars with dosimeters	Carbon steel	Dosimetry for ORR
8 CVN specimens	A212B, not HFIR material	Determine ΔNDT at low fluence, dose rate information
	Capsule 2	
5 CVN specimens	A212B (LT) HFIR surveillance specimens	Determine ΔNDT, index to HFIR surveillance
5 CVN specimens	A212B (TL) HFIR nozzle drop-out specimens without stress relief	Determine ΔNDT for TL orientation
10 CVN specimens	Nozzle qualification weld metal	Determine ΔNDT for nozzle welds
	Capsule 3	
5 CVN specimens	A212B (LT) HFIR surveillance specimens	Determine ΔNDT, index to HFIR surveillance
5 CVN specimens	A212B (TL) HFIR nozzle drop-out specimens with stress relief	Determine ΔNDT for TL orientation
10 CVN specimens	Vessel seam weld reproduction	Determine ΔNDT for vessel seam weld
	Capsule 4	
5 CVN specimens	Nozzle qualification weld metal	Increase data base
5 CVN specimens	Vessel seam weld reproduction	Increase data base
10 CVN specimens	A212B (TS) HFIR nozzle drop-out specimens	Determine ΔNDT for TS orientation

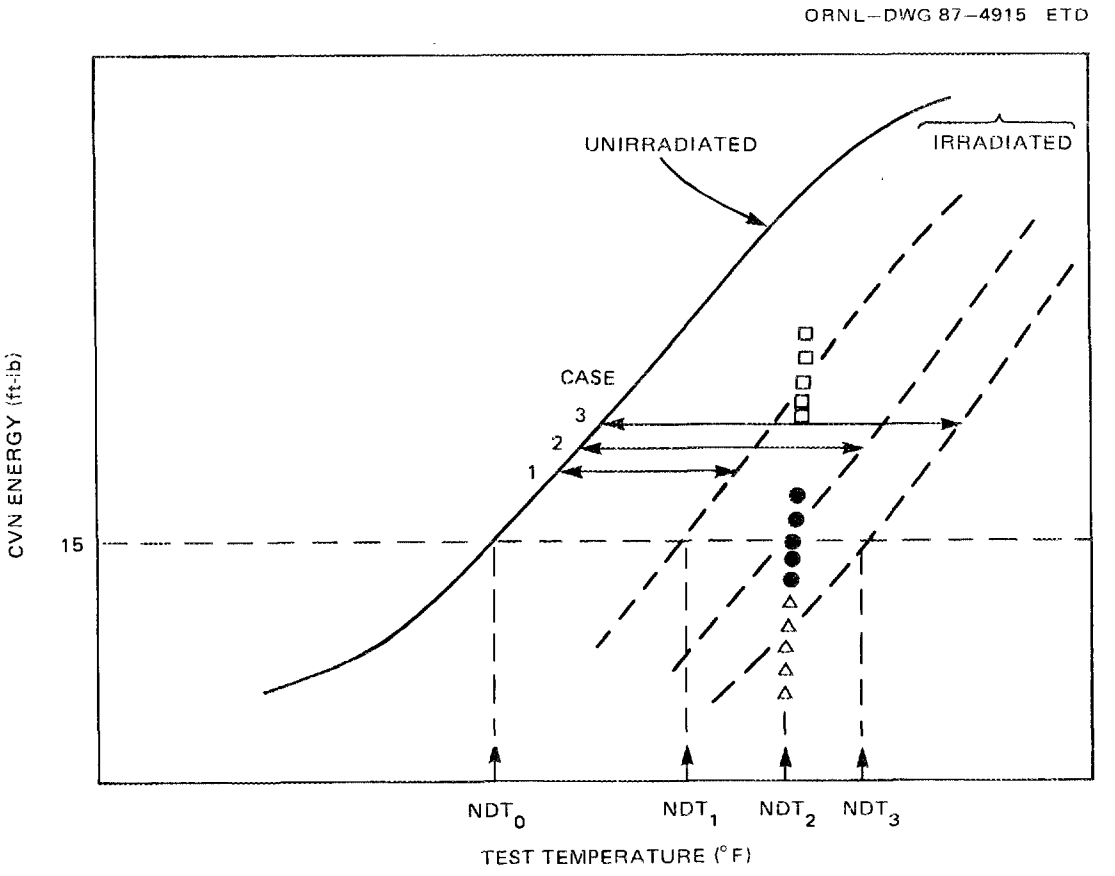

Fig. D.24. Concept for determination of NDT and ΔNDT from ORR irradiation results.

determined as shown by the horizontal arrow. The same method of construction is used for case 3 where the test results are below 15 ft-lb. For case 2 the mean energy is 15 ft-lb, so the test temperature is the irradiated NDT, and the ΔNDT is determined in the same manner. For the case where data are obtained at more than one test temperature, a curve is constructed through the mean energy values.

Using the results from the ORR irradiation, Fig. D.25 schematically shows how the ORR results are used. The solid curve is an approximate fit to the HFIR surveillance results for the A212 grade B (LT) that passes through the origin. If the ORR irradiation produces a ΔNDT of 100°F for the A212 grade B (LT), a point is plotted on the curve at a ΔNDT corresponding to 100°F. That indexes the result to the EFPY of HFIR operation. At that value of EFPY, the ΔNDT measured in ORR for the nozzle weld, for example, is plotted and a line drawn from the origin through the data point. In that manner, then, results for the weld metal can be interpolated or extrapolated as needed. The same procedure is followed for the A212 grade B (TL and TS) and the seam-weld reproduction.

The specimens from capsule 2 were tested before irradiation of capsule 3 to provide a basis for selection of exposure time for capsule 3. As mentioned earlier, uncertainties regarding dose-rate effects required

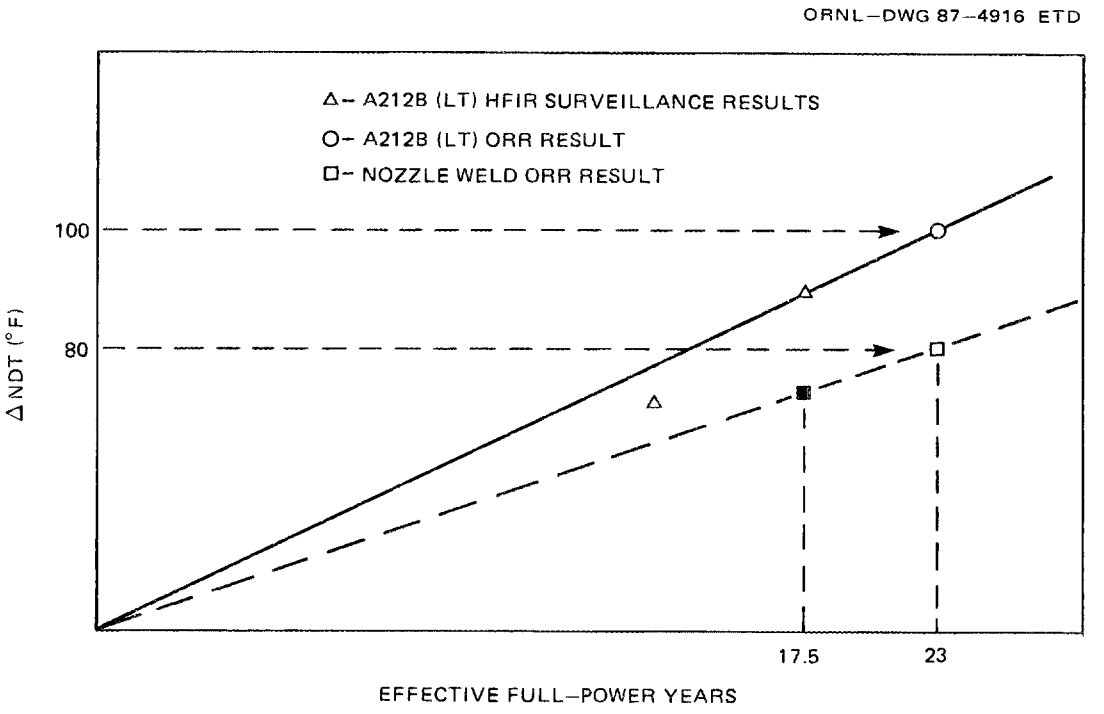

Fig. D.25. Concept of indexing ORR irradiation results to HFIR surveillance program. The method gives the expected ΔNDT in HFIR at key 7, position 8, after 17.5 EPFY.

that action to maximize efficient use of the available material. Because the results from capsule 2 were satisfactory with ~70 h of irradiation, capsules 3 and 4 were similarly exposed.

The results from this irradiation program, presented in Sect. D.5.6, provide a direct comparison of irradiated toughness for base metal and welds at the same exposure level in ORR, a test reactor. Using the linear technique of interpolation presented previously, then, the relative effects of radiation sensitivity can be compared for each material of interest in the HFIR vessel at 17.5 EFPY. To determine the actual toughness for each material, however, requires knowledge of the neutron fluences at specific locations of interest. Appendix E describes the method used for determination of the neutron flux distribution in the HFIR vessel. The fracture mechanics analyses in Chap. 5 incorporate the neutron fluence for each specific area relative to that for the A212 grade B (LT). In that way, the ORR results for each material are adjusted for higher or lower fluence as applicable.

As mentioned earlier, the information concerning sensitivity of pressure-vessel steels to neutron irradiation at 120°F is very limited. The general trend is one of increased sensitivity with decreasing temperature from the nominal operating temperature of LWRs, 550°F. It is generally held that the sensitivity reaches a threshold in the range of 400°F such that lower irradiation temperatures produce no further damage for most low-alloy pressure-vessel steels. It is also recognized by many

that individual steels likely exhibit significantly different behavior. The effects of compositional variations on sensitivity at 550°F is much better known because Cu, Ni, and P are accepted "bad actors," either individually or synergistically. The composition contribution cannot be separated from irradiation temperature, however, because the mechanisms operative at 550°F are not necessarily operative at 120°F.

Various studies have examined the roles of certain elements (e.g., B, Ni, P, O, Cu, V, N, Al, and Si). Steele[9] discusses the results of many researchers who have verified that nitrogen in solid solution is a major factor at irradiation temperatures below ~482°F. The observation is that nitrogen plus low-temperature radiation-induced defects are relatively stable complexes that dissolve at higher temperatures with the return of nitrogen to solution. Many of the investigations at low-exposure temperatures involved interstitial elements.

The temperature in this range may be critical because of the dependency of damage on the mobility of interstitials and the resultant effect on interstitial-point defect clusters. The role of substitutional elements is probably important mainly because they may modify the action of interstitials.[10] For example, aluminum is a strong nitride former and if present in a high enough concentration may remove the nitrogen from solid solution so it cannot interact with point defects. In a transmission electron microscope study of A212 grade B steel irradiated at about 200°F, Birkle and Rall[11] proposed that a steel with a high dislocation density and a low interstitial-impurity content would have improved resistance to neutron-induced notch embrittlement. Few papers reviewed in this assessment presented specific compositional levels at which the interstitial elements are effective for producing radiation sensitivity.

The microstructural studies described in Sect. D.6 may provide valuable insight concerning these mechanisms. Of special interest is a comparison of the defect structures of the HFIR surveillance specimens and the materials irradiated in the ORR. This comparison complements the toughness study and proposes some explanations of the observed dose-rate effects.

D.5.6 Results of the ORR Irradiation Program (R. K. Nanstad, W. R. Corwin, S. K. Iskander, and T. L. Hebble)

The results of testing the A212 grade B steel from capsule 1 were discussed earlier and demonstrated the apparent dose-rate effect. As a result, capsule 2 was exposed for 70 h. Capsules 3 and 4 were similarly exposed so that the average neutron flux (>1 MeV) for all specimens was 9.59×10^{12} neutrons/cm^2·s with one standard deviation of 4.2%. Thus, the average neutron fluence (>1 MeV) for all specimens was 2.43×10^{18} neutrons/cm^2 (see Appendix E).

Tables D.16–D.18 give the tabular data for all of the A212B CVN specimens exposed in capsules 2, 3, and 4. Figure D.26 shows the results for the A212B (LT). Those specimens were actual spare surveillance specimens machined in 1965 from the same nozzle dropout used for the surveillance specimens. A linear curve was fit to the mean energy values at the two test temperatures with a resultant ΔNDT of 100°F. Figures D.27 and D.28 show the results for the A212 grade B TS and TL orientations,

Table D.16. Charpy impact test results for A212 grade B archival surveillance samples, LT orientation, irradiated in the ORR[a]

Specimen No.	Test temperature (°F)	Fracture energy (ft-lb)	Fracture appearance (% shear)	Lateral expansion (mils)
		Capsule II		
A-71	90	6.3	25	1
A-155	90	15.7	30	6
A-130	120	21.5	45	10
A-151	120	36.1	40	18
A-158	120	21.7	40	14
		Capsule III		
A-125	90	5.4	10	0
A-127	90	25.8	35	10
A-139	90	6.8	15	0
A-143	120	25.4	40	12
A-162	120	34.3	40	14

[a] $\phi_N = 9.59 \times 10^{12}$ neutrons/cm^2·s; $\Phi = 2.43 \times 10^{18}$ neutrons/cm^2 (>1 MeV).

Table D.17. Charpy impact test results for A212 grade B, TS orientation (material from 1-in. depth)

Specimen No.	Test temperature (°F)	Fracture energy (ft-lb)	Fracture appearance (% shear)	Lateral expansion (mils)
		Unirradiated		
ND7B	−20	4.6	14	7
ND82	−20	16.6	12	19
ND57	20	31.6	31	32
ND87	20	15.0	36	22
ND7A	20	26.1	40	30
ND8B	20	21.3	34	27
ND76	60	56.6	96	60
ND83	60	65.3	99	61
ND86	60	60.5	98	58
ND73	60	56.3	98	59
ND55	120	70.7	100	60
QDP3	120	67.3	100	58
ND25[a]	120	47.6	99	49
		Irradiated in ORR[b]		
QDPB	95	21.2	55	11
ND33	95	11.7	45	3
QDP7	95	66.2	100	42
ND31	95	52.5	85	33
ND32	95	17.3	55	9
QDP2	120	24.7	75	9
QDPC	120	33.7	80	21
ND36	120	60.1	99	39
ND56	120	26	65	13
ND52	120	24.2	70	16

[a] From 1/4-in. layer.

[b] $\phi_N = 9.59 \times 10^{12}$ neutrons/cm^2·s; $\Phi = 2.43 \times 10^{18}$ neutrons/cm^2 (>1 MeV).

Table D.18. Charpy impact test results for A212 grade B, TL orientation

Specimen No.	Test temperature (°F)	Fracture energy (ft-lb)	Fracture appearance (% shear)	Lateral expansion (mils)
		Unirradiated, 1/4-in. depth		
ND78	20	14.3	20	21
ND81	20	18.0	37	23
ND84	20	15.2	21	22
ND7C	20	16.8	27	22
ND71	60	26.5	61	34
ND8C	60	22.6	60	29
ND79	60	27.6	63	35
ND88	60	22.0	48	26
ND89	120	37.5	99	44
ND85	120	38.0	99	46
		Unirradiated, 1-in. depth		
D93U	20	14.9	31	18
D93N	20	17.5	35	21
D93S	60	24.7	41	31
D93Q	60	28.8	63	36
QDP6	120	42.2	99	49
ND37	120	41.0	97	47
ND53	120	39.1	100	46
		Irradiated in ORR,[a] 1/4-in. depth		
ND24	120	19.0	40	8
ND26	120	19.7	65	8
ND61	120	20.0	60	8
ND67	120	22.7	65	7
ND66	120	19.1	40	5

[a] $\phi_N = 9.59 \times 10^{12}$ neutrons/cm^2·s; $\Phi = 2.43 \times 10^{18}$ neutrons/cm^2 (>1 MeV).

respectively. As shown, the TS orientation exhibited a ΔNDT of 100°F while the TL orientation shifted 85°F.

All of the data shown for A212 grade B are based only on specimens that were given the full stress-relief heat treatment of 950°F for 51 h. Although the irradiated data were obtained at only a couple of test temperatures, the results indicate that the irradiated Charpy curves have slopes similar to those for the unirradiated data.

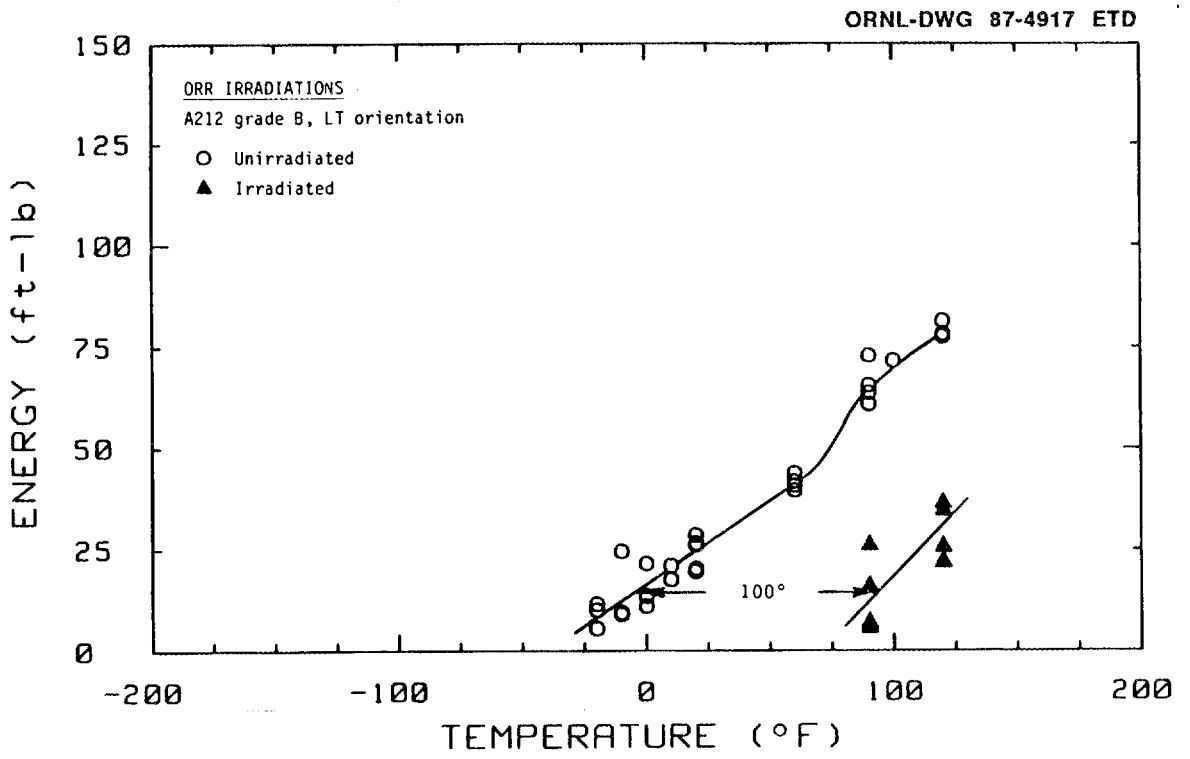

Fig. D.26. Charpy properties of A212 grade B HFIR vessel steel in LT orientation, unirradiated and irradiated in the ORR.

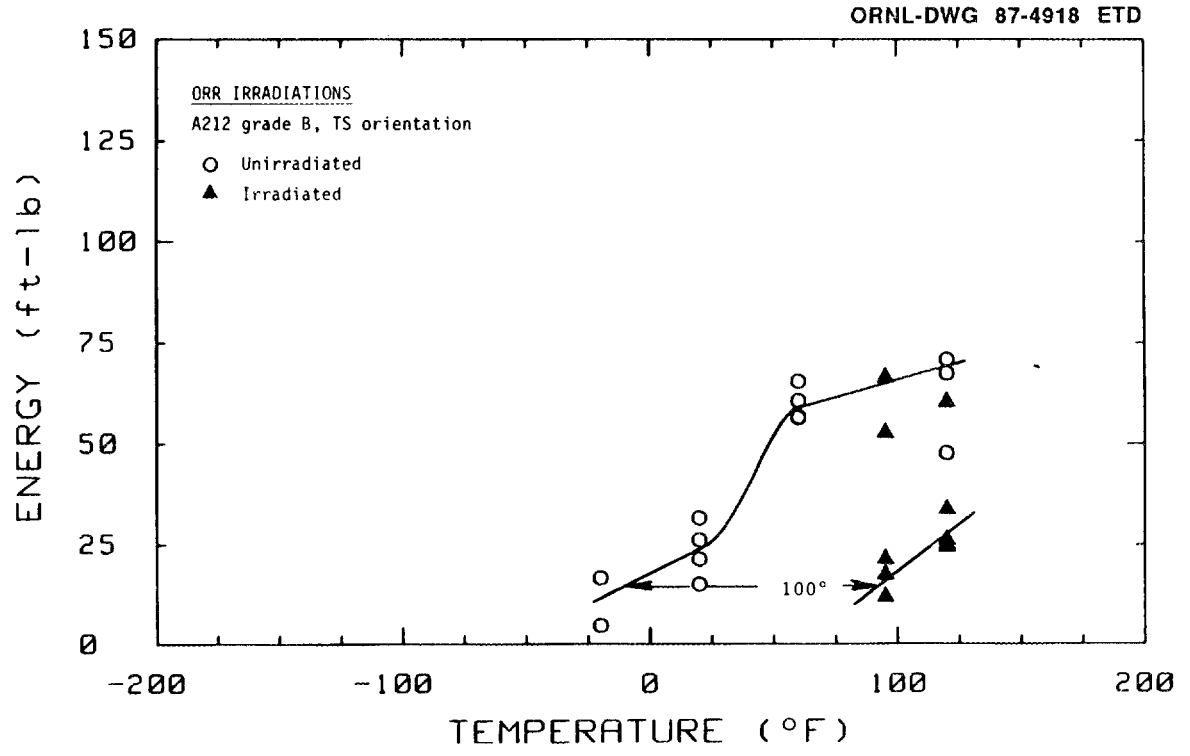

Fig. D.27. Charpy properties of A212 grade B HFIR vessel steel in TS orientation, unirradiated and irradiated in the ORR.

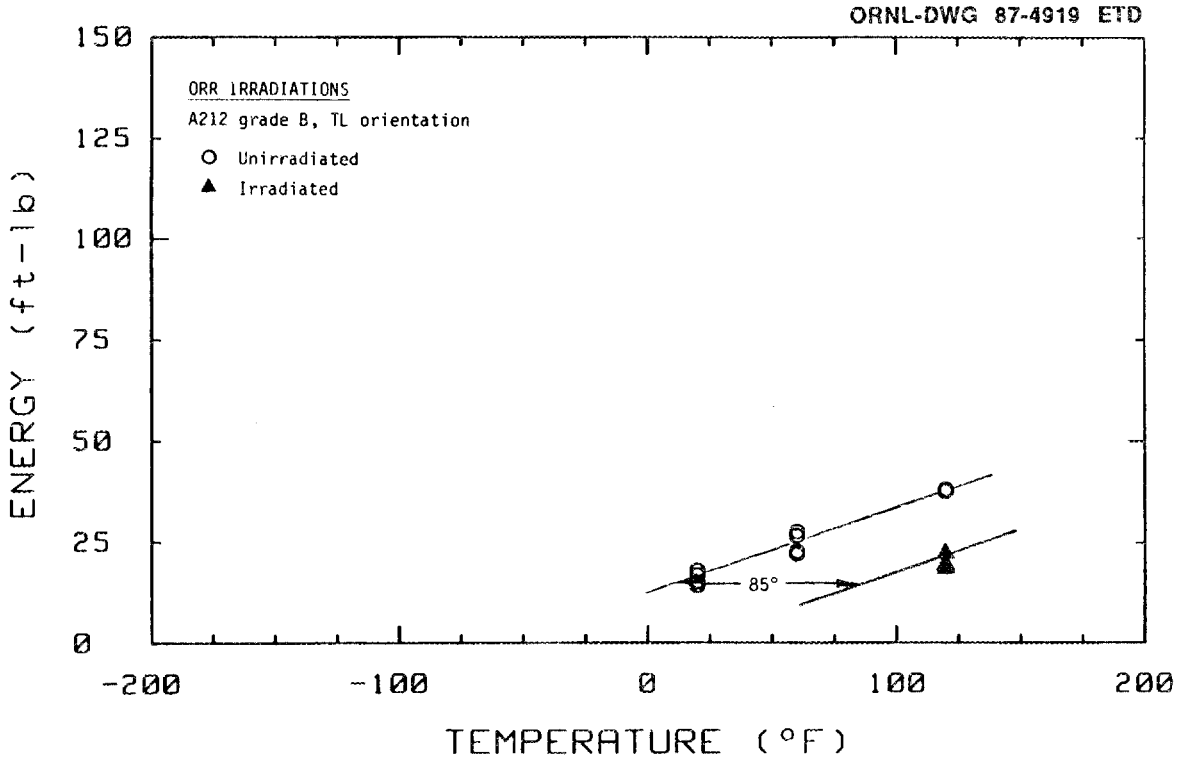

Fig. D.28. Charpy properties of A212 grade B HFIR vessel steel in TL orientation, unirradiated and irradiated in the ORR.

Figure D.27 for the TS orientation shows a relatively large degree of scatter compared with the A212 grade B in both the LT and TL orientations. No mechanical problems with the tests were identified to explain the observations, and they were statistically analyzed using outlier tests.

Outlier detection determines whether one or more observations do not come from a common distribution. Most tests are sensitive to the assumed underlying distribution, usually the normal distribution. Concluding that an observation is an outlier does not necessarily mean that it should be removed from the data, only that it should be given individual consideration. Unless it can be demonstrated that an observation was improperly measured or reported, it should remain a part of the data. Depending on the questions being asked, an outlier deemed real need not be part of the analysis; however, its existence must be noted.

The outlier tests were applied to three observations at two temperatures on specimens from the A212 grade B (TS). The 60.1-J value at 120°F was determined to be an outlier at the 0.05 significance level. However, the two values (66.2 and 52.5 J) at 95°F were not found to be outliers. In the latter case, when there are a total of only five values, it is difficult to know which group contains the outliers, and the tests reflect this uncertainty. In determining the ΔNDT, the three analyzed data points were not used to determine the mean energy values. That is a conservative approach because all three values were high in their respective data sets.

Close examination of the three suspected specimens did reveal small cracks normal to the fracture surfaces. Those small cracks impede the fracture process in the primary plane of fracture and undoubtedly cause an increase in the energy required to fracture the specimen.

Figures D.29 and D.30 show results for the seam-weld reproduction and the nozzle qualification weld; the data are tabulated in Tables D.19 and D.20, respectively. In each case, 15 irradiated CVN specimens were tested to define the ΔNDTs. As Fig. D.29 shows, two data points are far outside the distribution of the other four specimens tested at the same temperature. No mechanical problems with the test in either case were identified to explain the observations, and the two observations were tested using two outlier tests. Both the high value at 30°F and the low value at 120°F were found to be outliers at the 0.05 significance level or better. However, again adopting a conservative approach, the high value at 30°F was not included in calculating the mean energy while the low value at 120°F was used to calculate mean energy. Even if the low value at 120°F was not included in the analysis, the ΔNDT determination changes by only a couple of degrees. The figures show that the two weld metals have essentially the same sensitivity to irradiation under the conditions used. The seam-weld reproduction exhibited a ΔNDT of 85°F; that for the nozzle qualification weld was 80°F.

Using the technique discussed in Sect. D.5.5 and shown graphically in Fig. D.25, the results from the ORR irradiations were plotted as shown

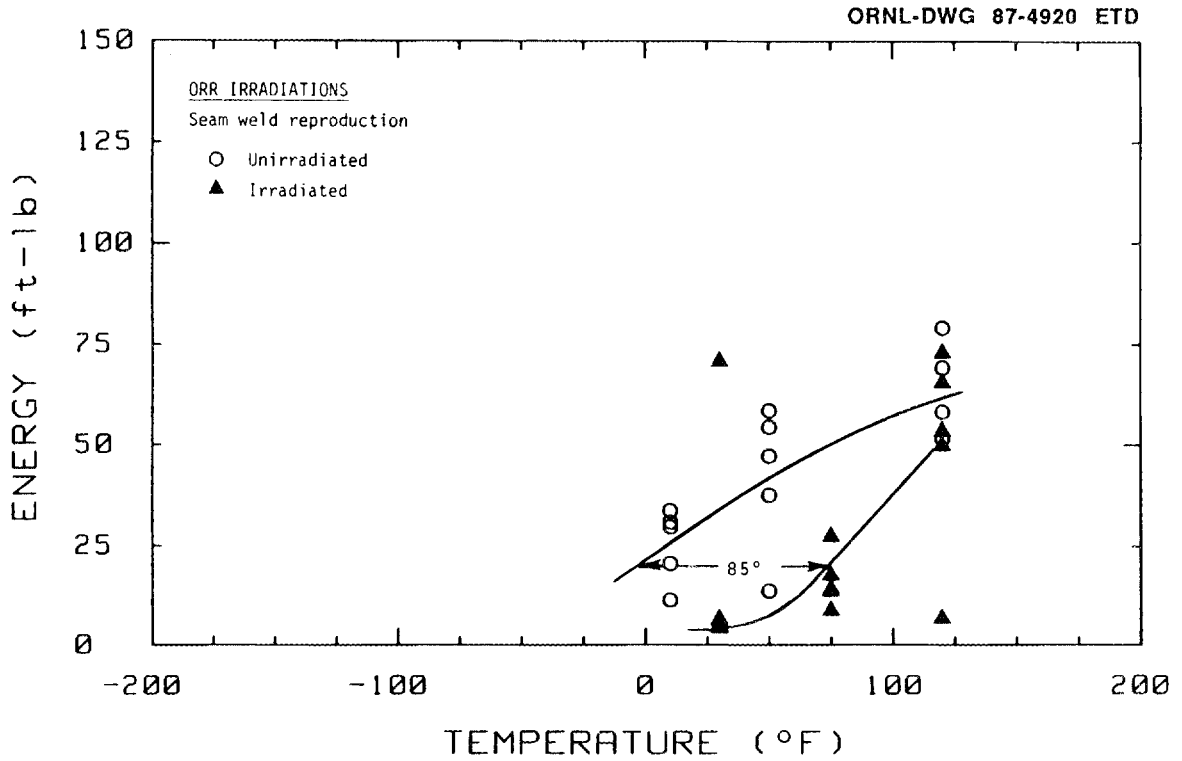

Fig. D.29. Charpy impact properties for HFIR seam weld reproduction, both unirradiated and irradiated in the ORR.

Table D.19. Charpy impact test results for HFIR seam weld reproduction following 51-h PWHT at 950°F

Specimen No.	Test temperature (°F)	Fracture energy (ft-lb)	Fracture appearance (% shear)	Lateral expansion (mils)
		Unirradiated		
HFE7B	10	33.7	14	28
HFE8C	10	11.3	22	15
HFD4B	10	20.6	11	18
HFD4C	10	30.9	32	32
HFF11C	10	29.7	25	28
HFE8B	50	47.2	37	39
HFF9C	50	54.3	59	48
HFF10B	50	37.5	24	31
HFF10C	50	58.4	61	47
HFF9B	50	13.6	21	18
HFE5B	120	51.6	50	41
HFE7C	120	69.1	80	61
HFE4C	120	79.0	91	66
HFD5B	120	58.1	60	49
HFF11B	120	51.4	65	46
		Irradiated in ORR[a]		
HFE1B	30	6.3	0	0.3
HFE4B	30	4.4	5	0.1
HFE1C	30	70.5	65	32.0
HFE2C	30	5.7	5	0.1
HFE5C	30	4.0	5	0
HFD1B	75	8.4	40	1.3
HFD1C	75	17.4	40	4.5
HFD5C	75	13.9	35	3.1
HFD6B	75	13.3	20	1.1
HFD6C	75	27.1	30	9.9
HFE2B	120	6.4	20	0.4
HFE3B	120	49.6	65	28.5
HFE6B	120	53.2	40	21.8
HFE3C	120	72.6	80	40.2
HFE6C	120	65.2	50	35.8

[a] $\phi_N = 9.59 \times 10^{12}$ neutrons/cm^2·s; $\Phi = 2.43 \times 10^{18}$ neutrons/cm^2 (>1 MeV).

Table D.20. Charpy impact test results for weld metal from HB2/HB3 nozzle weld qualification block

Specimen No.	Test temperature (°F)	Fracture energy (ft-lb)	Fracture appearance (% shear)	Lateral expansion (mils)
		Unirradiated		
QW274	−100	3.8	4	2
H2W11	−100	3.1	5	3
H2W31	0	22.3	26	16
H2W14	0	25.3	20	25
QW233	0	12.0	23	13
QW273	0	16.4	16	13
QW252	0	13.0	18	14
QW212	0	17.7	25	18
QW221	50	34.5	30	31
QW271	50	69.3	52	51
QW261	50	27.9	43	30
QW241	50	64.6	49	49
QW213	120	86.4	82	68
H2W21	120	81.2	78	64
H2W32	120	84.7	80	64
QW232	120	93.6	81	73
H2W22	150	74.8	81	58
		Irradiated in ORR[a]		
QW262	50	6.7	15	0.3
QW251	50	5.1	5	0.1
QW211	50	6.8	20	0.3
H2W12	90	20.7	35	5.7
H2W13	90	26.0	40	1.3
QW281	90	13.5	40	6.9
QW282	90	35.2	45	12.5
QW283	90	14.2	45	3.4
QW263	120	42.6	55	20.8
QW242	120	20.3	50	5.9
QW243	120	41.7	60	20.8
QW222	120	56.2	65	24.0
QW231	120	48.7	70	26.6
H2W33	170	52.3	80	32.6
QW223	170	95.2	95	47.0

[a] $\phi_N = 9.59 \times 10^{12}$ neutrons/cm^2·s; $\Phi = 2.43 \times 10^{18}$ neutrons/cm^2 (>1 MeV).

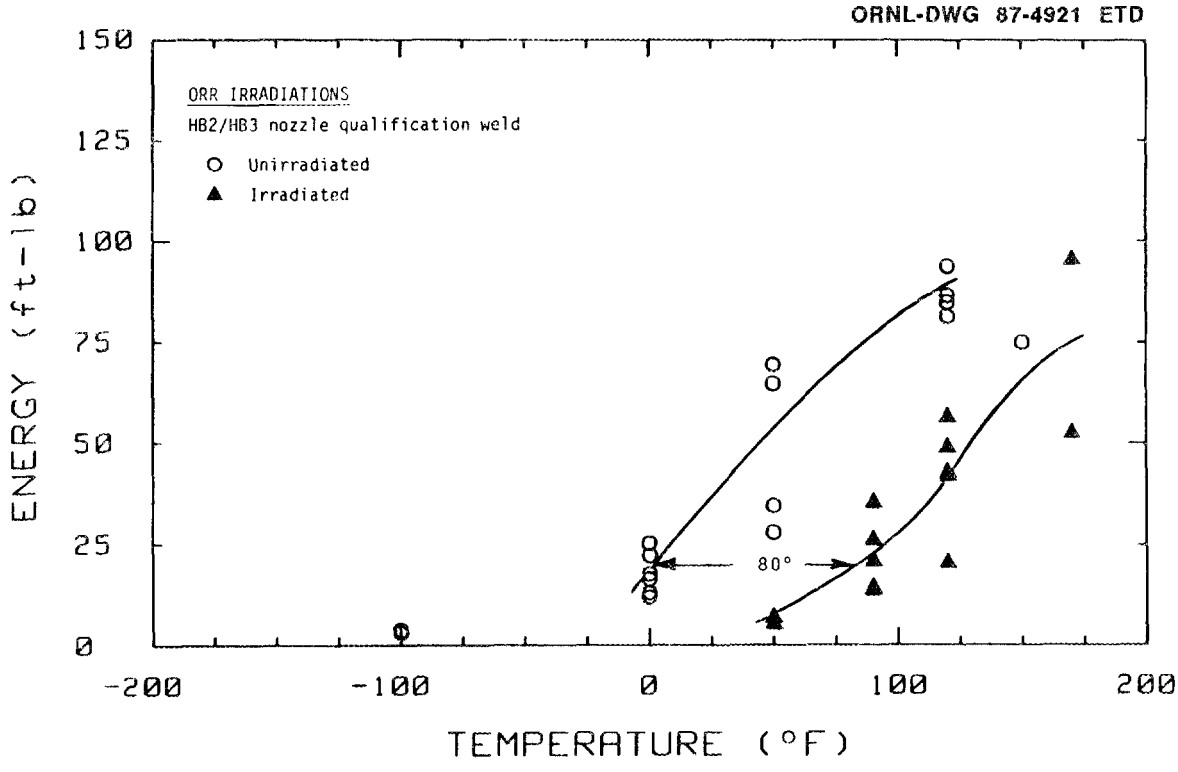

Fig. D.30. Charpy impact properties for unirradiated HB2/HB3 nozzle weld metal and HB2/HB3 nozzle weld metal irradiated in the ORR.

in Fig. D.31. The ΔNDT of 100°F for A212B (LT) was plotted on the curve of ΔNDT vs EFPY from the HFIR surveillance program. As discussed earlier, that indexes the ORR results to the time in HFIR required to attain a ΔNDT of 100°F for the A212B (LT). Because all of the other materials were irradiated in ORR to the same neutron fluence as the A212B (LT), the ΔNDT values were plotted, as shown, at the same value of EFPY. A linear curve was then constructed for each material from the origin.

Thus, under similar irradiation conditions and at the same exposure level, the HFIR vessel welds exhibit lesser decreases in Charpy toughness than does the A212 grade B steel. Regarding orientation effects in the pressure vessel shell, the TS and TL orientations showed equal or less ΔNDT than did the LT orientation used in the HFIR surveillance program.

The curves in Fig. D.31 were then used to translate to the ΔNDT value for each material in the HFIR as of 1986 (i.e., 17.5 EFPY). It is important to realize that the ΔNDT values so determined assume that each material in HFIR has been exposed to the same fluence as the A212B (LT) surveillance specimens. The actual exposures in HFIR vary, of course, and the analyses in Chap. 5 of the report account for the differences in exposure at each specific location.

Table D.21 summarizes the results of the ORR irradiations and the surveillance program. The damage rate values were determined from linear

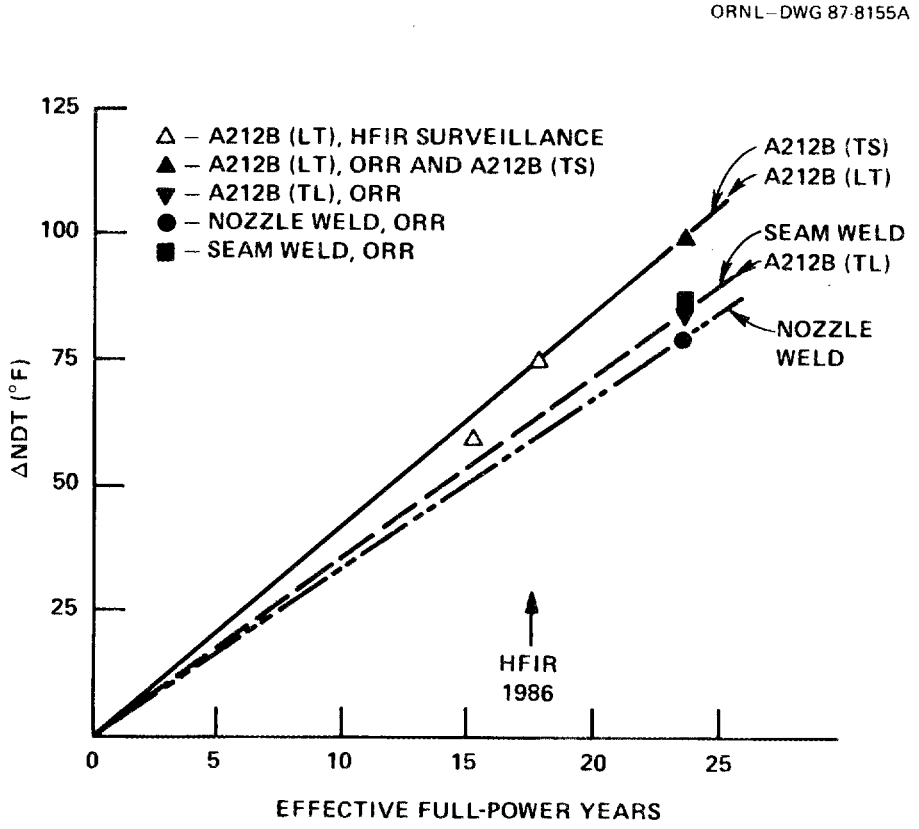

Fig. D.31. Results for HFIR pressure-vessel materials irradiated in ORR, indicating the way in which HFIR surveillance data were used to index the ORR results to HFIR. All materials in ORR were irradiated to the same fluence, and curves are linear fits through the origin.

fits to the ΔNDT vs EFPY data. In the case of the A212B and the welds irradiated in ORR, the curve passes through the origin as a conservative construction because of sparse data. For the nozzle materials, the surveillance data were sufficient (Fig. D.6) to fit linear curves that do not pass through the origin. As discussed earlier, the results presented in Table D.21 for the ORR irradiations must be corrected to the fluence in the HFIR at the specific location of interest by using the fluence of the A212B (LT) surveillance specimens from position 8 of key 7 as the reference (as shown in Appendix E, the fluence for position 8 of key 7 was 1.53×10^{17} neutrons/cm^2). The use of linear fits to the ΔNDT data is the current technique of choice primarily because of uncertainties regarding damage of these materials at 120°F.

Section D.6 includes a discussion of the use of nonlinear analyses (e.g., square root dependence of ΔNDT on fluence). That discussion strongly suggests the use of a nonlinear dependence model based on comparison with hardening models. For 3 EFPY of operation at ~85 MW, a

Table D.21. Summary of irradiation effects on HFIR pressure-vessel materials

Material	Unirradiated NDT (°F)	RT_{NDT}[a] (°F)	ΔNDT (°F)		Damage rate (°F/EFPY)
			ORR	HFIR 17.5 EFPY	
ORR irradiations					
A212B (LT)	−5	20	100	75	4.28
A212B (TL)	10	15[b]	85	64	3.64
A212B (TS)	−5	0	100	75	4.28
A212B (LS)	−10	−10	[c]	75[c]	4.28
Nozzle weld	0	10	80	60	3.42
Seam weld	−5	60	85	64	3.64
Surveillance data					
A212B (LT)	−5	20		75	4.28
A105 II	−80	−40		63	2.96
A350 LF3 (HB2)	−110	−110		117	5.94
A350 LF3 (HB3)	−80	−78		113	5.09

[a]Determined from T_{50} − 60°F, where T_{50} is the temperature at which the mean Charpy energy less one standard deviation is equal to 50 ft-lb.

[b]50 ft-lb not achieved in this orientation; RT_{NDT} determined from the temperature at which 0.035-in. lateral expansion is achieved less 60°F.

[c]Not irradiated in ORR; assume ΔNDT = ΔNDT of A212B (LT) and A212B (TS).

linear dependence predicts a ΔNDT for the A212B (LT) of ~11°F; a square root dependence predicts a ΔNDT of ~5°F. For short-term extension of reactor operation, the differences are not significant; however, for longer-term life extension (e.g., 10 years), the differences would be significant, and linear extrapolations would tend to be conservative. In the absence of a surveillance program, the choice of model would be important; however, because the operation plan for HFIR incorporates a surveillance program, periodic testing of irradiated specimens will provide direct evidence of the embrittlement, and extrapolation can always be short term, using all available data. Section D.7 describes the surveillance plan concept for reoperation.

D.6 RADIATION EFFECTS AND MECHANISTIC STUDIES

(A. F. Rowcliffe, G. R. Odette,* K. Farrell, D. N. Braski, M. K. Miller, S. Spooner,† C. A. Baldwin, J. Bentley, and P. J. Maziasz)

D.6.1 Introduction

The assessment of the structural integrity of the HFIR pressure vessel is based upon fracture mechanics procedures that utilize measurements of the energy absorbed in CVN tests. Low-temperature irradiation of pressure-vessel steels results in a decrease in the energy absorbed in a CVN test and a transition from ductile to brittle fracture, which occurs at progressively higher temperatures as the irradiation fluence increases. This phenomenon is generally thought to be due to the formation of small, stable clusters of point defects or solute atoms that impede dislocation movement and cause an increase in the yield stress. The radiation effects studies described here are concerned with a number of fundamental questions, including (1) the nature of the radiation-induced defects, their mechanism of formation, and their thermal stability; (2) the effect of damage rate on the nature and number of defects formed; and (3) the effect of damage level and damage rate on yield stress. These fundamental issues have a strong bearing on several engineering issues:

1. relating the HFIR surveillance data to the existing data base on pressure-vessel steels,
2. extrapolation of the HFIR surveillance data to predict shifts in ductile-to-brittle transition temperature (DBTT) at higher fluences, and
3. the application of DBTT data obtained from short-term irradiation experiments of seam and nozzle weldments in the ORR to assess the condition of weldments in the HFIR vessel.

It would require a major research effort to address these fundamental questions comprehensively; some have been under investigation for almost 20 years. Nevertheless, even partial answers can have a significant influence on the engineering issues. The ensuing sections describe the results of a brief experimental study in the radiation effects area. The current state of knowledge of low-temperature radiation effects is surveyed, and the results on the HFIR materials are discussed in the context of this survey. Finally, several of the engineering issues are discussed in light of these studies.

---

*Consultant, Department of Chemical and Nuclear Engineering, University of California, Santa Barbara.

†Solid State Division, ORNL.

D.6.2 Experimental Results

D.6.2.1 Radiation dose units

The dosimetry methods used for estimating neutron fluxes are described in Appendix E of this report. Neutron fluxes are reported here and in much of the open literature in units of $n \cdot cm^{-2} \cdot s^{-1}$ ($E > 1.0$ MeV). However, it is well established that structural damage in materials is dependent on neutron energy. It is, therefore, necessary to use a neutron spectrum-independent damage parameter to correlate property changes produced in different neutron spectra. The internationally accepted damage dose unit is the number of dpa, and methods for calculation are described in the *ASTM Standard Practice* E 693-79. The results of dpa calculations for various positions at the HFIR pressure vessel and at the A9 position in the ORR core are given in Appendix E. These calculations were carried out for neutron energies down to 0.1 MeV and show that the spectra in the two reactors at these locations are approximately equivalent in terms of producing displacements per unit of fluence. For the ORR A9 location, the ratio $\frac{\text{dpa/s}}{\phi(E > 1.0 \text{ MeV})}$ is 1.39×10^{-21}. The average value for the various HFIR surveillance positions is 1.49×10^{-21} (i.e., for a given fluence measured in terms of $E > 1.0$ MeV, the spectrum at the HFIR pressure vessel produces ~7% more displacements than are produced at the ORR A9 location). Thus, the choice of exposure unit for comparing HFIR data with ORR data will have no significant effect on the outcome — dpa or $\phi(E > 1.0$ MeV) will serve equally well. The use of the dpa unit will undoubtedly reduce the uncertainties in making correlations with literature data from various materials test reactors (MTRs). However, the necessary dpa calculations have not been done in most instances, and for the present we will continue to use the neutron flux ($E > 1.0$ MeV) as a damage parameter.

The flux of neutrons with $E > 1.0$ MeV at the ORR A9 location is $\sim 2.2 \times 10^{13}$ $n \cdot cm^{-2} \cdot s^{-1}$ (i.e., comparable to the fluxes in other MTRs that have been used in various countries to investigate pressure-vessel steel embrittlement). On the other hand, neutron fluxes ($E > 1.0$ MeV) at the various surveillance specimen locations in the HFIR range from 2.2×10^{8} to 1.2×10^{9} $n \cdot cm^{-2} \cdot s^{-1}$. These low fluxes represent a unique environment for the radiation effects point of view because damage levels have only reached $\sim 2 \times 10^{-4}$ dpa after 17 years of exposure.

D.6.2.2 Scanning electron microscopy (SEM) (D. N. Braski)

The fracture surfaces of broken CVN surveillance specimens of both A212B and A350LF3 steels removed from HFIR and tested in 1986 were examined using a remotely operated SEM. Unirradiated specimens were also examined. Both irradiated and unirradiated specimens exhibited predominantly dimpled rupture in specimens tested in the upper-shelf region. In the lower-shelf region, fracture occurred predominantly by transgranular cleavage. In the transition region, fracture occurred by a mixture of the two mechanisms. Typical micrographs are shown in Fig. D.32. There was no evidence for intergranular fracture in the irradiated materials.

ORNL PHOTO 1319–88

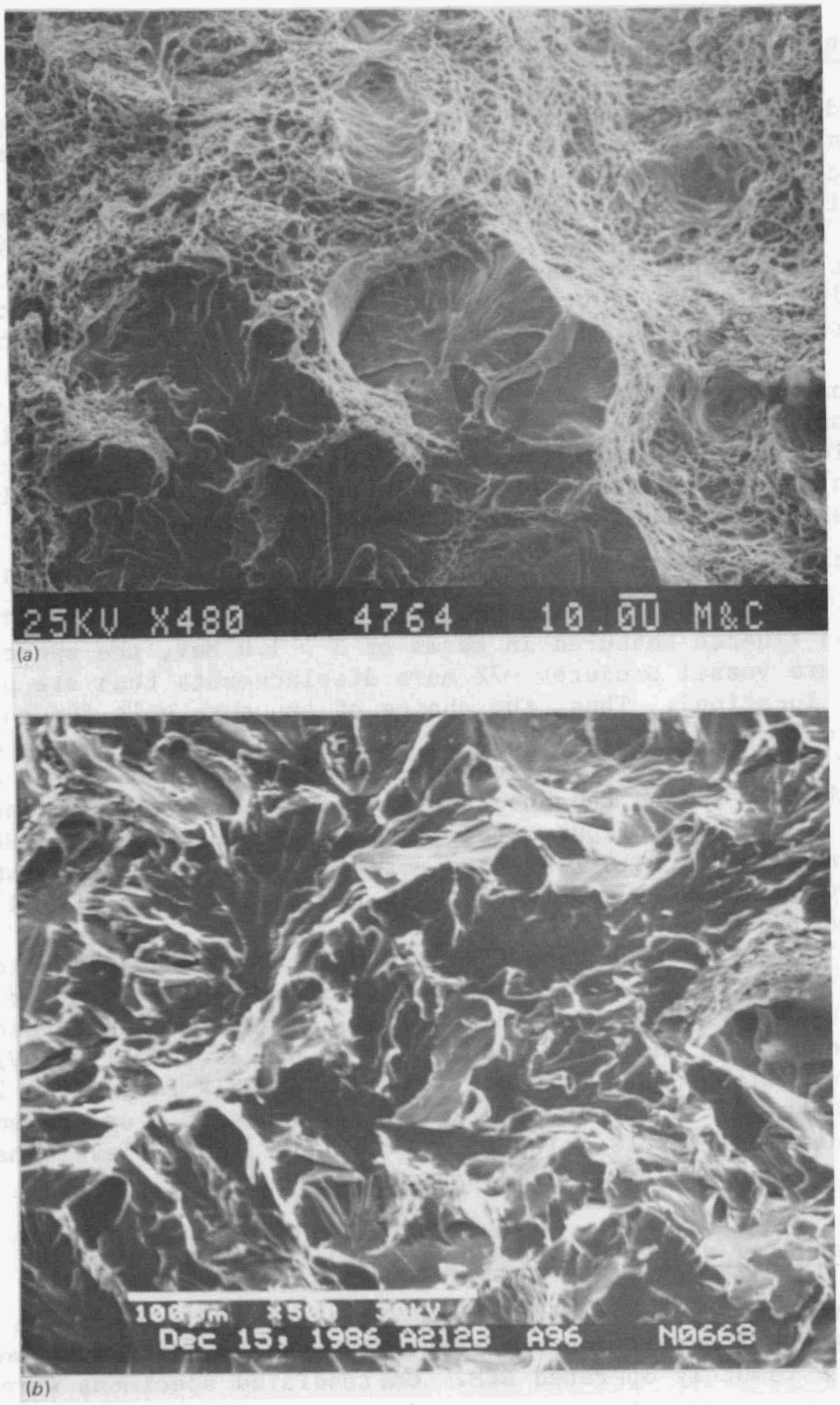

Fig. D.32. Scanning electron micrographs of fractured A212B Charpy specimens. (*a*) Unirradiated, specimen A83 tested at 33°C, 53.4 J, showing predominantly dimpled rupture with some transgranular cleavage fracture, (*b*) irradiated to 1.3×10^{17} neutrons/cm^2, specimen A96, tested at 36°C, 8.4 J, showing predominantly transgranular cleavage and some dimpled rupture.

Thus, it is very unlikely that radiation-induced segregation of minor elements or transmutants is playing a significant role in weakening interfaces and lowering the critical stress for crack propagation. The fractography results are entirely consistent with the hypothesis that the increased tendency toward cleavage fracture induced by irradiation to ~1.3 × 10^{17} n/cm^2 (E > 1.0 MeV) is primarily the result of radiation hardening.

D.6.2.3 Transmission electron microscopy (TEM) (J. Bentley and P. J. Maziasz)

Examination of HFIR surveillance specimens of both A212B and A350LF3 steels was carried out using a Philips EM430T analytical microscope. The initial precipitate morphology and dislocation structure of both steels were virtually unchanged after irradiation at 60°C (140°F) to ~1.3 × 10^{17} n/cm^2. Microchemical analysis of phases was not carried out because the likelihood of any significant changes involving long-range diffusional transport at 60°C is extremely small. Furthermore, changes in the nature of microstructural features on a scale >10 nm are unlikely to have any bearing on the observed property changes in these materials. Careful imaging of the matrix failed to reveal any defects that might account for the radiation hardening. Resolution was somewhat impaired by the ferromagnetic nature of the materials and the presence of persistent oxide films on foil surfaces. Because defects could not be detected, it was concluded that the defects responsible for the hardening must be smaller than 2 nm in diameter if they are in the form of dislocation loops or cavities and smaller than 4 to 5 nm in diameter if they are in the form of solute clusters.

D.6.2.4 Field-ion atom probe (M. K. Miller)

Preliminary atom probe field-ion microscopy has been carried out on unirradiated and irradiated A212B surveillance samples by using the ORNL energy-compensated atom probe. Two types of analyses were undertaken: (1) a series of field-ion micrographs were taken during field evaporation and (2) a series of atom probe composition profiles were collected through the ferrite matrix. Neither set of measurements revealed any evidence for point defect clusters, precipitates, or solute clusters in the ferrite matrix. It was found, however, that the copper was distributed very inhomogeneously in the ferrite matrix and ranged from 0.03 to 0.12 at. %. Examination of the ferrite-cementite interface did not reveal any visual evidence of segregation; however, atom probe chemical analyses to verify this observation were not carried out. Because these preliminary measurements failed to detect any radiation-induced defects, it is concluded that the observed hardening must be caused by defects that either are <0.5 nm in size, present at a number density below 10^{18} cm^3, or distributed very inhomogeneously. Because of the low irradiation temperature and low damage level, it is speculated that the most probable defect size range in these materials is 0.5 to 2 nm in diameter at a concentration level of ~10^{17} n/cm^2. Detection and identification of such defects would probably require 3 to 4 months of instrument time for a single sample.

D.6.2.5 Small-angle neutron scattering (SANS) (S. Spooner)

A preliminary examination of irradiated and unirradiated surveillance specimens of A212 grade B, A105 grade II, and A350 grade LF3 were carried out using the 10-m SANS machine at ORR. Data were collected for 2 h on each sample, and the corrected data were calibrated in absolute cross-section units. Scattering differences among the three types of steel were easily seen. Differences among samples within a steel class were barely outside the statistical error bars in these short experiments.

The scattering arising from irradiation effects is expected to occur at relatively large scattering angles and with very low intensity (because of point defects or alloy element clusters). Variations in background scattering are a significant fraction of the expected scattering signal. In addition, the scattering angle of the machine only begins to cover the range in which the scattering can be readily observed (recent studies on similar material at Harwell suggest this conclusion).

The use of applied magnetic fields will be important in the separation of different sources of scattering in these steels. Preliminary observations of magnetic field effects were made on an unirradiated sample of A212 grade B. A small degree of field-induced scattering anisotropy was seen and resembled a superparamagnetic behavior rather than the expected ferromagnetic response. The field was limited to 4000 gauss, so it appears that these materials will require a much higher field to achieve saturation. Magnetization measurements may be needed to determine the field requirement.

The Guinier analysis of small-angle scattering is the first and simplest line of attack in the interpretation of the data but is fraught with pitfalls and limitations. Nevertheless, the following statements are offered. All of the steel samples, irradiated and unirradiated, contain a significant fraction of scatterers of ~3 nm. Scattering at the smallest angles suggests the presence of scatterers in excess of 25 nm in both irradiated and unirradiated samples. Using the ORR facilities, it was not possible to detect any significant differences between irradiated and unirradiated materials. This suggests that the radiation-induced defects responsible for hardening are <3 nm in diameter. Detection and analyses of such defects require SANS facilities (such as those at HFIR) that can produce a more intense source of neutrons and the capability of measuring larger scattering angles.

D.6.2.6 Annealing experiments (D. N. Braski and K. Farrell)

Direct observation of the radiation damage in the HFIR surveillance materials is difficult because of the small sizes of the defects involved. An indirect approach is to study the annealing response of the damage. The kinetics of the annealing process should characterize the thermal stability of the damage structure and might provide a measure of the activation energy of the recovery process from which the nature of the basic defect responsible for radiation hardening could be deduced. Such annealing studies can also provide some guidance to consideration of the feasibility of restoring the original properties of the HFIR pressure vessel by annealing treatments.

The annealing study utilized small coupons that were cut with a slow-speed diamond saw from a broken A212B CVN surveillance specimen (#A140). The specimen had received a neutron fluence of 1.3×10^{17} n/cm^2. Anneals were carried out for 1 h in air at temperatures in the range of 204 to 510°C (400 to 950°F). Several longer-term anneals were carried out to 204 and 260°C (400 and 500°F). Hardness measurements were made at room temperature with a Vickers diamond pyramid indenter using a 500-g load. The results are shown in Table D.22 and Fig. D.33. Each datum point represents the average of five hardness measurements. For any given specimen, there is a large scatter in hardness values (of the order ±10 dph). Because of the duplex nature of the microstructure, varying proportions of the ferrite and the relatively hard pearlite are sampled by

Table D.22. Hardness data for A212B HFIR surveillance material

Annealing		1	2	3	4	5	Average
Time (h)	Temperature [°C (°F)]	(DPN)	(DPN)	(DPN)	(DPN)	(DPN)	(DPN)
		Unirradiated					
None		176	173	163	172	178	172
1	288 (550)	170	161	180	173	170	171
1	510 (950)	174	170	179	175	169	173
1	510 (950)	164	173	176	170	168	170
		Irradiated					
None		185	179	183	194	188	186
None		191	172	173	180	189	181
None		179	181	181	177	172	178
None		170	185	192	179	184	182
1.5	148 (300)	183	184	188	183	189	185
1	204 (400)	174	175	167	174	185	175
1	260 (500)	193	173	174	167	177	177
1	288 (550)	160	167	164	169	171	166
1	316 (600)	183	169	178	165	167	172
1	343 (650)	173	161	163	172	157	165
1	371 (700)	173	165	161	152	173	165
1	421 (790)	167	162	168	161	172	166
1	510 (950)	166	169	156	162	172	165
1.5	204 (400)	178	175	170	173	196	178
4	204 (400)	178	176	179	180	173	177
7	204 (400)	172	174	170	163	182	172
24	204 (400)	176	179	185	184	192	183
4	260 (500)	156	182	169	177	162	169
7	260 (500)	180	181	175	181	168	177
24	260 (500)	170	177	167	166	182	172

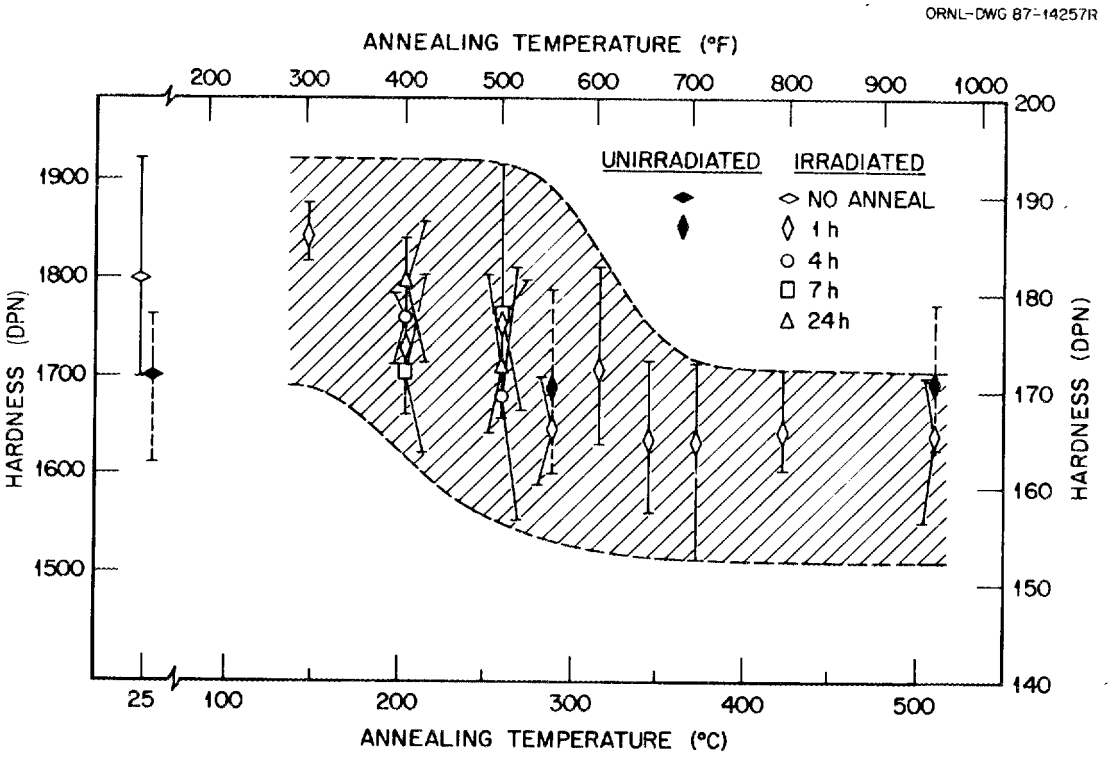

Fig. D.33. Annealing behavior of A212B HFIR surveillance material irradiated to a fluence of 1.3×10^{17} neutrons/cm^2 (E > 1.0 MeV).

successive indentations. The stringers of inclusions also interfere with making consistent hardness measurements. Irradiation to 1.3×10^{17} n/cm^2 caused an increase in the room temperature hardness of ~6%. Annealing of the damage begins during 1 h at 300°C (572°F) and appears to be complete after 1 h at ~375°C (707°F). Only partial recovery of damage occurs after a 24-h anneal at 200°C (392°F). Similar annealing treatments carried out on unirradiated archive material produced no change in hardness. Thus, the hardness changes observed in the irradiated material are indeed due to the annealing of radiation damage. This study was intended to be only preliminary in nature. If annealing the radiation-affected portion of the HFIR vessel becomes an attractive option, then clearly more rigorous annealing studies using tensile and CVN specimens will be required. From the viewpoint of investigating the nature of the defects responsible for hardening, further studies using electrical resistivity measurements are recommended. It would be instructive, for example, to compare the annealing behavior of samples irradiated to the same increment in hardness in HFIR and in ORR.

D.6.2.7 Tensile property measurements (K. Farrell, D. N. Braski, and C. A. Baldwin)

D.6.2.7.1 Introduction. Low-temperature radiation damage results eventually in the development of a population of extended defects in the

form of point defect clusters or dislocation loops. These defects form obstacles to the motion of glide dislocations and produce an increase in the yield stress and a corresponding reduction in ductility. Changes in yield stress provide a more quantitative and reliable measurement of radiation hardening than either CVN impact tests or hardness tests. Tensile tests complement CVN data and provide valuable information for fracture-mechanics analyses.

Tensile property measurements have been carried out on flat sheet specimens cut from HFIR surveillance specimens of A212B irradiated to three fluence levels. In addition, a series of irradiation experiments has been conducted in ORR covering a wide range of fluences to determine the fluence dependence of hardening in both A212B and A350LF3 steels.

D.6.2.7.2 Experiments. Flat tensile specimens, 25 mm long by 0.75 mm thick with a gage width of 1.5 mm and a gage length of 7.5 mm, were cut from halves of broken Charpy impact bars of the A212B and A350 steels used in the construction of the HFIR pressure vessel. The tensile specimens were excised with an orientation in which the long axis of the tensile specimen lay in the long axis of the Charpy bar and the width of the tensile specimen lay in the direction of the Charpy bar notch. The cutting procedure used electrodischarge machining with a thin wire electrode. Charpy bar Nos. A31, A96, and A140 provided tensile specimens of HFIR-irradiated surveillance material of the A212B steel. Charpy bar Nos. A59 and D41 gave unirradiated specimens of the A212B and A350 steels, respectively. The ends (heads) of these tensile specimens might intercept the deformed regions of the Charpy bars, but the gage sections are free of Charpy deformation and should be representative of the irradiated and unirradiated conditions. These tensile specimens were tested in air at 24°C (75°F) by using an in-cell Instron machine operating at a crosshead speed of $8.5 \times 10^{-3} \cdot mm^{-1} \cdot s^{-1}$.

Most of the tensile specimens cut from the unirradiated bars were used in irradiation experiments in the ORR over a range of neutron fluences that encompassed and greatly surpassed those experienced by the HFIR surveillance specimens. These ORR irradiations were made with the specimens in direct contact with the reactor cooling water at a temperature of ~43°C (110°F). To reduce the occurrence of rusting during irradiation, the specimens were first given a caustic anodizing treatment (black oxide coating), as described elsewhere in this report, for Charpy specimens irradiated in ORR. During irradiation the specimens were held in small baskets constructed from aluminum mesh and fitted into a bracket at the end of a rotating arm mounted on a floor post in the reactor pool outside the reactor core. In this assembly, the baskets were positioned at site P8, 10 mm from the core poolside faceplate opposite core lattice position A8 and with the basket centerline 30 mm below the core horizontal midplane. This arrangement had the advantage that baskets could be quickly swung in and out of the irradiation site without disrupting the operation of the reactor; the irradiation exposure time could be as short as a minute.

Following irradiation, the ORR specimens were tensile tested under the same conditions as the specimens cut from the HFIR-irradiated surveillance specimens. Despite the black oxide treatments, those ORR specimens that were irradiated for more than a few days displayed considerable rusting. Unirradiated reference specimens were tested with and without the black coating and showed no significant differences.

Neutron dosimetry analyses were carried out on dosimetry sensors irradiated alongside the tensile specimens. The results were similar to those obtained from dosimetry carried out in conjunction with the irradiation of the CVN specimens in the A9 core location. The flux values ($n \cdot cm^{-2} \cdot s^{-1}$) were determined to be (1) 1.26×10^{13} ($E > 1.0$ MeV), (2) 2.71×10^{13} ($E > 0.1$ MeV), and (3) 9.77×10^{13} (thermal). The displacement rate was calculated to be 1.89×10^{-8} dpa/s.

D.6.2.7.3 Results. The results of the tensile tests on the HFIR surveillance specimens of A212B are shown in Table D.23. The mean of six yield stress measurements made on specimens prepared from two unirradiated archive CVN specimens was 335 ± 11 MPa. Specimens prepared from CVN specimens irradiated in the key 6 and key 7 positions to fluences of 1.3 and 1.5×10^{17} n/cm^2, respectively, gave a mean value of 389 ± 11 MPa for each position. Thus, the radiation-induced hardening of the HFIR vessel raised the yield stress by ~16% at this strain rate. The irradiated material retained a high level of ductility and work-hardening capacity. Uniform elongation was reduced from an unirradiated value of ~16% to a value of ~12%.

Table D.23. Room-temperature tensile properties of A212B HFIR surveillance material

Specimen identity	HFIR position	Fluence, $E > 1.0$ MeV (n/cm^2)	Stress (MPa)			Elongation (%)	
			0.2% Yield	At 7.5% strain	Ultimate	Uniform	Total
A114-1		Unirradiated archive	339	527	561	16	31
A114-2		Unirradiated archive	333	523	561	17	30
A114-4		Unirradiated archive	352	535	566	15	27
A59-15		Unirradiated archive	336	520	550	16	25
A59-1		Unirradiated archive	318	525	534	18	27
A59-12		Unirradiated archive	333	540	571	16	27
A31-1	Key 5, 1983	1.2×10^{16}	331	528	555	16	26
A31-2	Key 5, 1983	1.2×10^{16}	318	507	539	18	29
A31-3	Key 5, 1983	1.2×10^{16}	333	523	547	16	26
A31-4	Key 5, 1983	1.2×10^{16}	334	530	552	14	26
A140-1	Key 6, 1986	1.1×10^{17}	388	549	562	13	22
A140-2	Key 6, 1986	1.1×10^{17}	400	550	570	11	19
A140-3	Key 6, 1986	1.1×10^{17}	384	526	540	11	18
A140-6	Key 6, 1986	1.1×10^{17}	386	529	543	12	20
A96-1	Key 7, 1986	1.3×10^{17}	394	545	568	13	24
A96-2	key 7, 1986	1.3×10^{17}	373	516	537	15	25
A96-3	Key 7, 1986	1.3×10^{17}	392	541	559	13	23
A96-4	Key 7, 1986	1.3×10^{17}	396	541	563	14	26

The specimens taken from the key 5 position in 1983 had accumulated a much lower fluence because of shielding by the ion chamber. This fluence is presently estimated to be ~1.2×10^{16} n/cm^2. Within the uncertainties of the tensile test, no change in yield stress could be detected at this fluence level. CVN tests on surveillance specimens from this position showed an increase in the DBTT of ~11°C (20°F), which is just outside the experimental uncertainty of ±8°C (15°F).

The tensile properties of the A212B and A350LF3 steels following irradiation in ORR are shown in Tables D.24 and D.25, respectively. Tensile properties are plotted against the logarithm of the neutron fluence in Figs. D.34 and D.35. For both steels, there is an incubation regime

Table D.24. Room-temperature tensile properties of A212B archive material irradiated in ORR

Specimen No.	Irradiation time (h)	Fluence, E > 1.0 MeV (n/cm^2)	Stress (MPa)		Elongation (%)	
			0.2% Yield	Ultimate tensile	Uniform	Total
HA-8	0.29	1.3×10^{16}	344	550	15	20
HA-9	0.29	1.3×10^{16}	340	549	18	30
HA-14	3.65	1.7×10^{17}	340	557	16	23
HA-2	16	7.3×10^{17}	381	551	14	23
HA-4	16	7.3×10^{17}	370	551	15	25
HA-3	38	1.7×10^{18}	409	550	13	19
HA-6	72	3.3×10^{18}	441	542	12	21
HA-7	72	3.3×10^{18}	463	573	11	18
HA-5	170	7.7×10^{18}	512	549	7	10
HA-10	384	1.7×10^{19}	528	538	3	5
HA-11	384	1.7×10^{19}	495	519	5	6

Table D.25. Room-temperature tensile properties of A350LF3 archive materials irradiated in ORR

Specimen No.	Irradiation time (h)	Fluence, E > 1.0 MeV (n/cm^2)	Stress (MPa)		Elongation (%)	
			0.2% Yield	Ultimate tensile	Uniform	Total
HB-18	Unirradiated		360	517	19	29
HB-1	0.33	1.5×10^{16}	356	509	20	28
HB-2	0.33	1.5×10^{16}	347	511	19	29
HB-3	3.3	1.5×10^{17}	372	510	20	30
HB-4	3.3	1.5×10^{17}	364	514	18	28
HB-5	38	1.7×10^{18}	451	506	14	21
HB-6	38	1.7×10^{18}	436	515	12	15
HB-7	170	7.7×10^{18}	665	665	0	10
HB-8	170	7.7×10^{18}	593	593	0	5

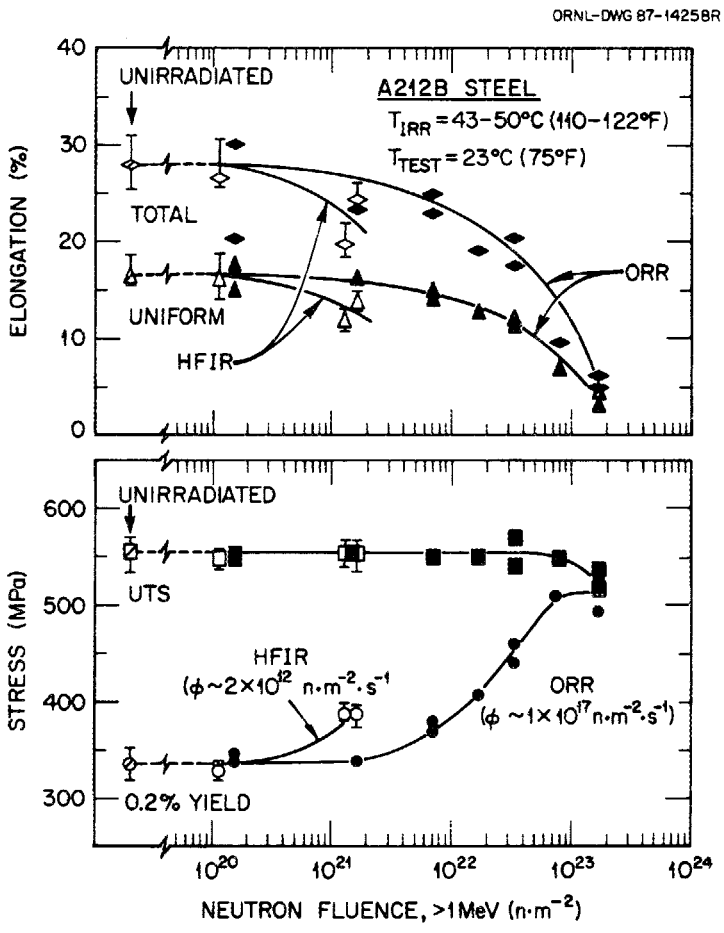

Fig. D.34. Tensile properties of A212B archive material irradiated in the ORR. The tensile properties of the HFIR surveillance material (open symbols) are included for comparison.

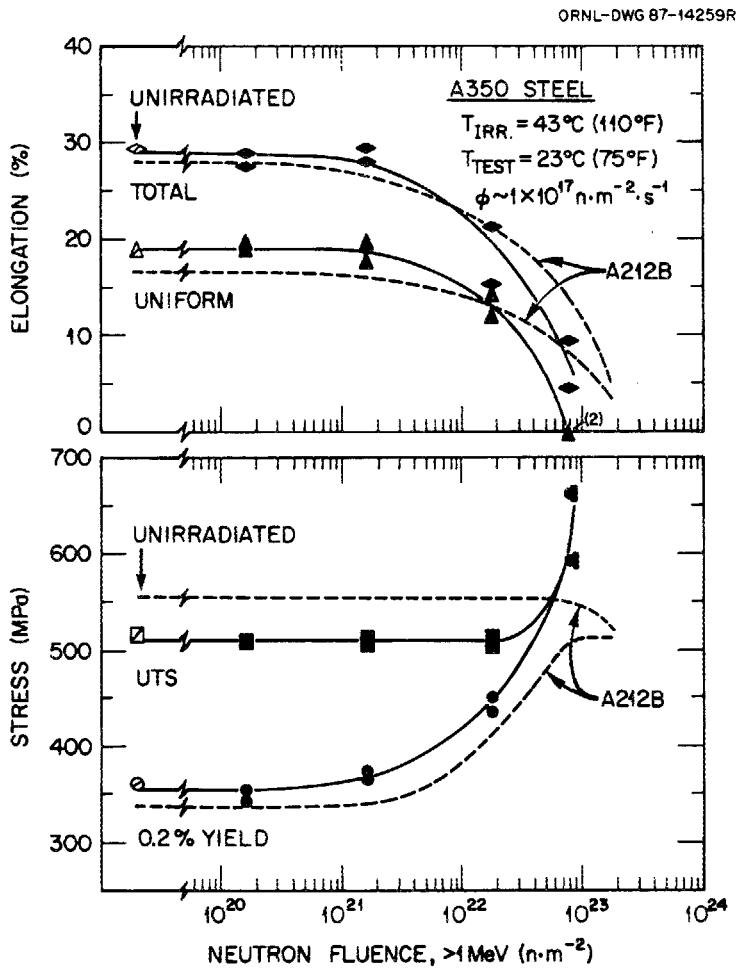

Fig. D.35. Tensile properties of the A350LF3 archive material irradiated in the ORR. The tensile properties of the HFIR surveillance material (open symbols) are included for comparison.

beyond which the yield stress increases with increasing fluence. After a fluence of ~10^{19} n/cm^2, the yield stress and ultimate tensile stress are approximately equal, and the material has no work-hardening capacity. The HFIR surveillance tensile data are included in Fig. D.34 and clearly demonstrate accelerated hardening compared with the ORR data.

D.6.3 Discussion

D.6.3.1 Low-temperature embrittlement behavior

There is a large amount of literature on low-temperature irradiation hardening and embrittlement in iron and low-alloy steels, low temperature being generally defined as below ~150°C (302°F). Fluences for these irradiations cover a range from <10^{16} to >10^{20} n/cm^2. Fluxes are generally in the range of ~10^{12} to 10^{13} n·cm^{-2}·s^{-1} (i.e., four to five orders of magnitude higher than the flux at the HFIR pressure vessel). Because of the extensive amount of literature on the subject, it is possible to summarize only briefly the broad trends in the data as a function of the key variables. Further, note that there are exceptions to the broad trends, and rigorous analysis of the data is often confounded by uncertainties in the key variables or the effects of uncontrolled variables. However, with these caveats, the embrittlement trends are described below, and the recent data obtained from the HFIR and ORR experiments are discussed in terms of these trends.

D.6.3.2 The relationship between hardening and DBTT shift

The yield stress data for the A212B material irradiated in both HFIR and ORR are plotted against the square root of the neutron fluence in Fig. D.36. For the ORR irradiations there is an initial incubation or threshold fluence during which very little change in strength occurs. This is followed by a regime in which yield stress increases in proportion to the square root of the fluence; the increase eventually saturates at a fluence of ~6 × 10^{18} n/cm^2. The HFIR radiation environment produces a dose rate that is lower than in ORR by a factor of ~5 × 10^4. Figure D.36 clearly demonstrates that hardening occurs more rapidly at the lower damage rate. This dose rate effect is also manifested in the DBTT shift data (Fig. D.37). The higher fluence ORR data point is taken from the weld evaluation irradiation experiments conducted in the ORR A9 position as described in Sect. D.5. The lower fluence point is from a preliminary ORR experiment that used a different heat of A212B.

The literature on low-temperature embrittlement often shows an implicit assumption of a direct relationship between irradiation hardening and CVN transition temperature shift. This follows from the theory of Cottrell.[12] For example, low-temperature data for irradiated A302B steels reported by Nichols[13] suggested a proportionality between shifts (ΔT) and yield stress increases ($\Delta\sigma y$) as

$$\Delta T = C\Delta\sigma y \ , \qquad (D.1)$$

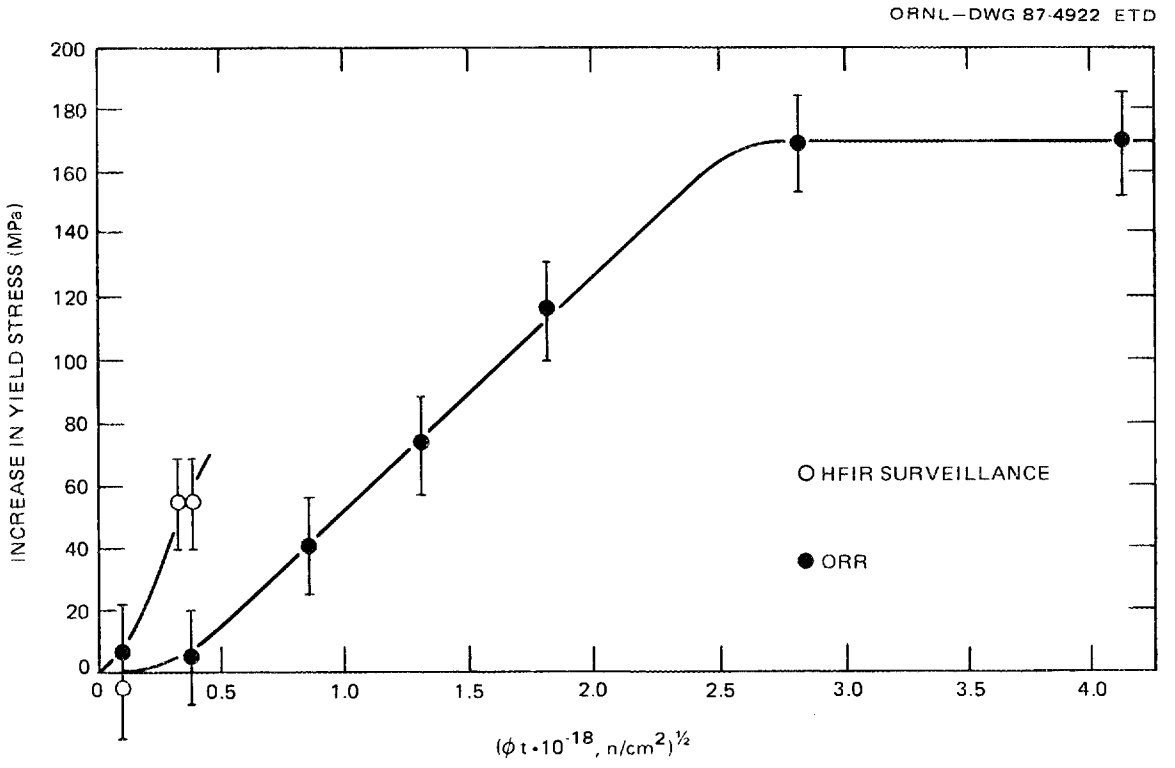

Fig. D.36. Increase in yield stress vs the square root of fluence (E > 1.0 MeV) for A212B HFIR surveillance specimens and for A212B archive material irradiated in the ORR.

where C ~ 0.5°C/MPa. This coefficient is comparable to average values found for plate and only slightly below the average value of ~0.65°C/MPa found for welds irradiated at elevated temperatures.[14] Recently, a study based on quantitative models of the micromechanics of cleavage fracture and a detailed analysis of the high-temperature embrittlement data base showed that the yield stress/shift coefficient is not constant but, rather, depends on the initial CVN properties (i.e., the lower knee elastic fracture temperature and the upper-shelf energy) and the magnitude of the yield stress change.[15] However, the average empirical trends noted above were accurately predicted by the model. Notably, the analysis demonstrated that temper embrittlement (i.e., nonhardening) mechanisms do not play a significant role in embrittlement at 300°C (572°F). Values of the coefficient C for the A212B material can be obtained from Figs. D.36 and D.37 by comparing the increase in yield stress and the corresponding increase in DBTT produced by a given increment of fluence. The value of C for the HFIR surveillance specimens is 0.67, and for the ORR irradiations C is 0.57. The average value of 0.60 agrees well with the empirical averages from the literature noted above and indicates a direct relationship between radiation hardening and DBTT shift.

Examination of the instrumented load-time traces for the CVN impact tests of unirradiated and irradiated (HFIR and ORR) indicated that the

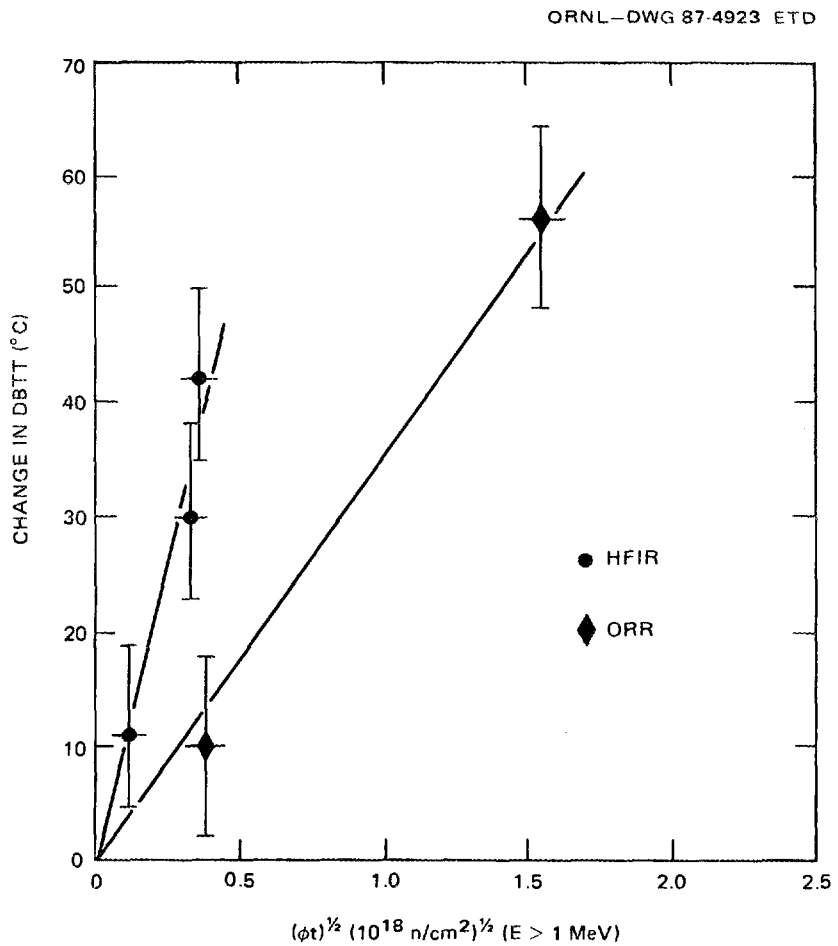

Fig. D.37. Change in DBTT vs the square root of fluence (E > 1.0 MeV) for A212B HFIR surveillance specimens and for archive specimens irradiated in the ORR.

dynamic yield stress increases compare favorably with the yield stress increases measured in static tensile tests and that there is no reduction in the load at the initiation of cleavage fracture. All of these observations, together with the fractographic evidence presented above, strongly support the hypothesis that the measured changes in the Charpy impact properties of the A212B steel are due to the well-documented radiation-hardening mechanism. This appears to be the case for both the HFIR surveillance specimens and the specimens irradiated in the high flux of the ORR.

D.6.3.3 Fluence dependence of hardening and DBTT shift

At low to intermediate fluence, both shift and hardening often can be correlated by an expression in the form[13,16,17]

$$\Delta T(\Delta\sigma y) = A[1 - \exp(-Bf)]^{0.5} , \qquad (D.2)$$

where A sets the magnitude of the hardening/embrittlement, f is the fluence, and B is a saturation parameter. At low fluences where Bf << 1, this reduces to a simple expression

$$\Delta T(\Delta\sigma y) = A\sqrt{f} \ . \qquad (D.3)$$

Other data sets[18,19] also suggest a simple power dependence on fluence with the form

$$\Delta T(\Delta\sigma y) = Af^{p} \ , \qquad (D.4)$$

where p ranges from ~0.15 to 0.5. Some data for relatively pure vacuum-melted iron show a very low fluence (~10^{16}) increment of hardening, which is ascribed to the rapid precipitation of unstable ε carbides; however, this hardening component does not persist at higher fluences.[20]

The magnitudes of A and B vary depending on the material and irradiation conditions. Typical values of A for sensitive steels are ~200 ± 60 MPa for hardening and ~130 ± 25°C for shift. The saturation behavior has been modeled in terms of a local exclusion volume where additional damage cannot be produced. Values of B typically range from ~0.25 to 2. For the neutron exposure regime of primary interest for assessing embrittlement in the HFIR vessel, the simple exponential dependence on fluence should be an adequate representation of the data. Figure D.38 shows a

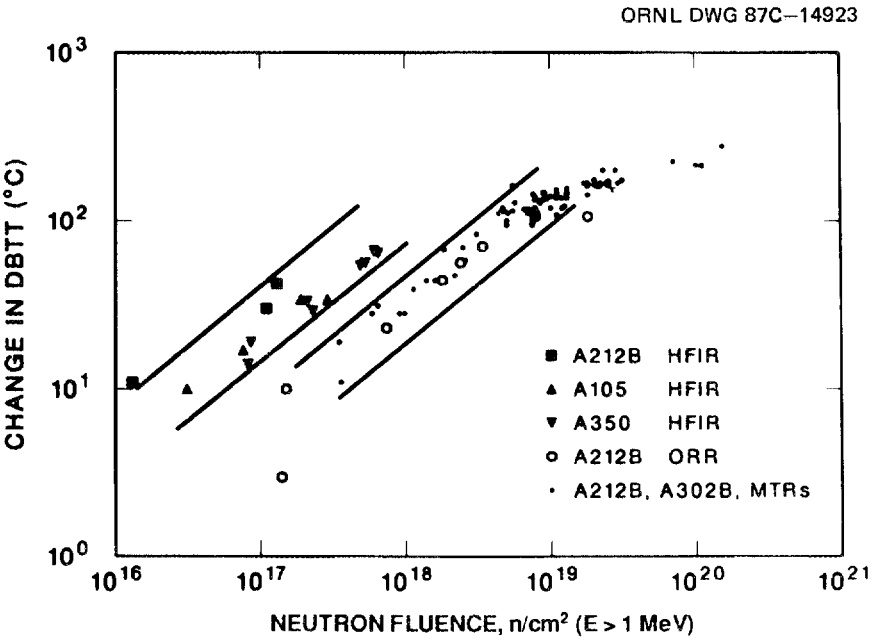

Fig. D.38. Log-log plot of DBTT shift vs neutron fluence (E > 1.0 MeV). The surveillance data for the three HFIR materials are shifted to the left of the MTR data by almost an order of magnitude. The ORR data for A212B fall within the MTR data band.

log-log plot of shifts vs fluence for the ORR and HFIR data for the A212B plate. The plot also includes shifts for other steels irradiated in HFIR (A350LF3 and A105), as well as MTR data for A302B and A212 correlation monitor steels.[21] These monitor steels were prepared from plate material under the auspices of the American Society for Testing and Materials and irradiated in various worldwide programs. The A212B yield stress data from the ORR irradiations are also included by calculating a DBTT shift and using the average coefficient (C = 0.6°C/MPa) derived above. The following are apparent from Fig. D.38:

1. The behavior of HFIR A212B plate irradiated in ORR is similar to the trends shown in MTR irradiations of other similar steels.
2. The MTR/ORR data follow a $\Delta T \propto f^{0.5}$ trend up to intermediate fluences.
3. The trend band for all of the steels irradiated in HFIR can also be described as $\Delta T \propto f^{p}$, where $p \sim 0.5$. This is a conservative estimate of the fluence exponent; the HFIR data could equally well be encompassed within a band having a slope of 0.25.
4. The trend band for the low-flux HFIR surveillance data is shifted downward in fluence by about an order of magnitude relative to the high-flux ORR/MTR irradiations.
5. The A212B plate data tend to fall slightly above the shifts for the other steels in the HFIR surveillance program.

It is important to recognize that there may be different microstructural regimes of damage and that the nature of the features that are the dominant cause of hardening at low fluences may differ somewhat from those responsible at higher fluences. Dividing the irradiation exposure into various regimes may be a useful way to distinguish more relevant from less relevant data. For example, regimes might be defined as precascade and postcascade overlap in unit sink cells of the lattice, transient vs quasi-steady-state average defect concentrations, and saturation regimes. Clearly, the HFIR data lie in a low-fluence regime (i.e., $\leq 3 \times 10^{18}$ n/cm^2). Figure D.39, which plots the data discussed above in this fluence regime, shows both general support for the square root of fluence behavior and the higher shifts observed at lower flux levels for irradiations to the same fluence. The uncertainties in these data are at least ±10°C for DBTT shifts and ±20% for the fluences. It has been shown that the scatter in the data for the correlation monitor steels, which were irradiated in a wide variety of neutron spectra, would be reduced if dpa was used as the exposure parameter instead of fluence ($E > 1.0$ MeV).[22] Figure D.39 illustrates that for a variety of steels, radiation embrittlement occurs approximately three times more rapidly in the low-flux regime compared with the higher-flux MTR environment.

Figure D.40 plots the HFIR surveillance data, along with least-squares fit lines for the three types of steel (note a 0 intercept is required). The fit for the HFIR A212B is

$$\Delta T = 326\sqrt{f} \ ; \qquad (D.5)$$

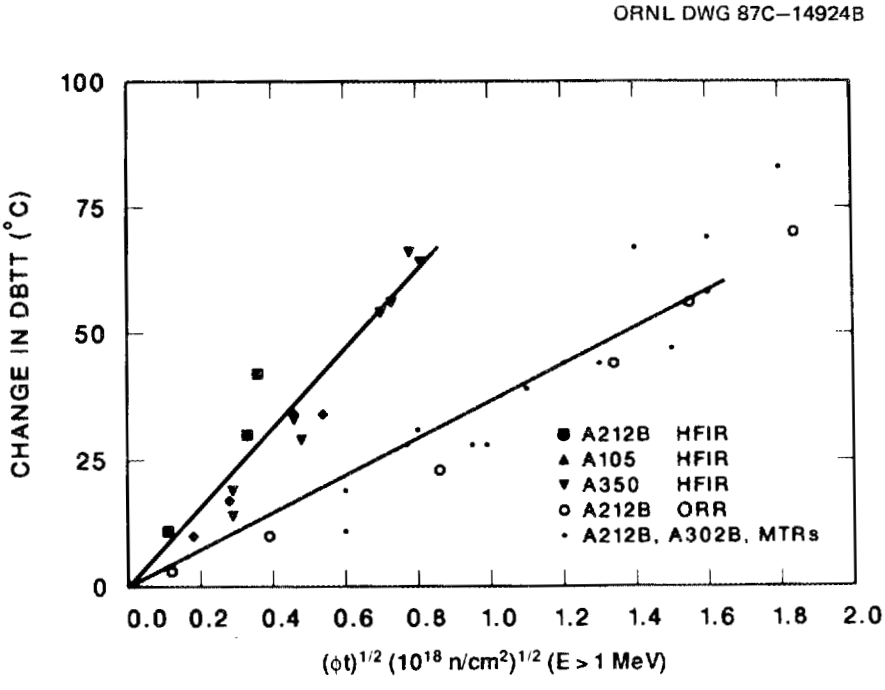

Fig. D.39. HFIR surveillance data and high-flux ORR and MTR data plotted vs the square root of fluence (E > 1.0 MeV).

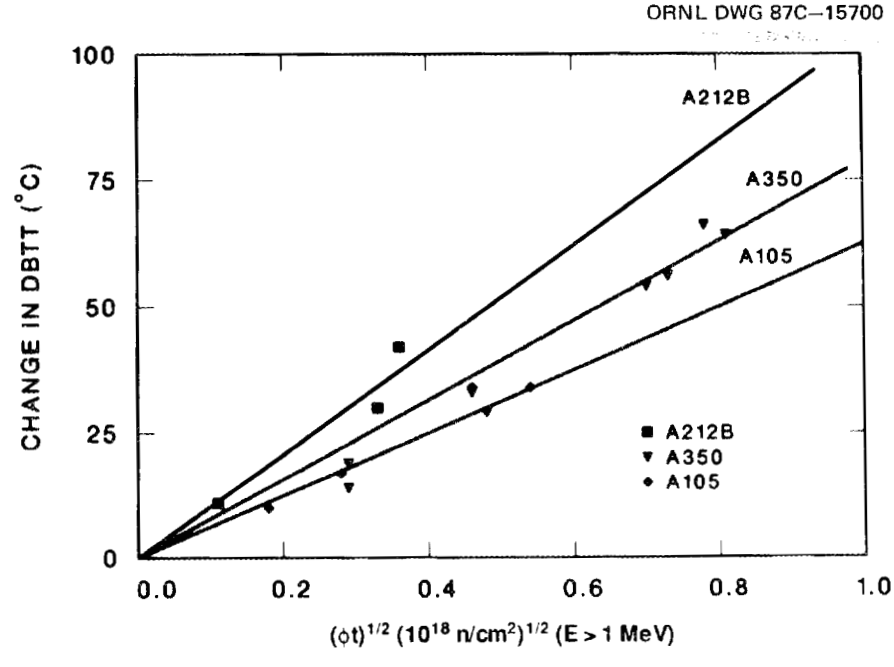

Fig. D.40. Least-squares fit to the HFIR surveillance ΔDBTT vs fluence (E > 1.0 MeV) data for three steels.

for A105

$$\Delta T = 208\sqrt{f} \ ; \qquad (D.6)$$

and for A350LF3

$$\Delta T = 261\sqrt{f} \ . \qquad (D.7)$$

The statistical fits are well within the uncertainties in the individual shift and fluence measurement uncertainties.

D.6.3.4 Assessment of weld behavior

An assessment of the radiation performance of welds was carried out using accelerated tests in ORR, as described in Sect. D.5. A determination was made of the ORR damage level needed to produce a DBTT shift in the A212B base metal of the same magnitude as that observed in the HFIR surveillance specimens. Charpy specimens of base metal and weld metal were then irradiated together at 60°C (140°F) to this damage level ($\sim 2 \times 10^{18}$ n/cm^2). It was shown that the DBTT shifts for the seam-weld and nozzle-weld materials were somewhat lower than the shift for the A212B base metal. In assessing the validity of the accelerated test as a means of assessing weld performance, it is necessary to consider (1) the relationship between hardening and shift in the two damage rate regimes and (2) the sensitivity of hardening in this low-temperature regime to metallurgical variables. It was shown in Sect. D.6.3.2 that the magnitude of the radiation-induced shift in DBTT for the A212B steel is directly proportional to the magnitude of the radiation-induced hardening and that the coefficient of proportionality is approximately the same in both reactors. In other words, irradiating to the same increment in yield stress in either reactor will produce the same shift in DBTT. This investigation has found no evidence for other types of embrittling mechanism, such as radiation-induced temper embrittlement or any form of intergranular or interfacial weakening. The observed shifts in DBTT for base metal appear to be entirely due to radiation hardening in both the ORR and HFIR environments.

Low-temperature embrittlement probably depends on metallurgical variables of composition and microstructure. Unfortunately, it is difficult to establish clear and unambiguous trends in the literature, and in a number of cases, apparently contradictory experimental results have been reported. In broad terms, the metallurgical effects can be summarized as follows.

1. There is considerable evidence that carbon and nitrogen (dissolved) enhance low-temperature embrittlement.[17,23] Nickel and copper have also been reported to enhance low-temperature embrittlement.[24] The effects of other elements are more ambiguous, perhaps because of complex effects on various metallurgical factors. For example, Brumovsky[25] found an interactive effect between carbon and manganese, in part mediated by microstructural variations associated with changes in these elements.

2. Ferrite is more sensitive to embrittlement than bainitic and martensitic microstructures and prior cold work decreases subsequent irradiation embrittlement.[25] Coarse grain size was also found to correlate with enhanced embrittlement in some studies.[16,18] The effect of coarse grain size on shifts may in part be due to a higher unirradiated transition temperature in such steels, which results in a higher coefficient relating hardening to shift.[15] Further, the general trends in hardening and shift changes are consistent with the defect survival model (Sect. D.6.3.6). Clustering is reduced if more point defects are lost to fixed sinks. There may also be other explanations, such as effects on grain strengthening and the superposition of preirradiation and postirradiation strengthening mechanisms.

3. There are significant heat-to-heat embrittlement variations in nominally similar steels.[16,21]

4. For a range of typical pressure-vessel steels (i.e., A302B and A212), the embrittlement response can be grouped into sensitive and less-sensitive classes.[13,16] Within these classes, the data overlap within mechanical property and fluence measurement uncertainties.

5. Weldments may be more sensitive or less sensitive than the corresponding base metal.[16] However, welds do not appear to have a higher embrittlement sensitivity than do sensitive plate materials.

6. The variation of embrittlement with metallurgical variables is less at low fluences.[16]

Figure D.41 shows a comparison of the behavior of the HFIR steels irradiated in ORR with the trends for sensitive correlation monitor steel

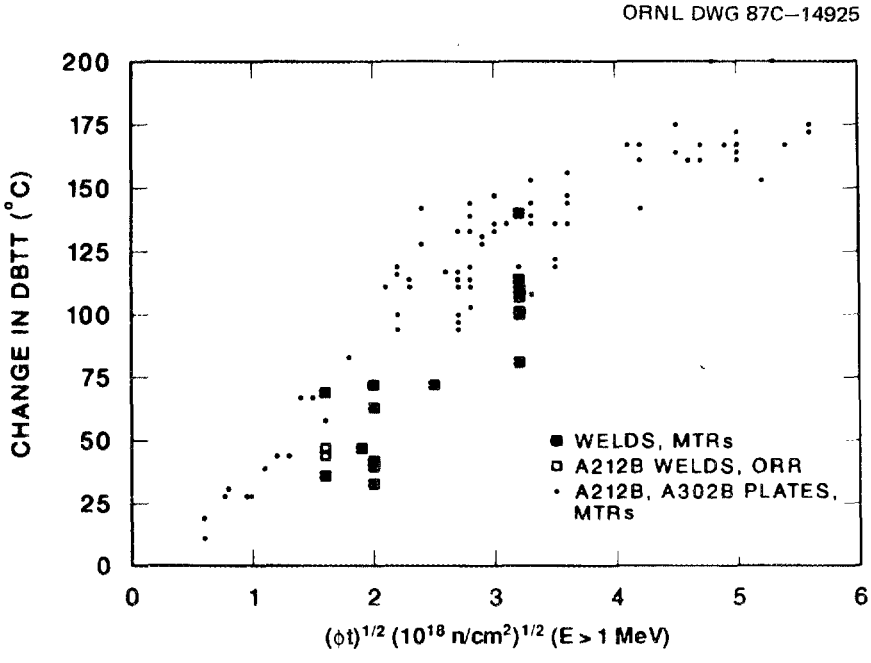

Fig. D.41. DBTT shifts for weld and base metal vs the square root of fluence (E > 1.0 MeV). In high-flux irradiations, the weld data tend to fall somewhat below the base metal data.

plates and data for a variety of welds taken from the literature,[16,26] as well as data for the HFIR welds irradiated in ORR. Figure D.42 shows these data in the lower fluence range, along with an upper-bound embrittlement curve for many steels.[16] These results show that the HFIR A212 plate falls near the upper limit on observed irradiation sensitivity in MTR irradiations. However, in ORR irradiations the HFIR welds appear to be slightly less sensitive than the plate. The relatively higher sensitivity of the HFIR A212 plate is also observed in the HFIR surveillance irradiations (Fig. D.39), even though at higher fluences the A350 steel is more sensitive than steels containing less nickel.[16] Based on these observations and the rather typical compositions and microstructures of the HFIR welds, there appears to be no basis to expect a change in the relative sensitivity of weld and base metal in translating the ORR data to HFIR vessel irradiation conditions.

The results of the ORR accelerated tests show that the A212B weld and the nozzle weld undergo DBTT shifts that are ~85 and ~80% of the shifts observed in the A212B base metal. Consideration of the radiation damage mechanisms involved and the existing literature supports the contention that this also represents the relative behavior of base metal and weld metal in the HFIR environment.

From Eq. (D.5) the DBTT shift for the seam weld is represented by

$$\Delta T = 277\sqrt{f} \ . \qquad \text{(D.8)}$$

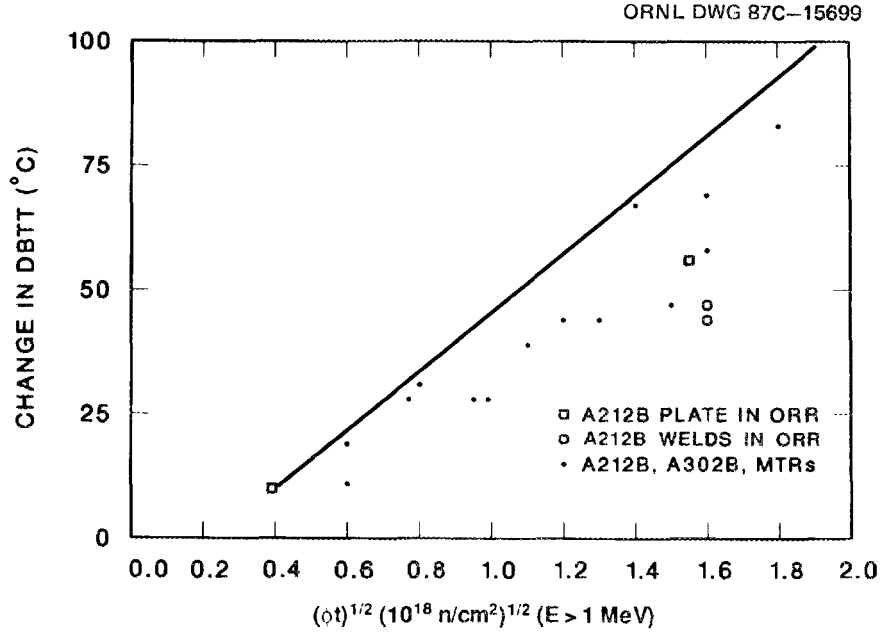

Fig. D.42. DBTT shift vs the square root of fluence (E > 1.0 MeV) for high-flux irradiations. Upper-bound line source: L. E. Steele, *Neutron Irradiation Embrittlement of Reactor Pressure-Vessel Steels*, Atomic Energy Review, Int. Atomic Energy Agency, Vienna, 1969. The A212B welds irradiated in ORR fall well below this line.

A more conservative approach would be to assume similar sensitivity between the A212 plate and weld; thus, the shifts for the welds could be estimated from Eq. (D.5). This probably represents an upper bound because the A212 has a near-maximum sensitivity in MTR irradiations.

D.6.3.5 Radiation hardening mechanisms

The defect microstructures that are responsible for low-temperature embrittlement have not been clearly identified in any study to date, primarily because of their small size (<1- to 2-nm diam). However, it is believed that the defects are small interstitial clusters in the form of dislocation loops and vacancy clusters, probably in the form of depleted zones or small microvoids.[17] Unlike some other body-centered-cubic and most face-centered-cubic alloys, cascade collapse to form vacancy loops has not been observed in iron. There is substantial experimental (e.g., internal friction, positron annihilation, strain aging, and annealing) and theoretical (e.g., computer simulations) evidence that interstitial impurities, such as carbon and nitrogen, interact with the point defect clusters to form complexes.[17,23] Such complexes are believed to have higher thermal stability and act as stronger dislocation barriers than the intrinsic defect clusters.

The detailed kinetics of cluster/complex formation have not been modeled. The primary damage is produced in displacement cascades in the form of small clusters and isolated defects. Experiments that show no effect of damage rate over two orders of magnitude of flux in iron and some mild steels[18,27] (see below) have been interpreted to suggest that the defects responsible for embrittlement are formed locally within cascades, perhaps as a consequence of the evolution of the nascent cascade structure. However, it is possible that nucleation and growth of clusters also occur outside cascades (e.g., at point defect trapping sites). In either case, if the net damage accumulation is roughly proportional to fluence, the characteristic exposure dependence can be rationalized on the basis of dispersed barrier hardening theory. For example, for the loop-hardening model of Fleisher,[28] the critical resolved shear stress will depend on the number (N) and size (d) of the loops as

$$\Delta\tau \sim 0.25\ \mu b \sqrt{Nd}\ , \qquad (D.9)$$

where $\Delta\tau$ is the shear stress increase, μ is the shear modulus, and b is the Burgers vector. If the loop number density (N) is proportional to the fluence, then this model predicts that hardening is proportional to the square root of fluence. Thus, this model supports the square root correlation of experimental data described by Eq. (D.3). Other strengthening models and/or defect microstructures give slightly different results. If the number of defects in a fixed number of clusters is proportional to f, a fluence exponent of p = 0.33 is predicted, weak barriers give p = 0.67, and diffusion-controlled growth of a fixed number of solute clusters that act as strong barriers yields a p ~ 0.25. The strengthening associated with various preirradiation and postirradiation microstructures must be properly superimposed, typically by a linear

addition for long- and short-range obstacles and a root mean square rule sum for weak/short range barriers. The assumed superposition rule can also affect the nominal fluence dependence. However, the most significant conclusion is that all of the simple models predict a fluence dependence of hardening/embrittlement that is significantly less than linear, consistent with observation.

Embrittlement at elevated temperatures (i.e., 300°C) can also be correlated as ΔT ($\Delta\sigma y$) $\propto f^p$. At high fluxes, p ranges from 0.35 to 0.65; at lower fluxes, p is generally lower and ranges from 0.2 to 0.3.[29]

D.6.3.6 Origin of neutron flux effects

We are aware of only two systematic studies on the effect of flux on low-temperature embrittlement. Barton and collaborators[27] evaluated hardening in mild steels irradiated to a fluence of 4×10^{17} n/cm^2 at fluxes from ~10^{13} to 10^{11} n•cm^{-2}•s^{-1} over a range of temperatures. Hinkle and collaborators[18] evaluated the hardening in nominally pure iron over a similar flux range for irradiations to 4×10^{18} n/cm^2 at ~90°C. Neither study revealed any significant and systematic effect of flux. Indeed, these results lead to the belief that flux was not a significant variable in low-temperature embrittlement. More recently, a study comparing surveillance and test reactor irradiations of mild steels at 180°C showed greater embrittlement for surveillance irradiations at a flux of ~10^8 n•cm^{-2}•s^{-1} than for the relatively high-flux MTR irradiations.[30] Small-angle neutron scattering studies also showed larger integrated scattering from the steels irradiated at low flux.

Note that for higher-temperature irradiations (i.e., ~300°C), there is an effect of flux for steels in which the copper concentration is >0.15%. At low fluences, embrittlement increases with decreasing flux. This has been interpreted as being due to the combined effects of flux, time, and temperature on the rate of precipitation of copper.[29]

Theoretical evaluation of potential flux effects is difficult because the basic processes are complex and not well understood and also because basic material parameters required for kinetic modeling are not well defined. For example, the vacancy migration enthalpy in pure iron has been variously estimated[31,32] to be ~0.6 to ~1.3 eV. At a temperature of 60°C, this difference translates into a difference in vacancy diffusion coefficient D_v of a factor of ~4×10^{10}. However, for an impure steel (e.g., containing many trapping sites) a migration enthalpy (H_m) on the order of 1.2 eV is probably reasonable; in contrast, interstitial migration enthalpy, even with trapping, should be less than ~0.8 eV with nominal values of ~0.33 eV.[33] Based on estimates[34] of typical sink densities for commercial steels $S_t \sim 5 \times 10^{10}$/cm^2, defect relaxation times needed to approach steady state concentrations can be computed as

$$\tau_{v,i} \sim 1/S_t D_{v,i} \sim 1/S_t \exp(-H_m/kT) \ , \qquad (D.10)$$

giving $\tau_v \sim 2.9 \times 10^7$ s and $\tau_i \sim 26$ s for nominal migration enthalpies of 0.8 and 1.2 eV for interstitials and vacancies, respectively. Variations

of several orders of magnitude from these values could be expected, depending on the actual sink densities and diffusion coefficients [as well as other complications (see below)]. Nevertheless, interstitials would be expected to relax to quasi-steady-state values for the total microstructure, including vacancies, for both MTR and surveillance irradiations. However, vacancy concentrations may or may not approach steady state values even in low-flux irradiations characteristic of HFIR surveillance conditions. Understanding of the point defect kinetics is required to account for the fate of the irradiation-induced defects (i.e., loss to fixed sinks or growing clusters resulting in some damage accumulation vs mutual annihilation of vacancies and interstitials by recombination).

The potential significance of recombination can be understood by a simple calculation of the frozen-in vacancy sink strength. A typical displacement cross section for water-moderated spectra[35] is $\sigma_{dpa} \sim 1500$b with an efficiency factor ε of the initial displaced atoms surviving immediate local recombination[36] of $\varepsilon \sim 0.4$. Thus, a fluence of $f = 10^{18}$ $n \cdot cm^{-2}$ gives a total vacancy concentration of

$$N_v \sim \sigma_{dpa}\, \varepsilon f N_0 \sim 5.2 \times 10^{19}/cm^3 \ . \qquad (D.11)$$

Assuming that all of the vacancies remain in the lattice and taking the interstitial capture radius of the vacancy at 5×10^{-8} cm, this gives a total vacancy sink strength of[37]

$$S_v \sim 4\pi r_v N_v \sim 3.3 \times 10^{13}/cm^2 \ . \qquad (D.12)$$

This is far in excess of the fixed sink strength (mostly dislocations) and even of the likely sink strength of defect clusters that had evolved as a consequence of irradiation. Thus, it is clear that in this situation, most of the irradiation-generated defects would have been lost to recombination and would, therefore, not be available to cause damage.

It is possible to write the more detailed kinetic defect balance equations, which can be integrated to calculate the time-dependent fate of the irradiation-generated defects. Further elaborations — including cluster nucleation and growth, impurity interactions, the structure of the nascent cascade defects, and stochastic effects of the discrete time and spatial character of the cascade damage — could, in principle, be added. Clearly, this is beyond the scope of this work. However, some sense of the importance of recombination can be determined from the solution of the simple steady state balance equations, which assume a homogeneous production of isolated defects. In this case, the significant parameter is the fraction of defects reaching sinks (e.g., surviving recombination) $F(\chi)$, where[37]

$$F(\chi) = (2/\chi)\{(1 + \chi)^{0.5} - 1\} \ , \qquad (D.13)$$

$$\chi = 4\, \alpha G / D_v S_t^2 \ , \qquad (D.14)$$

where

α = recombination parameter $\sim 10^{18}/cm^2$,

G = vacancy/interstitial generation rate = $\phi \varepsilon \sigma_{dpa}/s$,

ϕ = flux $n \cdot cm^{-2} \cdot s^{-1}$ ($E > 1$ MeV),

D_v = vacancy diffusion coefficient, $cm^{-2} \cdot s^{-1}$,

S_t = total fixed sink strength, cm^{-2}.

At large values of χ, $F(\chi)$ reduces to the form

$$F(\chi) = 2/\sqrt{\chi} \ . \qquad (D.15)$$

Using the parameters listed previously, $F(\chi)$ can be evaluated for flux levels characteristic of HFIR surveillance ($\phi \sim 5 \times 10^8$) and ORR ($\phi \sim 10^{13}$) irradiations. This gives values of $F_{HFIR}(\chi) \sim 0.98$ vs $F_{ORR}(\chi) \sim 0.05$ or a ratio of surviving defects in HFIR about 20 times that in ORR. Based on the dispersed barrier model of hardening that predicts a strength increase roughly proportioned to the square root of the net defect survival, embrittlement would occur at a rate ~4.5 times faster in HFIR than in ORR.

The amount of hardening associated with the surviving defects can be estimated and compared with experimental observations. A HFIR fluence of $f = 1.3 \times 10^{17}$ n/cm^2 corresponds to $\sim 2 \times 10^{-4}$ dpa or $\sim 6.7 \times 10^{18}$ interstitial/vacancy pairs/cm^3. Assuming that 100% survive and that 50% of the surviving defects are in clusters containing 60 defects yields $\sim 10^{17}$ defect clusters with diameters between 1.1 and 1.9 nm (depending on whether they are loops or microvoids). According to Eq. (D.9), these barriers could result in an increase in the critical resolved shear stress of ~42 MPa. Assuming a polycrystal Schmidt factor of 2.5 would result in a predicted yield stress increase of ~105 MPa. This is close to the observed value of ~75 MPa, suggesting that the estimates of the retained defects can account for the observed embrittlement.

Figure D.37 suggests an acceleration of embrittlement in HFIR relative to ORR of a factor of ~3, close to the estimate of the ratio of retained defects of 4.5. Indeed, the calculation probably underestimates the defect survival, particularly for ORR, because

1. steady state conditions may not be achieved and initial defect survival rates are higher;
2. intrinsic clustering of cascade vacancies and additional clustering because of short-range diffusion would decrease recombination;
3. the discrete character of cascade damage would reduce bulk recombination; and
4. defects produced directly in cascades, rather than formed by long-range diffusion, may cause much of the embrittlement.

Further, note that the simple defect survival model does not explain much of the observed phenomenology of low-temperature embrittlement for

MTR irradiations, including the moderate temperature sensitivity and the fluence dependence at higher exposures. Finally, it is possible that other mechanisms are important in one or both environments. For example, irradiation-enhanced precipitation of copper-rich phases, which is known to be important at higher temperatures, may also occur for low-flux, low-fluence irradiations at lower temperatures. Nevertheless, a reasonable working hypothesis is that the differences in HFIR and ORR irradiations are due to recombination and other defects discussed below but that the basic character of the effective damage microstructure is similar.

D.6.3.7 Irradiation temperature and postirradiation annealing

The effect of irradiation temperature on embrittlement below ~200°C, reported in the literature, is modest. Indeed, various studies[16,17,27] have yielded contradictory results — suggesting increases, decreases, or no effect on embrittlement for irradiation temperature increases from ~60 to 150°C. The lack of a strong temperature dependence has been interpreted to indicate that most of the embrittling defects are produced locally in cascades and, thus, are not subject to kinetic factors associated with long-range defect migration and cluster nucleation and growth mechanisms. However, there are two other explanations for such behavior: (1) conditions of the experiment are such that relaxation times for critical processes are not transgressed and (2) parallel, sequential and competing mechanisms have different temperature dependencies that, in effect, cancel each other.

The low-fluence data for mild steels of Barton[27] showed a substantial decrease in hardening at all flux levels for increase in temperature in the range of 100 to 200°C. In contrast, a number of data sets[15] suggest an increase in embrittlement in going from ~60 to 150°C. This behavior is consistent with the common observation of increase in strength for intermediate temperature anneals (~150 to 200°C) of steels irradiated at lower temperatures (<100°C).[17,23] This phenomenon, called "radiation anneal hardening" (RAH), has been interpreted to be a consequence of enhanced interactions of interstitial impurities (C,N) with point defect clusters and/or enhanced defect clustering. Both mechanisms would lead to stronger dislocation barriers and, thus, increased hardening. These mechanisms could also become operative at the longer times associated with the HFIR surveillance irradiations. Based on a factor of roughly 5×10^4 in damage rate between the HFIR and ORR irradiations and assuming a 100°C temperature difference is required to produce RAH for high-flux irradiations, processes with an activation energy of up to 1.2 eV could enhance embrittlement for low-flux irradiations.

The postirradiation annealing (PIA) experiments also give variable results for recovery temperatures and times.[16-18,23,38] Pachur[38] has reported four recovery stages with the lowest temperature at ~250°C and the highest temperature of ~400°C for complete recovery. In general, existing data suggest that the significant recovery of properties takes place in the range of 300 to 350°C. The PIA behavior is likely to be a function of the irradiation and metallurgical variables. Most annealing data are for relatively high exposures. However, the preliminary annealing data for the A212B steel, described in Sect. D.6.2.6, are consistent

with the literature data with recovery beginning at ~300°C and being complete at 375°C.

D.6.4 SUMMARY

The results of this brief study can be summarized as follows.

1. The observed changes in the toughness of the HFIR pressure-vessel materials are caused by radiation hardening. The shift in DBTT is directly proportional to the increase in yield stress; the constant of proportionality is similar for both HFIR and ORR irradiations and is consistent with values found for a variety of pressure-vessel materials irradiated in MTRs.
2. During PIA, significant recovery of the irradiated A212B occurs between 300 and 350°C, consistent with literature data on various pressure-vessel materials irradiated in MTRs.
3. Postirradiation examination of HFIR surveillance specimens, using TEM, field ion microscopy, and SANS, failed to reveal the defects responsible for the observed hardening, implying that the defects are <3 nm in diameter and at a concentration of the order of $10^{17}/cm^3$.
4. It is demonstrated from yield stress measurements that the degree of radiation hardening per unit of neutron fluence is a factor of ~3 higher for HFIR surveillance materials than for the same materials irradiated in ORR. This is a new and unexpected result and is related to the factor of $\sim 10^5$ lower neutron flux in the HFIR environment.
5. Enhanced hardening at low fluxes can be rationalized on the basis of both higher point defect survival from recombination and enhanced clustering and interaction of defect clusters with interstitial impurities.
6. The hardening and the DBTT shifts in the HFIR materials follow a square root dependence on fluence consistent with both dispersed barrier hardening theory and the large body of data derived from MTR irradiations.
7. Irradiations in ORR indicate that the simulated HFIR welds are somewhat less sensitive to radiation embrittlement than the plate materials. This is consistent with a broad body of literature data which indicate that for radiation-sensitive steels, welds do not have a higher tendency toward embrittlement than plate material.
8. Consideration of radiation hardening mechanisms and damage-rate effects supports the argument that the relative behavior of weld metal and base metal is probably the same in both the HFIR and ORR environments.
9. The observed flux effect could possibly lead to unexpected levels of hardening in pressure-vessel support structures in commercial nuclear power plants.

D.7 SURVEILLANCE PROGRAM FOR HFIR REOPERATION (R. K. Nanstad, J. R. McWherter, and D. M. McGinty)

As discussed in Sect. D.2, the existing HFIR surveillance program is described in detail in Ref. 1. The original program was designed to

accommodate an approximate operational lifetime of ~20 EFPY. As a result of the HFIR vessel evaluation discussed in this report, the surveillance plan requires modifications to accommodate the need for weld-metal surveillance, as well as to extend the operating life of the vessel beyond the original 20-EFPY design life.

The revised HFIR surveillance plan is currently in preparation and will be published as a separate document. The basic concepts of the plan, however, have been formulated with a view toward an extended lifetime of ~10 EFPY. The existing surveillance program will be maintained as the foundation of the revised plan in that the existing capsule design, capsule holders, key locations, and test specimen type (CVN impact) will remain the same. The remaining surveillance specimens in the reactor have been inventoried and their exposure levels noted. Because the number of A350 LF3 specimens remaining is relatively low, they will be combined and tracked as one group. This seems reasonable because both the HB2 and HB3 forgings were fabricated from the same heat of steel and have shown almost identical response to irradiation in the HFIR.

Sufficient numbers of A212B specimens exist in the reactor to accommodate a 10-EFPY extension; however, the specimens tested to date were removed from locations of higher flux in keys 6 and 7. For the revised plan, remaining specimens will be relocated to positions of higher flux, and existing exposures for each capsule will be noted and accounted for when removed from the reactor for testing. Sufficient numbers of specimens of A105 also exist for the revised plan and will be moved in a manner similar to that for the A212B.

For the submerged-arc reproduction seam weld and the shielded metal-arc nozzle qualification weld, only unirradiated material is available for use in surveillance. Specimens will be placed in surveillance locations that will allow for exposure at fluxes perhaps as high as five times greater than the actual welds in the vessel. This will allow for some acceleration of exposure but at low enough factors to mitigate dose-rate effects. Examination of Fig. D.6 shows that an exposure equivalent to ~2 or 3 EFPY gives ΔNDT results that fall in the linear range of ΔNDT vs EFPY. Thus, weld-metal specimens placed in surveillance locations with a neutron flux of, say, three times the flux at the actual vessel weld, would show an NDT shift equivalent to ~3 EFPY after only 1 year of exposure. In that way, the surveillance program for the welds can "catch up" with the program for the base metals over the projected life extension period of 10 EFPY. It is anticipated that some specimens would also be located in positions that provide no acceleration for purposes of validation in the later years of the program.

Reconstituting previously tested surveillance specimens for inclusion in the program was considered but rejected largely because of the developmental activities associated with the procedure. Welding of irradiated specimens requires maintaining the specimen at low-enough temperatures to mitigate annealing of radiation damage. Because the HFIR surveillance specimens were irradiated at 120°F, that requirement would be expensive to develop, especially for handling of irradiated material. Techniques for adhesive joining have been investigated and will be pursued, but the surveillance program now under development and described in this section is considered adequate.

There is considerable interest both from technical considerations and from a research perspective for the inclusion of tensile specimens to monitor the radiation damage. That course will be pursued but not as a part of the formal surveillance program. There is a body of opinion that more reliable data regarding radiation damage of pressure-vessel steels can be obtained with tensile properties and hardness than with Charpy impact specimens. There are conceptual plans for inclusion of subsize tensile specimens as part of a research surveillance program because of the high interest in the dose-rate observations from this evaluation. The observations of significantly higher than expected embrittlement rates for the low-temperature, low-flux conditions in HFIR have direct implications for some components outside the vessel in some commercial LWRs. HFIR represents a unique situation because ~20 years of exposure have already been accumulated and evaluated.

Thus, pursuit of research programs in this area has direct relevance to operating reactors in the public sector for normal operation and operations considered under life extension programs.

The above represents a preliminary discussion of the HFIR surveillance program for reoperation. The final concept and details of the program will be published separately.

REFERENCES

1. J. R. McWherter, R. E. Schappel, and J. R. McGuffey, *HFIR Pressure Vessel and Structural Components Material Surveillance Program*, ORNL-TM-1372, Union Carbide Corp. Nuclear Div., Oak Ridge Natl. Lab., January 1966.

2. "Standard Methods for Notched Bar Impact Testing of Metallic Materials," pp. 235–58 in *Annual Book of ASTM Standards*, Vol. 03.01, American Sociey for Testing and Materials, Philadelphia, 1985.

3. L. E. Steele and J. R. Hawthorne, *Effect of Irradiation Temperature on the Neutron-Induced Changes in Notch Ductility of Pressure-Vessel Steels*, NRL Report 5629, Naval Res. Lab., Washington, D.C., June 28, 1961.

4. *ASME Boiler and Pressure Vessel Code*, Sect. III, Div. 1, Subsect. NB, Class 1 Components, American Society of Mechanical Engineers, New York, July 1, 1983.

5. "Standard Method for Conducting Drop-Weight Test to Determine Nil-Ductility Transition Temperature of Ferritic Steels," pp. 373–92 in *Annual Book of ASTM Standards*, Vol. 03.01, American Society for Testing and Materials, Philadelphia, 1985.

6. "Standard Practice for Conducting Surveillance Tests for Light-Water Cooled Nuclear Power Reactor Vessels," pp. 354–62 in *Annual Book of ASTM Standards*, Vol. 03.01, American Society for Testing and Materials, Philadelphia, 1985.

7. R. W. Hobbs, Oak Ridge Natl. Lab., personal communication to K. R. Thoms, Oak Ridge Natl. Lab.

8. D. L. McElroy, Oak Ridge Natl. Lab., personal communication to K. R. Thoms, Oak Ridge Natl. Lab., March 11, 1987.

9. L. E. Steele, *Neutron Irradiation Embrittlement of Reactor Pressure Vessel Steels*, Technical Report Series No. 163, Int. Atomic Energy Agency, Vienna, 1975.

10. E. A. Little, "Neutron-Irradiation Hardening in Irons and Ferritic Steels," pp. 25–60 in *International Metals Reviews*, The Metals Society and the American Society for Metals, Metal Park, Ohio, March 1976.

11. A. J. Birkle and W. Rall, "A Thin-Foil Transmission Electron Microscopic Study of Neutron-Irradiated A212B Steel," *Trans. Metall. Soc. AIME* 230 (February 1964).

12. A. H. Cottrell, *Trans. Metall. Soc. AIME* 212, 192 (1958).

13. F. A. Nichols, *Phil. Mag.* 14, 355 (1966).

14. G. R. Odette and P. M. Lombrozo, *Physically-Based Regression Correlations of Embrittlement Data from Reactor Pressure Vessel Surveillance Programs*, EPRI-NP-3319, Electric Power Research Institute, Palo Alto, Calif., 1984.

15. G. R. Odette, P. M. Lombrozo, and R. A. Wullaert, *Effects of Radiation on Materials*, ASTM-STP 870, American Society for Testing and Materials, Philadelphia, 1985, p. 840.

16. L. E. Steele, *Neutron Irradiation Embrittlement of Reactor Pressure-Vessel Steels*, Atomic Energy Review, Int. Atomic Energy Agency, Vienna, 1969, p. 7.2.

17. E. A. Little, *International Metals Reviews*, March 25, 1976.

18. N. E. Hinkle, S. M. Ohr, and M. S. Weschler, *Effects of Radiation on Structural Materials*, ASTM-STP 426, American Society for Testing and Materials, Philadelphia, 1976, p. 572.

19. A. D. Ameav and N. F. Pravduyk, *Atomizad* 241 (1968).

20. S. B. McRickard, *Phil. Mag.* 18, 915 (1968).

21. J. R. Hawthorne, *Radiation Effects Information Generated on the ASTM Reference Correlation Monitor Steels*, ASTM-DS-54, American Society for Testing and Materials, Philadelphia, 1974.

22. G. R. Odette, *Proceedings of IAEA Technical Committee Meeting on Correlation Accuracy of Embrittlement of Pressure Vessel Steels*, KFA Jülich Conf. 37 (1982), p. 311.

23. M. S. Weschler, *The Influence of Impurity-Defect Interactions on Radiation Hardening and Embrittlement*, Proceedings of the ASME/CSNE Pressure Vessel and Piping Conference, Montreal, Canada, June 1978.

24. V. A. Nikolaev and V. 1. Badanin, *At. Energ.* 37—6, 491 (1974).

25. M. Brumovsky, *Effects of Irradiation on the Substructure and Mechanical Properties of Metals and Alloys*, ASTM-STP-529, American Society for Testing and Materials, Philadelphia, 1973, p. 46.

26. R. L. Gray, *Charpy-V-Notch Ductility Characteristics of Neutron Irradiated A527-B and A350-LF2 Steel Weldments*, NRL Report 7006, Naval Res. Lab., Washington, D.C., 1970.

27. P. J. Barton, D. R. Harries, and I. L. Mogford, *J. Iron Steel Inst.*, p. 507 (May 1965).

28. R. L. Fleisher, *Acta Metall.* 10, 835 (1962).

29. G. R. Odette and G. E. Lucas, *Radiation Embrittlement of Reactor Pressure Vessel Steels, An International Review* 2, ASTM-STP 909, L. E. Steele, ed., American Society for Testing and Materials, Philadelphia, 1986, p. 206.

30. R. H. Priest, W. Charnock, and B. K. Neale, *Effects of Irradiation on Materials*, ASTM-STP-870, American Society for Testing and Materials, Philadelphia, 1985, p. 1150.

31. H. E. Schaefer et al., *J. Scripta Metall.* 11, 803 (1977).

32. P. Hautojarvi et al., *J. Nucl. Mater.* 114, 253 (1983).

33. P. G. Lucasson and R. M. Walker, *Phys. Rev.* 127, 485 (1962).

34. G. E. Lucas et al., *Effects of Radiation on Materials*, Vol. 12, ASTM-STP-870, American Society for Testing and Materials, Philadelphia, 1985, p. 900.

35. W. N. McElroy, ed., *PSF Experiments Summary and Blind Test Results*, NUREG/CR-3320, U.S. Nuclear Regulatory Commission, 1985.

36. J. W. Kinney, M. W. Guinan, and Z. A. Munir, *J. Nucl. Mater.* 122, 1028 (1984).

37. P. T. Heald and M. V. Speight, *Acta Metall.* 23, 1389 (1975).

38. D. Pachur, *Nucl. Technol.* 59, 463 (1982).

Appendix E

NEUTRON DOSIMETRY ANALYSIS

R. L. Childs F. B. K. Kam
R. E. Maerker W. A. Rhoades
L. R. Williams
C. A. Baldwin

E.1 INTRODUCTION

A vessel materials surveillance program for the High Flux Isotope Reactor (HFIR) has been under way since reactor startup, as discussed in Sect. 3. Essential parameters in the evaluation of the radiation damage are the neutron flux (ϕ), or fluence rate, for E > 1.0 MeV and E > 0.1 MeV; and $\int_E \phi(E)\sigma dE$, displacements per atom per second (dpa/s), where σ is the dpa microscopic neutron cross section. The dosimetry sensors used consisted of 3-cm-long stainless steel (type 304) notch plugs that were inserted into the V-notched grooves of the Charpy specimens (Fig. E.1). After removal from the reactor, the stainless steel dosimeters were assayed to determine the activities of ^{58}Co, ^{54}Mn, and ^{60}Co from the $^{58}Ni(n,p)^{58}Co$, $^{54}Fe(n,p)^{54}Mn$, and $^{59}Co(n,\gamma)^{60}Co$ reactions, respectively. American Society for Testing and Materials (ASTM) Standards E181-82, E263-82, E264-82, and E262-85 were used to determine the activities at the time of removal from the reactor.

In parallel with the experimental determination of the neutron exposure, the neutron fluence rates and total neutron fluences were calculated at all important locations of the PV by using two- and three-dimensional (2- and 3-D) discrete ordinates transport analysis. The calculated reaction rates for the $^{58}Ni(n,p)^{58}Co$ and $^{54}Fe(n,p)^{54}Mn$ threshold sensors were compared with the measurements to obtain an estimate for the uncertainty of the calculations. The calculations were then combined with the measurements to obtain the best estimate of the exposure parameters at all points of interest, including locations where no measurements were available (see Sect. E.5).

A cross-sectional view of HFIR at the horizontal midplane of the reactor core is shown in Fig. E.2, and the vertical view is given in Fig. E.3. The three-dimensional discrete ordinates code TORT[1] was adopted for the HFIR calculations to mock-up the beam holes.

Because no weld materials were included in the HFIR surveillance program, an irradiation task was initiated at the Oak Ridge Research Reactor (ORR) to determine the irradiated toughness of the HFIR longitudinal and circumferential welds. This task required a dosimetry experiment at ORR to correlate the data at the two reactors. The ORR dosimetry results are reported in Sect. E.3.

E.2 METHOD OF NEUTRON FLUENCE RATE CALCULATION FOR THE ORR IRRADIATIONS

The ORR calculations involved (1) the use of VENTURE, a 3-D diffusion code, to obtain the fission source distribution for Cycle 178-DX2

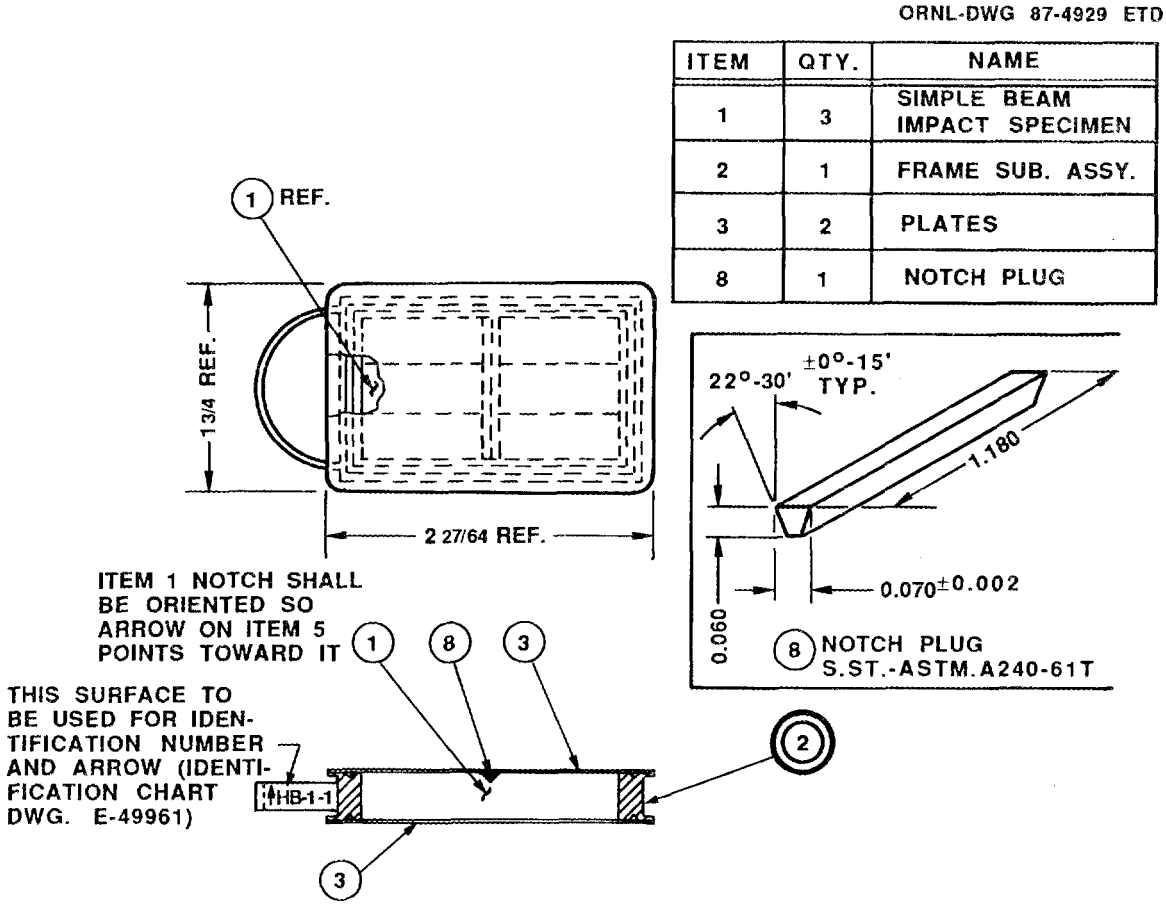

Fig. E.1. Surveillance specimen container assembly.

and (2) the use of the DOT-IV and ANISN, 2-D and one-dimensional (1-D) discrete ordinates transport codes, respectively, to obtain neutron fluence rates throughout ORR, as well as in the water beyond the aluminum window. Three-dimensional fluxes were synthesized from the results of the lower-order dimensional transport calculations by a procedure previously benchmarked against the PCA[2] and PSF[3] experiments. This procedure consists of deriving three "channel" sources from the results of the diffusion calculation:

$$S_g(X,Y) = \int_{-\infty}^{\infty} \chi_g S(X,Y,Z)dZ \ ,$$

$$S_g(Y,Z) = \int_{-\infty}^{\infty} \chi_g S(X,Y,Z)dX \ ,$$

$$S_g(Y) = \int_{-\infty}^{\infty} \chi_g dZ \int_{-\infty}^{\infty} S(X,Y,Z)dX \ ,$$

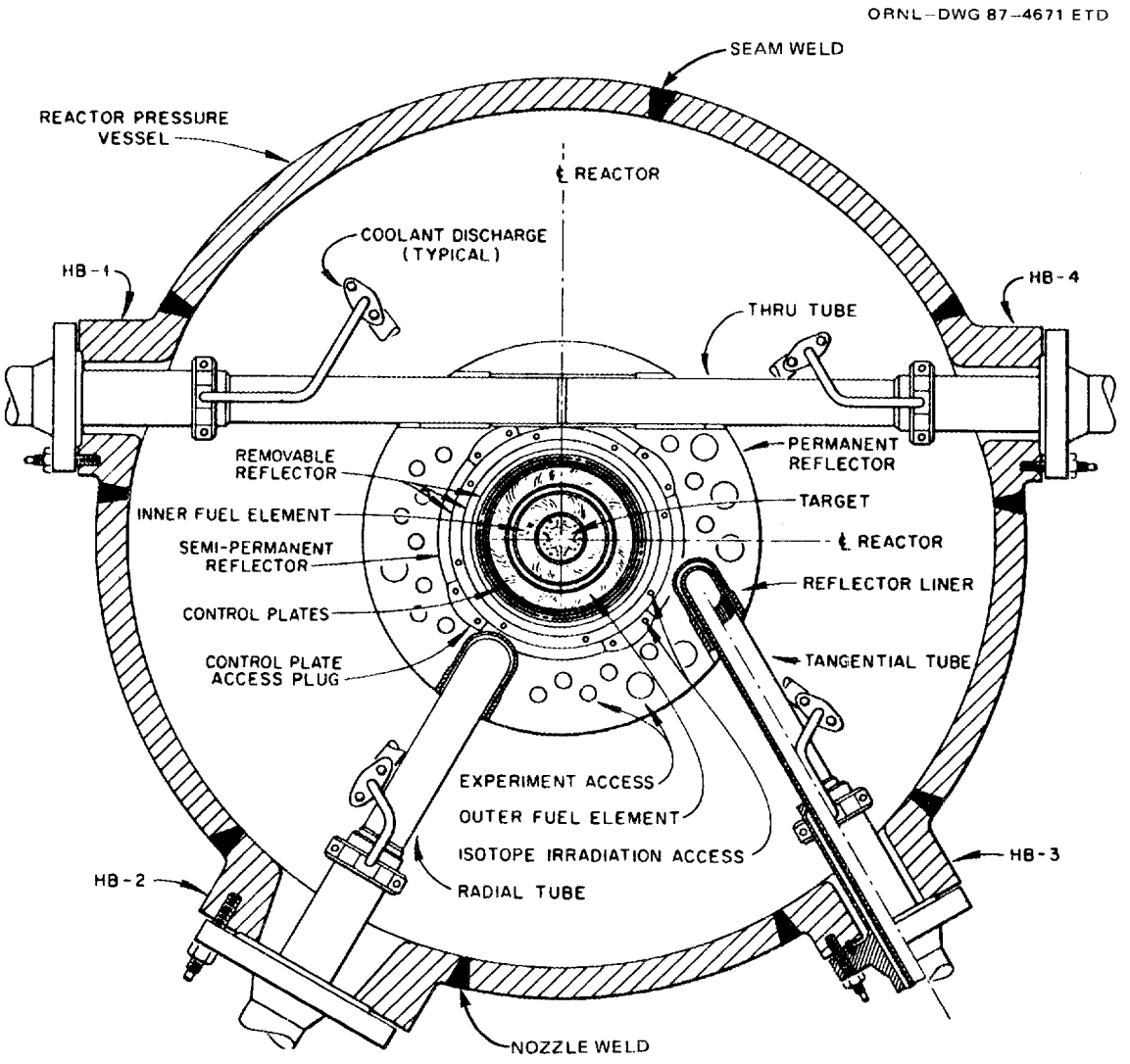

Fig. E.2. Horizontal midplane view of HFIR.

where χ_g is the normalized spectrum from thermal-neutron fission of U-235, $S(X,Y,Z)$ is the 3-D VENTURE source, and the left-hand sides represent the channel sources for each of three discrete ordinates transport calculations.

The fluxes from these three calculations were combined to form synthesized 3-D fluxes:

$$\phi_g(X,Y,Z) = \phi_g(X,Y)\phi_g(Y,Z)/\phi_g(Y) \ ,$$

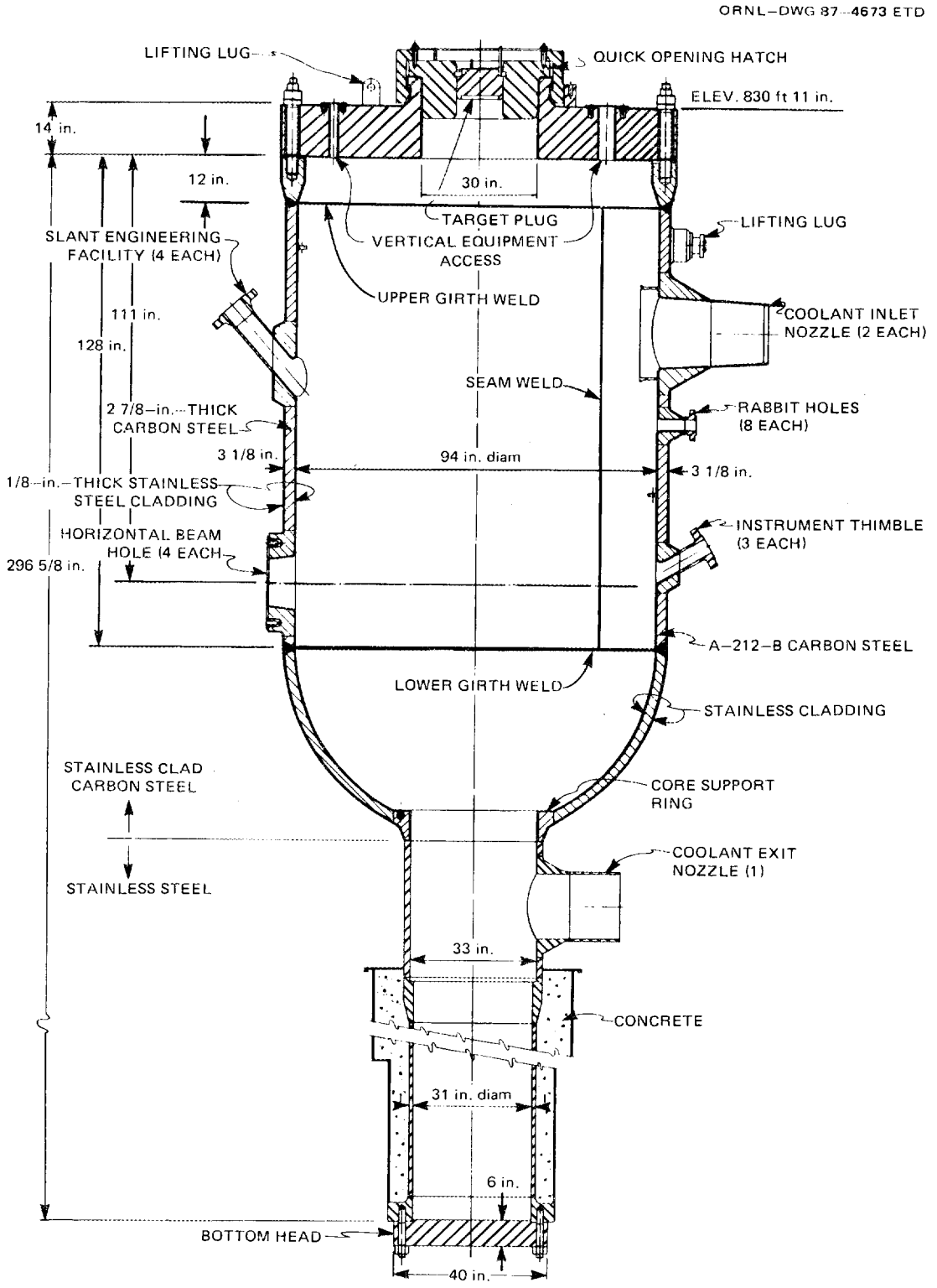

Fig. E.3. Vertical cross section of HFIR.

where

$\phi_g(X,Y)$ = the solution to the Boltzman transport equation using $S_g(X,Y)$,

$\phi_g(Y,Z)$ = the solution to the Boltzman transport equation using $S_g(Y,Z)$,

$\phi_g(Y)$ = the solution to the Boltzman transport equation using $S_g(Y)$.

In the above equation, Y is the horizontal dimension in the direction of the ORR rows, X is the horizontal lateral dimension, and Z is the vertical dimension. The geometries for the transport calculations represent appropriate slices through the 3-D geometry.

Activities were also synthesized:

$$A(X,Y,Z) = A(X,Y) \cdot A(Y,Z)/A(Y) ,$$

an operation that was more readily performed and virtually indistinguishable from the more rigorous expression

$$A(X,Y,Z) = \sum_g \sigma_g \phi_g(X,Y,Z) ,$$

where σ_g is the dosimetry cross section and $\phi_g(X,Y,Z)$ is the synthesized flux.

The discrete ordinates calculations used cross sections based on the ELXSIR library,[4] and they were followed in decreasing energy steps through the first 38 groups ($0.1 \leq E \leq 17.3$ MeV).

The loading of Cycle 178-DX2 is shown in Fig. E.4. The 3-D mesh used to describe the ORR geometry in the VENTURE calculation is shown in Fig. E.5. The DOT geometries employed the same mesh with an additional refinement in the A-9 geometry that describes the specimen and sensor orientation in accurate detail (Fig. E.6). The latter necessitated redefining the VENTURE source results, which did not use this refined geometry, in terms of the refined mesh used in the transport calculations.

E.3 NEUTRON EXPOSURE PARAMETER RESULTS FOR ORR IRRADIATIONS

Four capsules were irradiated in the ORR A-9 position in support of the HFIR PV Integrity Evaluation. Each capsule was identical to the one shown in Fig. E.7. The first capsule irradiation was primarily a dosimetry experiment that was combined with the transport calculations to provide a neutron spectral characterization of the metallurgical irradiation capsules that followed.

ORNL-DWG 87-4930 ETD

POOL

W

A-1	A-2	A-3	A-4	A-5	A-6	A-7	A-8	A-9
		N003	N018	B098	C033	N004		
DF	BE	208	322	340	302	210	BE	HFIR
B-1	B-2	B-3	B-4	B-5	B-6	B-7	B-8	B-9
		B051	UB003	N010	UB004	B053		
EU	IR	275	123	225	123	274	IR	EU
C-1	C-2	C-3	C-4	C-5	C-6	C-7	C-8	C-9
		MFE	N005	N001	N006	MFE	C040	
BE	340	7J	218	210	218	6J	340	BE
D-1	D-2	D-3	D-4	D-5	D-6	D-7	D-8	D-9
	N014	B045	UB005	C024	UB006	B046	C034	
EU	297	241	189		189	245	296	EU
E-1	E-2	E-3	E-4	E-5	E-6	E-7	E-8	E-9
	B100	HFED	B052	B047	N011		B099	
BE	339		267	247	242	IR	340	BE
F-1	F-2	F-3	F-4	F-5	F-6	F-7	F-8	F-9
		C038	UB001	N012	UB002	C039		
EU	IR	325	85	292	85	326	BE	DF
G-1	G-2	G-3	G-4	G-5	G-6	G-7	G-8	G-9
DF	BE	BE	BE	BE	BE	BE	BE	DF

S

N

E

Fig. E.4. ORR core configuration for dosimetry run on December 22, 1986.

ORNL-DWG 87-4931 ETD

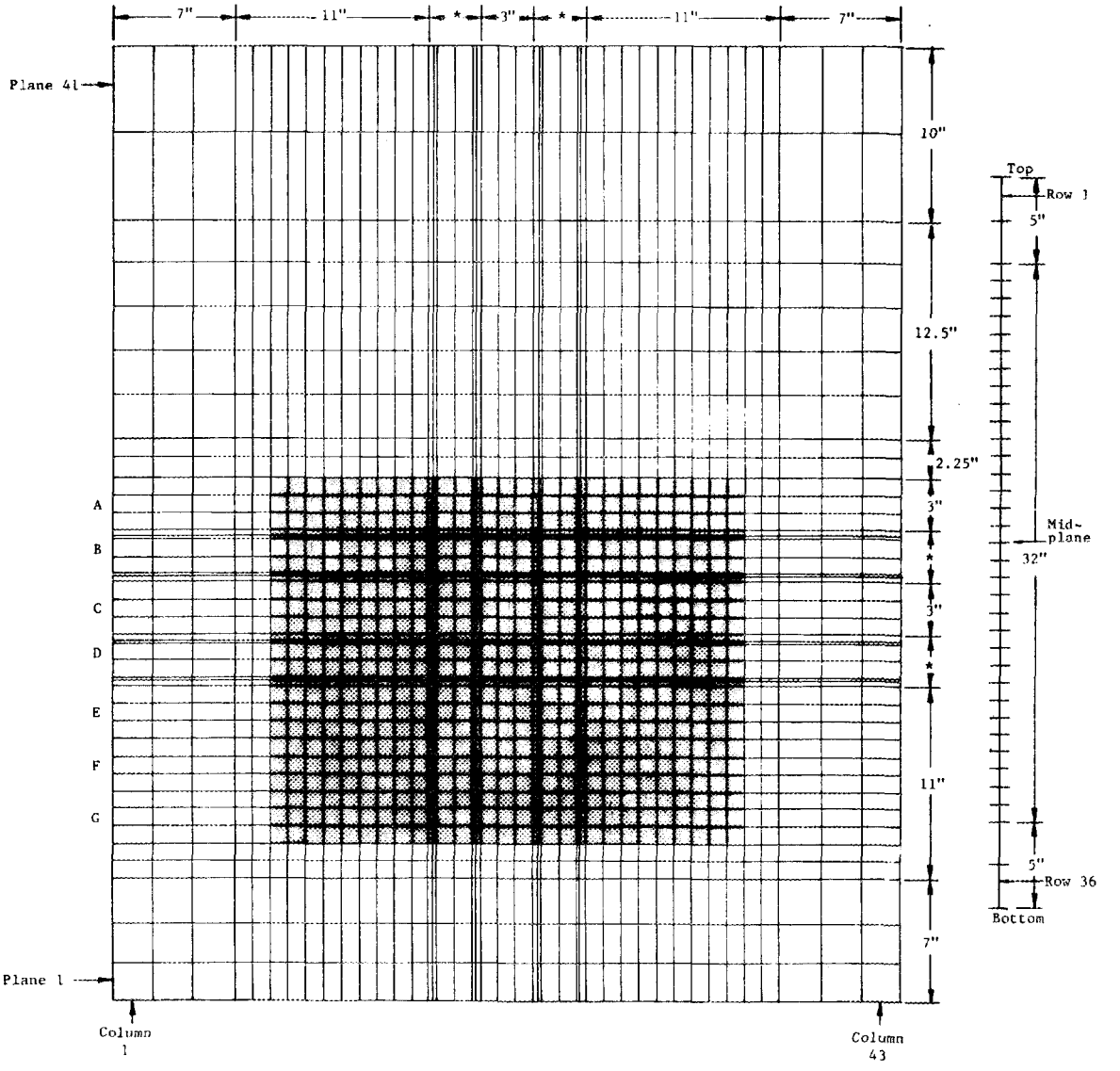

*0.3275, 0.14, 1.0325, 1.0325, 0.14, 0.3275 inches.

Fig. E.5. Mesh structure for ORR calculational model.

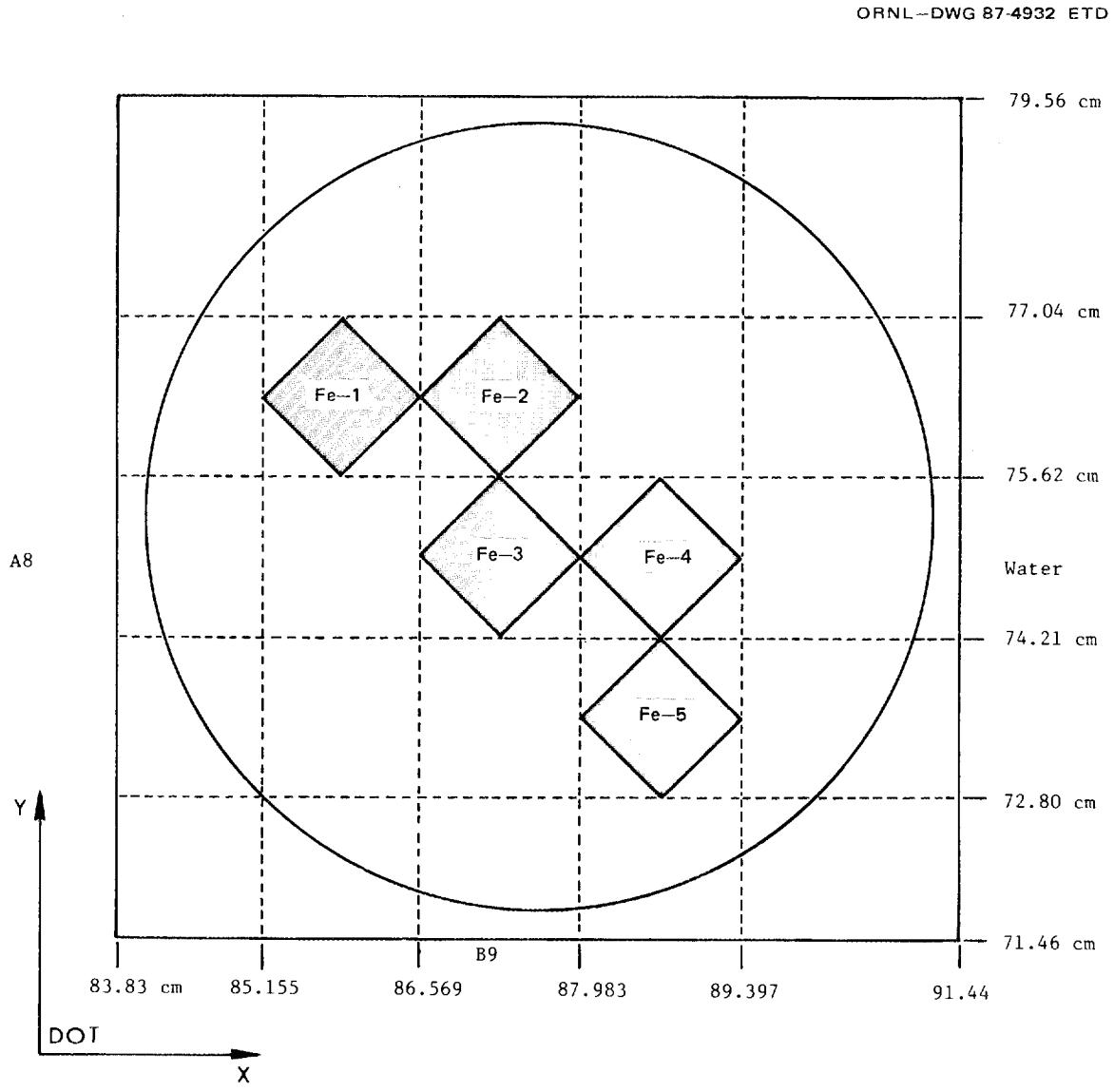

Fig. E.6. Geometric model for the ORR A-9 location.

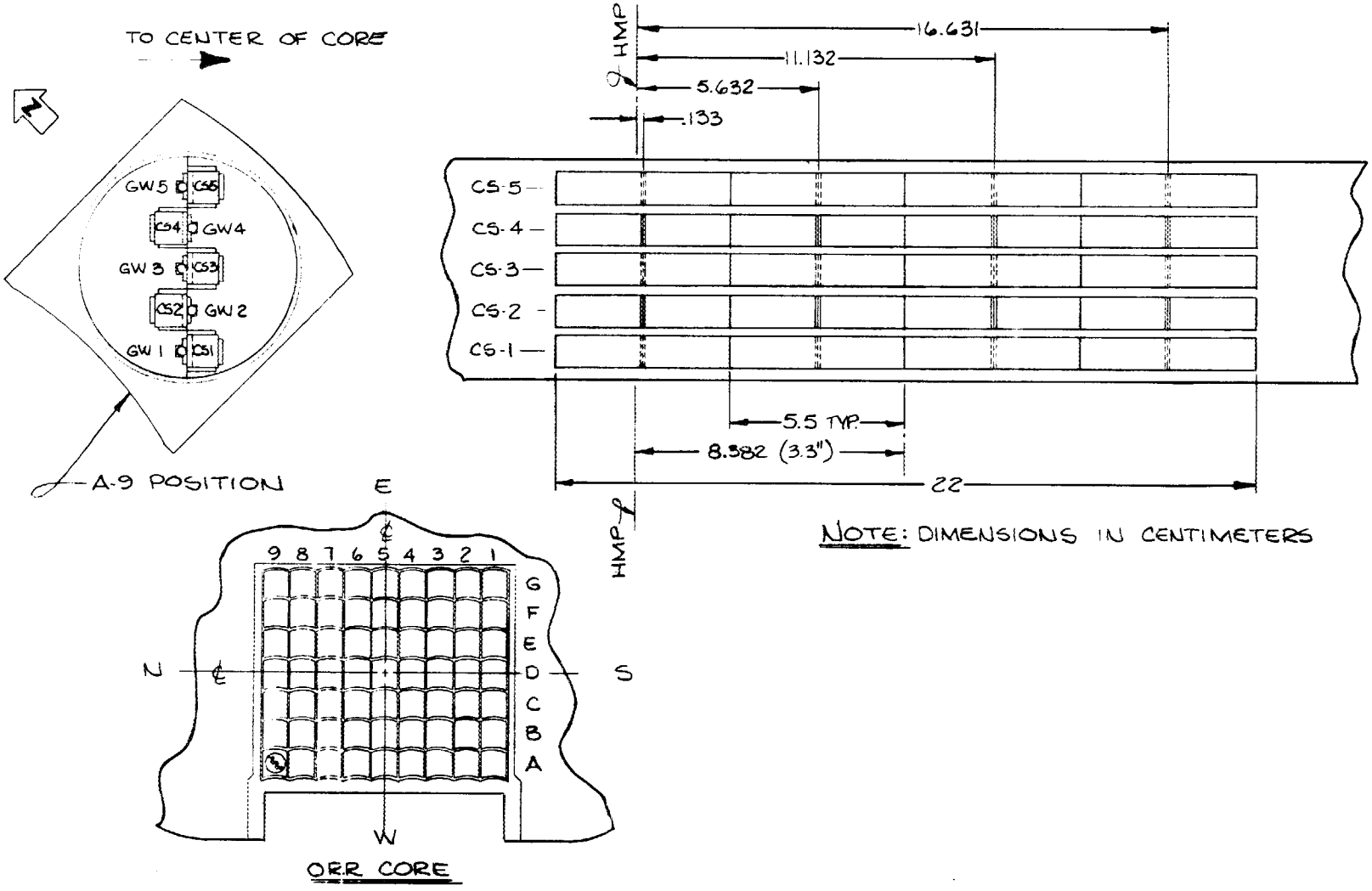

Fig. E.7. Cross section of A-9 experiment.

The transport calculations indicated that the variation of the neutron exposure parameters, fluence rates (E > 1.0 MeV and E > 0.1 MeV), and dpa/s, was very small throughout the irradiation volume. The dosimetry measurements for capsule 1 are given in Table E.1, and the resulting neutron exposure parameters derived from combining the measurements and calculations are given in Table E.2. In the dosimetry experiment, dosimetry sensors were inserted in dummy Charpy specimens where the neutron exposure parameters were required and in a location adjacent to Charpy locations. It was necessary to obtain the ratio of the sensors between the two locations because in the subsequent metallurgical irradiations it was not feasible to place sensors in the Charpy specimens.

In the three metallurgical irradiations that followed, dosimetry sensors were inserted adjacent to Charpy specimens, and the ratios from the dosimetry capsules above were used to obtain the magnitude of the neutron exposure parameters in the Charpy specimens. The neutron exposure results of capsules 2, 3, and 4 are given in Tables E.3–E.8. The average fluence rate (E > 1.0 MeV) for the three capsules was 9.59 E+12 with a one standard deviation of 4.2% (Table E.9).

E.4 NEUTRON FLUENCE RATE DETERMINATION FOR THE HFIR VESSEL AND SURVEILLANCE SPECIMENS

The streaming of neutrons through the beam tubes in HFIR increases the fluence rate in critical structural areas near the juncture of the tubes and the reactor vessel. The purpose of this calculation was to determine the fluence rate in those areas.

The calculation used an intermediate-source surface procedure developed for Department of Defense applications. First, a 2-D discrete ordinates neutronics calculation determined the fluence rate throughout the unperturbed system. A source surface was defined enclosing each beam tube and several centimeters of surrounding water. The angular fluence rate entering the enclosed volume was determined by remapping the 2-D data in both spatial and directional coordinates. The water surrounding the tube inside the surface ensured that the reflection back across the surface would be relatively unperturbed by the addition of the tube.

A 3-D geometric mock-up of the tube and the surrounding material was specified inside the source surface. A horizontal section through the mock-up of horizontal beam tube (HB-2) is shown in Fig. E.8. The tube extends from the circular reflector zone on the extreme left, through the water region, and outward through a support collar and the exit nozzle area at the right. The cross-hatched zone curving upward at the right is the reactor vessel. The geometric treatment of HB-3 and HB-4 was quite similar (Figs. E.9 and E.10) except that both sides of the tube were required; only a symmetrical half was required for HB-2. A separate mock-up of HB-1 was not required because its geometry was a mirror image of HB-4. An extended treatment of HB-4 (designated HB-4x) (Fig. E.11) used a somewhat coarser mesh to allow extension of the problem farther around the curve of the reactor vessel to include the seam weld.

Figure E.12 shows a cross section of the tube through the support collar. From the center outward, the materials in the zones are a void,

Table E.1. Neutron dosimetry measurements in ORR A-9 core location — Capsule 1 (dosimetry experiment)

Capsule location[a]	Dosimeter axial location[b]	Activities per milligram of dosimeter at the end of irradiation (Bq/mg)									
		$^{237}Np(n,f)^{140}Ba$	$^{238}U(n,f)^{140}Ba$	$^{58}Ni(n,p)^{58}Co$	$^{54}Fe(n,p)^{54}Mn$	$^{46}Ti(n,p)^{46}Sc$	$^{63}Cu(n,\alpha)^{60}Co$	$^{27}Al(n,\alpha)^{24}Na$[c]	$^{59}Co(n,\gamma)^{60}Co$[c]	$^{54}Fe(n,p)^{54}Mn$[d]	$^{58}Ni(n,p)^{58}Co$[d]
CS1[e]	−11.132	2.70E4	5.280E3	1.24E4	1.78E2	1.73E2	2.31	3.04E4	1.30E2		
CS3[e]	−0.133	2.88E4	4.840E3	1.11E4	1.61E2	1.38E2		2.65E4	1.07E2	1.16E2	1.03E3
CS3[e]	−5.632	3.09E4	5.040E3	1.18E4	1.86E2	1.60E2		2.90E4	1.30E2	1.23E2	1.11E3
CS3[e]	−11.132	2.57E4	5.280E3	1.21E4	1.87E2	1.50E2		2.89E4	1.25E2	1.26E2	1.14E3
CS3[e]	−16.631	2.96E4	4.850E3	1.15E4	1.82E2	1.44E2	2.00	2.74E4	1.10E2		
CS5[e]	−11.132	2.78E4	4.800E3	1.04E4	1.75E2	1.46E2	2.05	2.70E4	1.10E2		
GW1	−0.133			1.04E4	1.54E2	1.40E2	1.93	2.40E4	9.59E2		
GW1	−5.632			1.10E4	1.66E2	1.50E2	1.89	2.66E4	8.78E2		
GW1	−11.132			1.15E4	1.59E2	1.54E2	2.20	2.55E4	9.66E2		
GW1	−16.631			1.08E4	1.65E2	1.35E2	2.04	2.49E4	9.86E2		
GW2	−0.133			1.12E4	1.69E2	1.51E2	2.05	2.60E4	9.92E2		
GW2	−5.632			1.18E4	1.84E2	1.64E2	2.29	2.70E4	9.78E2		
GW2	−11.132			1.16E4	1.82E2	1.58E2	2.22	2.82E4	9.82E2		
GW2	−16.631			1.16E4	1.71E2	1.46E2	1.97	2.68E4	1.03E3		
GW3	−0.133			9.80E3	1.52E2	1.36E2	1.85	2.24E4	7.54E2		
GW3	−5.632			1.09E4	1.51E2	1.44E2	2.00	2.53E4	7.97E2		
GW3	−11.132			1.08E4	1.64E2	1.42E2	1.89	2.60E4	7.83E2		
GW3	−16.631			1.04E4	1.54E2	1.42E2	2.01	2.34E4	7.44E2		
GW4	−0.133			1.02E4	1.59E2	1.46E2	1.98	2.48E4	9.94E2		
GW4	−5.632			1.16E4	1.57E2	1.52E2	2.17	2.70E4	1.04E3		
GW4	−11.132			1.16E4	1.73E2	1.50E2	2.16	2.60E4	9.39E2		
GW4	−16.631			1.04E4	1.66E2	1.50E2	2.08	2.61E4	1.07E3		
GW5	−0.133			8.91E3	1.40E2	1.28E2	1.74	2.26E4	9.71E2		
GW5	−5.632			1.01E4	1.35E2	1.36E2	1.90	2.24E4	8.95E2		
GW5	−11.132			1.03E4	1.56E2	1.31E2	1.87	2.46E4	8.73E2		
GW5	−16.631			9.11E3	1.47E2	1.32E2	1.84	2.28E4	9.85E2		

[a] See Fig. 1.

[b] Location is relative to horizontal midplane (HMP) of ORR Reactor and is at the axial location of the C_v notches.

[c] Dosimeter is Al-Co alloy with 0.10 wt % cobalt and 99.9 wt % aluminum.

[d] Dosimeter is 304 SS with 68.62 wt % iron and 9.51 wt % nickel.

[e] Dosimeters in these capsules were gadolinium covered.

Table E.2. Neutron exposure parameters in A-9 core location — Capsule 1[a]

Charpy capsule identification	Axial location of V notch[b] (cm)	ϕ(E > 1.0 MeV) ($cm^{-2} \cdot s^{-1}$)	ϕ(E > 0.1 MeV)[c] ($cm^{-2} \cdot s^{-1}$)	dpa/s[d]
CS1	−0.133	1.06E13	2.80E13	1.47E-8
CS1	−5.632	1.13E13	2.98E13	1.57E-8
CS1	−11.132	1.15E13	3.04E13	1.60E-8
CS1	−16.631	1.10E13	2.90E13	1.53E-8
CS2	−0.133	1.01E13	2.67E13	1.40E-8
CS2	−5.632	1.09E13	2.88E13	1.52E-8
CS2	−11.132	1.08E13	2.85E13	1.50E-8
CS2	−16.631	1.10E13	2.67E13	1.40E-8
CS3	−0.133	1.02E13	2.69E13	1.42E-8
CS3	−5.632	1.10E13	2.90E13	1.53E-8
CS3	−11.132	1.11E13	2.93E13	1.54E-8
CS3	−16.631	1.08E13	2.85E13	1.50E-8
CS4	−0.133	9.58E12	2.53E13	1.33E-8
CS4	−5.632	1.02E13	2.69E13	1.42E-8
CS4	−11.132	1.03E13	2.72E13	1.43E-8
CS4	−16.631	9.95E12	2.63E13	1.38E-8
CS5	−0.133	9.64E12	2.54E13	1.34E-8
CS5	−5.632	1.01E13	2.67E13	1.40E-8
CS5	−11.132	1.05E13	2.77E13	1.46E-8
CS5	−16.631	9.98E12	2.63E13	1.39E-8
Average		(1.05 ± 0.05)E13	(2.77 ± 0.14)E13	(1.46 ± 0.08)E-8

[a] The average 2200-m/s thermal flux (ϕ_{2200}) is 3.81E13 $cm^{-2} \cdot s^{-1}$, based on a cadmium ratio of 8.42 determined from dosimetry experiment.

[b] Relative to horizontal midplane of the ORR.

[c] $\frac{\phi(E > 0.1 \text{ MeV})}{\phi(E > 1.0 \text{ MeV})} = (2.64 \pm 0.02)$.

[d] $\frac{\text{dpa/s}}{\phi(E > 1.0 \text{ MeV})} = (1.39 \pm 0.01)\text{E-}21$.

Table E.3. Neutron dosimetry measurements in ORR A-9 core location — Capsule 2

Capsule location[a]	Dosimeter axial location[b] (cm)	Activities per milligram of dosimeter at the end of irradiation (Bq/mg)					
		$^{58}Ni(n,p)^{58}Co$	$^{54}Fe(n,p)^{54}Mn$	$^{46}Ti(n,p)^{46}Sc$	$^{63}Cu(n,\alpha)^{60}Co$	$^{27}Al(n,\alpha)^{24}Na$[c]	$^{59}Co(n,\gamma)^{60}Co$[c]
GW1	−0.133	1.58E5	2.57E3	2.36E3	3.37E1		1.85E4
GW1	−5.632	1.69E5	2.78E3	2.38E3	3.32E1		1.84E4
GW1	−11.132	1.68E5	2.67E3	2.51E3	3.61E1		1.88E4
GW1	−16.631	1.61E5	2.58E3	2.32E3	3.38E1		1.78E4
GW2	−0.133	1.74E5	2.63E3	2.58E3	3.78E1		1.95E4
GW2	−5.632	1.82E5	3.02E3	2.62E3	3.48E1		2.06E4
GW2	−11.132	1.87E5	3.02E3	2.73E3	3.92E1		2.05E4
GW2	−16.631	1.70E5	2.80E3	2.50E3	3.61E1		1.92E4
GW3	−0.133	1.61E5	2.54E3	2.28E3	3.37E1	1.30E5	1.71E4
GW3	−5.632	1.67E5	2.64E3	2.36E3	3.18E1	1.36E5	1.76E4
GW3	−11.132	1.66E5	2.63E3	2.38E3	3.49E1	1.33E5	1.71E4
GW3	−16.631	1.54E5	2.42E3	2.20E3	2.90E1	1.24E5	1.67E4
GW4	−0.133	1.62E5	2.48E3	2.50E3	3.54E1		2.03E4
GW4	−5.632	1.76E5	2.78E3	2.52E3	3.70E1		2.10E4
GW4	−11.132	1.69E5	2.86E3	2.46E3	3.75E1		2.01E4
GW4	−16.631	1.59E5	2.42E3	2.40E3	3.14E1		1.98E4
GW5	−0.133	1.45E5	2.34E3	2.19E3	3.16E1		1.84E4
GW5	−5.632	1.54E5	2.45E3	2.17E3	3.24E1		1.78E4
GW5	−11.132	1.53E5	2.46E3	2.13E3	3.30E1		1.81E4
GW5	−16.631	1.41E5	2.08E3	2.10E3	2.78E1		1.73E4

[a] See Fig. 1.

[b] Location is relative to horizontal midplane (HMP) of ORR Reactor and is at the axial location of the C_v notches.

[c] Dosimeter is Al-Co alloy with 0.10 wt % cobalt and 99.9 wt % aluminum.

Table E.4. Neutron exposure parameters in A-9 core location — Capsule 2[a]

Charpy capsule identification	Axial location of V notch[b] (cm)	ϕ(E > 1.0 MeV) ($cm^{-2} \cdot s^{-1}$)	ϕ(E > 0.1 MeV)[c] ($cm^{-2} \cdot s^{-1}$)	dpa/s[d]
CS1	−0.133	1.03E13	2.72E13	1.43E-8
CS1	−5.632	1.07E13	2.83E13	1.49E-8
CS1	−11.132	1.10E13	2.90E13	1.53E-8
CS1	−16.631	1.03E13	2.72E13	1.43E-8
CS2	−0.133	9.86E12	2.60E13	1.37E-8
CS2	−5.632	1.01E13	2.67E13	1.40E-8
CS2	−11.132	1.07E13	2.83E13	1.49E-8
CS2	−16.631	9.86E12	2.60E13	1.37E-8
CS3	−0.133	1.03E13	2.72E13	1.43E-8
CS3	−5.632	1.05E13	2.77E13	1.46E-8
CS3	−11.132	1.07E13	2.83E13	1.49E-8
CS3	−16.631	9.65E12	2.55E13	1.34E-8
CS4	−0.133	9.34E12	2.47E13	1.30E-8
CS4	−5.632	9.95E12	2.63E13	1.38E-8
CS4	−11.132	9.86E12	2.60E13	1.37E-8
CS4	−16.631	8.86E12	2.34E13	1.23E-8
CS5	−0.133	9.53E12	2.52E13	1.33E-8
CS5	−5.632	9.81E12	2.59E13	1.36E-8
CS5	−11.132	9.81E12	2.59E13	1.36E-8
CS5	−16.631	8.81E12	2.33E13	1.23E-8
Average		(1.00 ± 0.06)E13	(2.64 ± 0.16)E13	(1.39 ± 0.08)E-8

[a] The average 2000-m/s thermal flux (ϕ_{2200}) is 4.17E13 $cm^{-2} \cdot s^{-1}$.

[b] Relative to horizontal midplane of the ORR.

[c] $\frac{\phi(E > 0.1 \text{ MeV})}{\phi(E > 1.0 \text{ MeV})} = (2.64 \pm 0.02)$.

[d] $\frac{\text{dpa/s}}{\phi(E > 1.0 \text{ MeV})} = (1.39 \pm 0.01)\text{E-}21$.

Table E.5. Neutron dosimetry measurements in ORR A-9 core location — Capsule 3

Capsule location[a]	Dosimeter axial location[b] (cm)	Activities per milligram of dosimeter at the end of irradiation (Bq/mg)				
		$^{58}Ni(n,p)^{58}Co$	$^{54}Fe(n,p)^{54}Mn$	$^{46}Ti(n,p)^{46}Sc$	$^{27}Al(n,\alpha)^{24}Na$[c]	$^{59}Co(n,\gamma)^{60}Co$[c]
GW1	−0.133	1.73E+5	2.63E+3		1.44E+5	2.02E+4
GW1	−5.632	1.82E+5	2.97E+3		1.52E+5	1.96E+4
GW1	−11.132	1.81E+5	2.90E+3		1.50E+5	2.00E+4
GW1	−16.631	1.66E+5	2.67E+3		1.36E+5	1.87E+4
GW2	−0.133	1.75E+5	2.76E+3		1.42E+5	2.12E+4
GW2	−5.632	1.87E+5	3.05E+3		1.52E+5	2.08E+4
GW2	−11.132	1.85E+5	2.99E+3		1.46E+5	2.14E+4
GW2	−16.631	1.72E+5	2.82E+3		1.46E+5	2.00E+4
GW3	−0.133	1.57E+5	2.40E+3		1.26E+5	1.72E+4
GW3	−5.632	1.66E+5	2.66E+3		1.42E+5	1.75E+4
GW3	−11.132	1.64E+5	2.61E+3		1.36E+5	1.74E+4
GW3	−16.631	1.50E+5	2.43E+3		1.20E+5	1.63E+4
GW4	−0.133	1.57E+5	2.45E+3		1.42E+5	2.06E+4
GW4	−5.632	1.66E+5	2.66E+3		1.42E+5	2.03E+4
GW4	−11.132	1.64E+5	2.61E+3		1.41E+5	2.04E+4
GW4	−16.631	1.52E+5	2.46E+3		1.28E+5	1.88E+4
GW5	−0.133	1.36E+5	2.12E+3		1.30E+5	1.82E+4
GW5	−5.632	1.41E+5	2.36E+3		1.23E+5	1.77E+4
GW5	−11.132	1.43E+5	2.25E+3		1.24E+5	1.77E+4
GW5	−16.631	1.28E+5	2.08E+3		1.12E+5	1.66E+4

[a] See Fig. 1.

[b] Location is relative to horizontal midplane (HMP) of ORR Reactor and is at the axial location of the C_v notches.

[c] Dosimeter is Al-Co alloy with 0.10 wt % cobalt and 99.9 wt % aluminum.

Table E.6. Neutron exposure parameters in A-9 core location — Capsule 3[a]

Charpy capsule identification	Axial location of V notch[b] (cm)	ϕ(E > 1.0 MeV) ($n/cm^{-2} \cdot s^{-1}$)	ϕ(E > 0.1 MeV)[c] ($n/cm^{-2} \cdot s^{-1}$)	dpa/s[d]
CS1	−0.133	1.05E+13	2.77E+13	1.46E-8
CS1	−5.632	1.14E+13	3.01E+13	1.58E-8
CS1	−11.132	1.12E+13	2.96E+13	1.56E-8
CS1	−16.631	1.02E+13	2.69E+13	1.42E-8
CS2	−0.133	9.39E+12	2.48E+13	1.31E-8
CS2	−5.632	1.02E+13	2.69E+13	1.42E-8
CS2	−11.132	9.95E+12	2.63E+13	1.38E-8
CS2	−16.631	9.48E+12	2.50E+13	1.32E-8
CS3	−0.133	9.45E+12	2.49E+13	1.31E-8
CS3	−5.632	1.04E+13	2.75E+13	1.45E-8
CS3	−11.132	1.01E+13	2.67E+13	1.40E-8
CS3	−16.631	9.00E+12	2.38E+13	1.25E-8
CS4	−0.133	8.75E+12	2.31E+13	1.22E-8
CS4	−5.632	9.14E+12	2.41E+13	1.27E-8
CS4	−11.132	9.01E+12	2.38E+13	1.25E-8
CS4	−16.631	8.35E+12	2.20E+13	1.16E-8
CS5	−0.133	8.79E+12	2.32E+13	1.22E-8
CS5	−5.632	9.01E+12	2.38E+13	1.25E-8
CS5	−11.132	8.92E+12	2.35E+13	1.24E-8
CS5	−16.631	8.10E+12	2.14E+13	1.13E-8
Average		(9.57 ± 0.90)E+12	(2.53 ± 0.24)E13	(1.33 ± 0.12)E-8

[a] The average 2200 m/s thermal flux (ϕ_{2200}) is 4.20E13 $cm^{-2} \cdot s^{-1}$.

[b] Relative to horizontal midplane of the ORR.

[c] $\frac{\phi(E > 0.1 \text{ MeV})}{\phi(E > 1.0 \text{ MeV})} = (2.64 \pm 0.02)$.

[d] $\frac{\text{dpa/s}}{\phi(E > 1.0 \text{ MeV})} = (1.39 \pm 0.01)\text{E-}21$.

Table E.7. Neutron dosimetry measurements in ORR A-9 core location — Capsule 4

Capsule location[a]	Dosimeter axial location[b] (cm)	Activities per milligram of dosimeter at the end of irradiation (Bq/mg)					
		$^{58}Ni(n,p)^{58}Co$	$^{54}Fe(n,p)^{54}Mn$	$^{46}Ti(n,p)^{46}Sc$	$^{27}Al(n,\alpha)^{24}Na$[c]	$^{59}Co(n,\gamma)^{60}Co$[c]	
GW1	−0.133	1.46E+5	2.18E+3			1.82E+4	
GW1	−5.632	1.62E+5	2.64E+3			1.86E+4	
GW1	−11.132	1.74E+5	2.85E+3			1.98E+4	
GW1	−16.631	1.76E+5	2.82E+3			2.05E+4	
GW2	−0.133	1.60E+5	2.36E+3			1.99E+4	
GW2	−5.632	1.72E+5	2.86E+3			2.01E+4	
GW2	−11.132	1.87E+5	3.03E+3			2.20E+4	
GW2	−16.631	1.91E+5	3.12E+3			2.25E+4	
GW3	−0.133	1.38E+5	2.14E+3		1.16E+5	1.54E+4	
GW3	−5.632	1.59E+5	2.50E+3		1.28E+5	1.70E+4	
GW3	−11.132	1.72E+5	2.68E+3		1.36E+5	1.82E+4	
GW3	−16.631	1.68E+5	2.72E+3		1.37E+5	1.88E+4	
GW4	−0.133	1.51E+5	2.29E+3			2.01E+4	
GW4	−5.632	1.61E+5	2.63E+3			2.06E+4	
GW4	−11.132	1.76E+5	2.87E+3			2.16E+4	
GW4	−16.631	1.77E+5	2.88E+3			2.22E+4	
GW5	−0.133	1.35E+5	2.03E+3			1.78E+4	
GW5	−5.632	1.46E+5	2.36E+3			1.81E+4	
GW5	−11.132	1.54E+5	2.48E+3			1.91E+4	
GW5	−16.631	1.54E+5	2.46E+3			1.97E+4	

[a] See Fig. 1.

[b] Location is relative to horizontal midplane (HMP) of ORR Reactor and is at the axial location of the C_v notches.

[c] Dosimeter is Al-Co alloy with 0.10 wt % cobalt and 99.9 wt % aluminum.

Table E.8. Neutron exposure parameters in A-9 core location — Capsule 4[a]

Charpy capsule identification	Axial location of V notch[b] (cm)	ϕ(E > 1.0 MeV) ($n \cdot cm^{-2} \cdot s^{-1}$)	ϕ(E > 0.1 MeV)[c] ($n \cdot cm^{-2} \cdot s^{-1}$)	dpa/s[d]
CS1	−0.133	8.32E+12	2.20E+13	1.16E-8
CS1	−5.632	9.66E+12	2.55E+13	1.55E-8
CS1	−11.132	1.04E+13	2.75E+13	1.45E-8
CS1	−16.631	1.04E+13	2.75E+13	1.45E-8
CS2	−0.133	7.99E+12	2.11E+13	1.11E-8
CS2	−5.632	9.14E+12	2.41E+13	1.27E-8
CS2	−11.132	9.86E+12	2.60E+13	1.37E-8
CS2	−16.631	1.01E+13	2.67E+13	1.40E-8
CS3	−0.133	8.49E+12	2.24E+13	1.18E-8
CS3	−5.632	9.66E+12	2.55E+13	1.34E-8
CS3	−11.132	1.04E+13	2.75E+13	1.45E-8
CS3	−16.631	1.03E+13	2.72E+13	1.43E-8
CS4	−0.133	7.64E+12	2.02E+13	1.06E-8
CS4	−5.632	8.48E+12	2.24E+13	1.18E-8
CS4	−11.132	9.27E+12	2.45E+13	1.29E-8
CS4	−16.631	9.09E+12	2.40E+13	1.26E-8
CS5	−0.133	7.73E+12	2.04E+13	1.07E-8
CS5	−5.632	8.66E+12	2.29E+13	1.20E-8
CS5	−11.132	9.12E+12	2.41E+13	1.27E-8
CS5	−16.631	9.08E+12	2.40E+13	1.26E-8
Average		(9.19 ± 0.90)E+12	(2.23 ± 0.24)E13	(1.29 ± 0.14)E-8

[a] The average 2200-m/s thermal flux (ϕ_{2200}) is 4.31E13 $cm^{-2} \cdot s^{-1}$.

[b] Relative to horizontal midplane of the ORR.

[c] $\frac{\phi(E > 0.1 \text{ MeV})}{\phi(E > 1.0 \text{ MeV})} = (2.64 \pm 0.02)$.

[d] $\frac{\text{dpa/s}}{\phi(E > 1.0 \text{ MeV})} = (1.39 \pm 0.01)\text{E-}21$.

Table E.9. Summary of fluence rate and fluence for ORR irradiations

Capsule No.	Capsule position	Specimen identification	Temperature (°F)	Absorbed energy (ft-lb)	Fracture appearance (% shear)	Lateral expansion (mil)	ϕ(E > 1.0 MeV) ($n \cdot cm^{-2} \cdot s^{-1}$)	ϕ (n/cm^2)
				Plates (irradiated at ORR)				
2	CS1-4	A71	90.0	6.3	25.0	1.0	9.59E12	2.43E18
2	CS5-2	A130	120.0	21.5	45.0	10.0	9.59E12	2.43E18
2	CS3-1	A151	120.0	36.1	40.0	18.0	9.59E12	2.43E18
2	CS2-1	A155	90.0	15.7	30.0	6.0	9.59E12	2.43E18
2	CS3-3	A158	120.0	21.7	40.0	14.0	9.59E12	2.43E18
3	CS1-1	A125	90.0	5.4	10.0	0.0	9.59E12	2.43E18
3	CS4-3	A127	90.0	25.8	35.0	10.0	9.59E12	2.43E18
3	CS2-3	A139	90.0	6.8	15.0	0.0	9.59E12	2.43E18
3	CS4-1	A143	120.0	25.4	40.0	12.0	9.59E12	2.43E18
3	CS1-2	A162	120.0	34.3	40.0	14.0	9.59E12	2.43E18
3	CS3-3	ND24	120.0	19.0	40.0	8.0	9.59E12	2.43E18
3	CS3-2	ND26	120.0	19.7	65.0	8.0	9.59E12	2.43E18
3	CS1-4	ND61	120.0	20.0	60.0	8.0	9.59E12	2.43E18
3	CS4-2	ND64	120.0	22.7	65.0	7.0	9.59E12	2.43E18
3	CS1-3	ND66	120.0	19.1	40.0	5.0	9.59E12	2.43E18
4	CS5-4	QDPB	95.0	21.2	55.0	11.0	9.59E12	2.43E18
4	CS4-2	ND33	95.0	11.7	45.0	3.0	9.59E12	2.43E18
4	CS4-3	QDP7	95.0	66.2	100.0	42.0	9.59E12	2.43E18
4	CS2-3	ND31	95.0	52.5	85.0	33.0	9.59E12	2.43E18
4	CS2-4	ND32	95.0	17.3	55.0	9.0	9.59E12	2.43E18
4	CS1-2	QDP2	120.0	24.7	75.0	9.0	9.59E12	2.43E18
4	CS1-3	QDPC	120.0	33.7	80.0	21.0	9.59E12	2.43E18
4	CS3-1	ND36	120.0	60.1	99.0	39.0	9.59E12	2.43E18
4	CS3-3	ND56	120.0	26.0	65.0	13.0	9.59E12	2.43E18
4	CS5-2	ND52	120.0	24.2	70.0	16.0	9.59E12	2.43E18
2	CS2-2	ND22	120.0	19.8	50.0	9.0	9.59E12	2.43E18
2	CS2-3	ND63	120.0	17.7	45.0	6.0	9.59E12	2.43E18
2	CS2-4	ND65	120.0	16.8	45.0	6.0	9.59E12	2.43E18
2	CS1-2	QDPA	120.0	17.1	45.0	4.0	9.59E12	2.43E18
2	CS5-4	QDP4	120.0	19.0	50.0	9.0	9.59E12	2.43E18

Table E.9 (continued)

Capsule No.	Capsule position	Specimen identification	Temperature (°F)	Absorbed energy (ft-lb)	Fracture appearance (% shear)	Lateral expansion (mil)	ϕ(E > 1.0 MeV) ($n \cdot cm^{-2} \cdot s^{-1}$)	ϕ (n/cm^2)
				Nozzle welds (irradiated at ORR)				
2	CS1-1	H2W33	170.0	52.3	80.0	32.6	9.59E12	2.43E18
2	CS1-3	QW263	120.0	42.6	55.0	20.8	9.59E12	2.43E18
2	CS3-2	QW262	50.0	6.7	15.0	0.3	9.59E12	2.43E18
2	CS3-4	QW251	50.0	5.1	5.0	0.1	9.59E12	2.43E18
2	CS5-1	QW242	120.0	20.3	50.0	5.9	9.59E12	2.43E18
2	CS5-3	QW243	120.0	41.7	60.0	20.8	9.59E12	2.43E18
2	CS4-1	QW211	50.0	6.8	20.0	0.3	9.59E12	2.43E18
2	CS4-2	QW222	120.0	56.2	65.0	24.0	9.59E12	2.43E18
2	CS4-3	QW223	170.0	95.2	95.0	47.0	9.59E12	2.43E18
2	CS4-4	QW231	120.0	48.7	70.0	20.6	9.59E12	2.43E18
4	CS1-4	H2W12	90.0	20.7	35.0	5.7	9.59E12	2.43E18
4	CS2-1	H2W13	90.0	26.0	40.0	1.3	9.59E12	2.43E18
4	CS2-2	QW281	90.0	13.5	40.0	6.9	9.59E12	2.43E18
4	CS4-1	QW282	90.0	35.2	45.0	12.5	9.59E12	2.43E18
4	CS3-5	QW283	90.0	14.2	45.0	3.4	9.59E12	2.43E18
				Seam welds (irradiated at ORR)				
3	CS3-4	HFE1B	30.0	6.3	0.0	0.3	9.59E12	2.43E18
3	CS3-1	HFE2B	120.0	6.4	20.0	0.4	9.59E12	2.43E18
3	CS4-4	HFE3B	120.0	49.6	65.0	28.5	9.59E12	2.43E18
3	CS5-3	HFE4B	30.0	4.4	5.0	0.1	9.59E12	2.43E18
3	CS2-4	HFE6B	120.0	53.2	40.0	21.8	9.59E12	2.43E18
3	CS2-1	HFE1C	30.0	70.5	65.0	32.0	9.59E12	2.43E18
3	CS2-2	HFE2C	30.0	5.7	5.0	0.1	9.59E12	2.43E18
3	CS5-1	HFE3C	120.0	72.6	80.0	40.2	9.59E12	2.43E18
3	CS5-4	HFE5C	30.0	4.0	5.0	0.0	9.59E12	2.43E18
3	CS5-2	HFE6C	120.0	65.2	50.0	35.8	9.59E12	2.43E18
4	CS4-4	HFD1B	75.0	8.4	40.0	1.3	9.59E12	2.43E18
4	CS1-1	HFD1C	75.0	17.4	40.0	4.5	9.59E12	2.43E18
4	CS5-1	HFD5C	75.0	13.9	35.0	3.1	9.59E12	2.43E18
4	CS5-3	HFD6B	75.0	13.3	20.0	1.1	9.59E12	2.43E18
4	CS3-2	HFD6C	75.0	27.1	30.0	9.9	9.59E12	2.43E18

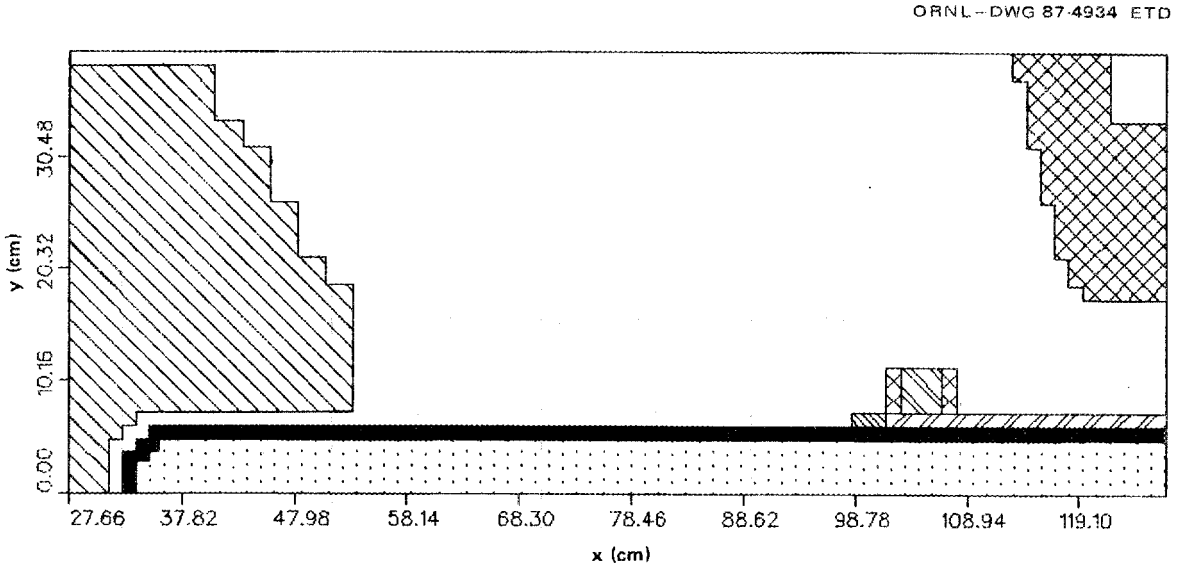

Fig. E.8. HFIR beam tube 2.

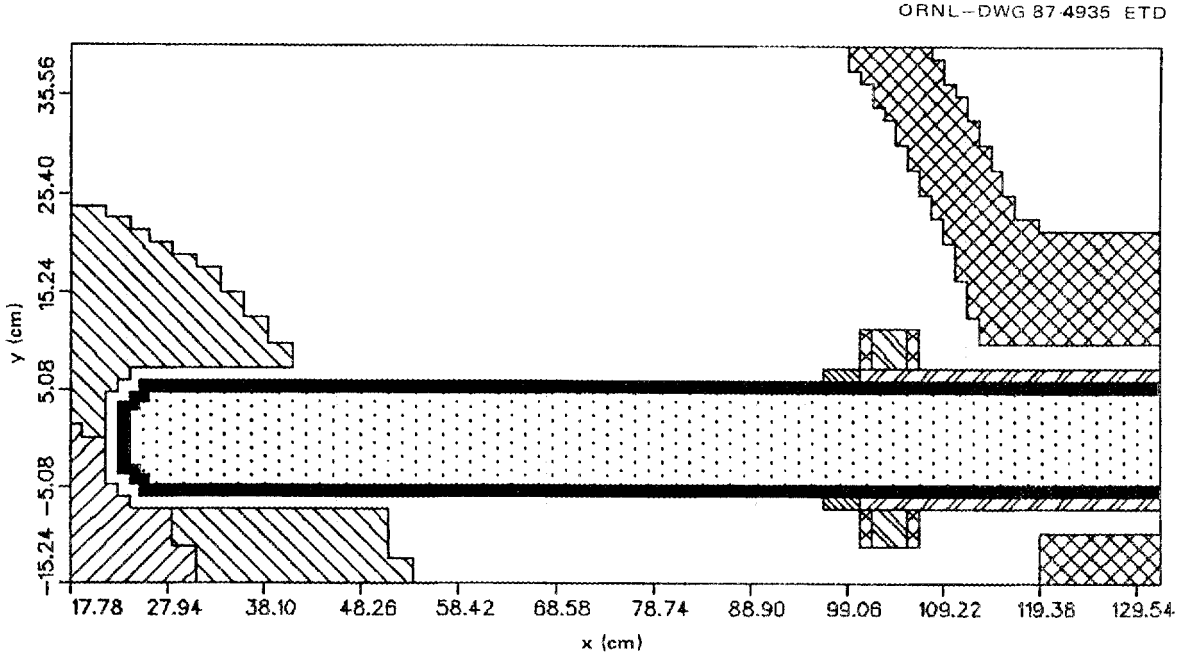

Fig. E.9. HFIR beam tube 3.

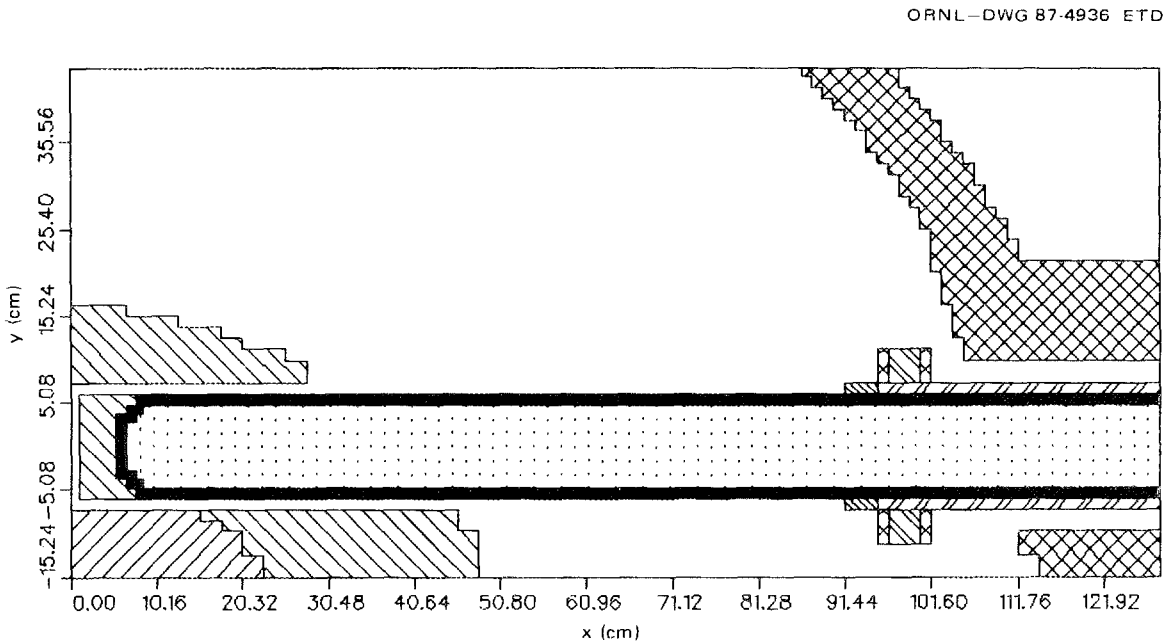

Fig. E.10. HFIR beam tube 4.

the aluminum liner, the steel tube surrounding the aluminum, and the collar region. Metal components in each of the last three zones were homogenized with water also enclosed within the zones to preserve the proper material composition. The coordinate system (Figs. E.8–E.11) was such that x direction was along the length of the tube headed outward, y was upward in the figure, and z was out of the page. The total mesh sizes for the problems were as shown in Table E.10. The 56-group ELXSIR cross-section library used for the 2-D work was also used for the 3-D problems. All problems used a symmetrical S10 direction set having 140 directions.

The 3-D discrete ordinates calculation determined the averaged fluence rate in each mesh cell as a function of energy. The five response functions (Table E.11) were then folded with the fluence rate to give

Table E.10. Space mesh sizes for the geometric mock-ups

Tube model	Mesh		
	x	y	z
2	53	32	12
3	57	44	15
4	66	47	12
4x	32	33	6

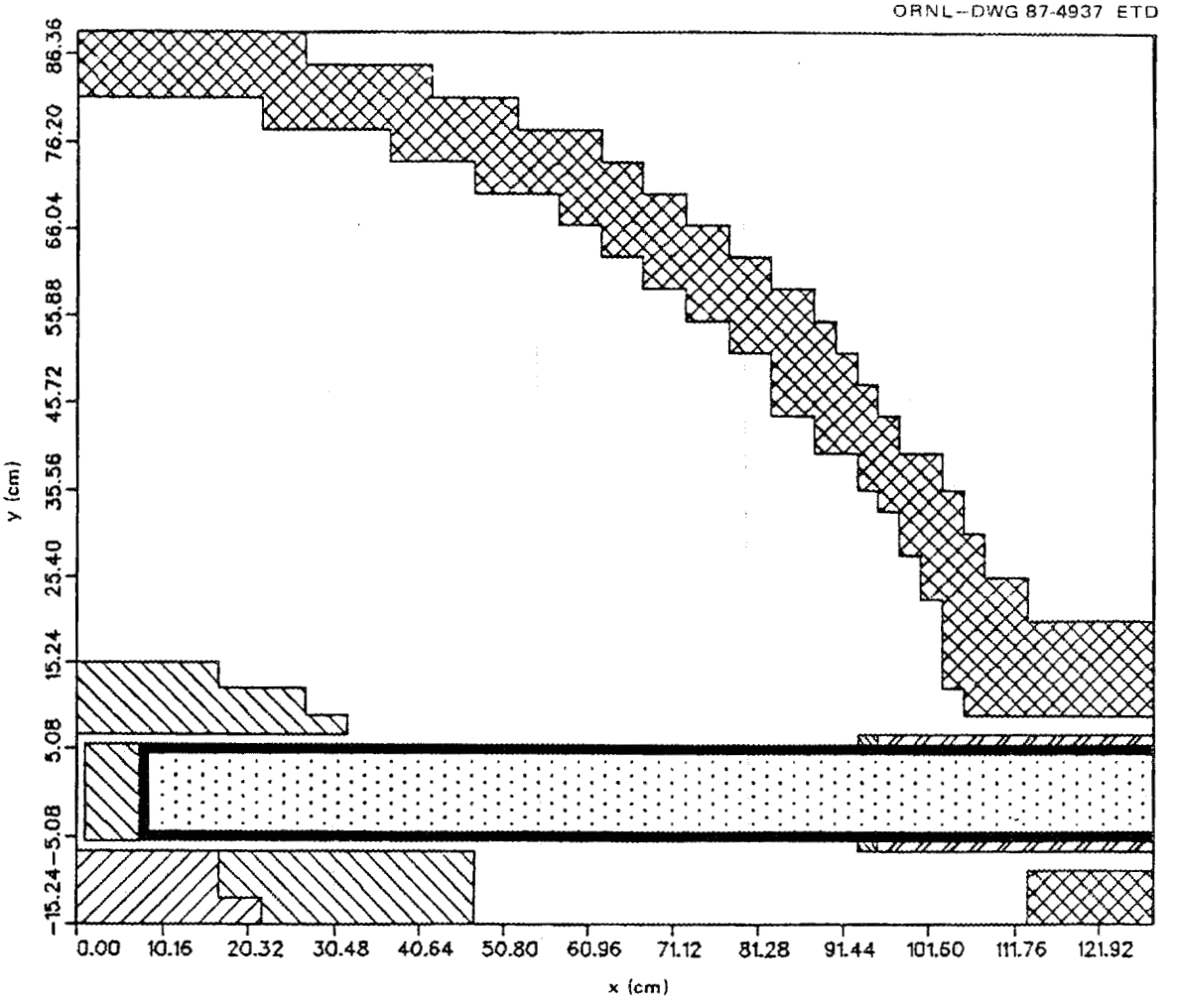

Fig. E.11. HFIR beam tube model HB-4x.

Table E.11. Response functions

$^{58}Ni(n,p)^{58}Co$
$^{54}Fe(n,p)^{54}Mn$
Displacements per atom
Fluence with E > 0.1 MeV
Fluence with E > 1.0 MeV

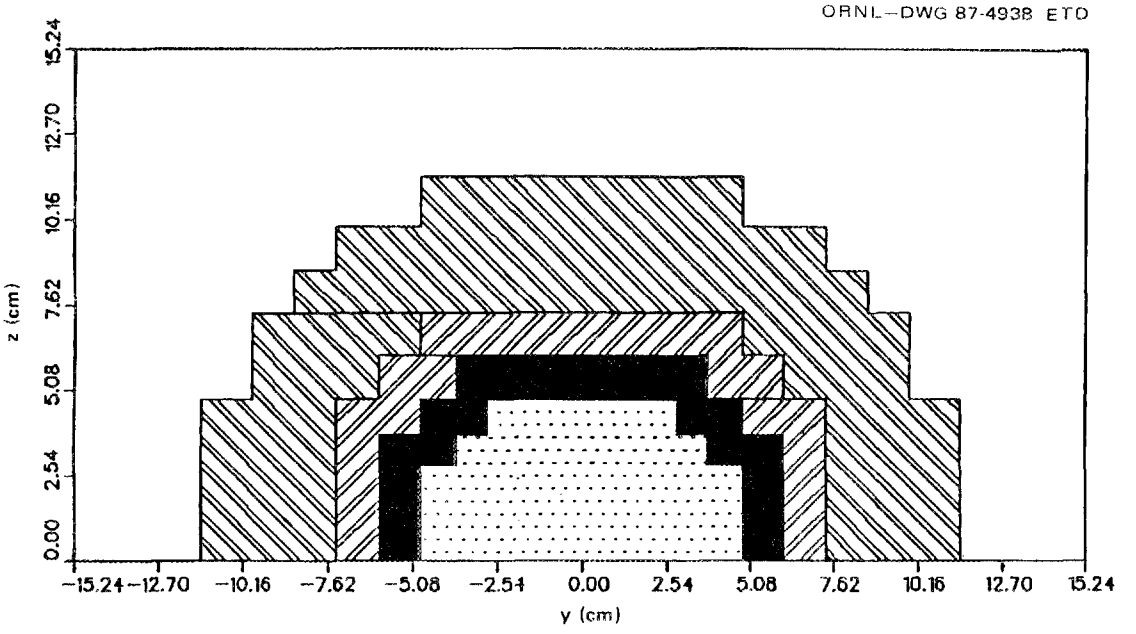

Fig. E.12. HFIR beam tube 4.

integral response maps. The responses at specific points were found from these maps. Linear interpolation between cell centers was used to improve accuracy in areas where the response change from cell to cell was significant.

Three flux calculations were conducted as checks on accuracy:

1. Comparison of 3-D and 2-D models: A comparison of the TORT 3-D calculation to a more conventional 2-D calculation for the same geometry (no beam tubes) shows a ratio of 1.056 at the inner surface of the vessel. This satisfied the requirement of good agreement for the simple geometry.
2. Mesh convergence: Two mesh sizes were used for the 3-D model. The finer mesh resulted in a 5% lower value of the flux. This indicated that a sufficiently fine mesh was being used.
3. Size of model: As explained earlier, 3-D models were constructed for areas enclosing a single beam tube. The proximity of the boundaries to the beam tube affects the accuracy of the calculation and, of course, limits the area of the vessel over which fluxes can be calculated. The position of the boundaries parallel to the beam tube was varied to establish that the boundaries were sufficiently removed from the beam tube.

It was anticipated that because of neutron source uncertainties, the absolute values of the calculated fluxes could have a significant error. However, the relative values, which are the ones required for the fracture-mechanics analysis, were expected to be more precise. To correct for a possible source error and also to serve as a check on the accuracy of relative values, calculated values of the flux were compared

with experimental values associated with the surveillance capsule flux monitors. The results are shown in Table E.12.

The nickel-to-iron ratio for three of the monitors showed anomalous results and were discarded in determining the average calculated-to-experimental (C/E) ratio. Inclusion of these three sensors would have resulted in fluence values ~3% higher. The average C/E ratio was 0.69 with a one standard deviation of 10%.

The 304 stainless steel dosimeters used in the HFIR surveillance capsules have also been checked against pure iron and nickel monitors that have received a quality assurance assessment in the Nuclear Regulatory Commission Surveillance Dosimetry Improvement Program. The results indicate that the 304 stainless steel dosimeter activities are within 5% of the pure nickel and iron monitor activities.

Calculated fluxes for the vessel wall are presented in Figs. E.13–E.17 and in Tables E.13–E.18. Figure E.15 also includes data for HB-1-A and HB-4-A surveillance capsules, as does Table E.19; Figs. E.18 and E.19 and Tables E.20 and E.21 include data for HB-1, HB-3, and HB-4 surveillance capsules.

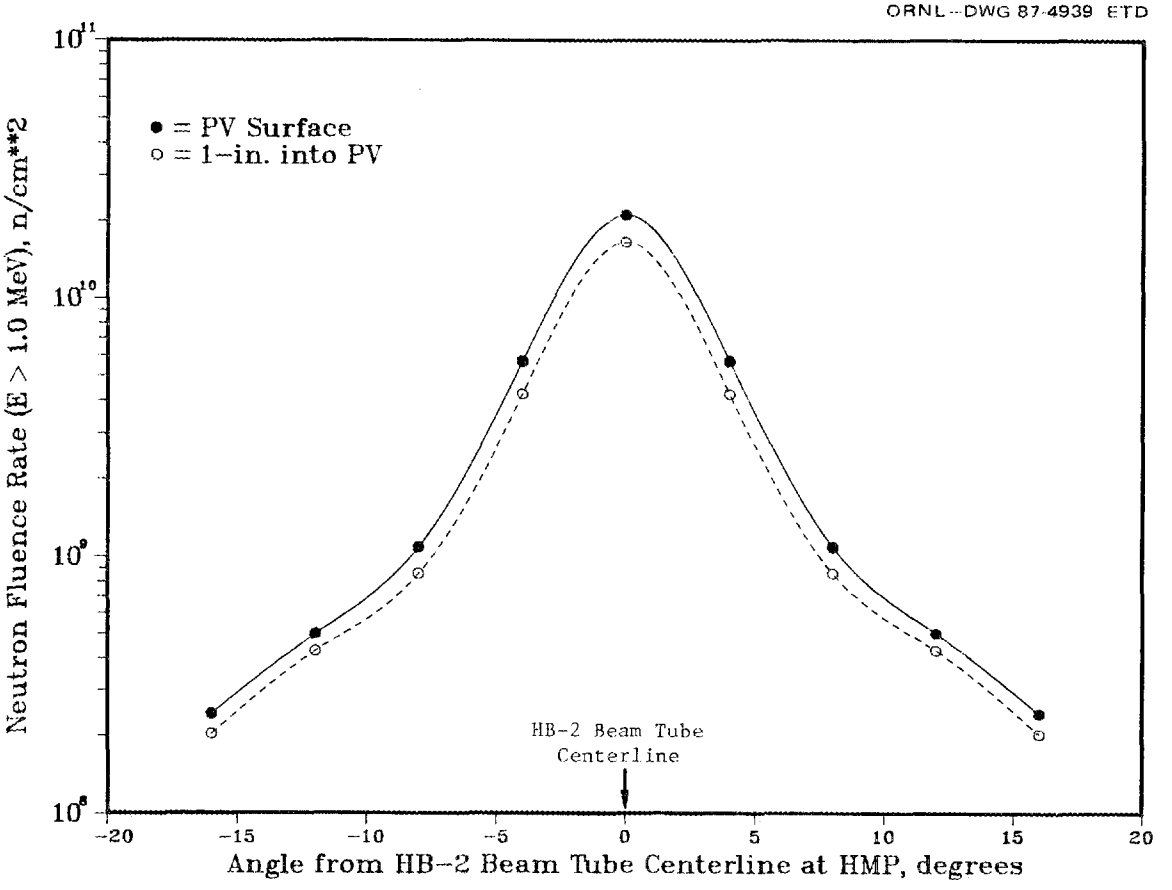

Fig. E.13. Neutron flux (E > 1 MeV) at horizontal midplane vs angle from center of HB-2 beam tube.

Table E.12. Comparison of measured and calculated reaction rates for the surveillance samples removed in 1986

Key	Coupon identification	Bail identification	$^{58}Ni(n,p)^{58}Co$			$^{54}Fe(n,p)^{54}Mn$			Calculated values of ϕ^a		
			C (Bq/atom)	E (Bq/atom)	C/E	C (Bq/atom)	E (Bq/atom)	C/E	$\phi_C(E > 1.0\ MeV)$ $(n \cdot cm^{-2} \cdot s^{-1})$	$\phi_C(E > 0.1\ MeV)$ $(n \cdot cm^{-2} \cdot s^{-1})$	dpa/s
1	3	HB-1-25	8.58E-17	1.47E-16	0.584	6.71E-17	1.11E-16	0.605	5.03E+8	1.14E+9	7.47E-13
4	3	HB-4-31[b]	4.05E-17	5.85E-17	0.692	3.17E-17	3.52E-17	0.901	2.31E+8	4.88E+8	3.38E-13
4	8	HB-4-32[b]	8.58E-17	8.52E-17	1.010	6.71E-17	5.69E-17	1.180	5.03E+8	1.14E+9	7.47E-13
2	7	HB-2-9	1.49E-16	2.47E-16	0.607	1.17E-16	1.95E-16	0.638	7.67E+8	1.34E+9	1.09E-12
2	5	HB-2-11	1.49E-16	2.35E-16	0.634	1.17E-16	1.82E-16	0.643	7.67E+8	1.34E+9	1.09E-12
3	5	HB-3-42[b]	1.27E-16	1.37E-16	0.927	9.90E-17	8.67E-17	1.140	8.10E+8	1.82E+9	1.16E-12
3	8	HB-3-48	2.11E-16	3.17E-16	0.666	1.65E-16	2.36E-16	0.699	1.23E+9	2.65E+9	1.80E-12
3	3	HB-3-50	9.69E-17	1.34E-16	0.723	7.49E-17	1.03E-16	0.727	6.30E+8	1.33E+9	8.93E-13
6	2	HB-1-A-68	4.29E-17	5.68E-17	0.755	3.44E-17	4.88E-17	0.705	1.62E+8	2.40E+8	2.44E-13
6	3	HB-1-A-69	4.36E-17	5.68E-17	0.768	3.50E-17	4.88E-17	0.717	1.61E+8	2.35E+8	2.44E-13
7	8	HB-4-A-73	5.05E-17	7.01E-17	0.720	4.03E-17	5.96E-17	0.676	2.07E+8	3.32E+8	3.08E-13
7	6	HB-4-A-77	4.78E-17	5.51E-17	0.868	3.84E-17	4.61E-17	0.833	1.75E+8	2.54E+8	2.65E-13

[a] Not corrected for C/E.

[b] Points discarded in determining average C/E ratio.

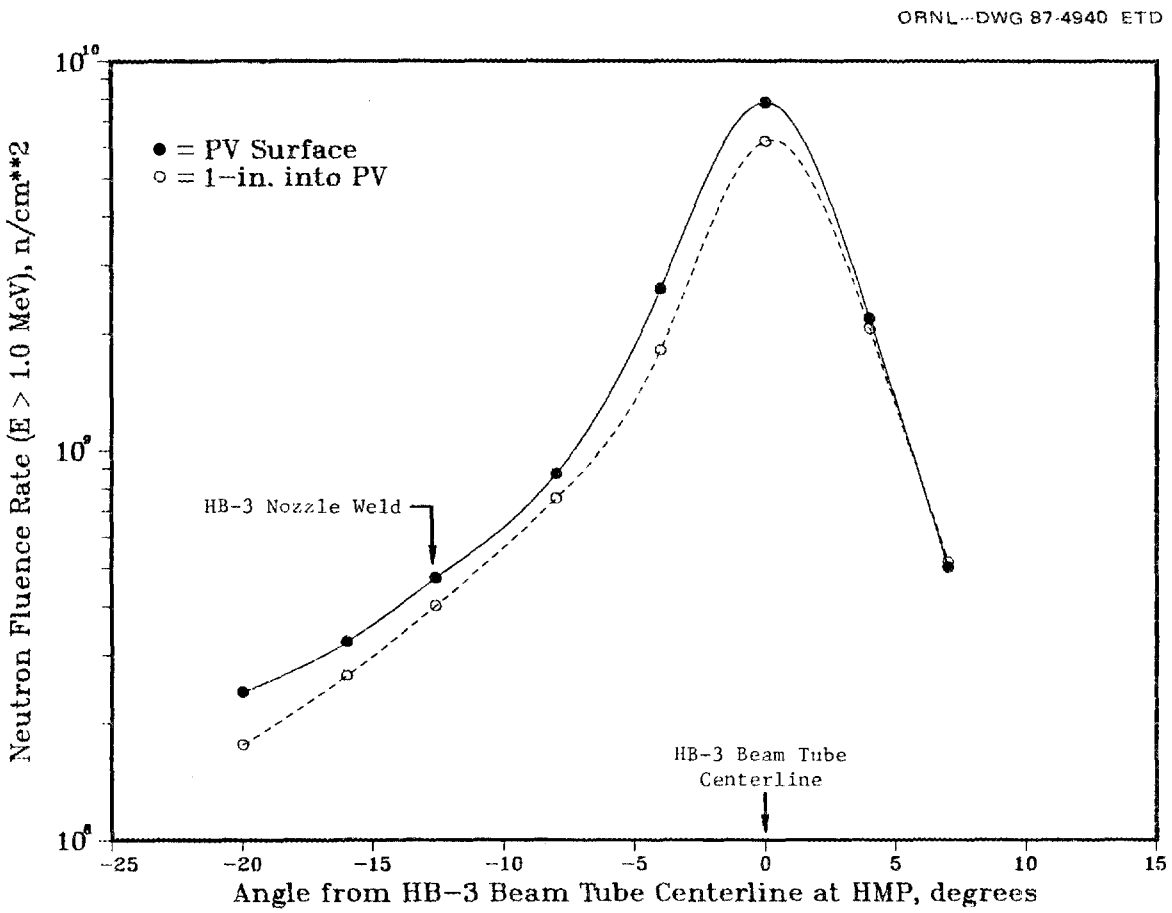

Fig. E.14. Neutron flux (E > 1 MeV) at horizontal midplane vs angle from center of HB-3 beam tube.

The angle referred to for the vessel wall fluxes lies in the horizontal midplane of the core and is measured from a line that extends from the center of the core to a point on the centerline of each beam tube that is a distance from the center of the core equal to the inner radius of the vessel. A positive angle extends around the vessel in a clockwise direction looking down on the vessel.

Fluxes were also calculated for the specific locations of the HB-1, HB-4, and HB-3 nozzle welds and the seam weld, all in the horizontal midplane (Table E.22). In addition, fluxes were calculated as a function of axial and radial positions without the beam tubes present (Figs. E.20 and E.21). At the location of the vertical center of the seam weld, the flux with the beam tubes included was 1.61 times that without the beam tubes. The flux at the location of the lower girth weld was 1.4 times that at the core horizontal midplane, indicating that the beryllium-water combination is a better shield than water alone.

Based on the above data, fluxes were tabulated for each of the Charpy surveillance specimens. These data are included in Table E.23.

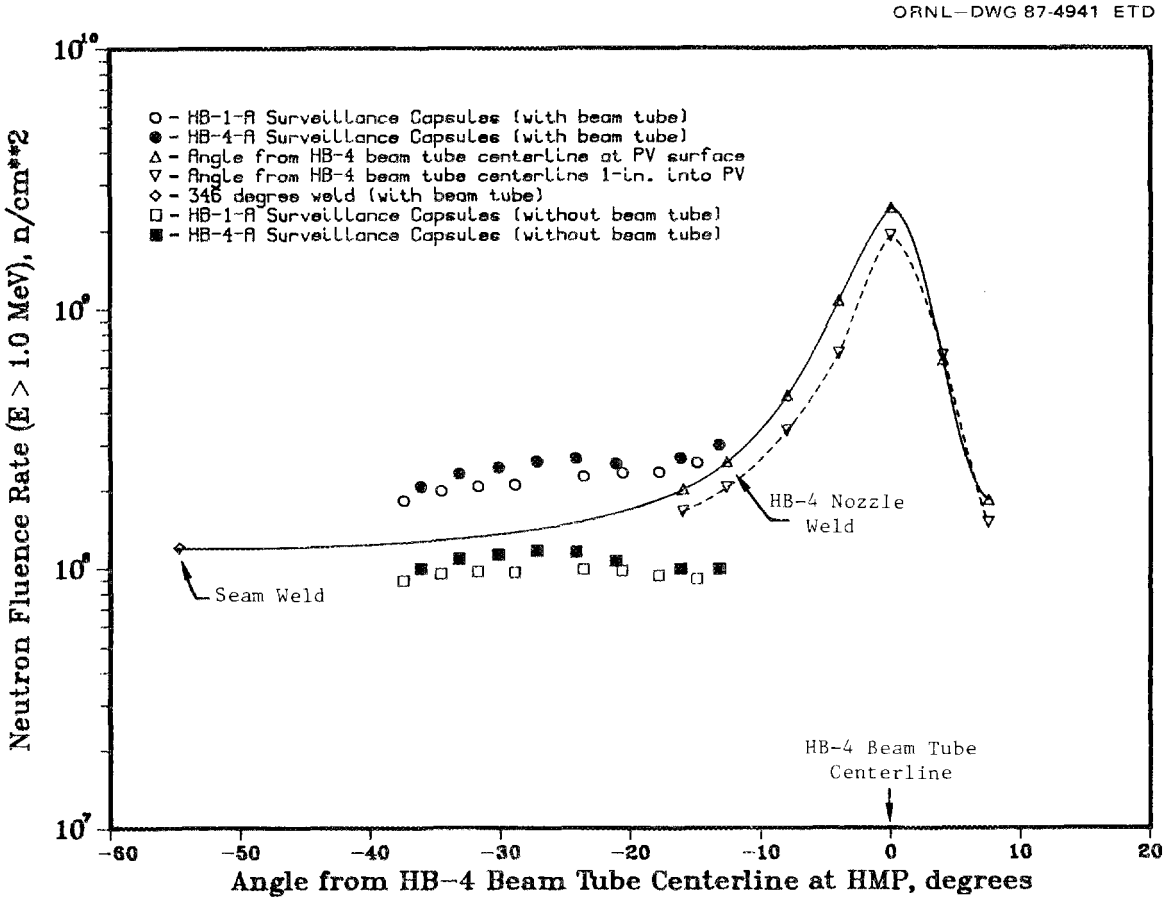

Fig. E.15. Neutron flux (E > 1 MeV) at horizontal midplane vs angle from center of HB-4 beam tube.

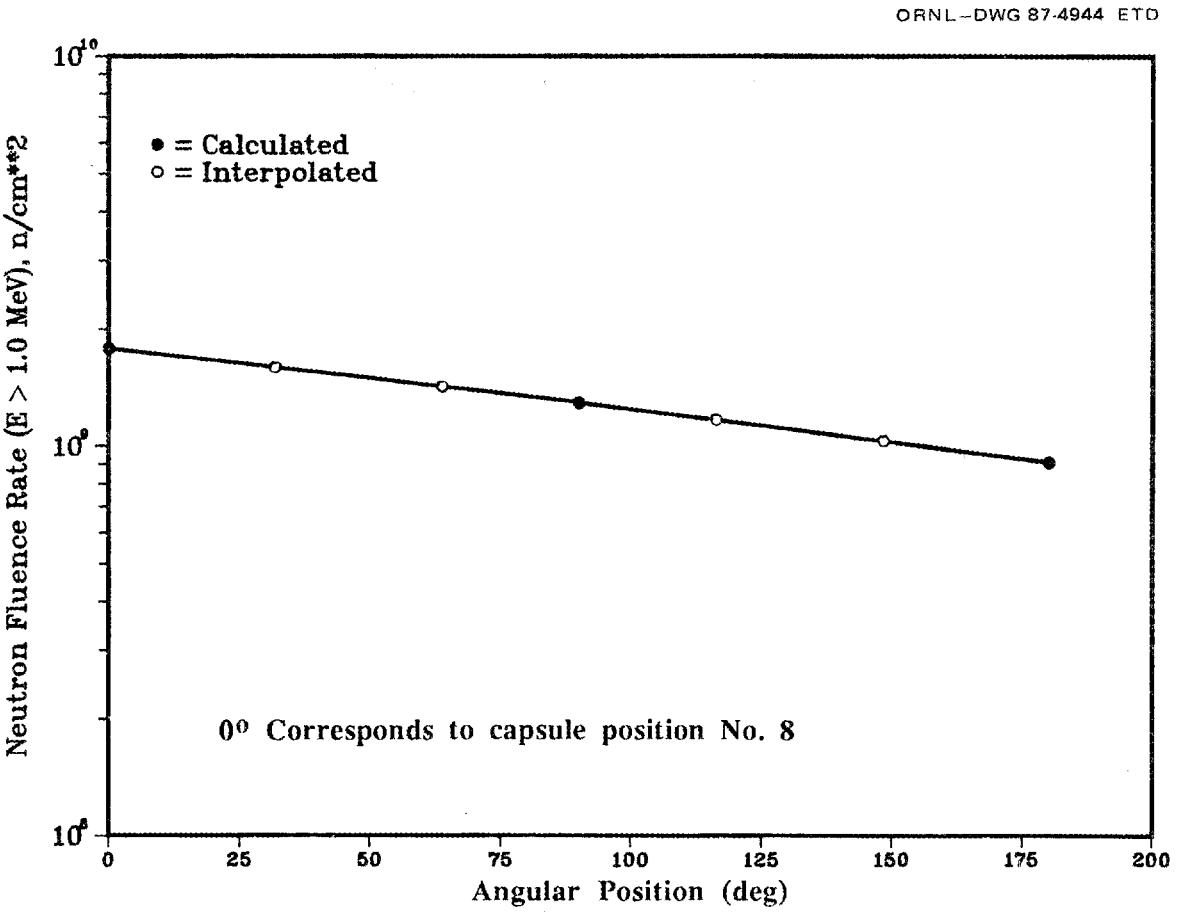

Fig. E.16. Neutron flux (E > 1 MeV) in surveillance capsules around collar of HB-3 beam tube.

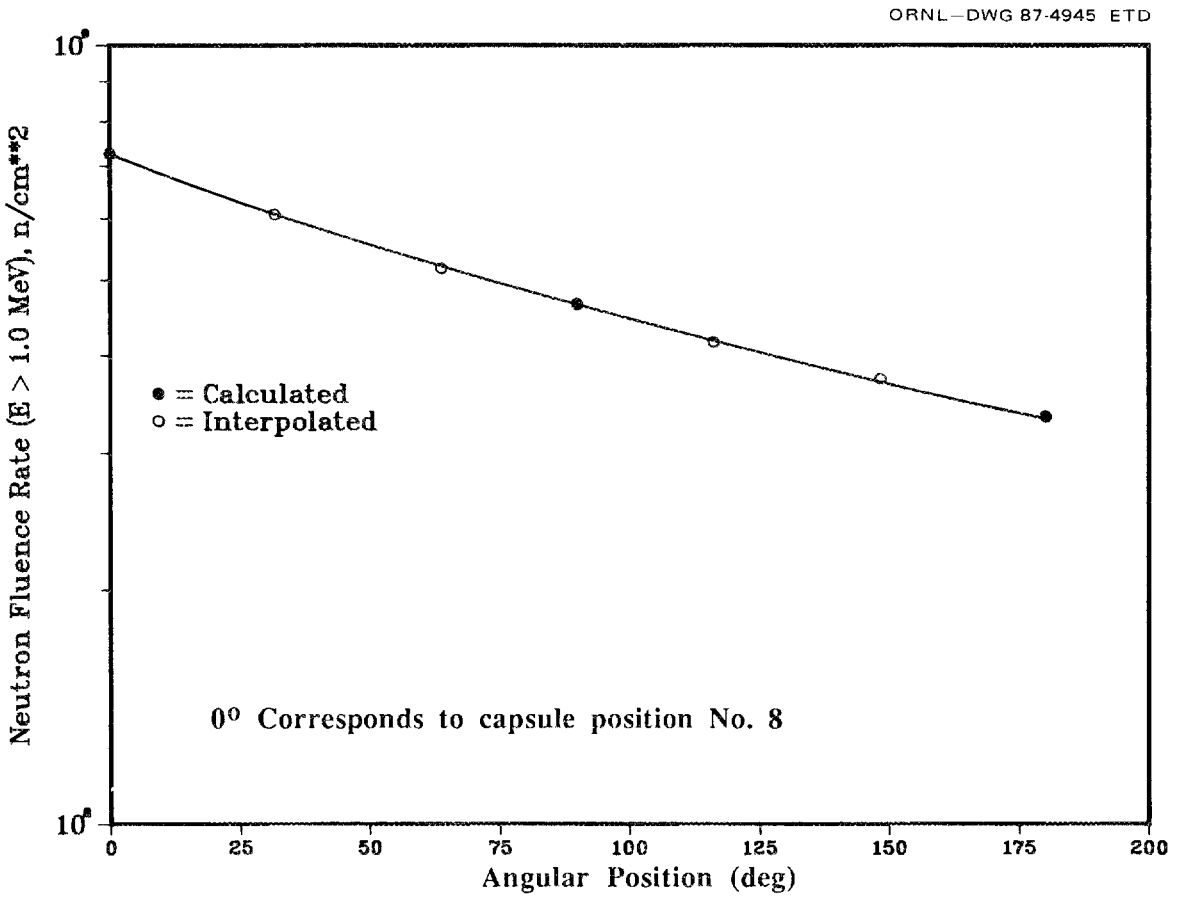

Fig. E.17. Neutron flux (E > 1 MeV) in surveillance capsules around collar of HB-4 beam tube.

Table E.13. Neutron fluence rate vs angle from HB-2 centerline at horizontal midplane

Angle from beam tube centerline at HMP (deg)	Pressure-vessel surface [n/(cm^{-2}•s^{-1})]	1 in. into pressure vessel [n/(cm^{-2}•s^{-1})]
0	2.10E10	1.65E10
4	5.69E9	4.25E9
8	1.09E9	8.59E8
12	5.00E8	4.29E8
16	2.44E8	2.03E8

Table E.14. Neutron fluence rate vs angle from HB-3 centerline at horizontal midplane

Angle from beam tube centerline at HMP (deg)	Pressure-vessel surface [n/(cm^{-2}•s^{-1})]	1 in. into pressure vessel [n/(cm^{-2}•s^{-1})]
7.0	5.03E8	5.19E8
4.0	2.18E8	2.05E9
0.0	7.98E9	6.21E9
−4.0	2.60E9	1.81E9
−8.0	8.71E8	7.54E8
−12.6	4.73E8	4.02E8
−16.0	3.25E8	2.66E8
−20.0	2.41E8	1.76E8

Table E.15. Neutron fluence rate vs angle from HB-4 centerline at horizontal midplane

Angle from beam tube centerline at HMP (deg)	Pressure-vessel surface [n/(cm^{-2}•s^{-1})]	1 in. into pressure vessel [n/(cm^{-2}•s^{-1})]
7.0	1.84E8	1.50E8
4.0	6.34E8	6.59E8
0.0	2.44E9	1.92E9
−4.0	1.08E9	6.75E8
−8.0	4.62E8	3.41E8
−12.6[a]	2.56E8	2.05E8
−16.0	2.02E8	1.66E8
−54.7	1.21E8	1.01E8

[a]HB-4 nozzle weld location.

Table E.16. Neutron fluence rate vs distance into pressure vessel at nozzle opening of HB-3

Distance into pressure vessel (cm)	Fluence rate [n/(cm^{-2}•s^{-1})]
0.0	1.78E9
2.54	1.50E9
5.08	1.23E9

Table E.17. Neutron fluence rate vertical distribution from horizontal midplane

Z (cm)	Fluence rate from beam tube centerline — plane of collar [n/(cm^{-2}•s^{-1})]	
	HB-2	HB-4
0	2.92E10	4.15E9
4	3.00E10	4.03E9
8	8.31E9	1.22E9
12	2.95E9	4.94E8
14	1.93E9	3.60E8
14.6	1.67E9	3.25E8
17.8[a]	1.10E9	

[a]Extrapolated.

Table E.18. Neutron fluence rate vertical distribution from horizontal midplane at HB-3

Z (cm)	Fluence rate at nozzle weld [n/(cm^{-2}•s^{-1})]	Fluence rate from beam tube centerline — PV surface [n/(cm^{-2}•s^{-1})]	Fluence rate from beam tube centerline — plane of collar n/(cm^{-2}•s^{-1})]
0	4.97E8	5.52E9	8.45E9
4	4.74E8	5.42E9	8.27E9
8	4.73E8	1.63E9	2.41E9
12	4.57E8	7.29E8	9.28E8
12.37			8.90E8
14			6.60E8
16			4.83E8
23.8		1.62E8	

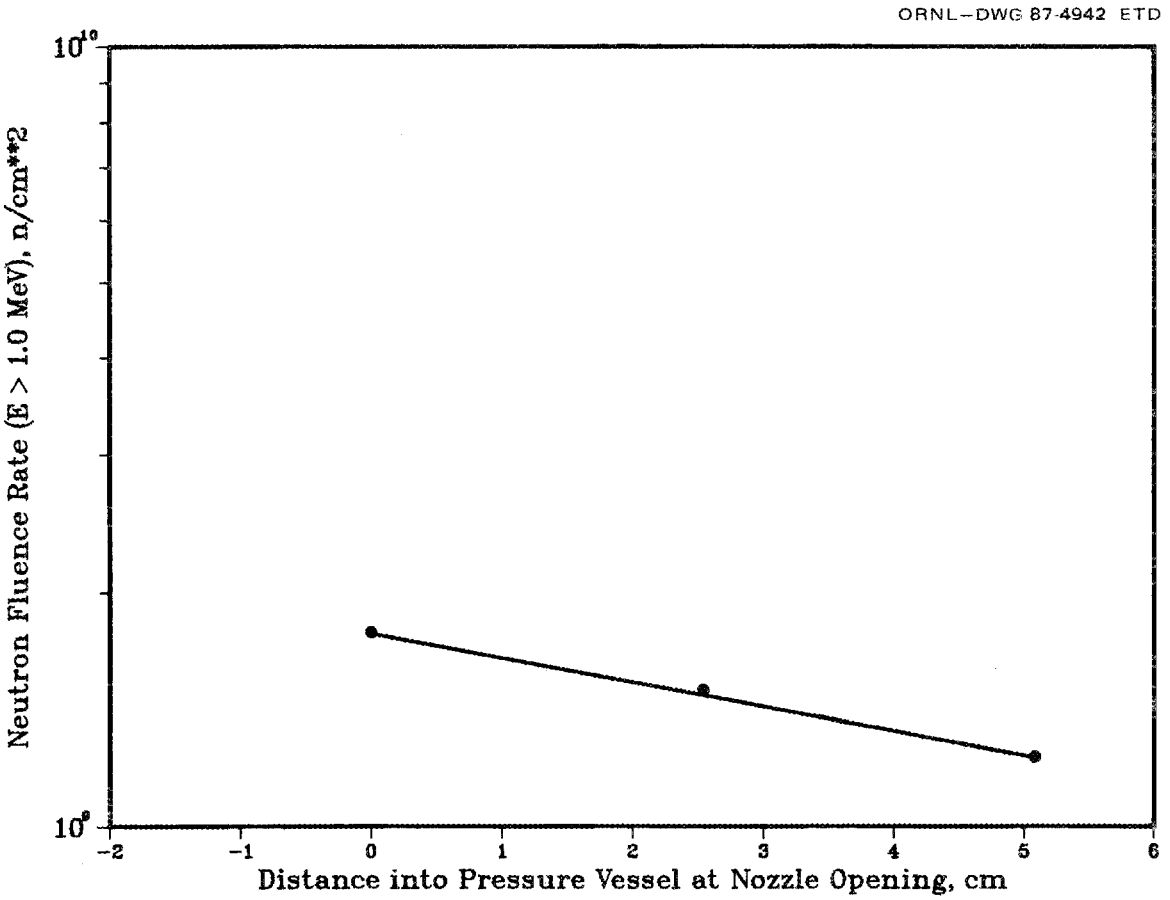

Fig. E.18. Neutron flux (E > 1 MeV) at horizontal midplane vs distance into pressure vessel at HB-3 nozzle opening.

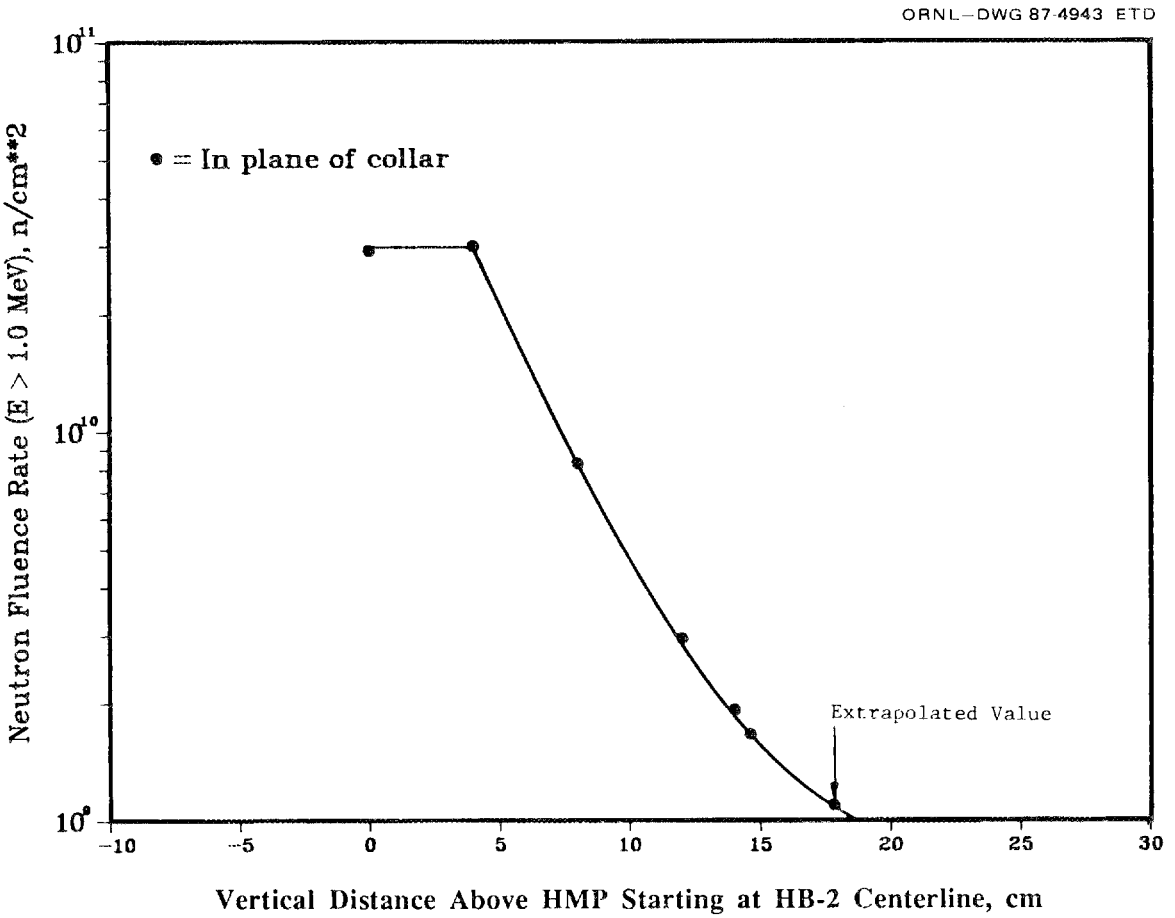

Fig. E.19. Neutron flux (E > 1 MeV) vs vertical distance above center of HB-2 beam tube.

Table E.19. Neutron fluence rate vs surveillance capsule locations at HB-1-A and HB-4-A

Degrees	Key	Coupon identification	Fluence rate [n/(cm^{-2}·s^{-1})]		
			No beam tubes (coarse mesh)	With beam tubes (coarsh mesh)	With beam tubes (fine mesh)
−14.9	6	1	9.09E7	2.54E8	2.38E8
−17.8	6	2	9.39E7	2.34E8	2.40E8
−20.6	6	3	9.81E7	2.33E8	2.21E8
−23.6	6	4	9.91E7	2.27E8	
−28.9	6	5	9.68E7	2.11E8	
−31.7	6	6	9.74E7	2.07E8	
−34.5	6	7	9.54E7	1.99E8	
−37.4	6	8	8.96E7	1.82E8	
−36.1	7	1	1.00E8	2.07E8	
−33.2	7	2	1.09E8	2.31E8	
−30.2	7	3	1.13E8	2.46E8	
−27.2	7	4	1.17E8	2.59E8	
−24.2	7	5	1.16E8	2.66E8	
−21.1	7	6	1.07E8	2.53E8	2.37E8
−16.1	7	7	9.96E7	2.66E8	2.50E8
−13.2	7	8	9.54E7	2.99E8	2.76E8

Table E.20. Neutron fluence rate vs surveillance capsule location at HB-3

Angle around beam tube (deg)	Key	Coupon identification	Fluence rate in plane of collar [n/(cm^{-2}·s^{-1})]
0.0	3	8	1.78E9
31.7	3	7 and 9	1.59E9
63.8	3	6 and 10	1.42E9
90.0	3		1.29E9
116.0	3	1 and 5	1.17E9
148.3	3	2 and 4	1.03E9
180.0	3	3	9.10E8

Table E.21. Neutron fluence rate vs surveillance capsule location at HB-1 and HB-4

Angle around beam tube (deg)	HB-1		HB-4		Fluence rate [n/(cm^{-2}•s^{-1})]
	Key	Coupon identification	Key	Coupon identification	
0.0	1	3	4	8	7.27E8
31.7	1	2 and 4	4	7 and 9	6.06E8
63.8	1	1 and 5	4	6 and 10	5.17E8
90.0	1		4		4.65E8
116.0	1	6 and 10	4	1 and 5	4.16E8
148.3	1	7 and 9	4	2 and 4	3.73E8
180.0	1	8	4	3	3.34E8

Table E.22. Fluence rate and fluence for HFIR weld materials

Position	ϕ(E > 1.0 MeV)[a] (n•cm^{-2}•s^{-1})	ϕ[b,c] (n•cm^{-2})
30° nozzle weld at HB-4	2.56E8	1.40E17
96° nozzle weld at HB-3	4.73E8	2.62E17
346°30' seam weld:		
at PV surface — HB-4x	1.21E8	6.69E16
1/2 in. into weld — HB-4x	1.11E8	6.14E16
1 in. into weld — HB-4x	1.01E8	5.58E16

[a]Fluence rates (E > 1.0 MeV) are obtained by dividing the calculated values by the average C/E ratio of 0.69.

[b]Fluence values are obtained by multiplying the fluence rates by the effective full-power seconds.

[c]Fluence corresponds to 17.3 EFPY (1.73 × 10^3 MW years).

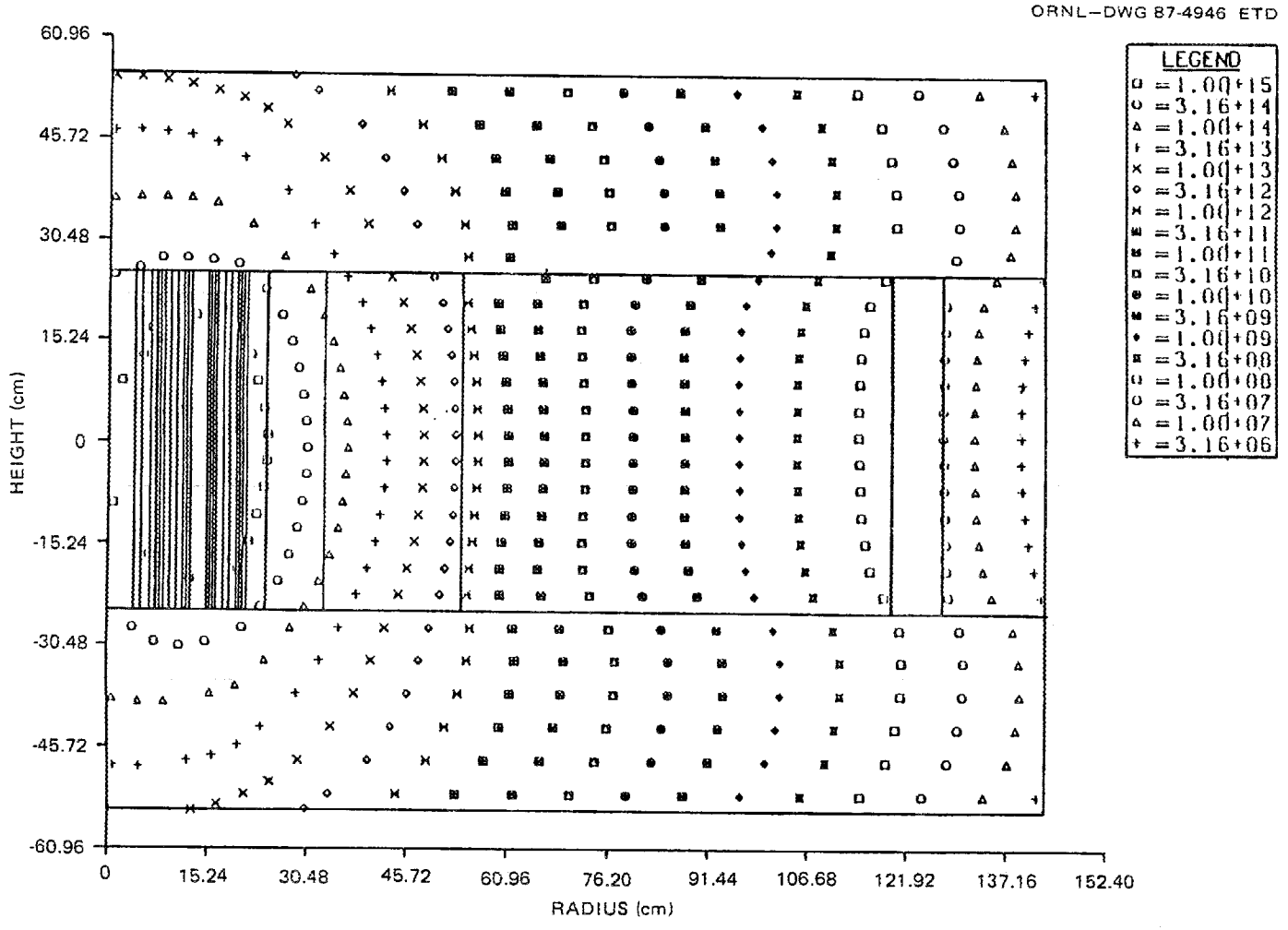

Fig. E.20. Isofluxes (E > 0.1 MeV) from 2-D (R-Z) analysis without beam tubes.

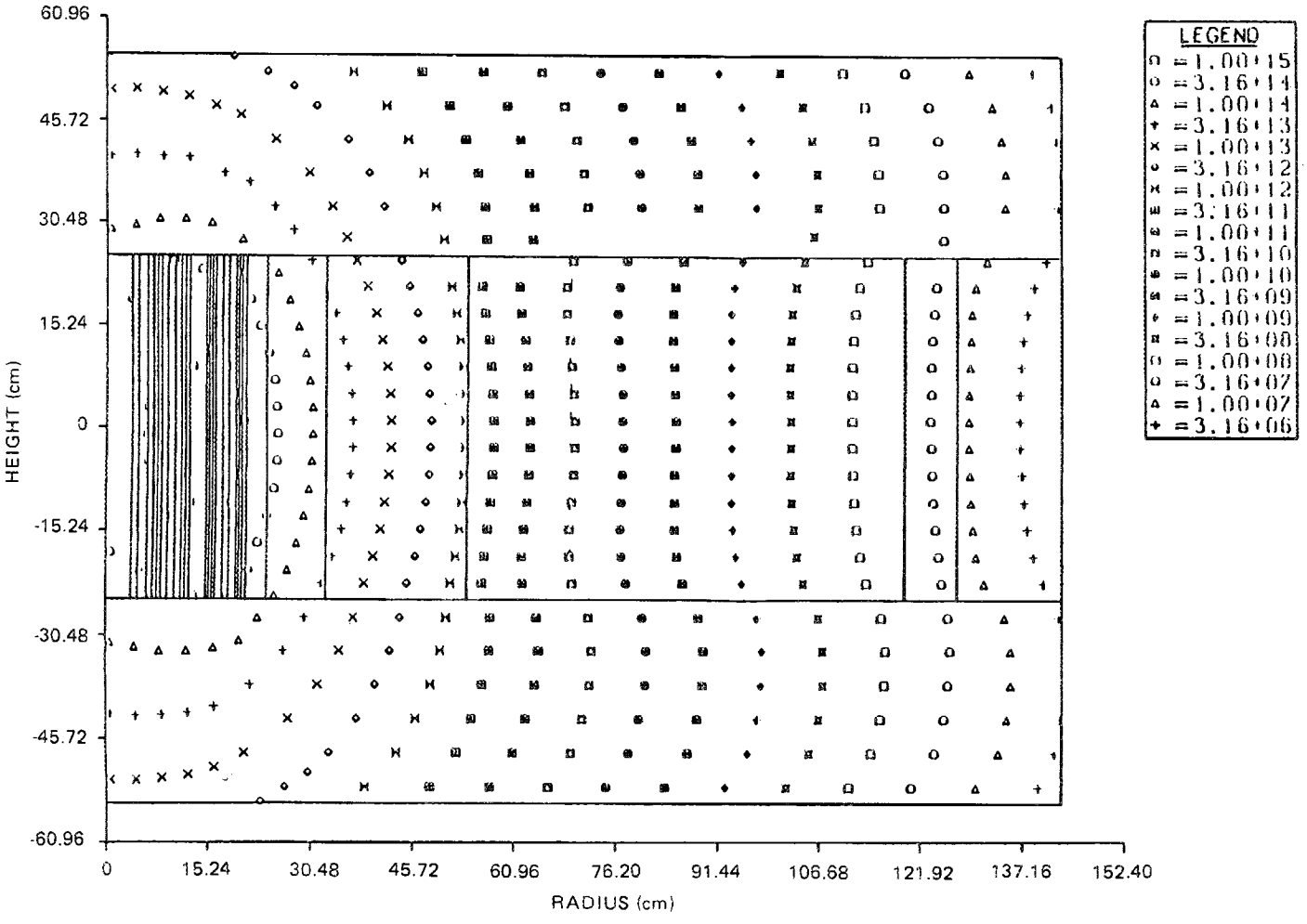

Fig. E.21. Isofluxes (E > 1.0 MeV) from 2-D (R-Z) analysis without beam tubes.

Table E.23. Fluence rate and fluence for HFIR pressure-vessel surveillance specimens

Key	Coupon identification	Date removed	Specimen No.	Test temperature (°F)	Absorbed energy (ft-lb)	Fracture appearance (% shear)	Lateral expansion (mil)	ϕ_N[a] ($n \cdot cm^{-2} \cdot s^{-1}$)	ϕ[b] ($n \cdot cm^{-2}$)
1	1	1969	B7	−40.0	20.0	9.0	0.0	5.17E8	3.81E16
			B19	0.0	43.0	26.0	0.0	5.17E8	3.81E16
			B8	40.0	46.0	51.0	0.0	5.17E8	3.81E16
1	2	1983	B44	−40.0	9.7	10.0	8.5	6.06E8	2.87E17
			B43	0.0	20.1	30.0	4.5	6.06E8	2.87E17
			B45	40.0	30.0	30.0	19.0	6.06E8	2.87E17
1	3	1986	B36	−50.0	15.4	5.0	1.7	7.27E8	4.02E17
			B34	−20.0	5.7	5.0	0.7	7.27E8	4.02E17
			B35	50.0	61.8	55.0	31.7	7.27E8	4.02E17
1	4	1974	B4	−22.0	37.0	0.0	27.5	6.06E8	1.23E17
			B5	40.0	41.0	0.0	33.3	6.06E8	1.23E17
			B6	80.0	67.5	0.0	51.6	6.06E8	1.23E17
1	5[c]		B31					5.17E8	
			B32					5.17E8	
			B33					5.17E8	
1	6	1969	B1	−80.0	14.0	5.0	0.0	4.16E8	3.06E16
			B2	0.0	44.0	43.0	0.0	4.16E8	3.06E16
			B3	60.0	65.0	66.0	0.0	4.16E8	3.06E16
1	7[c]		B25					3.73E8	
			B26					3.73E8	
			B27					3.73E8	
1	8[c]		B21					3.34E8	
			B22					3.34E8	
			B23					3.34E8	

Table E.23 (continued)

Key	Coupon identification	Date removed	Specimen No.	Test temperature (°F)	Absorbed energy (ft-lb)	Fracture appearance (% shear)	Lateral expansion (mil)	ϕ_N[a] ($n \cdot cm^{-2} \cdot s^{-1}$)	ϕ[b] ($n \cdot cm^{-2}$)
1	9	1974	B42	−42.0	20.0	0.0	13.8	3.73E8	7.58E16
			B38	0.0	39.0	0.0	29.9	3.73E8	7.58E16
			B37	90.0	89.0	0.0	63.7	3.73E8	7.58E16
1	10[c]		B46					4.16E8	
			B47					4.16E8	
			B48					4.16E8	
2	1	1969	C37	−140.0	16.0	0.0	0.0	1.11E9	8.18E16
			C32	−60.0	43.0	44.0	0.0	1.11E9	8.18E16
			C31	0.0	66.0	77.0	0.0	1.11E9	8.18E16
2	2	1983	C38	−25.0	24.0	30.0	0.0	1.11E9	5.26E17
			C40	−10.0	26.2	25.0	0.0	1.11E9	5.26E17
			C39	25.0	53.6	40.0	0.0	1.11E9	5.26E17
2	4	1974	C41	−60.0	31.0	0.0	0.0	1.11E9	2.26E17
			C49	−4.0	49.0	0.0	0.0	1.11E9	2.26E17
			C48	60.0	95.0	0.0	0.0	1.11E9	2.26E17
2	5	1986	C21	−20.0	17.8	25.0	0.0	1.11E9	6.14E17
			C27	15.0	36.9	50.0	0.0	1.11E9	6.14E17
			C26	40.0	48.8	60.0	0.0	1.11E9	6.14E17
2	7	1986	C16	15.0	25.8	40.0	0.0	1.11E9	6.14E17
			C17	15.0	34.2	30.0	0.0	1.11E9	6.14E17
			C10	40.0	56.0	55.0	0.0	1.11E9	6.14E17
2	8[c]		C58					1.11E9	
			C60					1.11E9	
			C62					1.11E9	

Table E.23 (continued)

Key	Coupon identification	Date removed	Specimen No.	Test temperature (°F)	Absorbed energy (ft-lb)	Fracture appearance (% shear)	Lateral expansion (mil)	ϕ_N[a] ($n \cdot cm^{-2} \cdot s^{-1}$)	ϕ[b] ($n \cdot cm^{-2}$)
2	10[c]		C51					1.11E9	
			C52					1.11E9	
			C57					1.11E9	
2	11[c]		C6					1.11E9	
			C8					1.11E9	
			C9					1.11E9	
2	13	1974	C29	−100.0	9.0	0.0	0.0	1.11E9	2.26E17
			C28	−40.0	47.0	0.0	0.0	1.11E9	2.26E17
			C30	0.0	53.0	0.0	0.0	1.11E9	2.26E17
2	14	1969	C18	−140.0	17.0	0.0	0.0	1.11E9	8.18E16
			C19	−80.0	30.0	6.0	0.0	1.11E9	8.18E16
			C20	−20.0	52.0	58.0	0.0	1.11E9	8.18E16
3	1	1969	D43	−120.0	8.0	0.0	0.0	1.17E9	8.62E16
			D44	−40.0	32.0	28.0	0.0	1.17E9	8.62E16
			D45	20.0	58.0	65.0	0.0	1.17E9	8.62E16
3	2	1983	D25	−20.0	18.6	25.0	0.0	1.03E9	4.88E17
			D23	20.0	28.6	35.0	0.0	1.03E9	4.88E17
			D24	60.0	44.4	40.0	0.0	1.03E9	4.88E17
3	3	1986	D47	35.0	34.4	45.0	0.0	9.10E8	5.03E17
			D48	35.0	37.7	40.0	0.0	9.10E8	5.03E17
			D46	80.0	49.1	55.0	0.0	9.10E8	5.03E17
3	4	1974	D26	−40.0	23.5	0.0	0.0	1.03E9	2.09E17
			D27	0.0	40.0	0.0	0.0	1.03E9	2.09E17
			D28	60.0	95.0	0.0	0.0	1.03E9	2.09E17

Table E.23 (continued)

Key	Coupon identification	Date removed	Specimen No.	Test temperature (°F)	Absorbed energy (ft-lb)	Fracture appearance (% shear)	Lateral expansion (mil)	ϕ_N[a] ($n \cdot cm^{-2} \cdot s^{-1}$)	ϕ[b] ($n \cdot cm^{-2}$)
3	5	1986	D17	0.0	14.8	20.0	0.0	1.17E9	6.47E17
			D16	35.0	22.0	40.0	0.0	1.17E9	6.47E17
			D15	80.0	57.5	50.0	0.0	1.17E9	6.47E17
3	6	1969	D56	−100.0	20.0	0.0	0.0	1.42E9	1.05E17
			D57	−20.0	48.0	57.0	0.0	1.42E9	1.05E17
			D58	40.0	84.0	100.0	0.0	1.42E9	1.05E17
3	7[c]		D33					1.59E9	
			D34					1.59E9	
			D35					1.59E9	
3	8	1986	D36	120.0	79.8	85.0	0.0	1.78E9	9.84E17
			D37	120.0	70.5	80.0	0.0	1.78E9	9.84E17
			D38	120.0	75.2	85.0	0.0	1.78E9	9.84E17
3	9	1974	D55	−60.0	20.0	0.0	0.0	1.59E9	3.23E17
			D54	−20.0	29.0	0.0	0.0	1.59E9	3.23E17
			D53	30.0	63.0	0.0	0.0	1.59E9	3.23E17
3	10[c]		D5					1.42E9	
			D6					1.42E9	
			D8					1.42E9	
4	1	1969	B104	−40.0	17.0	10.0	0.0	4.16E8	3.06E16
			B106	0.0	30.0	37.0	0.0	4.16E8	3.06E16
			B105	40.0	45.0	49.0	0.0	4.16E8	3.06E16
4	2	1983	B116	−20.0	19.5	10.0	6.5	3.73E8	1.77E17
			B117	−20.0	17.1	20.0	4.5	3.73E8	1.77E17
			B118	−20.0	13.4	10.0	1.0	3.73E8	1.77E17

Table E.23 (continued)

Key	Coupon identification	Date removed	Specimen No.	Test temperature (°F)	Absorbed energy (ft-lb)	Fracture appearance (% shear)	Lateral expansion (mil)	ϕ_N[a] ($n \cdot cm^{-2} \cdot s^{-1}$)	ϕ[b] ($n \cdot cm^{-2}$)
4	3	1986	B65	−50.0	6.1	5.0	1.2	3.34E8	1.85E17
			B66	−20.0	18.1	20.0	0.7	3.34E8	1.85E17
			B64	50.0	41.8	55.0	22.6	3.34E8	1.85E17
4	4	1974	B63	−20.0	22.0	0.0	14.6	3.73E8	7.58E16
			B62	20.0	29.0	0.0	26.1	3.73E8	7.58E16
			B61	60.0	69.0	0.0	49.4	3.73E8	7.58E16
4	5[c]		B86					4.16E8	
			B87					4.16E8	
			B88					4.16E8	
4	6	1969	B101	−60.0	14.0	5.0	0.0	5.17E8	3.81E16
			B102	0.0	48.0	40.0	0.0	5.17E8	3.81E16
			B103	60.0	44.0	57.0	0.0	5.17E8	3.81E16
4	7[c]		B107					6.06E8	
			B108					6.06E8	
			B111					6.06E8	
4	8	1986	B81	−50.0	11.6	20.0	0.2	7.27E8	4.02E17
			B82	−20.0	15.3	20.0	1.3	7.27E8	4.02E17
			B70	−20.0	13.9	10.0	0.7	7.27E8	4.02E17
4	9	1974	B83	0.0	21.0	0.0	17.6	6.06E8	1.23E17
			B84	40.0	37.0	0.0	31.3	6.06E8	1.23E17
			B85	80.0	75.0	0.0	55.5	6.06E8	1.23E17
4	10[c]		B112					5.17E8	
			B113					5.17E8	
			B114					5.17E8	

Table E.23 (continued)

Key	Coupon identification	Date removed	Specimen No.	Test temperature (°F)	Absorbed energy (ft-lb)	Fracture appearance (% shear)	Lateral expansion (mil)	ϕ_N[a] ($n \cdot cm^{-2} \cdot s^{-1}$)	ϕ[b] ($n \cdot cm^{-2}$)
5	1	1983	A30	0.0	5.6	10.0	1.0		
			A36	30.0	22.0	25.0	8.5		
			A31	60.0	41.3	25.0	21.0		
5	2[c]		A37						
			A40						
			A43						
5	3[c]		A45						
			A48						
			A51						
5	4[c]		A52						
			A76						
			A77						
5	5[c]		A82						
			A86						
			A87						
5	6[c]		A137						
			A144						
			A146						
5	7[c]		A150						
			A157						
			A58						
6	1	1983	A1	0.0	3.6	10.0	1.5	2.38E8	1.13E17
			A7	40.0	7.4	20.0	1.5	2.38E8	1.13E17
			A2	80.0	35.1	35.0	10.0	2.38E8	1.13E17

Table E.23 (continued)

Key	Coupon identification	Date removed	Specimen No.	Test temperature (°F)	Absorbed energy (ft-lb)	Fracture appearance (% shear)	Lateral expansion (mil)	ϕ_N[a] ($n \cdot cm^{-2} \cdot s^{-1}$)	ϕ[b] ($n \cdot cm^{-2}$)
6	2	1986	A136	55.0	7.6	30.0	0.4	2.40E8	1.33E17
			A140	65.0	10.9	30.0	0.3	2.40E8	1.33E17
			A135	120.0	37.1	65.0	18.8	2.40E8	1.33E17
6	3	1986	A145	55.0	14.9	20.0	0.7	2.21E8	1.22E17
			A141	65.0	8.5	25.0	0.0	2.21E8	1.22E17
			A142	150.0	70.6	90.0	39.6	2.21E8	1.22E17
6	4[c,d]		A147					2.27E8	
			A148					2.27E8	
			A149					2.27E8	
6	5[c,d]		A18					2.11E8	
			A19					2.11E8	
			A23					2.11E8	
6	6[c,d]		A132					2.07E8	
			A133					2.07E8	
			A134					2.07E8	
6	7[c,d]		A25					1.99E8	
			A27					1.99E8	
			A131					1.99E8	
6	8[c,d]		A152					1.83E8	
			A154					1.83E8	
			A159					1.83E8	
7	1[c,d]		A115					2.07E8	
			A118					2.07E8	
			A119					2.07E8	

Table E.23 (continued)

Key	Coupon identification	Date removed	Specimen No.	Test temperature (°F)	Absorbed energy (ft-lb)	Fracture appearance (% shear)	Lateral expansion (mil)	ϕ_N[a] ($n \cdot cm^{-2} \cdot s^{-1}$)	ϕ[b] ($n \cdot cm^{-2}$)
7	2[c,d]		A163					2.31E8	
			A164					2.31E8	
			A165					2.31E8	
7	3[c,d]		A100					2.46E8	
			A105					2.46E8	
			A108					2.46E8	
7	4[c,d]		A166					2.58E8	
			A167					2.58E8	
			A168					2.58E8	
7	5[c,d]		A109					2.66E8	
			A111					2.66E8	
			A114					2.66E8	
7	6	1986	A120	65.0	18.6	35.0	5.0	2.37E8	1.31E17
			A161	85.0	20.1	30.0	7.2	2.37E8	1.31E17
			A124	120.0	38.0	65.0	24.4	2.37E8	1.31E17
7	7	1983	A94	55.0	22.4	25.0	8.5	2.50E8	1.19E17
			A95	55.0	24.0	20.0	7.5	2.50E8	1.19E17
			A92	60.0	19.3	25.0	6.5	2.50E8	1.19E17
7	8	1986	A96	65.0	6.2	20.0	0.0	2.76E8	1.53E17
			A97	85.0	36.7	45.0	17.5	2.76E8	1.53E17
			A99	85.0	23.5	35.0	7.8	2.76E8	1.53E17

[a]Fluence rates (E > 1.0 MeV) are obtained by dividing the calculated values by the average C/E ratio of 0.69.

[b]Fluence values are obtained by multiplying the fluence rates by the effective full-power seconds.

[c]Still in reactor.

[d]Values not adjusted by (fine mesh/coarse mesh) correction factor. Adjusted values are 5% lower.

REFERENCES

1. W. A. Rhoades and R. L. Childs, *The TORT Three-Dimensional Discrete Ordinates Neutron/Photon Transport Code*, ORNL-6268, to be published at Oak Ridge Natl. Lab.

2. R. E. Maerker, "6.10 Analysis of Participant A," *LWR Pressure Vessel Surveillance Dosimetry Improvement Program: PCA Experiments and Blind Test*, NUREG/CR-1861, U.S. Nuclear Regulatory Commission, July 1981.

3. R. E. Maerker and M. L. Williams, *Calculations of Two Series of Experiments Performed at the Poolside Facility Using the Oak Ridge Research Reactor*, NUREG/CR-2696 (ORNL/TM-8326), U.S. Nuclear Regulatory Commission, May 1982.

4. M. L. Williams et al., *The ELXSIR Cross-Section Library for LWR Pressure Vessel Irradiation Studies, Part of the LEPRICON Computer Code System*, NP-3654, Electric Power Research Institute, Palo Alto, Calif., September 1984.

Appendix F

CONSEQUENCES OF VESSEL FAILURE

T. E. Cole J. R. McWherter

In view of the possibility that the present High Flux Isotope Reactor (HFIR) vessel integrity study would indicate some noncompliance with the American Society of Mechanical Engineers (ASME) Code, the early evaluation of the consequences of vessel failure[1] was reviewed, and a probabilistic fracture-mechanics analysis was performed in an effort to justify the possible noncompliance. The probabilistic fracture-mechanics study is included in this report as Appendix G, and a memorandum reviewing the early consequences evaluation is included in this appendix. As indicated by the review, failure of the vessel in a manner consistent with the very localized nature of the radiation-embrittlement would result in no consequences to the public.

REFERENCE

1. F. T. Binford, T. E. Cole, and E. N. Cramer, *The High Flux Isotope Reactor Accident Analysis*, ORNL-3573, Union Carbide Corp. Nuclear Div., Oak Ridge Natl. Lab., April 1967.

MARTIN MARIETTA

Internal Correspondence

MARTIN MARIETTA ENERGY SYSTEMS, INC.

February 9, 1987

RECEIVED
FEB 11 1987

R. D. Cheverton, Bldg. 9204-1, MS-6

HFIR Pressure Vessel — Public Consequences of a Failure

This memo is in response to your request that we assess the consequences of a failure of the HFIR pressure vessel in terms of the estimated radiation effects to the public. We have reviewed the HFIR descriptive report[1] and the HFIR accident analysis report[2] and we have examined the consequences of a pressure vessel failure relative to the HFIR maximum credible accident (MCA) and associated consequences. We have concluded that a failure of the pressure vessel concurrent with the HFIR MCA does not increase the consequences to the public beyond that resulting from the HFIR MCA. We also have concluded that a spontaneous failure of the pressure vessel during otherwise normal full power operation would result in public consequences of much smaller magnitude than those from the HFIR MCA.

In order to provide some perspective regarding the consequences of the HFIR MCA, Attachment 1 sets forth radiation dosage values for locations designated as significant by NRC. These values are taken from the accident analysis report.[2]

Before stating the bases for our conclusions, we believe that it should be noted that the primary coolant system of HFIR operates with bulk coolant temperatures below the boiling point of water at atmospheric pressure, the system has no free gas volume, and pressure is maintained by a balance between flow into the system from a pressurizer pump and flow out of the system via pressure controlled valves. For this system a change from 600 psi to atmospheric pressure requires only the release of about 33 gallons of water. As a consequence a major leak, while of great concern, would not in itself result in the great commotion attendant on a similar failure in an operating light water power reactor where the temperature, pressure and volume of the coolant system are such that a very large amount of stored energy relative to atmospheric conditions is present. In addition, we made several estimates of the rate of pressure decrease, the possible effects of transient flows induced by the rapid pressure change, etc. We did not find any significant effects and we conclude that this is not an area of critical concern.

---

[1]The High Flux Isotope Reactor, A Functional Description. ORNL-3572 (Rev. 2).

[2]The High Flux Isotope Reactor Accident Analysis - ORNL-3573.

The HFIR MCA is postulated to be "--- an extensive meltdown of the reactor core concurrent with a failure of the primary containment sufficiently severe to allow some of the fission products to escape directly into the building, but not violent enough to grossly rupture the reactor vessel or the high-pressure piping."[3] The primary containment referred to in this case was the reactor pressure vessel and the failure referred to was described as due to leaking flanges, broken beam tubes, etc.[4] To some extent the definition of the MCA may seem contradictory to other statements in the accident analysis; however, the MCA was chosen on the basis that it represented a reasonable upper bound on fission product releases from a broad range of accidents. The potential for physical damage resulting from discharge of the limited volume of water has been examined and was judged as not significant in terms of damage to the reactor pool.[5] The rupture of the reactor vessel concurrent with the MCA in terms of release of vessel pressure and an accompanying opening for fission products to escape to the pool, while not explicitly defined, is considered to be covered by the assumptions of vessel leakage which lead to the fission product release to the pool. It should be noted that the MCA definition is couched in terms of f.p. release not in terms of the size of the leak; the behavior would be relatively independent of leak or crack size. Gross rupture of the vessel as used in the accident analysis would include the effects of an explosion, blowing the top head off, etc. and this was judged to be sufficiently unlikely to allow it to be ruled out.

As a consequence of the assumptions made regarding vessel leakage during the MCA, we conclude that a pressure vessel failure of the type presently being considered, a through-the-wall crack, would not exacerbate the MCA in terms of public consequences.

For the case of a spontaneous rupture of the pressure vessel during normal operation, we believe the immediate effect would be a rapid decrease in primary system pressure. This decrease would trigger a complex series of events and associated phenomena as the reactor scrammed in response to the pressure decrease, the main pumps would trip, etc. It appears possible to construct a detailed mathematical model which might be useful in terms of providing a better understanding; however, many of the assumptions would be essentially guesses and therefore the results would be open to question. During the course of the HFIR accident analysis review, a question was raised by the ACRS regarding the thermal effects on the core of a rapid depressurization of the primary

---

[3]ORNL-3573, Section 6, p. 23, paragraph 2.

[4]ORNL-3573, top of page 20.

[5]ORNL-3573, Q&A, 59, page 206.

system.[6] An analysis of the effects of a step change in pressure from 40 atm. to 1 atm was made in response to the question. The results of the analysis indicated that the average core temperature reached only 648°F, well below the melting point. The hot-spot temperatures were calculated to reach 1210°F and it was judged that, even if a complete Al-U_3O_8 reaction were to proceed, the needed heat of fusion would not be available and melting would not occur. The results were followed by a disclaimer regarding the validity of the details, but the overall conclusion was that the maximum temperatures were fairly realistic.

For the latter case, it is our conclusion that a spontaneous failure of the pressure vessel would result in essentially no fission product release and therefore little or no consequences to the public.

Please let me know if you have questions on the above. We will be happy to discuss these results with you at your convenience.

T. E. Cole, Bldg. 9201-3, MS-2
Engineering Technology Division

J. R. McWherter
Consultant

cc: R. M. Harrington
A. L. Lotts
J. G. Merkle
J. H. Swanks
R. S. Wiltshire

---

[6]ORNL-3573, Q&A, 23.B-C, page 131.

Attachment 1

The doses set forth below for the HFIR MCA are taken from the HFIR accident analysis report, ORNL-3573, Table 1.6.1, page 26. The NRC 10CFR100 offsite radiation exposure reference values to which the HFIR MCA values may be compared are:

Exclusion Area Boundary, 2-hr dose:	25 rem, whole body 300 rem thyroid (due to iodine)
Low Population Boundary, ∞ dose:	25 rem, whole body 300 rem, thyroid (due to iodine)

The predicted 2-hour doses at the exclusion area boundary (2.82 km SE) are 2.8 rem to the thyroid, 13 rad whole-body gamma and 11 rad whole-body beta. The corresponding doses for infinite-time exposure at the low population boundary (5.72 km) are 1.5 rem to the thyroid, 7.2 rad whole-body gamma and 6.2 rad whole-body beta. The main body of ORNL lies at 1.34-2.06 km NNW-WNW and the 2-hour doses are: thyroid 3.5-4.8 rems, whole-body gamma 17-26 rads and whole-body beta 15-23 rads.

The MCA is based on a meltdown of not more than 50% of the fuel with discharge of the fission products to the atmosphere from the HFIR stack following washout, deposition, and filtration, as provided in the HFIR dynamic confinement system. Meteorological conditions were based on an average of "worst average" and "most representative" conditions for the area based on available information at that time. The percentage of time the wind direction is toward the cited locations is of the order of 3%. Preliminary estimates based on the present much more detailed data of hourly wind speeds and directions occurring during the year indicate that the dose values should be reduced by a factor of 1.5-2 from those estimated in the HFIR accident analysis report.

Appendix G

PROBABILITY OF FLAW PROPAGATION IN THE HFIR VESSEL

R. D. Cheverton D. G. Ball

The probability of flaw propagation has been estimated for the High Flux Isotope Reactor (HFIR) vessel using the OCA-P code,[1,2] which was developed at Oak Ridge National Laboratory (ORNL) as a part of the Heavy-Section Steel Technology (HSST) and Integrated Pressurized Thermal Shock (IPTS) programs. Consistent with Monte Carlo methodologies, OCA-P simulates a large number of vessels, each with a different combination of the various values of the different parameters involved in the analysis of flaw behavior. For each of these vessels and for a given loading condition, a deterministic fracture-mechanics analysis is performed (calculation of K_I, K_{Ic}, and K_{Ia}) to determine whether flaws will propagate through the wall. The probability of "failure" (through-wall cracking) for the specific loading condition is simply the number of vessels that fail divided by the number of vessels simulated. For a single vessel, the conditional probability of failure represents the chance of vessel failure when the load is applied. If a specific load is applied infrequently, the frequency of failure can be obtained from

$$\phi(F) = \sum_i \phi_i(E)\, P_i(F|E) , \qquad (G.1)$$

where

$\phi(F)$ = total frequency of failure,

$\phi_i(E)$ = frequency of event i,

$P_i(F|E)$ = probability of failure for event i.

The parameters simulated in OCA-P for the HFIR analysis include the fast neutron fluence at the inner surface of the vessel (F_o), the initial value of the reference nil-ductility temperature ($RTNDT_o$), the increase in RTNDT as a result of radiation damage (ΔRTNDT), the static crack-initiation fracture toughness (K_{Ic}), and flaw depth. Except for flaw depth, the distributions for the parameters were assumed to be normal; standard deviations and truncation values are shown in Table G.1.

The flaw-depth density function included in OCA-P was taken from the Marshall report[3] and is shown graphically in Fig. G.1. The corresponding equation is

$$f(a) = 4.1e^{-4.1a}, \text{ in.}^{-1} , \qquad (G.2)$$

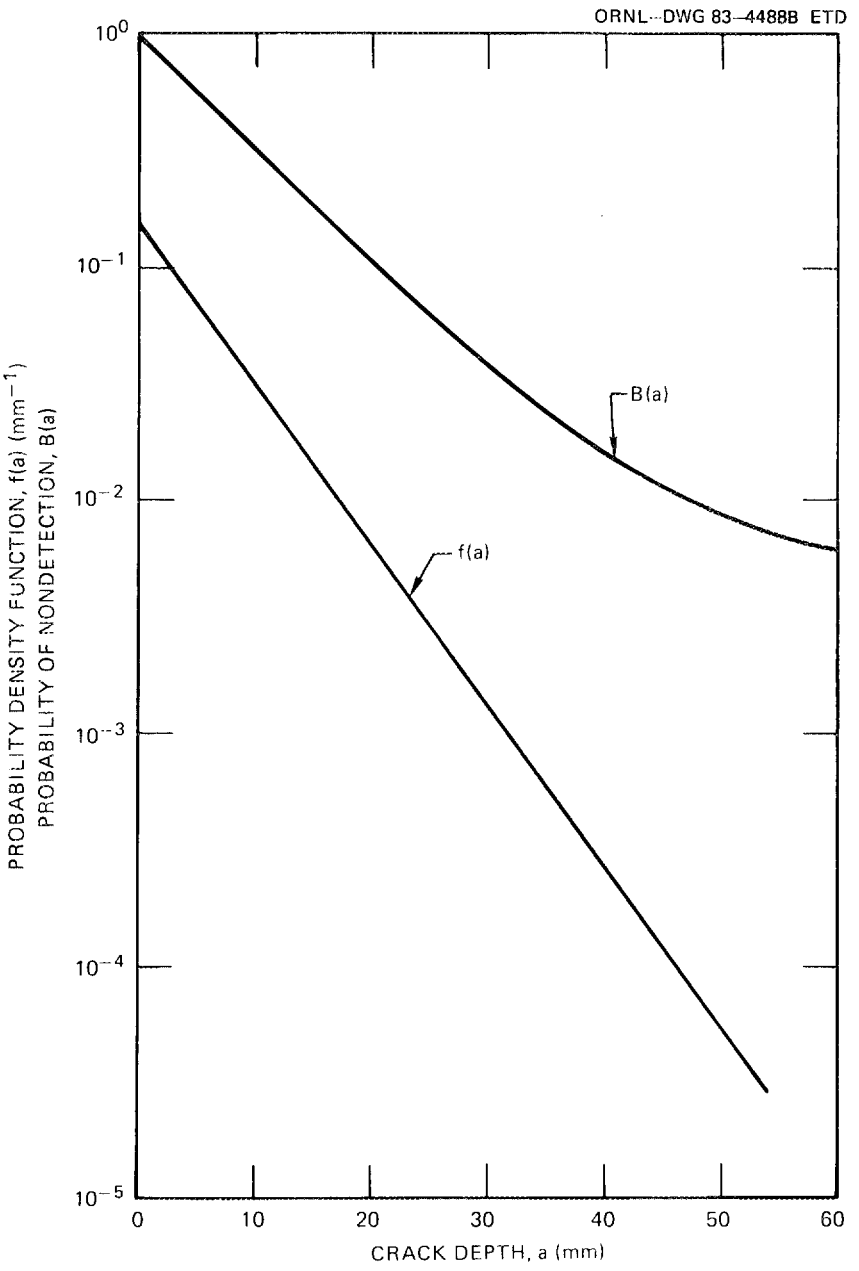

Fig. G.1. Flaw-depth-density and flaw-nondetection probability functions.

Table G.1. Parameters simulated in OCA-P

Parameter	Standard deviation (σ)	Truncation
$RTNDT_o$	$17°F^a$	a
$\Delta RTNDT$	$24°F^a$	a
K_{Ic}	$0.15\ \mu(K_{Ic})$	$\pm 4\sigma$
K_{Ia}	$0.10\ \mu(K_{Ia})$	$\pm 4\sigma$
Flaw depth		2.2 in.

$$^{a}\sigma_{(RTNDT)} = \left[\sigma^2_{(RTNDT_o)} + \sigma^2_{(\Delta RTNDT)}\right]^{1/2},$$

truncated at $\pm 3\sigma$.

where

a = crack depth, in.,
f(a) = (fraction of cracks with depths in the range a → a + da)/da.

Thus,

$$\int_{a=0}^{a=w} f(a)\ da = 1\ , \qquad (G.3)$$

where

w = wall thickness.

Equation (G.2) describes the flaw-depth density before preservice inspection and repair. To obtain the density corresponding to the time at which the vessel goes into service, Eq. (G.2) must be multiplied by the probability of nondetection associated with the final preservice inspection, the assumption being made that any flaw detected is repaired or otherwise disposed of. An expression for the probability of nondetection was also taken from the Marshall report.[3] It, too, is shown in Fig. G.1, and the corresponding equation is

$$B(a) = 0.005 + 0.995\ e^{-0.113a}\ , \qquad (G.4)$$

where

$B(a)$ = (number of cracks in the range $a \rightarrow a + da$ when vessel goes into service)/(total number of cracks in the range $a \rightarrow a + da$ before repairs).

Thus, the number of cracks in a specific region of the vessel with depths in the range Δa_i as the vessel goes into service is

$$P(\Delta a_i) = NA \int_{\Delta a_i} f(a)\, B(a)\, da\,, \qquad (G.5)$$

where

N = number of flaws of all sizes per unit surface area of specific region of vessel before preservice inspection,
A = surface area of specific region of vessel,
Δa_i = a specified range of crack depths about a_i such that $\sum_i \Delta a_i = w$.

Table G.2 lists the values of Δa_i and $\bar{a}_i$ that were used for the HFIR study.

Table G.2. Flaw depths and related data for 2-D flaws simulated in OCA-P

Δa_i (mm)	$\bar{a}_i$ (mm)	A^a	B^b
4.3180	2.1590	0.69121788	0.69121788
4.7235	6.6797	0.22306607	0.91428395
5.1670	11.6250	0.06445519	0.97873914
5.6522	17.0345	0.01655962	0.99529877
6.1829	22.9521	0.00376842	0.99906719
6.7635	29.4253	0.00076296	0.99983014
7.3986	36.5063	0.00014054	0.99997069
8.0933	44.2523	0.00002481	0.99999550
8.8533	52.7255	0.00000450	1.00000000

$$a_A = \int_{\Delta a_i} f(a)\, B(a)\, da \Big/ \int_0^w f(a)\, B(a)\, da.$$

$$b_B = \sum_1^i \int_{\Delta a_i} f(a)\, B(a)\, da \Big/ \int_0^w f(a)\, B(a)\, da.$$

The conditional probability of vessel failure P(F|E) is obtained from

$$P(F|E) = \frac{N'_{fj}}{N'_{vj}} P_j(\Delta a_i) \ , \qquad (G.6)$$

where

N'_{fj} = actual number of failures calculated for vessels with a flaw in jth region,
N'_{vj} = actual number of vessels simulated that contain a flaw in the jth region.

Each term in Eq. (G.6) represents the probability of a flaw in the jth region resulting in vessel failure.

The flaw density N in Eqs. (G.5) and (G.6) is not well known. For the HFIR studies, a value obtained from Ref. 3 indicates that a volumetric density of ~0.03 flaws/ft^3 is reasonable for pressurized-water reactor (PWR) vessels. Converted to a surface density for HFIR, the value becomes 7×10^{-3} flaws/ft^2. According to Ref. 3, this flaw density includes embedded, as well as surface, flaws and flaws of all orientations. Because axially oriented surface flaws normal to the surface are of greatest concern, the flaw density used for HFIR tends to be conservative.

The fracture toughness of the HFIR vessel materials as a function of T — RTNDT was based on the fracture-toughness data included in Sect. XI of the ASME Code for light water reactor (LWR) vessels. Two crack-initiation fracture-toughness curves were defined: $\overline{K}_{Ic} = 1.43\ K_{Ic}$ and $\overline{K}_{Ic} = 1.25\ K_{IR}$, where K_{Ic} is the Code lower bound for static initiation and K_{IR} is the Code lower bound for the K_{Ia} data (the coefficients are derived in Ref. 1). The use of the former relation may not adequately account for the contribution of low-toughness sites; the latter relation, however, very likely overestimates the contribution. Thus, failure probabilistics were calculated using both.

P(F|E) was calculated for semielliptical surface flaws with a surface-length to depth ratio of six, and the flaws were assumed to be located in, or adjacent to, the HB-3 nozzle weld at the high-flux side of the nozzle (the high-flux zone is limited to an area of ~1 ft^2). A vessel life extension of ~10 years was considered, for which RTNDT = 140°F at the particular location. Two vessel temperatures (120 and 90°F) and four primary-system pressures were also considered. The temperatures correspond to possible extremes, and the pressures correspond approximately to the hydrostatic proof test, the relief-valve setting, the pressurizer-pump cutoff, and normal operation. Values of P(F|E) are included in Tables G.3 and G.4 for these pressures; as indicated, they are $<10^{-6}$. Values based on K_{Ia} data are less than a factor of 10 greater than those based on K_{Ic} data. When fuel is in the reactor, P(F|E) < 2×10^{-7}.

Tables G.3 and G.4 also contain estimates of the frequency of the specific events $\phi(E)$ and the corresponding frequencies of vessel failure $\phi(F)$. As indicated, these latter values are very small, ranging

Table G.3. Values of $P(F|E)$ and $\phi(F)$ for $RTNDT_o = 20°F$, $RTNDT = 140°F$, $N = 7.1 \times 10^{-3}$ flaws/ft^2, $A = 1.0$ ft^2, $\overline{K}_{Ic} = 1.43\ K_{Ic}$ (Code Lower Bound)

Condition	Pressure (psid)	$P(F\|E)$		$\phi(E)$ Y^{-1}	$\phi(F)$, failures/Y	
		$T_v = 90°F$	$T_v = 120°F$		$T_v = 90°F$	$T_v = 120°F$
Hydro test	900	1.3×10^{-7}	6.6×10^{-8}	1.0	1.3×10^{-7}	6.6×10^{-8}
Safety valve	680	3.2×10^{-8}	1.6×10^{-8}	0.1	3.2×10^{-9}	1.6×10^{-9}
PP cutoff	508	6.4×10^{-9}	2.7×10^{-9}	0.5	3.2×10^{-9}	1.4×10^{-9}
Normal operation	458	3.6×10^{-9}	1.2×10^{-9}			

Table G.4. Values of $P(F|E)$ and $\phi(F)$ for $RTNDT_o = 20°F$, $RTNDT = 140°F$, $N = 7.1 \times 10^{-3}$ flaws/ft^2, $A = 1.0$ ft^2, $\overline{K}_{Ic} = 1.25\ K_{IR}$

Condition	Pressure (psid)	$P(F\|E)$		$\phi(E)$ Y^{-1}	$\phi(F)$, failures/Y	
		$T_v = 90°F$	$T_v = 120°F$		$T_v = 90°F$	$T_v = 120°F$
Hydro test	900	5.8×10^{-7}	3.7×10^{-7}	1.0	5.8×10^{-7}	3.7×10^{-7}
Safety valve	680	1.6×10^{-7}	9.2×10^{-8}	0.1	1.6×10^{-8}	9.9×10^{-9}
PP cutoff	508	3.7×10^{-8}	2.0×10^{-8}	0.5	1.9×10^{-8}	1.0×10^{-8}
Normal operation	458	1.8×10^{-8}	9.9×10^{-9}			

from 1×10^{-9} to 6×10^{-7} failures/year. When fuel is in the reactor, $\phi(F) < 2 \times 10^{-8}$. The total frequency of failure associated with infrequent events with fuel in the reactor is $<4 \times 10^{-8}$ failures/year. The chance of failure during normal operation is $<2 \times 10^{-8}$.

Areas other than that around HB-3 will contribute to the probability of failure, but because of the lower values of RTNDT in these areas, the contribution is quite small.

Note that even if the assumed flaw density for HFIR were increased by a factor of 10, the calculated probabilities would still be very small ($<5 \times 10^{-6}$).

The acceptability of the estimated probabilities for HFIR can be evaluated to some extent by comparison with what the Nuclear Regulatory Commission (NRC) accepts for PWRs. As indicated in an NRC draft regulatory guide[4] pertaining to pressurized thermal-shock loading conditions, a frequency of failure of 5×10^{-6} failures/reactor year is permissible. Thus, even without considering the enormous difference in consequences of vessel failure for a large commercial PWR and the relatively small low-temperature HFIR, the calculated probabilities of vessel failure for HFIR appear to be acceptable.

REFERENCES

1. R. D. Cheverton and D. G. Ball, *OCA-P, A Deterministic and Probabilistic Fracture-Mechanics Code for Application to Pressure Vessels*, NUREG/CR-3618 (ORNL-5991), Martin Marietta Energy Systems, Inc., Oak Ridge Natl. Lab., May 1984.

2. D. G. Ball and R. D. Cheverton, *Adaptation of OCA-P, A Probabilistic Fracture-Mechanics Code, to a Personal Computer*, NUREG/CR-4468 (ORNL/CSD/TM-233), Martin Marietta Energy Systems, Inc., Oak Ridge Natl. Lab., January 1986.

3. W. Marshall, *An Assessment of the Integrity of PWR Pressure Vessels*, Second Report, United Kingdom Atomic Energy Authority, March 1982.

4. *Format and Content of Plant-Specific Pressurized Thermal-Shock Safety Analysis Reports for Pressurized Water Reactors, Draft Regulatory Guide and Value/Impact Statement*, U.S. Nuclear Regulatory Commission, Office of Nuclear Regulatory Research, January 1986.

Appendix H

ANALYSIS OF HYPOTHETICAL OVERLOAD TRANSIENTS

J. G. Merkle

During the original safety analysis[1] for the High Flux Isotope Reactor (HFIR), various transients were examined with regard to their credibility. The control system was designed to handle, without significant core damage, a reactivity addition consisting of the insertion of the worst possible void into the flux trap region with the target still present. This transient does not result in a significant increase in pressure loading on the vessel, and more severe transients, in terms of primary-system pressure buildup, are of such low probability that they are considered incredible. Even so, in response to an Advisory Committee on Reactor Safeguards (ACRS) question regarding energy absorption capability of the vessel, Oak Ridge National Laboratory (ORNL) considered more-severe reactivity transients. The evaluation is discussed in Ref. 1, and this study has been conducted to evaluate the effect of radiation damage to the vessel.

Several approaches were used in Ref. 1 for estimation; the most severe with respect to the vessel was based on the conservative assumption that a reactivity transient can release energy as fast as a TNT explosion. For this assumption, a semiempirical analysis based on experimental data obtained with scale models at the U.S. Naval Ordnance Laboratory (NOL)[2] was employed to calculate the allowable energy release in terms of pounds of TNT. The primary variables in this calculation are the vessel inner and outer radii, the unit weight and tensile properties of the vessel material, and the presence or absence of coolant in the vessel and water shielding around the vessel. The effects of weld flaws and nozzle-region strain concentrations were considered in the NOL analysis by employing a safety factor of three on strain tolerance. The NOL formula for the limiting energy release capacity is[2]

$$\overline{W}_{R_{max}}^{\frac{1}{0.811}} = \frac{0.1563\,(2\sigma_y + \sigma_u + \sigma_u\varepsilon_u)\,\varepsilon_u \left(3.41 + 0.117\,\frac{R_i}{h_o}\right)\left(\frac{w^{0.85}}{100}\right)\left(R_e^2 - R_i^2\right)^{1.85}}{\left(1.47 + 0.0373\,\frac{R_i}{h_o}\right)^{0.15} R_i^{0.15}}, \quad \text{(H.1)}$$

where

$(\overline{W}_R)_{max}$ = maximum explosive charge weight for real vessel without rupture, lb,

σ_y = yield stress, ksi,

σ_u = engineering ultimate stress, ksi,

ε_u = engineering ultimate tensile strain,* dimensionless,

R_i = vessel internal radius, ft,

R_e = vessel external radius, ft,

h_o = vessel wall thickness, ft,

w = wall unit weight, lb/ft^3.

Equation (H.1) includes the safety factor of three applied to the strain ε_u. In developing and applying Eq. (H.1) NOL[3,4] found that the safety factor of three provides a degree of conservatism sufficient to permit using the total elongation in place of the less commonly available uniform elongation as the value of ε_u. Subsequently, calculations for the HFIR vessel in the unirradiated condition were made on this basis by Wise.[1] The calculated energy release capacity of the HFIR primary system, expressed in terms of a weight of TNT, was 55 lb. The numerical values used as input to Eq. (H.1) for this calculation are shown in Table H.1. Because the tensile properties used by Wise were the minimum specified values,[5] the energy release capacity of the HFIR primary system still exceeds the originally calculated value, as explained below.

*An alternate definition was also developed by NOL for use only in combination with the safety factor of three. See the following discussion.

Table H.1. HFIR vessel characteristics relevant to the estimation of transient energy release capacity of the primary system

Tensile properties

Property	Unirradiated		Irradiated in HFIR, measured
	Minimum specified	Measured	
σ_y	38 ksi	47.1	56.5
σ_u	70 ksi	82.4	80.3
ε_t	22%	31	19.8

Other vessel characteristics

R_i = 3.9167 ft

R_e = 4.1667 ft

h_o = 0.25 ft

w = 490 lb/ft^3

As discussed in Appendix D (see Sects. D.4.3.5 and D.6.2.7), tensile tests were conducted by ORNL on both unirradiated and irradiated specimens from the A212B material in the HFIR vessel. The irradiated specimens were subsize specimens with a thickness of 0.03 in. Some of the unirradiated specimens were also subsize with the same thickness, and the rest were larger with a diameter of 0.20 in. There were no significant size effects in the unirradiated data. The irradiated specimens were machined from the broken halves of three surveillance specimens, and the unirradiated subsize specimens were machined from two companion unirradiated archive specimens, as indicated in Table D.23 of Appendix D. The 0.2-in.-diam unirradiated tensile specimens were machined from Charpy blanks taken from the nondestructive examination (NDE) nozzle dropout. Table H.1 lists the tensile properties used analytically in the present study. The measured unirradiated data are the average values for the 0.2-in.-diam specimens. The irradiated data are the average values for the four specimens taken from the broken halves of surveillance specimen No. A140.

The fluence at the HB-3 weld on the core horizontal midplane (HMP) is greater than the fluence at the A212B surveillance specimen locations. Therefore, it is necessary to estimate the tensile properties at the governing location in the vessel by extrapolation. The mode of failure relevant to the energy containment calculation is tensile instability in the plastic range. Residual stresses will have no effect, and the tensile instability load should be governed by the through-thickness average ductility at the location of least ductility. This quantity was estimated as the through-thickness average ductility near the HB-3 weld at the core HMP, based on the through-thickness average flux relative to the flux at the surveillance specimen location.

Referring to Table 5.2, the through-thickness average flux near the HB-3 weld was estimated as the average of the inside-surface flux in the nozzle weld adjacent to the nozzle forging (5.30×10^8 n/cm^2•s) and the outside surface flux in the adjoining base metal (2.96×10^8 n/cm^2•s). Thus, the estimated through-thickness average flux is 4.13×10^8 n/cm^2•s. The surveillance specimen flux is given in Table 5.2 as 2.68×10^8 n/cm^2•s. Thus, the ratio of the fluence at the governing location after a service life extension of 10 effective full-power years (EFPY) and the fluence at the surveillance specimen location in 1986 is

$$\frac{\Phi}{\Phi_{REF}} = \frac{4.13\ [17.53 + (10)(0.846)]}{(2.68)(17.53)} = 2.28 \ .$$

As noted in Sect. D.6.3.3 of Appendix D, the damage trends for the HFIR surveillance data are well represented by a power-law expression in which the exponent has the value of 0.25. Thus, the ratio of the change in total elongation at the governing location to that determined from the 1986 surveillance material is estimated to be

$$\frac{\Delta\varepsilon_t}{\Delta\varepsilon_{t,REF}} = (2.28)^{0.25} = 1.23 \ ,$$

and the total elongation at the governing location at the end of the additional 10-EFPY operating period is estimated to be

$$\varepsilon_t = 31 - 1.23\ (31 - 19.8) = 17.2\% \ .$$

A conservative calculation of the minimum total elongation for which the energy release capacity of the HFIR primary system will still be equal to, or greater than, that calculated by Wise[1] for the vessel in its original condition can be made by solving Eq. (H.1) for ε_u. For the vessel characteristics given in Table H.1, Eq. (H.1) becomes

$$(\overline{W}_R)_{max}^{\frac{1}{0.811}} = 4.262\ (2\sigma_y + \sigma_u + \sigma_u\varepsilon_u)\ \varepsilon_u \ . \qquad (H.2)$$

Based on the minimum specified unirradiated tensile properties given in Table H.1, the calculated value of $(\overline{W}_R)_{max}$ is 58.6 lb. Evidently, the 55 lb given by Wise was rounded down to the nearest 5 lb. Using the above calculated value of $(\overline{W}_R)_{max}$ and the irradiated yield and ultimate tensile stresses given in Table H.1, with no allowance for their further increase during the additional 10-EFPY operating period, Eq. (H.2) can be solved as a quadratic for ε_u, giving $\varepsilon_u = 17.1\%$. Because the calculated value of ε_t at the end of the additional 10-EFPY operating period exceeds this value, it follows that the capability of the HFIR vessel for energy containment will remain greater than the originally calculated value of 55 lb of TNT during an additional 10-EFPY operating period.

REFERENCES

1. F. T. Binford, T. E. Cole, and E. N. Cramer, *The High Flux Isotope Reactor Accident Analysis*, ORNL-3573, Union Carbide Corp. Nuclear Div., Oak Ridge Natl. Lab., April 1967.

2. W. R. Wise, Jr. and J. F. Proctor, *Explosion Containment Laws for Nuclear Reactor Vessels*, NOLTR 63-140, U.S. Naval Ordnance Lab., White Oak, Md., August 16, 1965.

3. Personal communication between J. F. Proctor, U.S. Naval Surface Weapons Lab., White Oak, Md., and J. G. Merkle, Oak Ridge Natl. Lab., Oak Ridge, Tenn., February 12, 1987.

4. Personal communication between W. R. Wise, Pittsford, N.Y., and J. G. Merkle, Oak Ridge Natl. Lab., Oak Ridge, Tenn., April 7, 1987.

5. "Tentative Specification for High Tensile Strength Carbon-Silicon Steel Plates for Boilers and Other Pressure Vessels," pp. 501–3 in *1955 Book of ASTM Standards, Part 1*, ASTM A 212-54aT, American Society for Testing Materials, Philadelphia, Pa., 1955.

Appendix I

CONSEQUENCES OF CRACK EXTENSION

J. G. Merkle

I.1 INTRODUCTION

Although no recordable indications have been found in the High Flux Isotope Reactor (HFIR) vessel during previous inspections, and linear elastic fracture mechanics (LEFM) analysis shows that even a flaw 1 in. deep will not propagate, the consequences of hypothetical crack extension have been investigated. Three through-wall propagating crack configurations have been studied. The first configuration is a through-wall crack propagating axially in both directions from the HB-3 nozzle weld at its intersection with the core horizontal midplane. The second configuration is a through crack propagating from the same origin but following the HB-3 nozzle-to-cylinder weld. The third configuration is a through crack propagating axially in the plane containing the nozzle axis, originating either in the HB-3 nozzle weld or at the inside nozzle corner. The crack running axially from the core horizontal midplane has the greatest tendency for continued propagation, but based on average crack-arrest toughness properties, it will be arrested. Based on even lower-bound crack-arrest toughness properties, the other two crack paths lead to arrest.

I.2 CRACK RUNNING AXIALLY FROM THE CORE HORIZONTAL MIDPLANE

A reasonable procedure for analyzing a through-wall crack running axially from the HB-3 nozzle weld at the core horizontal midplane is to assume that it can run beyond the height of both the core and the nozzle and to analyze it as an axial through crack in a pressurized cylinder. At a height of 15 in. above the core horizontal midplane, the midwall neutron flux should be essentially equal to the value determined by the two-dimensional analysis, which, from Fig. E.21, is 0.44×10^8 n/cm^2•s. For this analysis, the midwall flux at that height will be assumed to be 0.5×10^8 n/cm^2•s.

For a through-crack propagating in the axial direction, the governing toughness corresponds to the LT orientation. Using Eq. (8) in Chap. 5 and referring to Table 5.2, the rate of increase of RT_{NDT} with time at full power is given by

$$S_{FP} = 4.28 \left(\frac{0.5}{2.68}\right) = 0.799°F/year.$$

Therefore,

$$RT_{NDT-86} = 20 + (17.53)(0.799) = 34°F ,$$

and for Δt = 3 years* and P = 84.6 MW,

$$RT_{NDT} = 34 + (0.846)(3)(0.799) = 36°F .$$

For a midwall temperature of 107.5°F, $T - RT_{NDT}$ = 71.5°F and K_{IR} = 61.86 ksi•$\sqrt{in.}$ It is unlikely that this lower-bound toughness would be sufficient to arrest a 30-in.-long running crack. However, to be more realistic about the likelihood of arrest of this hypothetical running crack, it is reasonable to use an estimate of the mean crack-arrest toughness instead of a lower bound. Based on the observation of Cheverton and Ball,[1] an estimate can be made that the average crack-arrest toughness implied by a compilation of thick-section thermal-shock and wide-plate crack-arrest data is 75% above the lower bound (Fig. I.1). Thus, the governing

*Note that the calculations in this appendix were based on a life extension of 3 years. However, for a life extension of 10 years, the toughnesses decrease only slightly and the results remain qualitatively the same.

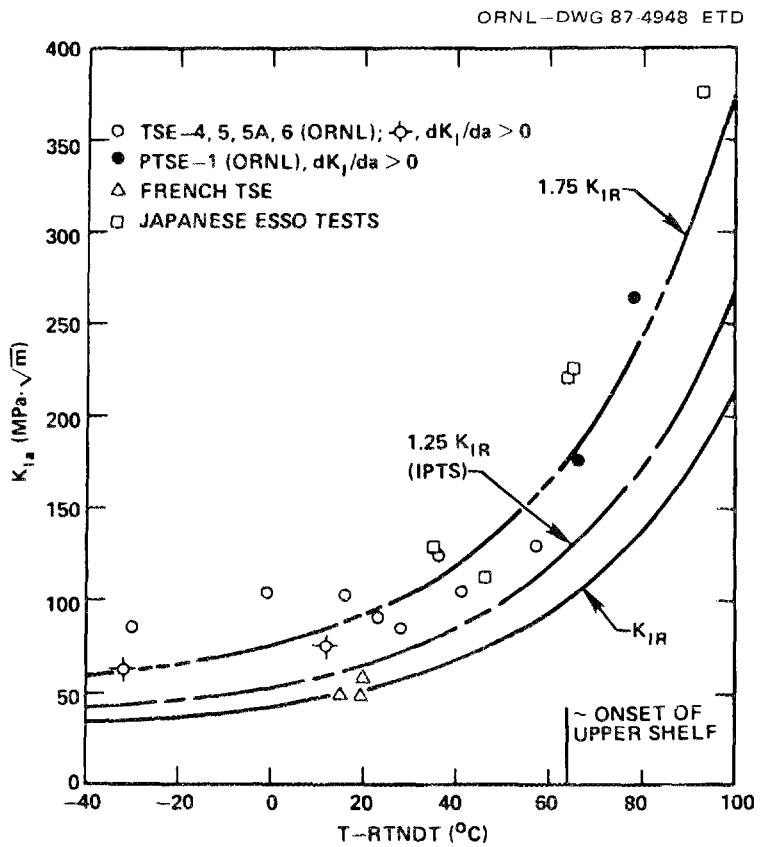

Fig. I.1. Comparison of large specimen crack-arrest data with curves representing K_{IR}, 1.25 K_{IR}, and 1.75 K_{IR}. *Source*: R. D. Cheverton and D. G. Ball, "The Role of Crack Arrest in the Evaluation of PWR Pressure Vessel Integrity During PTS Transients," *Eng. Fract. Mech.* 23(1), 71–80 (1986).

crack-arrest toughness is

$$K_{Ia} = 1.75\ K_{IR} = 108\ \text{ksi}\cdot\sqrt{\text{in.}}$$

For an axial through crack in a thin, pressurized cylinder, the geometry factor in Eq. (14) of Chap. 5 is given by[2]

$$C = \sqrt{1 + 1.61\,\frac{a^2}{Rt}} \quad . \tag{I.1}$$

For a = 15 in., R = 47 in., and t = 3 in.,

$$C = 1.889 \ .$$

For a pressure of 508 psi, the average hoop stress is given by

$$\sigma = p\left(\frac{R}{t}\right) = 7.96\ \text{ksi} \ ,$$

and the applied stress-intensity factor is given by

$$K_I = C\,\sigma\sqrt{\pi a} = (1.889)(7.96)\sqrt{\pi(15)} = 103\ \text{ksi}\cdot\sqrt{\text{in.}}$$

In this calculation, a crack-tip plastic zone size is not added to the crack length because recent Heavy-Section Steel Technology (HSST) Program wide-plate crack-arrest tests have shown that the plastic zone size for a fast running crack is very small.[3] Because the average crack-arrest toughness exceeds the applied value of K_I, crack arrest is predicted.

The reasonableness of the foregoing analysis can be demonstrated by plotting the estimated crack-arrest toughness and the applied value of K_I, along with the measured crack-arrest toughness data for A212B steel obtained by Nordell and Hall[4] (Fig. I.2). Besides justifying the prediction of crack arrest for an axial through crack, Fig. I.2 also shows the conservatism of applying the K_{IR} curve to A212B steel. The nil-ductility transition (NDT) value used for plotting Fig. I.2 is 20°F, a value estimated by Irwin[5] probably because it is the temperature at which the longitudinal Charpy V-notch impact energy is close to 15 ft-lb.[6]

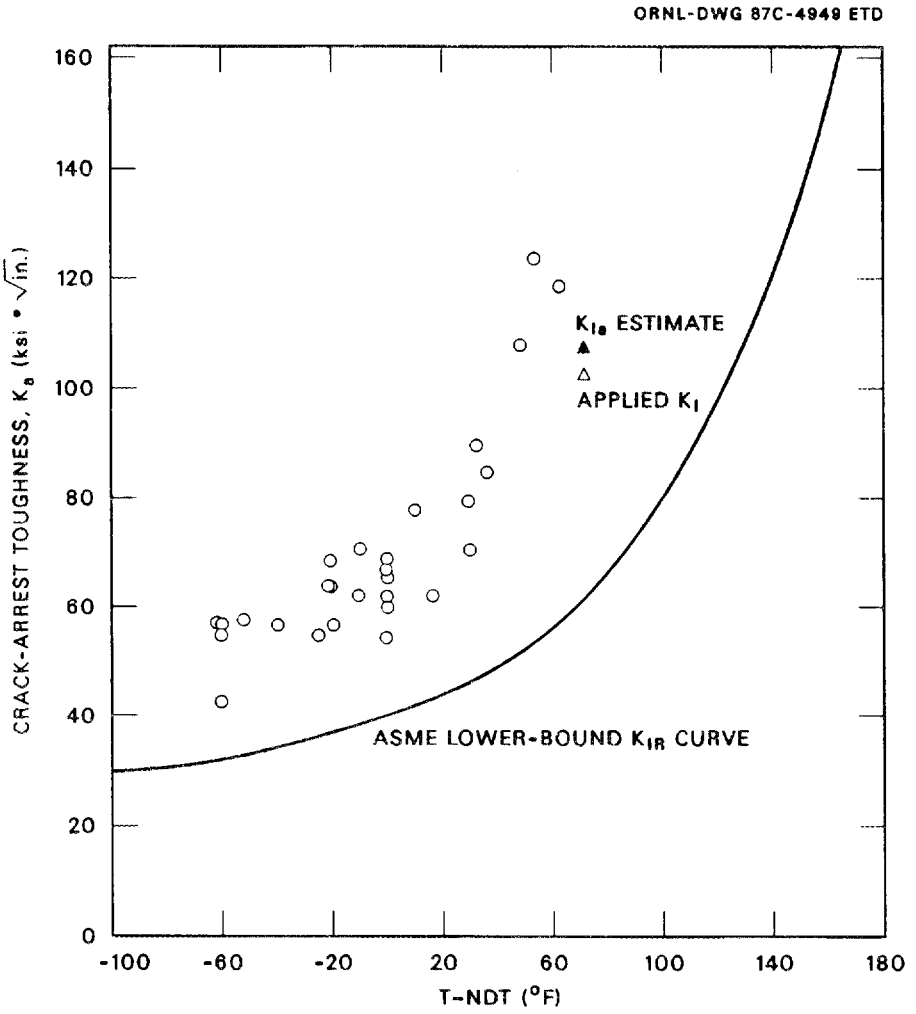

Fig. I.2. Comparison of estimated K_I and K_{Ia} values for a hypothetical 30-in.-long axial propagating crack in the HFIR vessel with crack-arrest toughness data from wide-plate tests for A212B steel [*source*: W. J. Nordell and W. J. Hall, "Two Stage Fracturing in Welded Wide Steel Plate," *Weld. J.*, Research Supplement, 44(3), 124-s to 134-s (1965)] and the K_{IR} curves.

I.3 CIRCULAR CRACK FOLLOWING THE HB-3 NOZZLE WELD

Because the HB-3 nozzle-to-cylinder weld is a controlling region with regard to fracture safety, the case of hypothetical crack extension following this weld was considered. The assumed origin of crack extension is the HB-3 nozzle-to-cylinder weld at the core horizontal midplane, and the crack describes a circular arc of 10-in. radius, propagating in both directions following the weld. Two modes of crack extension occur simultaneously: Mode I involving crack opening and Mode II involving forward shear. Mode III, involving transverse shear, may also occur

because of vessel internal pressure, but its interaction with the other two modes should be negligible because it makes no contribution to the mean tensile stress near the crack tip.

The stress-intensity factor solutions for this problem appear in the handbook by Rooke and Cartwright.[7] The solutions take the forms

$$\frac{K_I}{\sigma_\theta\sqrt{\pi R_1}} = \sqrt{\sin\theta}\left[G_1(0,\theta) + \frac{\sigma_z}{\sigma_\theta} G_1\left(\frac{\pi}{2},\theta\right)\right] \tag{I.2}$$

and

$$\frac{K_{II}}{\sigma_\theta\sqrt{\pi R_1}} = \sqrt{\sin\theta}\left[G_2(0,\theta) + \frac{\sigma_z}{\sigma_\theta} G_2\left(\frac{\pi}{2},\theta\right)\right] , \tag{I.3}$$

where θ is the position angle of the upper crack tip measured from the core horizontal midplane, the factors G_1 and G_2 are functions of the angles defining the stress axis and the crack-tip locations, and R_1 is the radius of the crack path. For a vessel internal pressure of 508 psi and a transverse residual stress of 1.7 ksi,

$$\frac{\sigma_z}{\sigma_\theta} = 0.588 .$$

At fracture the interaction of Modes I and II is assumed to be governed by the relationships suggested by Hellan,[8]

$$\frac{K_I}{K_{Ic}} + \left(\frac{K_{II}}{K_{IIc}}\right)^2 = 1 , \tag{I.4}$$

and

$$K_{IIc} = \sqrt{\frac{2}{3}}\, K_{Ic} . \tag{I.5}$$

Substituting K_{IR} for K_{Ic}, combining Eqs. (I.4) and (I.5), and generalizing the result give

$$\frac{K_I}{K_{IR}} + 1.5\left(\frac{K_{II}}{K_{IR}}\right)^2 = \lambda , \tag{I.6}$$

where propagation occurs for $\lambda > 1$ and arrest occurs if $\lambda < 1$. Using the midthickness toughness at the core horizontal midplane, which is quite conservative, $RT_{NDT} = 116.8°F$ at the end of the additional 3-year operating period, $T - RT_{NDT} = -9.3°F$, and $K_{IR} = 37.65$ ksi$\cdot\sqrt{\text{in.}}$ Figure I.3 shows the variation of the propagation parameter λ with angle θ. Propagation can occur for $\theta > 30°$, but arrest occurs near $\theta = 90°$, meaning that the hypothetical crack cannot propagate more than half-way around the nozzle-to-cylinder weld.

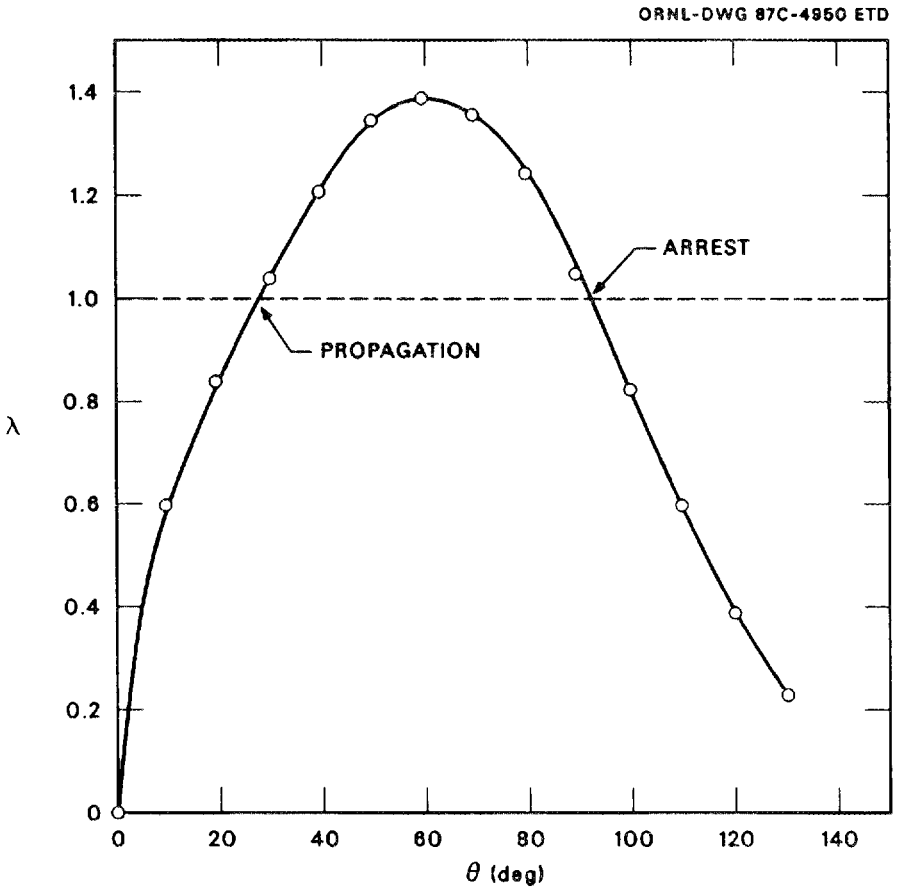

Fig. I.3. Variation of the crack propagation parameter λ with crack-tip position angle θ for hypothetical crack propagating in combined Modes I and II around the HB-3 nozzle-to-cylinder weld.

I.4 CRACK EXTENDING AXIALLY ABOVE THE NOZZLE AXIS

For the hypothetical extension of an axial crack above the nozzle axis, it is assumed that the crack either originates at, or extends to, the inside nozzle corner and, also, to some distance above the nozzle

axis. For this analysis, it will be determined if the crack could propagate beyond a distance of 15 in. above the nozzle axis.

The crack configuration is analyzed as a crack extending radially from a hole in a plate under biaxial loading. For this configuration, the stress distribution is separated into an equibiaxial component and a uniaxial component, and the stress-intensity factor is written as[9]

$$K_I = (F_{1B}\,\sigma_B + F_{1U}\,\sigma_U)\,\sqrt{\pi\,L}\quad , \tag{I.7}$$

where the subscripts on the nondimensional geometry factors denoted by F indicate the number of radial cracks (one in this case) and the stress component (biaxial or uniaxial), respectively, and L is the crack length measured from the edge of the hole. The F factors are functions of L/R_2, where R_2 is the hole radius. For

$$\frac{L}{R_2} = \frac{15 - 4}{15} = 2.75\quad ,$$

$F_{1B} = 0.95$ and $F_{1U} = 0.97$. For 2:1 biaxial loading, $\sigma_B = \sigma_U = pr/2t$, and for $p = 508$ psi, the value of K_I is given by

$$K_I = (0.96)(7.96)\sqrt{\pi(11)} = 44.92\ \text{ksi}\cdot\sqrt{\text{in.}}$$

Because this value is less than the value of K_{IR} 15 in. above the core horizontal midplane, crack arrest will occur. Thus, crack arrest occurs for all three crack configurations.

REFERENCES

1. R. D. Cheverton and D. G. Ball, "The Role of Crack Arrest in the Evaluation of PWR Pressure Vessel Integrity During PTS Transients," *Eng. Fract. Mech.* 23(1), 71–80 (1986).

2. G. T. Hahn, M. Serrate, and A. R. Rosenfield, "Criteria for Crack Extension in Cylindrical Pressure Vessels," *Int. J. Fract. Mech.* 5, 187–210 (1969).

3. D. J. Naus et al., *Crack Arrest Behavior in SEN Wide-Plates of Quenched and Tempered A533B Steel Tested Under Nonisothermal Conditions*, ORNL-6388, Martin Marietta Energy Systems, Inc., Oak Ridge Natl. Lab., August 1987.

4. W. J. Nordell and W. J. Hall, "Two Stage Fracturing in Welded Wide Steel Plate," *Weld. J.*, Research Supplement, 41(3), 124-s to 134-s (1965).

5. G. R. Irwin et al., *Basic Aspects of Crack Growth and Fracture*, NRL Report 6598, U.S. Naval Res. Lab., Washington, D.C., November 21, 1967.

6. W. J. Hall, W. J. Nordell, and W. H. Munse, "Studies of Welding Procedures," *Weld. J.*, Research Supplement, 41(11), 505-s to 518-s (November 1962).

7. D. P. Rooke and D. J. Cartwright, *Compendium of Stress Intensity Factors*, Her Majesty's Stationery Office, London, 1976.

8. K. Hellan, *Introduction to Fracture Mechanics*, McGraw-Hill, New York, 1984.

9. P. C. Paris and G. C. Sih, "Stress Analysis of Cracks," pp. 30–83 in *Fracture Toughness Testing and Its Applications*, ASTM STP 381, American Society for Testing and Materials, Philadelphia, 1965.

Internal Distribution

1. J. L. Anderson
2. C. A. Baldwin
3. D. G. Ball
4. S. J. Ball
5. J. Bentley
6. D. N. Braski
7. W. K. Brown
8. S. E. Burnette
9. J. A. Carter
10-19. R. D. Cheverton
20. R. L. Childs
21. T. E. Cole
22. D. H. Cook
23. B. L. Corbett
24 W. R. Corwin
25. W. G. Craddick
26. T. L. Dahl
27. M. B. Farrar
28. K. Farrell
29. R. E. Fenstermaker
30. J. A. Getsi
31. G. M. Goodwin
32. T. P. Hamrick
33. R. M. Harrington
34. T. L. Hebble
35. J. T. Hummel
36. S. S. Hurt
37. S. K. Iskander
38. M. L. Jones
39. F. B. K. Kam
40-49. A. L. Lotts
50. R. E. Maeker
51. P. J. Maziasz
52. D. M. McGinty
53. J. R. McWherter
54. P. E. Melroy
55-64. J. G. Merkle
65. J. R. Merriman
66. M. K. Miller
67. B. H. Montgomery
68. F. R. Mynatt
69-78. R. K. Nanstad
79. D. J. Naus
80. T. W. Pickel
81. H. B. Piper
82. C. E. Pugh
83. W. A. Rhoades
84. P. L. Rittenhouse
85. A. F. Rowcliffe
86. S. Spooner
87. R. M. Stinnett
88. W. E. Thomas
89. K. R. Thoms
90. P. J. Thornton
91. H. E. Trammell
92. D. B. Trauger
93. L. R. Williams
94. R. S. Wiltshire
95. A. Zucker
96. ORNL Patent Section
97. Central Research Library
98. Document Reference Section
99-100. Laboratory Records Department
101. Laboratory Records (RC)
102-121. Research Reactors Division Library

External Distribution

122. Office of Assistant Manager for Energy Research and Development, U.S. Department of Energy, Oak Ridge Operations Office, Oak Ridge, TN 37831
123. S. W. Ahrends, U.S. Department of Energy, Oak Ridge Operations Office, Downtown Concourse, Oak Ridge, TN 37831
124. G. A. Arlotto, Division of Engineering, Nuclear Regulatory Commission, Washington, DC 20555
125. Dr. S. H. Bush, Review & Syntheses Associates, 630 Cedar Avenue, Richland, WA 99352

126. W. C. Gilbert, U.S. Department of Energy, Oak Ridge Operations Office, Oak Ridge, TN 37831
127. Dr. A. N. Goland, Brookhaven National Laboratory, Building 179-A, Upton, NY 11973
128. Dr. J. M. Hendrie, Brookhaven National Laboratory, Building 179-A, Upton, NY 11973
129. E. E. Hoffman, U.S. Department of Energy, Oak Ridge Operations Office, Oak Ridge, TN 37831
130. T. M. Jelinek, U.S. Department of Energy, Oak Ridge Operations Office, Oak Ridge, TN 37831
131. G. R. Irwin, 7306 Edmonston Avenue, College Park, MD 20740
132. G. C. Manthey, U.S. Department of Energy, Oak Ridge Operations Office, Oak Ridge, TN 37831
133-143. C. L. Matthews, U.S. Department of Energy, Oak Ridge Operations Office, Oak Ridge, TN 37831
144. Michael E. Mayfield, Division of Engineering, Nuclear Regulatory Commission, Washington, DC 20555
145. Dr. D. J. Michel, Department of Mechanical Engineering, Naval Post Graduate School, Monterey, CA 93940
146. L. K. Price, U.S. Department of Energy, Oak Ridge Operations Office, Oak Ridge, TN 37831
147. P. N. Randall, Division of Engineering, Nuclear Regulatory Commission, Washington, DC 20555
148. J. D. Rothrock, U.S. Department of Energy, Oak Ridge Operations Office, Oak Ridge, TN 37831
149. C. Z. Serpan, Division of Engineering, Nuclear Regulatory Commission, Washington, DC 20555
150. D. W. Sheffey, U.S. Department of Energy, Oak Ridge Operations Office, Oak Ridge, TN 37831
151. Dr. P. G. Shewmon, 2477 Lytham Road, Columbus, OH 43220
152. L. E. Steele, 7624 Highland Street, Springfield, VA 22150
153. J. R. Strosnider, Region I, Nuclear Regulatory Commission, 631 Park Avenue, King of Prussia, PA 19406
154. A. P. L. Turner, Dominion Engineering, 6862 Elm Street, Suite 460, McClean, VA 22102
155. D. L. Underwood, U.S. Department of Energy, Oak Ridge Operations Office, Concourse Bldg., Oak Ridge, TN 37831
156. M. Vagins, Division of Engineering, Nuclear Regulatory Commission, Washington, DC 20555
157. Dr. J. R. Weeks, Brookhaven National Laboratory, Building 703, Upton, NY 11973
158-167. Office of Scientific and Technical Information, P.O. Box E, Oak Ridge, TN 37831